



**Naval Research Laboratory**

Washington, DC 20375-5320

NRL/MR/6720--01-8538

# **Advanced Radiation Theory Support — Annual Report 2000, Final Report**

JACK DAVIS  
RADIATION HYDRODYNAMICS BRANCH

*Plasma Physics Division*

May 21, 2001

20010628 042

Approved for public release; distribution is unlimited.

REPORT DOCUMENTATION PAGE			Form Approved OMB No. 0704-0188	
Public reporting burden for this collection of information is estimated to average 1 hour per response, including the time for reviewing instructions, searching existing data sources, gathering and maintaining the data needed, and completing and reviewing the collection of information. Send comments regarding this burden estimate or any other aspect of this collection of information, including suggestions for reducing this burden, to Washington Headquarters Services, Directorate for Information Operations and Reports, 1215 Jefferson Davis Highway, Suite 1204, Arlington, VA 22202-4302, and to the Office of Management and Budget, Paperwork Reduction Project (0704-0188), Washington, DC 20503.				
1. AGENCY USE ONLY (Leave Blank)	2. REPORT DATE May 21, 2001	3. REPORT TYPE AND DATES COVERED Final Report		
4. TITLE AND SUBTITLE Advanced Radiation Theory Support — Annual Report 2000, Final Report			5. FUNDING NUMBERS	
6. AUTHOR(S) Jack Davis and Radiation Hydrodynamics Branch				
7. PERFORMING ORGANIZATION NAME(S) AND ADDRESS(ES) Naval Research Laboratory Washington, DC 20375-5320			8. PERFORMING ORGANIZATION REPORT NUMBER NRL/MR/6720--01-8538	
9. SPONSORING/MONITORING AGENCY NAME(S) AND ADDRESS(ES) Defense Threat Reduction Agency 6801 Telegraph Road Alexandria, VA 22310			10. SPONSORING/MONITORING AGENCY REPORT NUMBER	
11. SUPPLEMENTARY NOTES This research was sponsored by the Defense Threat Reduction Agency under Job Order Title "Advanced Radiation Theory Support," MIPR No. 00-2022.				
12a. DISTRIBUTION/AVAILABILITY STATEMENT Approved for public release; distribution is unlimited.			12b. DISTRIBUTION CODE	
13. ABSTRACT (Maximum 200 words)  This report describes the work of the Radiation Hydrodynamics Branch during FY 2000 in support of the DTRA PRS program. Critical issues covered are: (1) novel load designs for improving PRS loads, (2) analyzing spatially resolved line spectra emitted by Z pinches, (3) the development of multidimensional radiation transport schemes for use in multidimensional magnetohydrodynamics codes, (4) wire array dynamics and modeling, (5) hydrodynamic modeling of nested-plasma Z pinches, (6) the role of electron viscosity in plasma shock heating, and (7) improved bremsstrahlung radiation production by electrode decontamination.				
14. SUBJECT TERMS Decade Enhanced energy dissipation Diagnostic line ratios Longtime implosions Large radius implosions Radiation MHD Transport coefficients Z pinch physics Rayleigh-Taylor instability Plasma radiation source			15. NUMBER OF PAGES 204	
			16. PRICE CODE	
17. SECURITY CLASSIFICATION OF REPORT UNCLASSIFIED	18. SECURITY CLASSIFICATION OF THIS PAGE UNCLASSIFIED	19. SECURITY CLASSIFICATION OF ABSTRACT UNCLASSIFIED	20. LIMITATION OF ABSTRACT UL	

# CONTENTS

Executive Summary .....	v
I. A Load Design Proposal .....	1
II. Analyzing Spatially Resolved Line Spectra Emitted by Z Pinches .....	11
III. An Efficient Non-Lte Radiation Transport Model Suitable for Multidimensional Hydrodynamics Calculations .....	32
IV. Wire Load Dynamics and Modeling .....	65
V. Hydrodynamic Modeling of Nested-Plasma Z Pinches .....	99
VI. A Role for Electron Viscosity in Plasma Shock Heating .....	156
VII. Improved Bremsstrahlung Radiation Production by Electrode Decontamination .....	188

## EXECUTIVE SUMMARY

This report describes the theory support of DTRA's Plasma Radiation Source (PRS) program carried out by NRL's Radiation Hydrodynamics Branch (Code 6720) in FY 2000. Included is work called for in DTRA MIPR 00-2022 - "Plasma Radiation Theory Support" and in Sandia National Laboratories document number 8591 - "Diagnostic and Spectroscopic Calculations and Analysis".

This was a year for testing K-shell yield scaling with atomic number on the Z machine at Sandia National Laboratories. Z's capability of driving a PRS load with 15-20 mega-amperes of current allowed us to explore higher Z plasma radiation source (PRS) loads like nickel ( $z=28$ ) and copper ( $z=29$ ). The experimental nickel, and copper K-shell yields of 16 kJ and 12 kJ, respectively, are world records. Another world record yield was also set on Z for argon, 275 kJ. This was a major accomplishment considering that it was the first time a gas puff experiment had ever been fielded on the Z machine. This record argon yield was large enough to be in the so called "efficient" scaling regime and it represents the first time an efficient argon yield was ever achieved using a large radius nozzle. Given this success, it would be interesting to further explore the atomic number scaling of K-shell emission by imploding a krypton gas puff load on Z. These recent record yields along with previous titanium and stainless steel yields give us confidence that the basic ideas about PRS behavior that have been developed over the years by Code 6720 are valid and provide DTRA with a reasonable foundation upon which future PRS experiments can be designed and built.

Given that it may be some time before the Z machine is upgraded, and given that the Decade Quad will be only a 5 MA to 8 MA machine, it will be awhile before K-shell yields are substantially increased or substantially extended in energy and efficiency due to higher driving currents. Therefore, in order to increase yields with our present inventory of machines supplying the drive current, it becomes increasingly important to fine tune our PRS knowledge so that we can design higher performance PRS loads. This fine tuning has been initiated by substantial progress in many aspects of PRS technology. In this report the progress made in load design, model development and assessment, and in diagnostic development for the purpose of fine tuning our understanding of Z-pinch behavior is discussed section by section:

(1) Experience has taught us that improved symmetry and stability are the keys to better load design. Indeed, it was close consideration of these key issues that allowed Sandia National

Laboratories to achieve their record radiative powers with wire array loads on the Saturn machine, which ultimately led to dramatic changes in their entire fusion program. A proven method for achieving better initial load symmetry is to use more wires. However, the drive power of the machine sets limits on the amount of mass that can be imploded and ionized to the K-shell. This in turn limits the number of wires that can be used in an experiment because of the practical limitations on the minimum mass-per-unit-length of wire that can be manufactured. In order to (1) improve comparisons between theory and experiment, (2) avoid the problems and uncertainties associated with wire gap spacing, or for gas puffs, uncertainties in the initial gas distribution, (3) test our understanding of radiation-hydrodynamics, (4) explore alternate avenues for initiating plasmas and (5) determine prospects for producing high density compressions and K-shell blackbody radiators, we are proposing a new family of loads that are thin cylinders of plastic foil. These cylindrical foils allow for the possibility of depositing thin layers of higher atomic number materials onto the foil surface that become the K-shell emitters following implosion. In a sense this proposed load represents an evolutionary step along the way toward x-ray simulators with enough current to implode solid cylinders with sufficient amounts of high Z materials to achieve efficient K-shell emission. This load design is discussed in detail in Section I.

(2) There has to be reliable feedback between experiment, model development and load design if there is to be sustained progress in understanding Z-pinch behavior. Plasma diagnostics and analysis are responsible for a large part of this feedback. By directly comparing as much spectral information as is available (e.g, measured total powers, K-shell powers, the size of the K-shell emission region, K-shell line ratios, spatially resolved spectra, and time integrated and resolved spectra) with corresponding calculated information using our collisional radiative equilibrium ionization dynamics models and our one-dimensional (1D) radiation transport plasma models, we are making steady progress in improving our inferences about the state of the plasma. Our models have been improved to the point where time integrated and time resolved radial gradients in plasma temperature and density can be inferred. The work that is presented in Section II of this report demonstrates how these models can be used to infer the radial profiles of electron temperature and density by matching model calculations with radially resolved spectroscopic line measurements of the Z pinches created in Double Eagle aluminum-silicon wire array experiments. Diagnostic techniques and analysis such as this provide us with knowledge of the state of the experimental

plasmas. Matching the state of the plasma as calculated using our 1D and 2D radiation MHD models to this inferred knowledge of the experimental state of the plasma is the main method we employ to improve our understanding of the dynamics of PRS loads.

(3) A straightforward approach to establishing a theoretical relationship between the initial asymmetries or the Rayleigh Taylor (RT) instabilities of a z-pinch and its ability to efficiently radiate K-shell photons would be to perform two-dimensional (2D) or three-dimensional (3D), time dependent, non-local thermodynamic equilibrium (non-LTE), full radiation transport, magneto-hydrodynamic (MHD) calculations. However, this capability has never been demonstrated by the z-pinch community because the computer requirements for performing the zone-to-zone coupling needed to solve the equation of radiative transfer in a 2D or a 3D plasma are severe. In the past, our 2D MHD model, PRISM, which stands for Plasma Radiating Imploding Source Model, inadequately modeled the radiation field by assuming either that the plasma was optically thin or that a local escape model could be used to model some of the photon self-absorption physics. Another model widely used by the z-pinch community, the LTE radiative diffusion model, is also inadequate for modeling the radiation physics of PRS loads designed for K-shell emission because neither the diffusion approximation nor the LTE assumption are valid for K-shell plasma conditions produced by present day Z-pinch. In Section III we describe a newly developed, computationally efficient, multi-dimensional, radiation transport method for modeling Z-pinch plasmas that are in collisional radiative equilibrium. This method is superior to diffusion methods because: (1) the source function is based on a self-consistent non-LTE calculation, not an *ad hoc* assumption that it is Planckian, (2) the optically thin radiation is allowed to escape, not subjected to an inappropriate diffusion equation, and (3) accurate line-by-line escape probabilities are used, not diluted as in diffusion, by frequency groups that mix line and continuum opacities. This multi-dimensional radiation transport model is employed by our 2D PRISM code to analyze the effect of Rayleigh-Taylor instability growth on argon K-shell yield production. In particular gas puff loads driven by a Z machine circuit are modeled.

(4) Wire arrays have proven to be reliable PRS loads for achieving record radiative powers and yields. The progress made in the research and development of these loads, which represent such a prominent element of DTRA's PRS program, is described in Section IV. Early insight into the behavior of a wire array load was provided by the Wire Dynamic Model (WDM) wherein

each wire is treated as a distinct circuit element. This model has successfully described mass and current interchange in nested arrays over broad current and mass ranges. Improvements to the WDM model that allow the treatment of bias inductance and wire resistance are discussed as well as treatment of the precursor plasma that forms as the wires heat. Treating this tenuous precursor plasma stresses conventional MHD codes to the point of validity. In order to more accurately model the precursor plasma we are evolving the WDM model into a true fluid particle model and progress made toward this goal is described.

(5-6) Extensive experience in modeling plasma radiation sources over many years has raised our awareness of the large sensitivity of model results to initial conditions, zoning assumptions, model platforms - i.e., Eulerian versus Lagrangian reference frames, and transport coefficients. In the work presented in Section V, sensitivity issues related to the design and modeling of titanium, nested-plasma, Z-pinch loads are investigated. Specifically, the K-shell emission sensitivity to the initial plasma mass distribution, and the role of electron viscosity in directly converting viscous energy into electron thermal energy are examined. Typically, in past calculations, the electron viscosity was ignored and all the viscous energy went into heating the ions. Consequently, the calculated ion temperatures are very high - higher than line broadening measurements have indicated. In order to examine the sensitivity of K-shell emission to this viscosity issue, the standard form of artificial viscosity was used, but the heating it produced was divided between electrons and ions according to the ratio of their classical viscosities. The role of electron viscosity in plasma shock heating is discussed in detail in Section VI.

(7) Decontamination of the anode in the bremsstrahlung diode has substantially improved bremsstrahlung radiation production. This improvement was demonstrated experimentally on Gamble II last year and a similar set of experiments is to take place on DECADE MODULE 2 (DM2) in March of 2001. The success of the DM2 decontamination experiments is important for achieving similar improvements in bremsstrahlung production on the DECADE machine. This section describes experimental and theoretical work that has been and will be done to understand the role that heating the tantalum anode in a bremsstrahlung diode to 2000 - 3000 K plays in improving bremsstrahlung production.

## I. A LOAD DESIGN PROPOSAL

Three important features of Z-pinch dynamics that influence its PRS performance are evident from past comparisons between Z-pinch theory and Z-pinch experiments. One, experiments using tracer elements as well as theory show that K-shell emissions originate from the core of the plasma that assembles on axis, and this radiation generally traverses a colder (L-shell emitting) outer plasma. Two, the outer portion of the assembled plasma is generally much larger than the core region, and it extends well beyond one-dimensional (1-D) computer calculation predictions. Part or possibly all of this added extent has sometimes been explained by the growth of Rayleigh-Taylor instabilities at the outer surface of the plasma. However, this is not a firm comparison between theory and experiment since it depends on how much initial perturbation one applies at the beginning of a calculation and on how much one imagines that the lengthy spikes being calculated correspond to the qualitative features that are seen in x-ray pinhole pictures. In any case, both 1-D and 2-D (r-z) calculations assume perfectly cylindrically shaped plasmas initially that do not exist in experiments. Consequently, three, experiments always show a dependence of K-shell yields and powers on initial wire gap spacing or initial gas distribution. The difficulty of controlling the initial mass distribution of the plasma load generally degrades the ability, in particular, of moderate atomic number plasmas to compress into tight uniform pinches on axis that can radiate with reasonable efficiency from the K-shell.

The constraint that has prevented elimination of this unwanted dependence on wire number and wire gap spacing in the past has always been the limited amount of current that can be delivered to a Z-pinch load. With too low a current drive, the masses of cylindrical, foil-type loads made from solid materials are generally too large to be imploded to high enough velocities to radiate well, if at all, from the K-shell. However, the Z generator at Sandia National Laboratories has reduced this limitation considerably and may allow for the fabrication of a new family of loads of the kind proposed here. Figure 1 illustrates a possible design. A set of support pins are mounted at the initial radius of the load on both the nominal cathode and anode surfaces. For simplicity, the figure shows only six pins and the same number of support pins as return current posts. They are situated at the same angular positions as the posts to compensate somewhat for the only approximately cylindrical shape of the surface. A thin foil of plastic is stretched and attached to the support pins and becomes the Z-pinch load that undergoes implosion. As shown in the figure, this load design allows for the possibility of depositing thin layers of higher atomic number materials, such as titanium, iron, or copper, onto the inner surface of the foil that become the K-shell emitters following implosion.

A Z-pinch load of the kind depicted in Figure 1 solves a number of problems and creates others. The use of support pins gives the load structural stability unavailable in an unsupported, thin film, design (although foam cylinders may have such stability and sufficiently light weight when they become available). When Z-pinch experiments were done in the past with thick wires, it was observed that some fraction of the wires had been left behind unimploded and in their original positions at the time when the pinch was assembling on axis. Thus, the support pins should not interfere with the foil implosion if they are not allowed to form a closed electrical circuit. The use of a foil eliminates gap spacings; however, there are problems (as with wires) as to how one should initiate a discharge in such a way as to convert solid material into a cylindrically symmetric plasma. However, if such initial conditions can be achieved, the first truly unambiguous comparisons



between 1- and 2-D calculations and experiment should be possible without the need to guess at the influence of hidden experimental variables. By eliminating gap spacings, one could also eliminate the premature arrival of plasma on axis ahead of the main body of plasma. Calculations show that such precursor plasma is preheated, and that it impedes the compression of the plasma core, which is beneficial to the production of K-shell radiation. The implosion of a plastic foil could become the first implosion of a true plasma shell. It would allow a far more accurate evaluation of the influence of Rayleigh-Taylor instabilities on the K-shell performance of Z-pinch loads than has been possible to date. Moreover, the fact that the load is not initially in the shape of a perfect cylinder could actually be a benefit since it compensates somewhat for the slight reduction in the size of the  $\mathbf{j} \times \mathbf{B}$  forces away from the support rods because of the finite number of return current posts generally used in experiments.

The ability to undercoat the plastic with angstrom-sized thicknesses of moderate atomic number ( $Z$ ) elements could also be a major benefit. Calculations have shown (see Section xx of this final report), that in a true 1-D-like implosion, the plasma core is compressed and heated, while the compressing plasma remains at higher densities and lower temperatures. The K-shell emission in moderate  $Z$  element implosions comes from this core plasma. However, it is not necessary to have a moderate  $Z$  element do the compressing and heating of the core. The replacement of moderate- $Z$  with a low- $Z$  element in the outer plasma has several advantages. Plastic is less dense than titanium or copper, and therefore, a thicker shell of material can be used in the load design. The density of plastic is roughly  $1 \text{ gm/cm}^3$ , 4.5 times less dense than titanium and 9 times less dense than copper. Thus, a 1 cm radius cylinder of  $10 \text{ }\mu\text{m}$  thick plastic would only have a mass of 6.3 mg/cm, while an identical titanium cylinder would be 4.5 times heavier and an identical copper cylinder 9 times heavier. Furthermore, by having a fully ionized carbon-hydrogen plasma in front of the K-shell emitting core plasma instead of a partially ionized, moderate- $Z$ , plasma, the absorption losses of the K-shell emissions are reduced.

Two sets of 0-D calculations were carried to illustrate the potential interest of experiments on the Z generator that use pure plastic loads like the one in Figure 1. Figures (2a) and (2b) contain the results of these calculations. For reference purposes, Figure (2a) shows the locations of the mass breakpoint curves (both soft and hard) for a carbon plasma as well as the implosion velocities corresponding to  $\eta$  values of  $\eta = 4$  and  $\eta = 20$  for carbon. For implosion velocities between or greater than these values, carbon is a highly optically-thick and efficient emitter of K-shell radiation. Two series of 0-D implosion calculations of different massed carbon loads were carried out using an early (somewhat approximate but close) version of the Z generator circuit. In one series of calculations, the initial load radius was 1 cm, and in the other series, it was 1.5 cm. Figure (2b) shows the implosion velocities these loads achieved in calculations that were stopped after the load had imploded to a radius of 2 mm. They demonstrate that the Z generator has the capability to drive carbon loads of masses between 10 and 20 mg/cm to velocities well beyond those needed for the efficient production of (highly opaque) K-shell radiation. Important questions thus arise that are in need of experimental investigation. How close to a blackbody spectrum can such emissions get? How close to the tungsten emission spectra could the carbon K-shell spectra get as a result of the greater mass of the carbon loads and their potentially greater implosion symmetry?

A previous theoretical study<sup>1</sup> of CH foams heated by ion beams from the Particle Beam

---

<sup>1</sup> J. P. Apruzese, J. E. Rogerson, R. W. Clark, and M. C. Coulter, Naval Research Laboratory

Fusion Accelerator II at Sandia National Laboratories (Z's predecessor) addressed some of these questions. In this study, it was demonstrated that low atomic number plasmas of the mass range and material composition discussed above can radiate from the K-shell as near-blackbody sources (see Figures 3 through 7). Two factors contribute to this behavior. First, the extreme optical depths produced by such large mass plasmas saturates the line emission at the blackbody curve and increases continuum emissions. Second, low atomic number elements such as carbon have high collisional excitation and deexcitation rates coupling different ionization stages and bound states within a given stage. This coupling results in local thermodynamic equilibrium (LTE) being achieved at lower ion densities than is the case for medium or high atomic number elements.

Figures 3-7 show the progression towards blackbody emission of different amounts of carbon plasma at the uniform plasma conditions indicated in the figures. Two sets of calculations were done. In one set, the plasma had a uniform temperature of 100 eV; in the other, its temperature was raised to 200 eV. In all cases, the plasma was a cylinder of 4 mm diameter. At 100 eV, 5 mg/cm of carbon plasma was already sufficient to closely approximate blackbody emission [Fig. (3)], while 10 mg/cm fully achieved blackbody emission [Fig. (4)]. For a cylinder 2 cm in length with a 4 mm diameter radiating as a 100 eV blackbody, the power output would be 26 TW, a value easily achievable on the Z generator. By upping the blackbody temperature to 200 eV, the power output increases to 410 TW, in excess of what tungsten wire arrays have achieved on Z. Figures 5-7 show that carbon has the capability to radiate as a blackbody at 200 eV from the K shell but only for masses at or in excess of 20 mg/cm.

Because the size of the plasma remained fixed at 4 mm diameter in all of the Figure 3-7 calculations, the density of the plasma increased in proportion to the mass. One might question whether a density of  $8 \times 10^{21}$  ions/cm<sup>3</sup> is attainable in a dynamic pinch, since such high densities have not been attained to date. However, several factors work in favor of this possibility. One, experimentally, a gapless cylinder-like plasma has never been imploded and compressed on axis before. Two, carbon plasmas do not need to be heated beyond 200 eV. And three, the number of electrons per ion is much smaller in carbon than in higher atomic number loads. Thus, if the same pressures are generated in a carbon plasma on Z as have been generated in higher atomic number loads, then higher densities should be achievable in carbon than have been achieved in other loads. Most importantly, experiments on plastic loads should enlighten the Z-pinch community considerably on the radiative-hydrodynamics of Z-pinch loads.

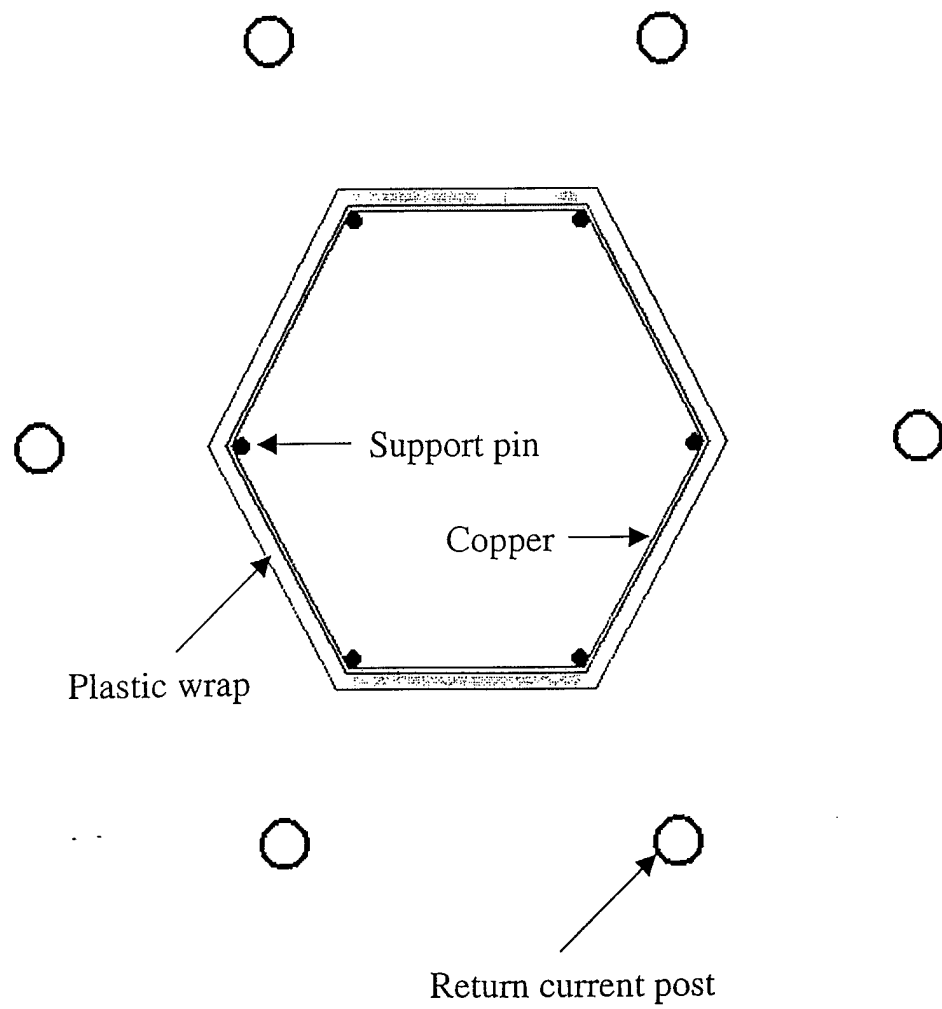


Figure 1

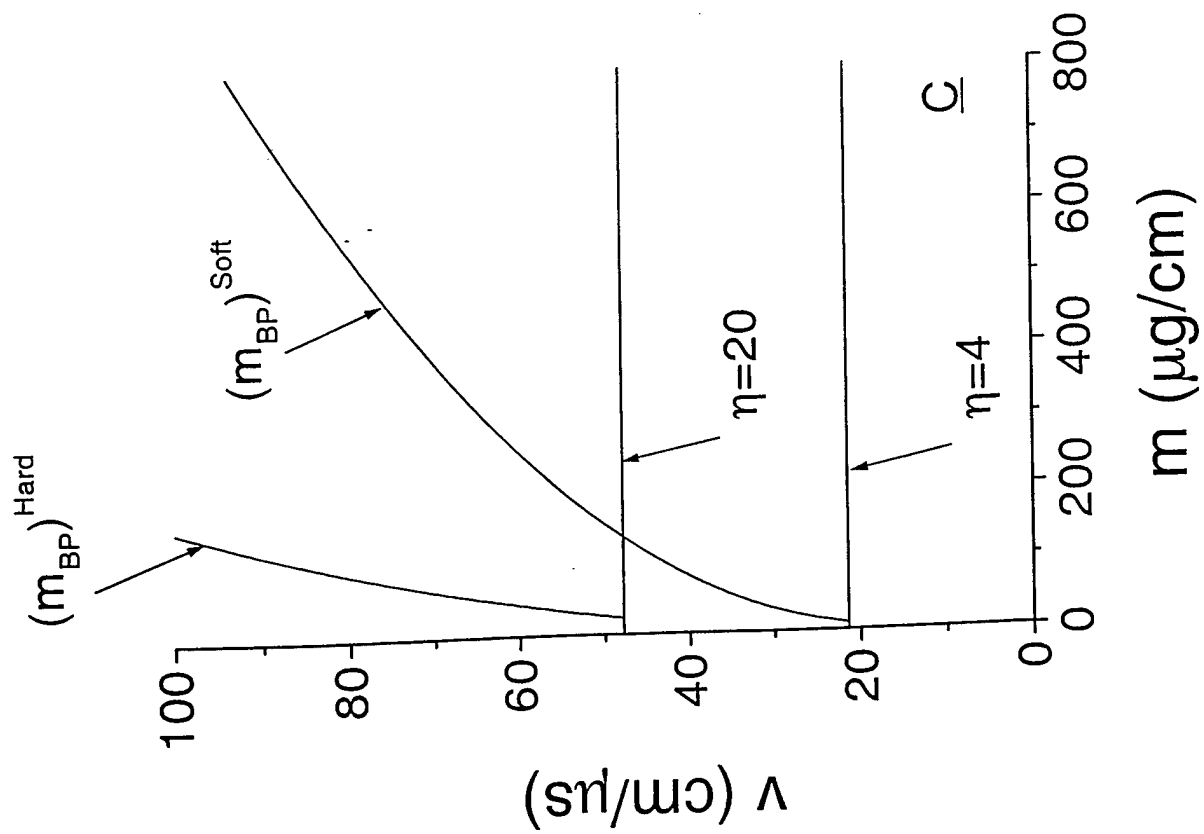


Figure 2a

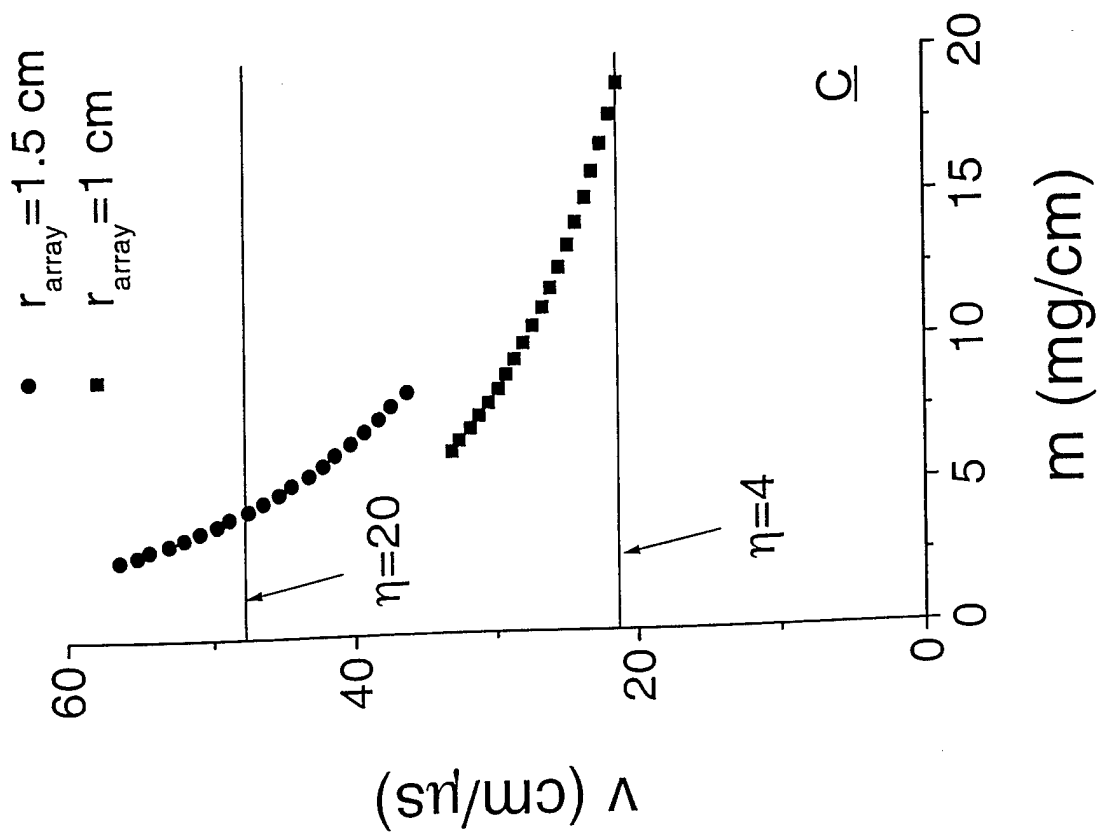


Figure 2b

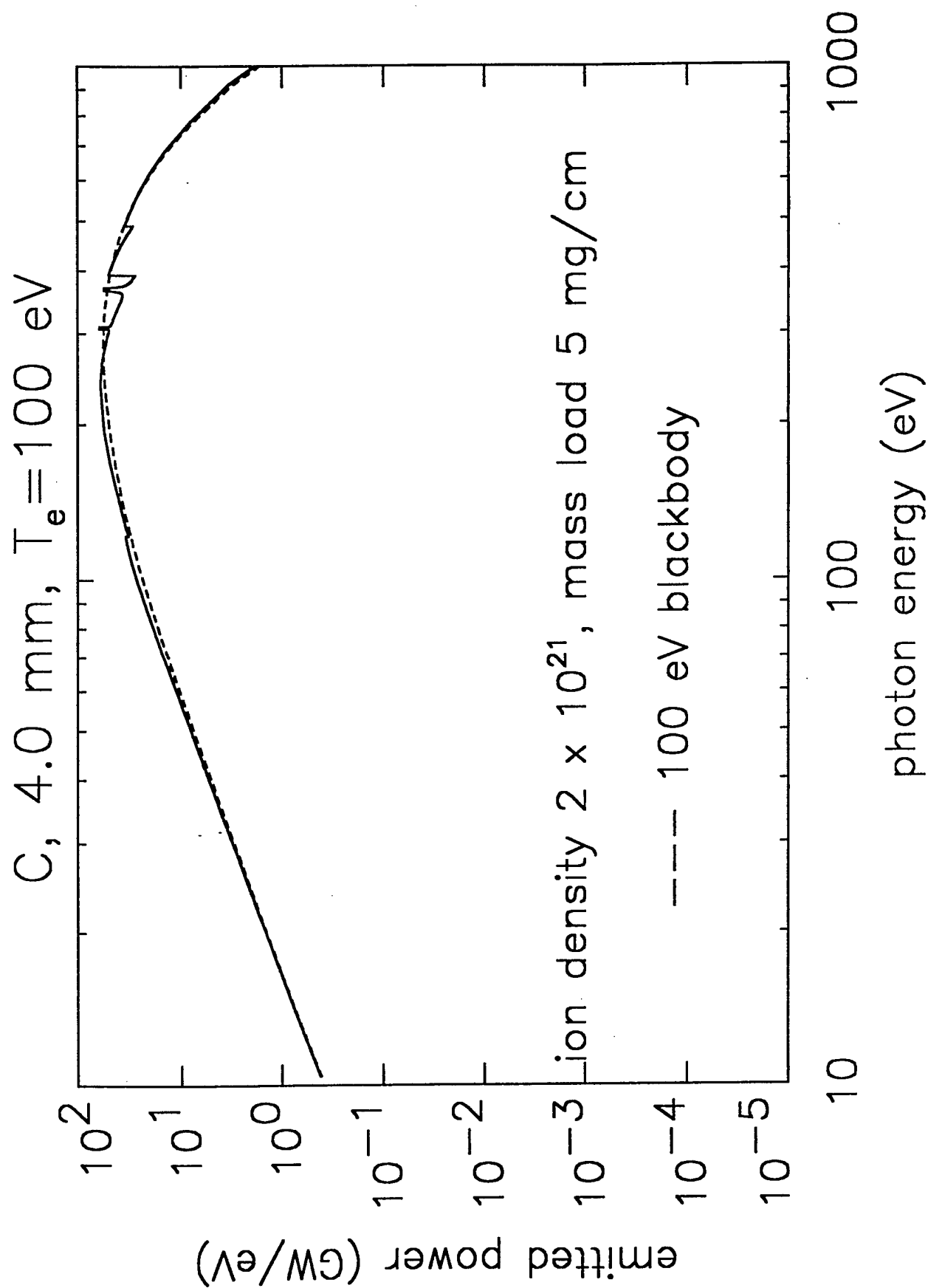


Figure 3

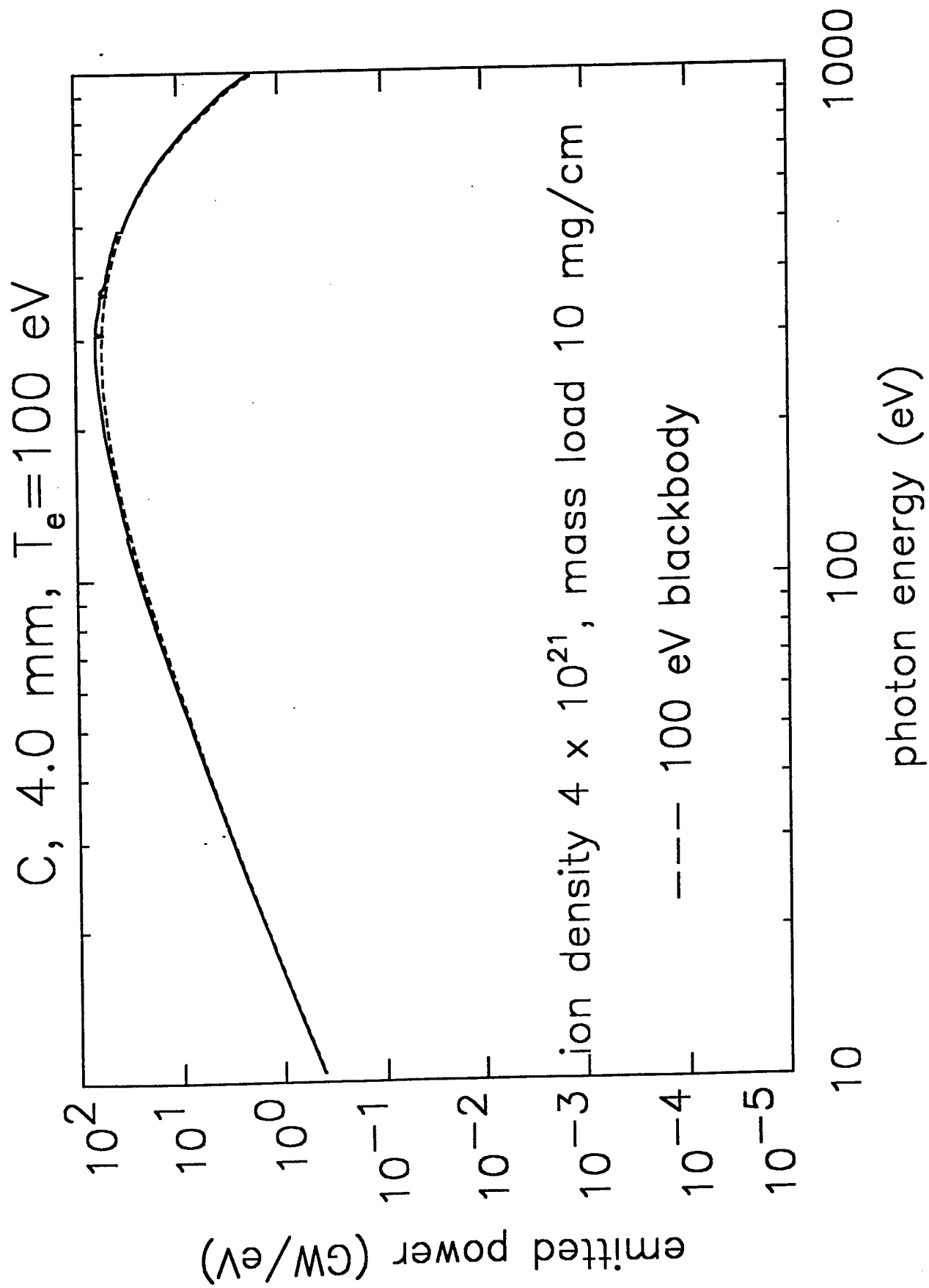


Figure 4

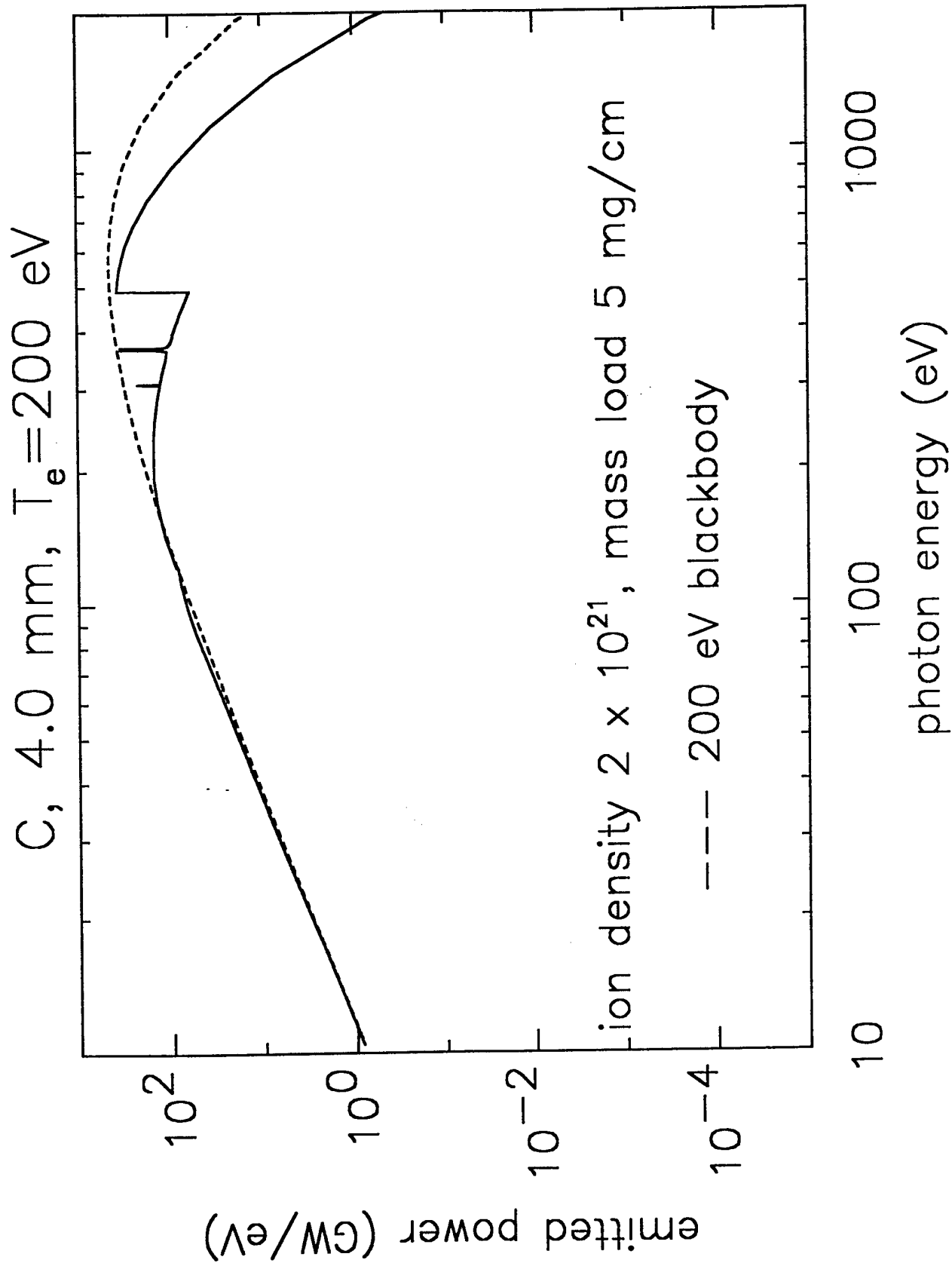


Figure 5

C, 4.0 mm,  $T_e = 200$  eV

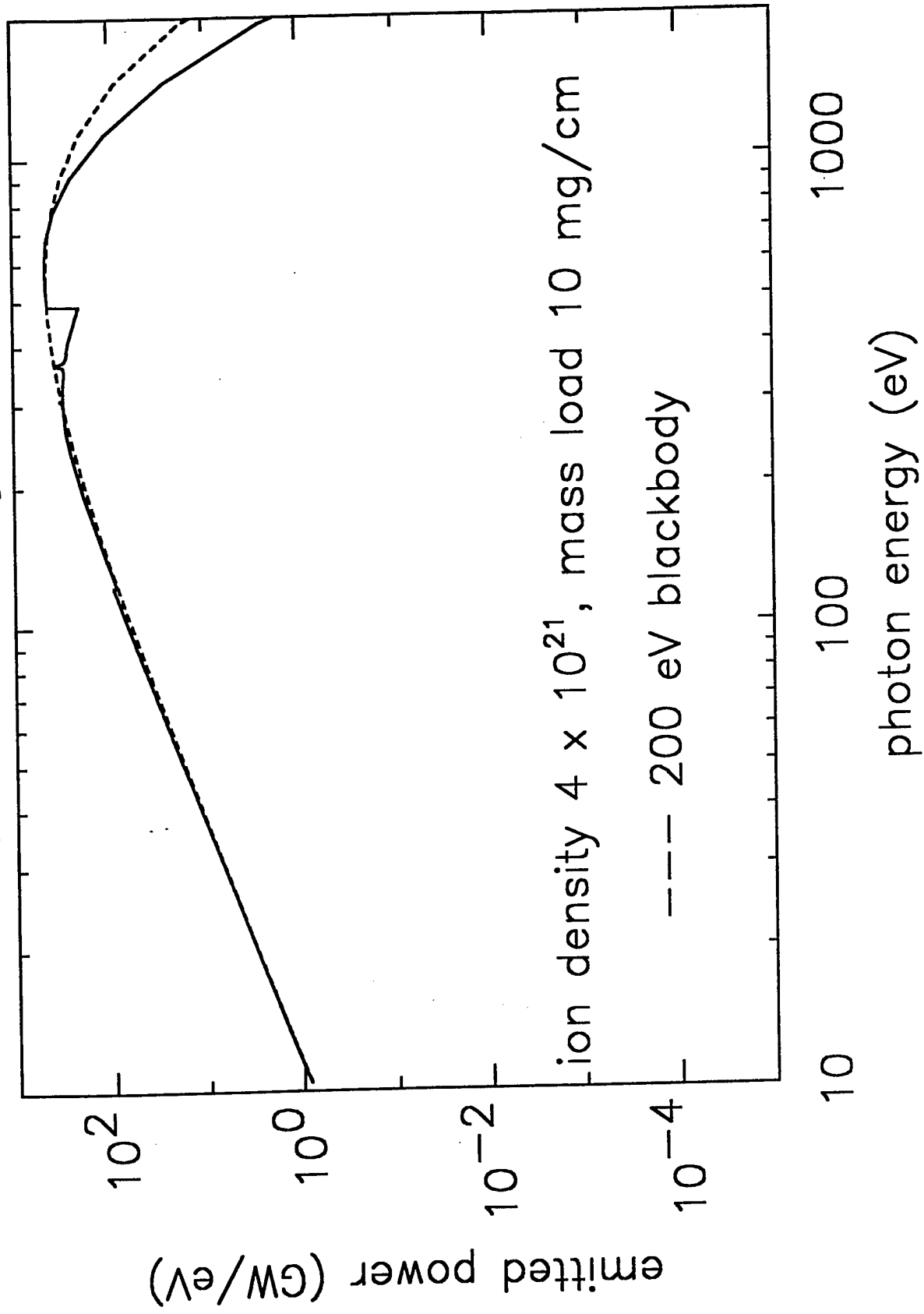


Figure 6



C, 4.0 mm,  $T_e = 200$  eV

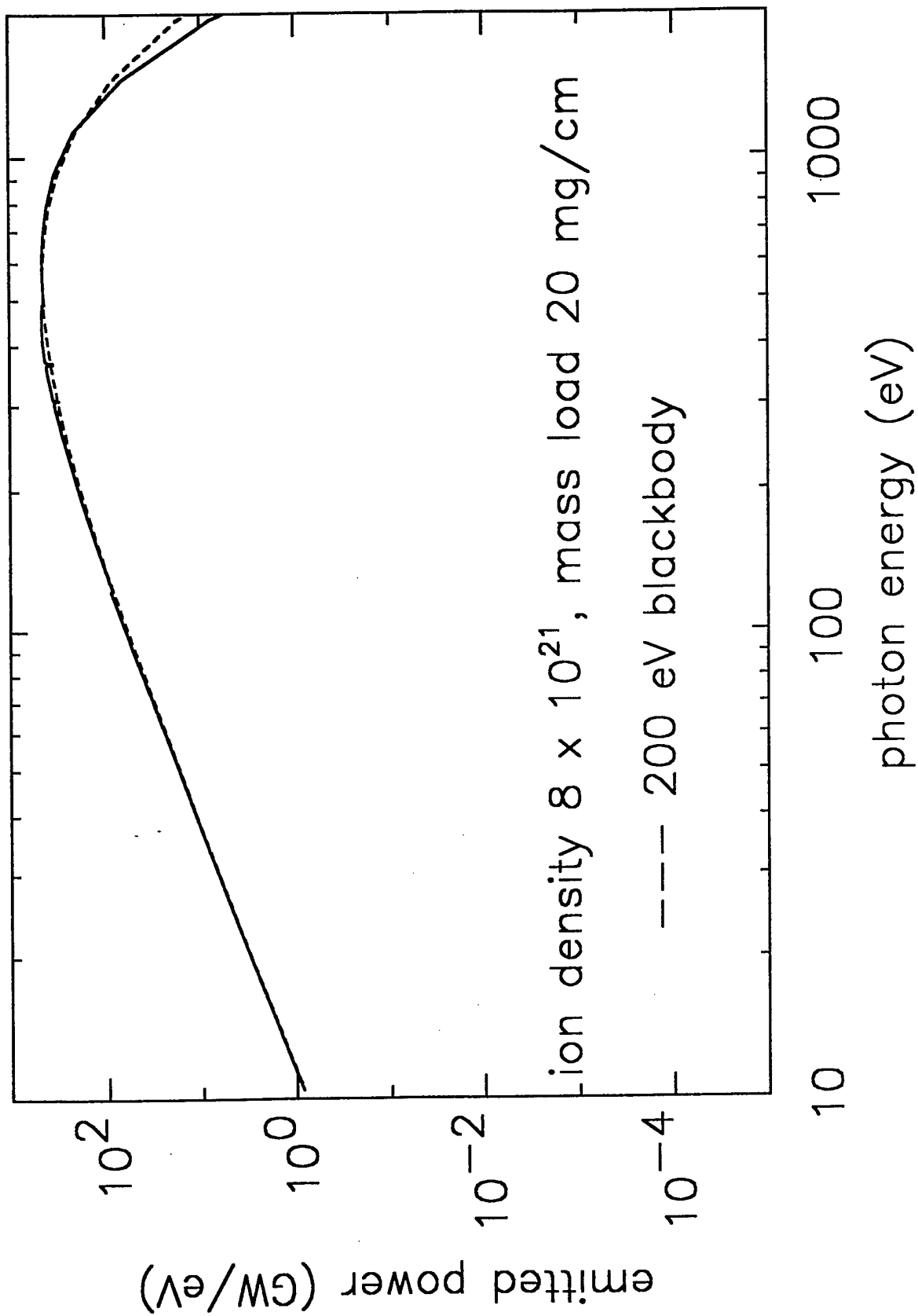


Figure 7

## II. ANALYZING SPATIALLY RESOLVED LINE SPECTRA EMITTED BY Z PINCHES

### SUMMARY

The spatial profiles of key physical variables such as electron temperature and density are crucial in determining the overall radiating efficiency of a Z pinch as well as the emitted photon energy distribution. The work reported in this chapter uses spatially resolved x-ray lines emitted from shots taken on the 4 MA Double EAGLE generator [C. Deeney *et al.*, Phys. Rev. A **44**, 6762 (1991)] at Maxwell Physics International to infer such profiles. The loads were arrays of 15 wires consisting of 95% Al, 5% Si, producing nearly 50 kJ of K-shell radiation with relatively long pulsewidths of 41-43 ns. We find that the spatial profile of the He-like intercombination to resonance line ratio is critically affected by self-absorption and re-emission (scattering) of resonance line photons emitted from the hot, dense interior of the pinch. This ratio cannot be correctly interpreted without taking the scattering into account. Also, at densities somewhat lower than those achieved by these pinches, this line ratio becomes more temperature than density dependent. The inferred temperature gradient is much less steep than that which had been diagnosed previously for a pinch emitting a much shorter x-ray pulsewidth of 13 ns.

### I. INTRODUCTION

When pulsed-power generators implode well-designed loads with currents of several MA or more, total x-ray yields of 100 kJ or more are typically produced from the resulting Z pinch<sup>1-13</sup>. The highest energy x-rays are often derived from emission processes in the H- and He-like ionization stages of the load element(s), i.e., the K shell. X-ray yields from

the K shell are correlated with the temperature and density profiles of the pinch. It is these profiles which determine how much of the imploded load is both heated to temperatures and compressed to densities sufficient for the K-shell ions to exist in abundance and to radiate efficiently. Accordingly, major goals of analyzing experimental data are to determine the fraction of the original load mass which is ionized to the K shell, and, if possible, to make quantitative inferences of the temperature and density gradients. To date, much of the work in this direction has employed a single temperature-dependent line ratio, usually that of the H-like to He-like  $\alpha$  lines, together with the measured diameter and K-shell power of the pinch, to deduce an average temperature and density<sup>3,4,6,9,11,13-15</sup>. Although this approach averages over the spatial variations and thus only indirectly considers the gradients present, it has led to some significant insights. For instance, using lighter loads generally increases the electron temperature of the assembled pinch while reducing its density<sup>4</sup>. Also, the fraction of the original load mass which participates in the K-shell radiation (as obtained from the spatially averaged analysis) has been found to correlate directly with the observed K-shell yields<sup>11</sup>. Rarely does the radiating mass fraction approach 100% of the load, indeed, excellent yielding shots commonly exhibit mass participations<sup>4,9,11,13</sup> of 10-60%, depending on the load element, current, and load design. Such low mass fractions suggest that there is room for further improvement in the K-shell radiating efficiency of Z pinches. Clearly, more detailed knowledge of how the gradients present in Z pinches are formed is needed along with the factors which may influence their formation.

As would be expected, inferring temperature and density profiles from spectral data requires more extensive data and analysis than is needed to infer average values. The use of spatially resolved spectroscopy<sup>10,16</sup> is the method chosen in the present work. Other techniques which have been employed are: the replication of several line intensities in spatially-integrated spectra<sup>17,18</sup> whose differing optical depths make possible the inference of plasma conditions at various depths in the pinch, laser interferometry<sup>19-21</sup>, and measuring the absorption of a backlighting laser or x-ray source<sup>22,23</sup>. The present work

explores the potential of spatially resolved line intensities and ratios to diagnose critical features of the gradient structure of Z pinches. The experiments and data are described in Sec II, the analysis in Sec. III, and the results are put into perspective in Sec. IV.

## II. EXPERIMENTS AND DATA

The experiments analyzed in the present work were conducted on the Double EAGLE generator at Maxwell Physics International<sup>6</sup>. This pulsed power waterline machine implodes a typical wire array load with peak currents near 4 MA reached in a risetime of about 110 ns for a short circuit load. The two shots considered here, 4116 and 4117, employed arrays of 15 Al wires coated with Si for an overall mass ratio of 95% Al, 5% Si, and mass load of 0.22 mg/cm. The length of the arrays was 2 cm, and their initial diameter, 2.5 cm. On each of the shots, an extensive suite of electrical and radiation diagnostics was fielded, including filtered x-ray diodes (XRDs), photoconducting detectors (PCDs), calorimeters, x-ray spectrometers, Rogowski coils to measure the load current, and time-gated pinhole cameras filtered to image K-shell radiation. These instruments produced excellent agreement (better than 10%) in all of the major electrical and radiation measurements when comparing the two shots. Therefore, we have analyzed the specific results from shot 4116 as representative of the experiments. A K-shell yield of 47 kJ was produced within a full width at half maximum (FWHM) of 43 ns. Despite this quite long pulsewidth (often seen when relatively few wires are employed), the K-shell yield of 47 kJ is excellent, not far shy of the record of 58 kJ for comparable currents and photon energies<sup>6</sup>. This shot produced a total x-ray yield of 170 kJ. The current at peak x-ray power was 4.0 MA. While large numbers of finer wires are evidently necessary to obtain sub-10 ns pulsewidths and high radiated powers<sup>8,11-13</sup>, excellent yields, albeit with long pulsewidths and low powers, can still be attained with a small number of thicker wires. The present analysis can contribute to understanding the differences between short-pulse and long-pulse pinches as well as to the development and implementation of spatially resolved

spectroscopic diagnostics for Z pinches in general.

The instrument upon which much of the foregoing analysis is based is a high-resolution, radially resolving Johann spectrometer. By aligning the slit along the pinch axis, radially resolved, but axially and time-integrated profiles of individual x-ray lines were obtained. Typical spatial resolution was  $\sim 0.5$  mm, and spectral resolution  $(\lambda/\Delta\lambda) \sim 1.25 \times 10^3$ . Emitted by only 5% of the plasma, the Si lines are much less opaque than their Al counterparts and have provided most of the spectroscopic data analyzed in the present work. The He-like Si  $1s^2-1s2p^3P$  intercombination (IC) line is optically thin and its Doppler-broadened profile is consistent with an ion temperature of 5.4 keV. Strictly speaking, this time-integrated data can only provide an upper limit for the ion temperature. However, given a nearly stationary pinch during the 43 ns when about 85% of the K-shell radiation is emitted, this measurement is likely not compromised by bulk motional broadening.

For shot 4116, the measured spatial profiles of the He-like Si IC to He- $\alpha$  resonance line ( $1s^2-1s2p^1P$ ) ratio, the (He- $\alpha$ +IC) intensity, and the ratio of the H-like Si  $1s-2p$  (Ly- $\alpha$ ) to (He- $\alpha$ +IC) line are shown in Fig. 1 (solid lines). Note the gradual and monotonic decline with radius of all three of these quantities. The intensity profile of the Si He- $\alpha$ +IC lines indicates a spatial FWHM of 3.5 mm averaged over the length of the pinch. The radial profile of the He-like Al  $1s^2-1s3p^1P$  (He- $\beta$ ) line (not shown) has a FWHM of 3.8 mm. This indicates that any spatial separation of the Al and Si is mild, and in the analysis we will assume that the Al and Si are fully intermixed. The overall experimental uncertainty of the quantities plotted in Fig. 1 is estimated to be 15%. Beyond a radius of 2.5 mm, some radiation is still detected, especially in He- $\alpha$ , but the signal is so close to background that the uncertainty quickly rises to the 30-60% level. Therefore, we have confined our quantitative analysis to within 2.5 mm of the pinch axis.

### III. ANALYSIS

#### A. Model and fitting procedure

The principal analytical tool which we have employed is an ionization dynamics and radiation transport model of a one-dimensional (1D) cylindrical plasma model containing detailed configuration atomic structure for the Li-, He-, and H-like ionic stages of Al and Si. This model is described in more detail in Ref. 15. It includes all the important atomic collisional and radiative processes coupling the levels, To get accurate photoexcitation rates and to correctly calculate the self- absorption and power outputs, all optically thick lines are transported, as well as the two free-bound continua arising from radiative recombination to the K-shell ground states. The model solves for the steady-state populations of the individual levels assuming collisional-radiative equilibrium (CRE). Spatial profiles of the spectral lines are also calculated. Once the populations are calculated, the (monodirectional) intensity  $I$  of an x-ray transition emergent along a chord perpendicular to the pinch axis is given by  $I = (A_{ul}/4\pi)h\nu \int_{chord} N_u(s)P_e(s)ds$  where  $A_{ul}$  is the spontaneous decay rate for the transition,  $N_u$  is the upper level population density as a function of the distance  $s$  along the chord, and  $P_e(s)$  is the line escape probability for a Voigt profile<sup>24</sup>. This aspect of the model calculation is carried out for 41 chords whose impact parameters range from  $r=0$  (intersecting the axis) to within 1.5% of the outer radius of the pinch.

Use of the calculated K-shell spectrum to fit the data (intensities, line ratios, powers, spatial profiles) is similar to that described in Ref. 18. The assumed temperature and density profiles are iterated, typically requiring dozens to hundreds of separate calculations to find the best fit. Initially, simple but versatile analytic forms for the profiles are adopted, such as power laws or generalized Gaussians. As the calculations approach the data, hand adjustments of the profiles based on the observed variable sensitivities are made to fine tune the spectrum and zero in on an optimum fit. Based on the number of calculations, and the fact that similar but not identical profiles degrade the agreement with the data, we believe that the fits are unique in the sense that no profile differing significantly from the one deduced could fit the data as well. However, they cannot be proven to be so.

## **B. The intercombination to resonance line ratio diagnostic**

The theory behind the use of the He-like IC to resonance line ratio to diagnose a plasma's average density has been reviewed by Griem<sup>25</sup>, who also provides some early references. Some recent uses of this line ratio to diagnose densities of plasma focus discharges and laser-driven plasmas are described in Refs. 26 and 27, respectively. The density sensitivity of this ratio arises from the much larger spontaneous decay rate of the resonance line (for Si,  $3.76 \times 10^{13} \text{ sec}^{-1}$ ), compared to that of the intercombination line ( $1.58 \times 10^{11} \text{ sec}^{-1}$ ). As the electron density increases, the intercombination transition is increasingly quenched by collisional de-excitation of the  $1s2p^3P$  level, whereas the resonance line continues to radiate freely because its very high spontaneous decay rate well exceeds that of electron collisional de-excitation. Therefore, as the density increases, the ratio of the intercombination to resonance lines decreases. This diagnostic principle is illustrated in Fig. 2 where the results of CRE calculations for a 3 mm diameter cylinder are presented in the form of isocontours of this (Si) ratio vs. electron temperature and Si ion density for a 95% Al, 5% Si plasma. Above ion densities of  $\sim 10^{17} \text{ cm}^{-3}$ , the contours are mostly vertical, indicating the dominance of density dependence, and do decrease in value with increasing density, consistent with the theory summarized above. This density range includes those of most Z pinches, therefore, this line ratio can still be considered to be an effective density diagnostic for such plasmas. However, below this density, the contours become horizontal, indicating an almost pure temperature dependence at Si ion densities lower than  $\sim 10^{16} \text{ cm}^{-3}$  (electron densities lower than  $\sim 2 \times 10^{18} \text{ cm}^{-3}$ ). What accounts for this unexpected result showing that this line ratio can be used for temperature diagnosis for low density plasmas?

The answer to this question lies in the collisional excitation rates from the He-like  $1s^2\ ^1S$  ground state to the  $n=2$  singlet and triplet levels from which arise the resonance and intercombination lines, respectively. Our calculations show that, as function of temperature, excitation to the singlet level rises much more steeply than that to the triplet. For instance, as the electron temperature increases from 0.5 to 1.5 keV, the excitation rate to the Si triplet

level increases by a factor of 5, but to the singlet level, by a factor of 15. The calculations of Zhang and Sampson<sup>28</sup> demonstrate the same trend. Quantum mechanically, it is the differing effects of exchange as a function of projectile energy on the direct and spinflip transitions which produce the relative increase in excitation of the resonance line. The temperature dependence shown in the lower density sector of Fig. 2 follows this trend, i.e., as the temperature increases, the resonance line intensity increases relative to that of the intercombination line, reducing the ratio. In this low density regime, neither line is collisionally quenched. At higher density, the quenching effects predominate, producing the usually quoted density dependence described above.

### C. Results of data fit

The temperature and density profiles which are employed to reproduce the line ratios and intensities of the data of Fig. 1 are shown in Fig. 3. Note from the dotted lines of Fig. 1 that both the Si line ratios and intensity profiles predicted by the model lie within the estimated experimental uncertainty of 15%. The electron density profile, when translated into Si and Al ion densities, accounts for only 40% of the initial mass load. The gentle decline in electron temperature shown in Fig. 3 (from 1.24 to 1.04 keV, axis to outer edge) is required to replicate the gradual decline in the measured temperature-sensitive  $\text{Ly-}\alpha/(\text{He-}\alpha+\text{IC})$  ratio shown in Fig. 1. This analysis can be used to determine only the inner K-shell core conditions of the pinch, as a cooler outer halo exists which emits only the softer L-shell component of the total x-ray output. The decline in temperature and density with increasing radius is also consistent with the observed decrease of the intensity of the  $(\text{He-}\alpha+\text{IC})$  lines. What is initially puzzling and apparently paradoxical is the decrease in density with radius, despite the concurrent decrease of the  $\text{IC}/\text{He-}\alpha$  ratio. According to the standard theory outlined above in Sec. II B and Fig. 2, a decreasing line ratio should indicate increasing density.

The explanation of this surprising result is the presence of line photon scattering



combined with the drastically differing absorption cross sections of the resonance and intercombination lines. The upper levels of both lines are competitively populated by collisional excitation, and also by radiative excitation by the flux of line photons emitted from the hotter, denser pinch interior. The collisional excitation coefficients of both lines drop sharply with decreasing electron temperature, and in the outer regions of the K-shell emitting core, radiative excitation becomes increasingly dominant for the resonance line as is shown in Fig. 4. Note that, at the outer edge, the He- $\alpha$  resonance line is populated twice as often by photoexcitation as by collisional excitation. However, as also shown in Fig. 4, radiative excitation of the intercombination line's  $^3P$  upper level is at most a 1% effect. This is a straightforward consequence of the fact that the photoexcitation cross section of the intercombination line is less than that of the resonance line by a factor of 230. With increasing radius, resonance line emission is increasingly photo-excited by the flux of x-rays from the hotter, denser interior whereas this population mechanism is not available to the intercombination line. Thus, only the spatially resolved intensity of the resonance line is enhanced by this scattering mechanism, reducing the IC/resonance ratio even though the electron density is decreasing.

Failure to properly take this mechanism into account can lead to erroneous and seriously misleading density inferences. Fig. 5 shows the electron density profile that is derived from the observed IC/resonance line ratio when x-ray scattering is neglected. Note that the density increases with radius, in accord with the usual interpretation of this line ratio. When this new density profile is used, the spatially resolved intensity of the (He $\alpha$ +IC) lines is found to increase with increasing radius, as also plotted in Fig. 5, and in contrast to the data.

The reversal of the normal density dependence of the IC/resonance line ratio is a space dependent phenomenon. However, most of the energy for driving both lines comes from collisional excitation in the hot, dense interior near the axis. Therefore, the spatially integrated ratio would preserve the usual density dependence. In Fig. 6, the calculated

spatial profiles of the IC/resonance line ratio are displayed for three different density profiles, the inferred profile of Fig. 3 for Double EAGLE shot 4116, and also profiles representing a doubling and halving of this original density distribution at each point. Note that for each profile, the ratio declines with radius along with the electron density. However, for the highest electron density the overall ratio is lowest and vice-versa, in accord with the usual interpretation of its density dependence. Therefore, in a spatially unresolved spectrum, a high IC/resonance ratio does indicate a relatively low average density and a low ratio a high average density. But, to correctly infer density profiles within this overall density range, it is necessary to account for photoexcitation and its spatial dependence.

How do the averages of spatial temperature and density profiles compare with those that would be derived from the more often employed spatially integrated spectroscopic analysis using the dominant pinch component, i.e., Al? As described in Sec. I, the spatially averaged analysis uses the measured K-shell power and pinch diameter together with a temperature-dependent line ratio such as  $\text{Ly-}\alpha/(\text{He-}\alpha+\text{IC})$  to infer an electron temperature and ion density. For this shot, the time-integrated  $\text{Ly-}\alpha/(\text{He-}\alpha+\text{IC})$  ratio is 1.3, the peak Al K-shell power is 0.5 TW/cm, and the diameter of the pinch in the Al He- $\beta$  line is 3.8 mm. Employing CRE-calculated contour plots similar to those presented in Ref. 15, and using the peak K-shell power quoted above, an Al ion density of  $1.4 \times 10^{19} \text{ cm}^{-3}$  and electron temperature of 0.98 keV are obtained. These values are in only fair agreement with the density of  $8.0 \times 10^{18} \text{ cm}^{-3}$  and temperature of 1.15 keV which are obtained by spatially averaging (over 3.8 mm) the profiles of Fig. 3. However, when the 0.25 TW/cm average K-shell power during the pulse, (excluding the 100 ns "foot" which begins when the K-shell power has declined to 20% of its peak value) is employed as input to the Al spectroscopic analysis instead of the peak power, much better agreement is achieved, namely an Al ion density of  $9.8 \times 10^{18}$ , and electron temperature of 1.11 keV. Therefore the two methods are complementary and consistent provided that the time-averaged power is used for the spatially integrated analysis to correspond to time integrated intensities and

line ratios employed in the spatially resolved analysis.

#### IV. CONCLUDING REMARKS

Much of the spectroscopic analysis of Z-pinchs that has been carried out to date has employed spatially integrated data. Such a comparatively simple approach implicitly averages over the gradients which are present to varying degree in all pinchs. However, it has nonetheless yielded quantitative connections between the radiative output of Z pinchs and the atomic number of the load and the currents and pulsewidths with which they are driven. Thus, even for shots in which the best K-shell yields are obtained, it is common for well under half the load mass to be producing the K-shell radiation. This presents the opportunity to enhance the K-shell yield by designing experiments that involve more of the mass heated to K-shell temperatures. However, to effectively carry out such experiments, the gradients which hold the key to the lack of full mass participation must be routinely diagnosed.

The work described in this report shows one example of how this diagnostic challenge can be met through the use of detailed spatially resolved spectra. Such data were analyzed from two identical shots on the 4 MA Double EAGLE generator which produced consistent K-shell yields, approaching 50 kJ, from a mixture of 95% Al, 5% Si. In the analysis, we noted that the ratio of the intercombination to He- $\alpha$  lines, normally considered to be a density diagnostic, could be used as an excellent temperature diagnostic for densities up to two orders of magnitude lower than those normally encountered in Z pinchs. For Z-pinch densities, this ratio can be an effective density diagnostic, and we have reconciled its use with that of absolute powers to determine the average and spatially resolved densities. In diagnosing the density profile within the pinch from spatially resolved data, however, it is necessary to properly take into account photoexcitation to avoid seriously misleading inferences (see Fig. 5).

To fully realize the benefits of this kind of data analysis a greater variety of shots needs

to be systematically analyzed for their gradient structure. However, it is interesting to compare the present results to those previously obtained from shot 70 on the Z generator at Sandia National Laboratories<sup>18</sup>, which was also predominantly Al. From the Z shot, a K-shell yield of 122 kJ was obtained within a 13 ns pulse, much shorter than the 41-43 ns characteristic of the presently considered Double EAGLE experiments. The K-shell yield on Z was far below the implosion kinetic energy of  $\sim 1.1$  MJ, whereas on Double EAGLE, the K-shell yield of 47 kJ was much closer to the kinetic energy of  $\sim 63$  kJ, with the total radiative yield of 170 kJ nearly triple the coupled kinetic energy. On Z, the total yield and coupled kinetic energy were about equal for the Al shots. The temperature gradient diagnosed on Z shows the electron temperature falling from 1.6 keV to 0.2 keV within 1 mm, whereas a much gentler fall in temperature from 1.2 to 1.0 keV within 2.5 mm is inferred for the Double EAGLE shot. These sharply contrasting factors in yield vs. coupled kinetic energy, temperature gradient, and K-shell pulsewidth, may be related to, or a consequence of, differences in plasma opacity, implosion dynamics or energy coupling mechanisms, such as the "magnetic bubble" energy deposition mechanism recently proposed<sup>29</sup>. Further investigation and more comprehensive and systematic analysis is needed to verify these relationships.

## REFERENCES

1. M. Gersten, W. Clark, J. E. Rauch *et al.*, Phys. Rev. A **33**, 477 (1986).
2. K. G. Whitney, J. W. Thornhill, J. P. Apruzese, and J. Davis, J. Appl. Phys. **67**, 1725 (1990).
3. M. C. Coulter, K. G. Whitney, and J. W. Thornhill, J. Quant. Spectrosc. Radiat. Transfer **44**, 443 (1990).
4. C. Deeney, T. Nash, R. R. Prasad, L. Warren, K. G. Whitney, J. W. Thornhill, and M. C. Coulter, Phys. Rev. A **44**, 6762 (1991).
5. K. G. Whitney, J. W. Thornhill, J. L. Giuliani, Jr. *et al.*, Phys. Rev. E **50**, 2166 (1994).
6. C. Deeney, P. D. LePell, B. H. Failor *et al.*, Phys. Rev. E **51**, 4823 (1995).
7. K. G. Whitney, J. W. Thornhill, J. P. Apruzese, J. Davis, C. Deeney, P. D. LePell, and B. H. Failor, Phys. Plasmas **2**, 2590 (1995).
8. T. W. L. Sanford, G. O. Allshouse, B. M. Marder *et al.*, Phys. Rev. Lett. **77**, 5063 (1996).
9. K. G. Whitney, J. W. Thornhill, P. E. Pulsifer, J. P. Apruzese, T. W. L. Sanford, T. J. Nash, R. C. Mock, and R. B. Spielman, Phys. Rev. E **56**, 3540 (1997).
10. K. L. Wong, P. T. Springer, J. H. Hammer *et al.*, Phys. Rev. Lett. **80**, 2334 (1998).
11. C. Deeney, T. J. Nash, R. B. Spielman *et al.*, Phys. Plasmas **5**, 2431 (1998).
12. R. B. Spielman, C. Deeney, G. A. Chandler *et al.*, Phys. Plasmas **5**, 2105 (1998).
13. T. W. L. Sanford, R. C. Mock, T. J. Nash, K. G. Whitney, P. E. Pulsifer, J. P. Apruzese, D. Mosher, D. L. Peterson, and M. G. Haines, Phys. Plasmas **6**, 1270 (1999).

14. C. Deeney, C. A. Coverdale, M. R. Douglas *et al.*, Phys. Plasmas **6**, 2081 (1999).
15. J. P. Apruzese, K. G. Whitney, J. Davis, and P. C. Kepple, J. Quant. Spectrosc. Radiat. Transfer **57**, 41 (1997).
16. T. J. Nash, T. W. L. Sanford, C. Deeney *et al.*, J. Quant. Spectrosc. Radiat. Transfer **60**, 97 (1998).
17. J. P. Apruzese, J. W. Thornhill, K. G. Whitney *et al.*, IEEE Trans. Plasma Sci. **26**, 1185 (1998).
18. J. P. Apruzese, P. E. Pulsifer, J. Davis *et al.*, Phys. Plasmas **5**, 4476 (1998).
19. N. Qi, S. F. Fulghum, R. R. Prasad, and M. Krishnan, IEEE Trans. Plasma Sci. **26**, 1127 (1998).
20. S. V. Lebedev, I. H. Mitchell, R. Aliaga-Rossel, S. N. Bland, J. P. Chittenden, A. E. Dangor, and M. G. Haines, Phys. Rev. Lett. **81**, 4152 (1998).
21. C. H. Moreno, M. C. Marconi, K. Kanizay, J. J. Rocca, Yu. A. Uspenskii, A. V. Vinogradov, and Yu. A. Pershin, Phys. Rev. E **60**, 911 (1999).
22. E. J. Yadlowsky, T. B. Settersten, R. C. Hazelton, J. J. Moschella, G. G. Spanjers, J. P. Apruzese, and J. Davis, Rev. Sci. Instrum. **66**, 652 (1995).
23. D. H. Kalantar and D. A. Hammer, Phys. Rev. Lett. **71**, 3806 (1993).
24. J. P. Apruzese, J. Quant. Spectrosc. Radiat. Transfer **34**, 447 (1985).
25. H. R. Griem, *Principles of Plasma Spectroscopy* (Cambridge University Press, Cambridge, 1997), pp. 273-278.
26. K. N. Koshelev, Yu. A. Sidel'nikov, G. Decker *et al.*, Opt. Spectrosc. **76**, 198 (1994).
27. S. H. Glenzer, C. A. Back, K. G. Estabrook *et al.*, Phys. Rev. E **55**, 927 (1997).

28. H. Zhang and D. H. Sampson, *Astrophys. J. Suppl. Ser.* **63**, 487 (1987).
29. L. I. Rudakov, A. L. Velikovich, J. Davis, J. W. Thornhill, J. L. Giuliani, Jr., and C. Deeney, *Phys. Rev. Lett.* **84**, 3326 (2000).

## FIGURE CAPTIONS

FIG. 1. The indicated experimental and theoretical line ratios and intensities are plotted vs. radius for Double EAGLE shot 4116. The experimentally measured quantities are indicated by the triangles connected by solid lines, the model fit results given by the dashed line curves. Overall experimental uncertainty is estimated at 15%.

FIG. 2. Calculated isocontours of the intercombination to resonance line ratio for the He-like Si ion are shown as a function of electron temperature and Si ion density for a 3 mm diameter cylindrical plasma composed of 95% Al, 5% Si.

FIG. 3. Electron density and temperature profiles inferred from the data presented in Fig. 1, for Double EAGLE shot 4116.

FIG. 4. The ratio of radiative to collisional excitation is plotted for the profiles of Fig. 3, for the Ly- $\alpha$ , He- $\alpha$ , and intercombination lines of K-shell Si ions.

FIG. 5. The electron density inferred when photoexcitation is neglected, and the (He- $\alpha$ +IC) intensity profile predicted from this inferred density are plotted vs. displacement from the axis. Also shown are the electron density obtained from the full model as well as the measured (He- $\alpha$ +IC) intensity profile.

FIG. 6. The calculated spatial profiles of the IC/resonance line ratio are plotted for the electron density profile of Fig. 2 as well as for profiles in which this density distribution has been halved and doubled at each point (central electron density is indicated).



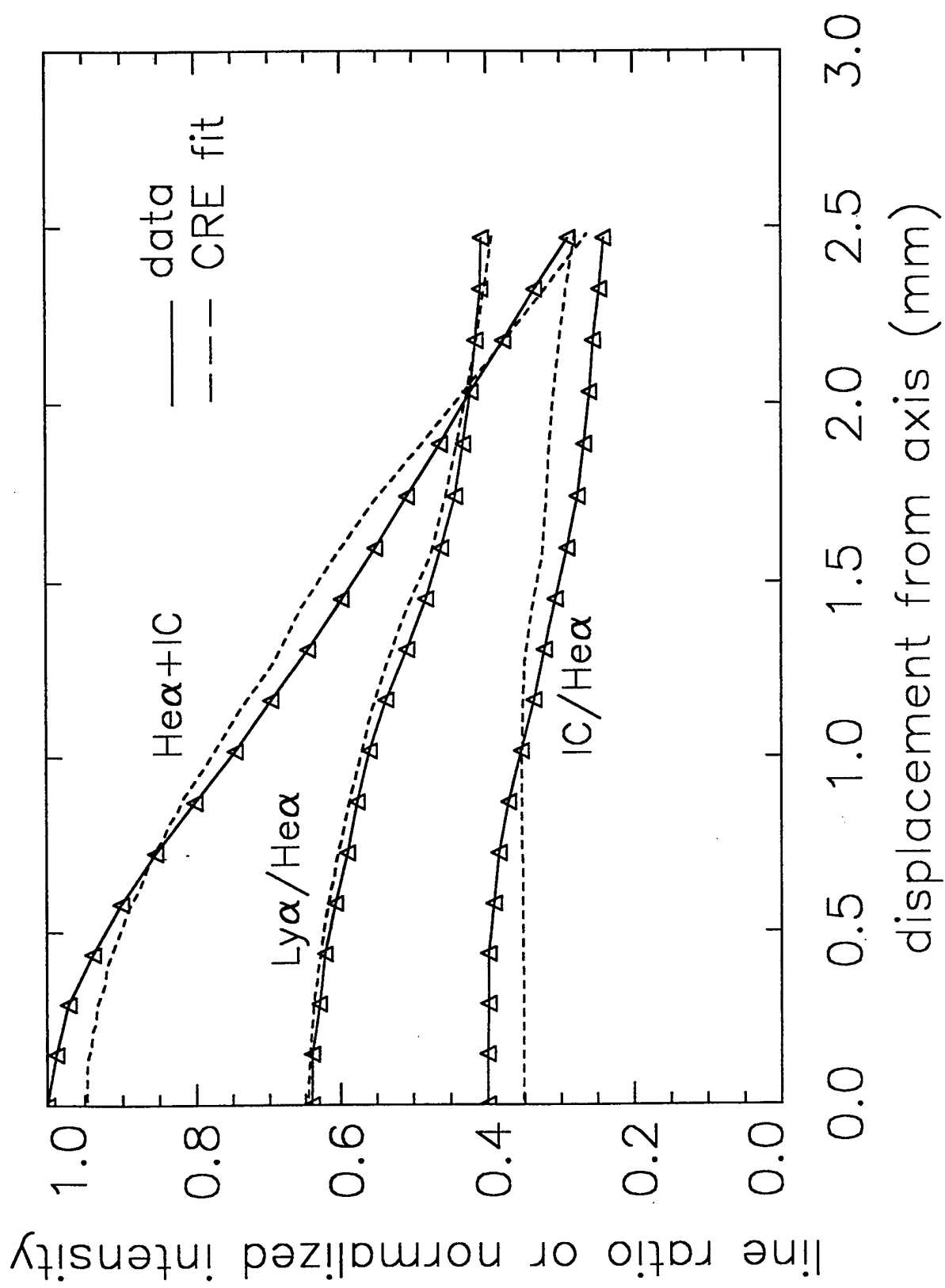


FIG. 1

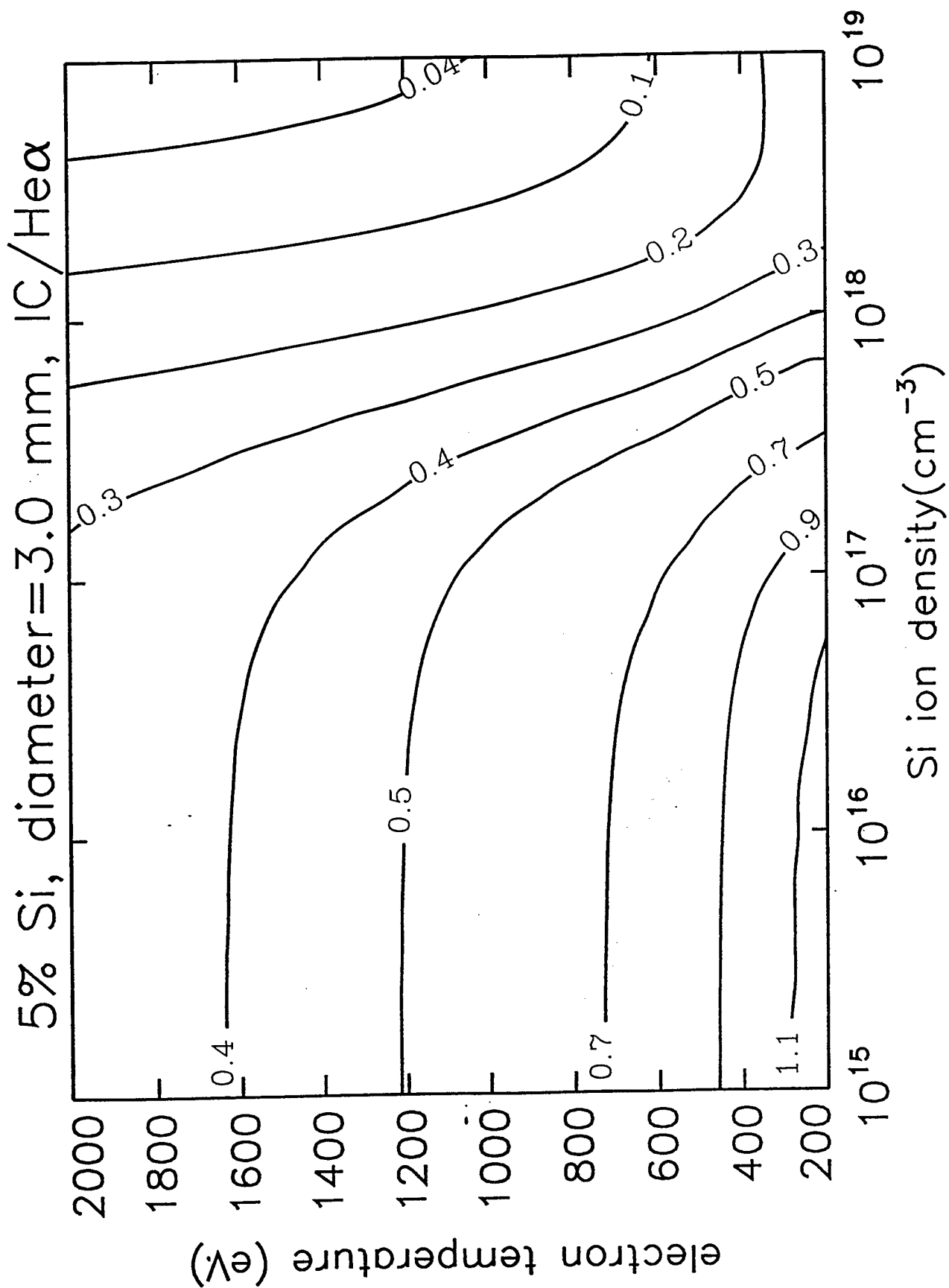


FIG. 2

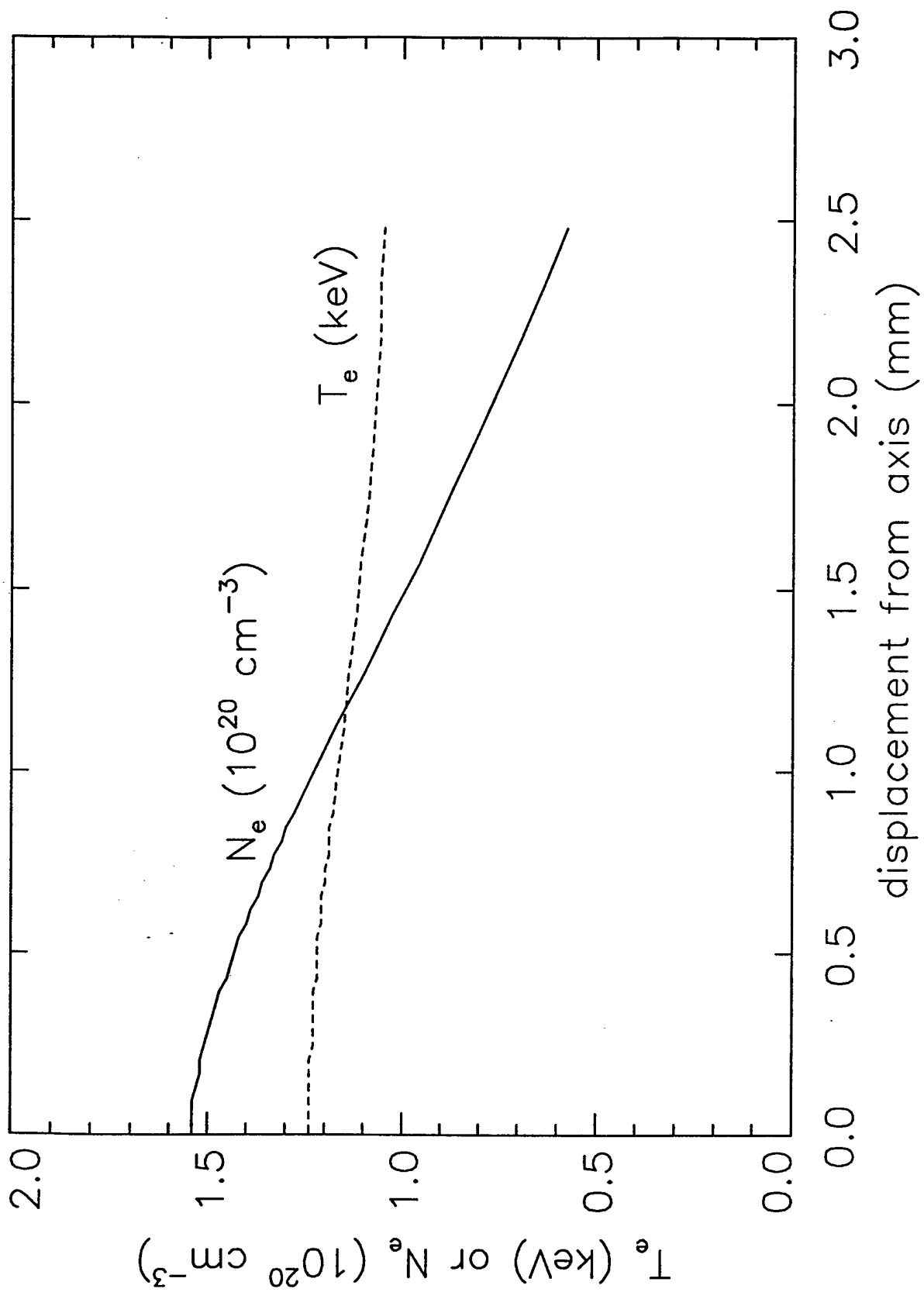


FIG. 3

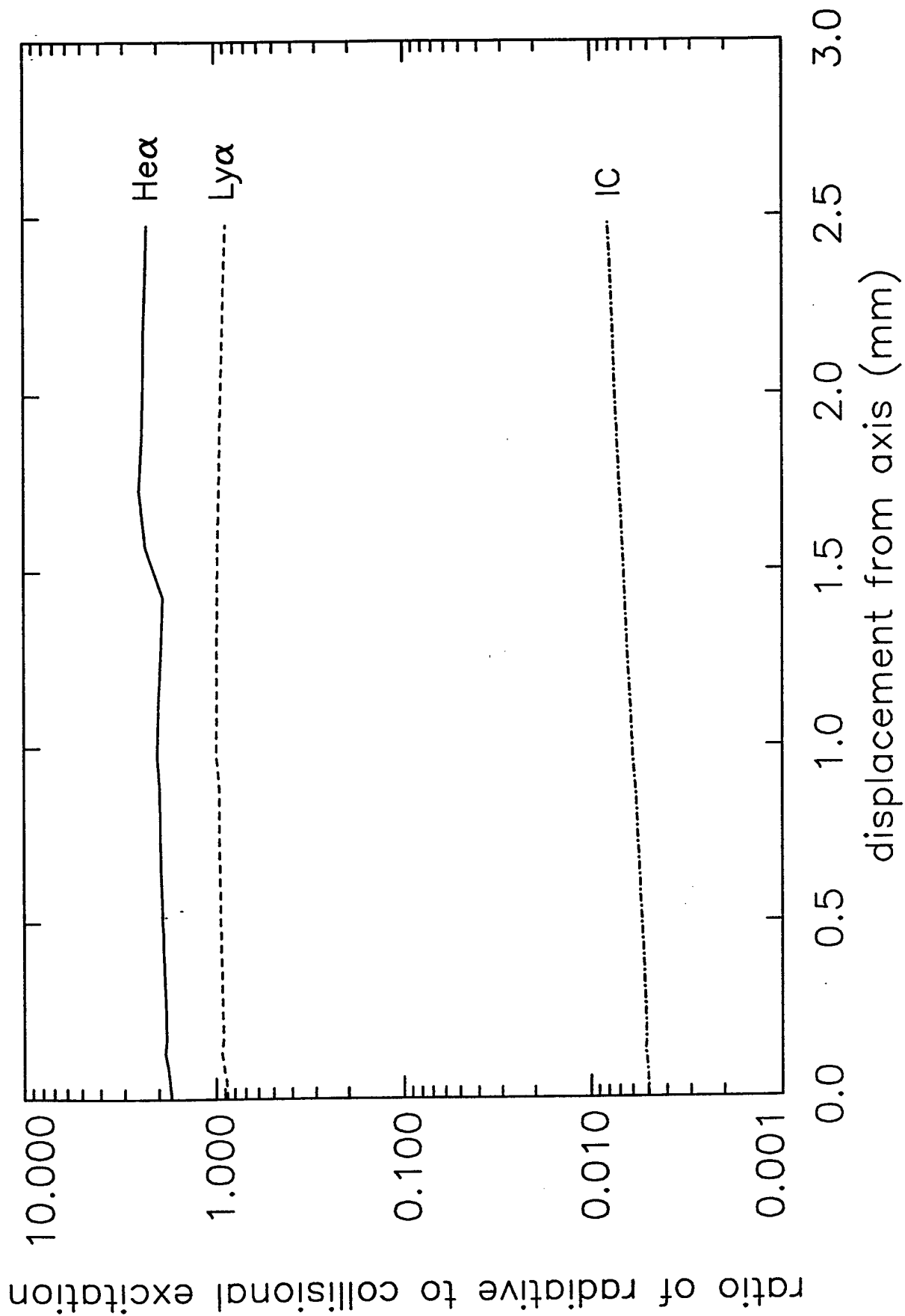
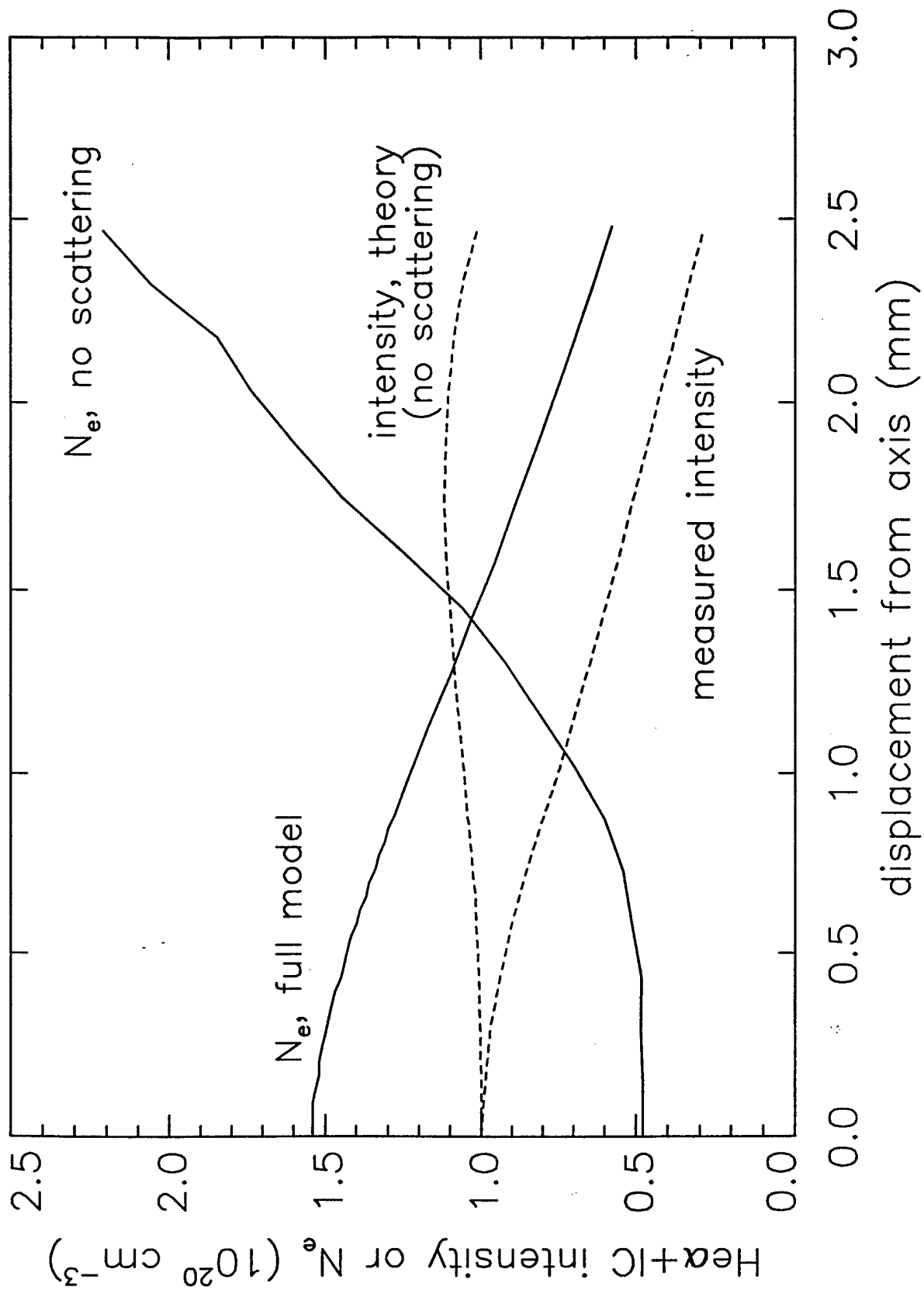


FIG. 4



F1G.5

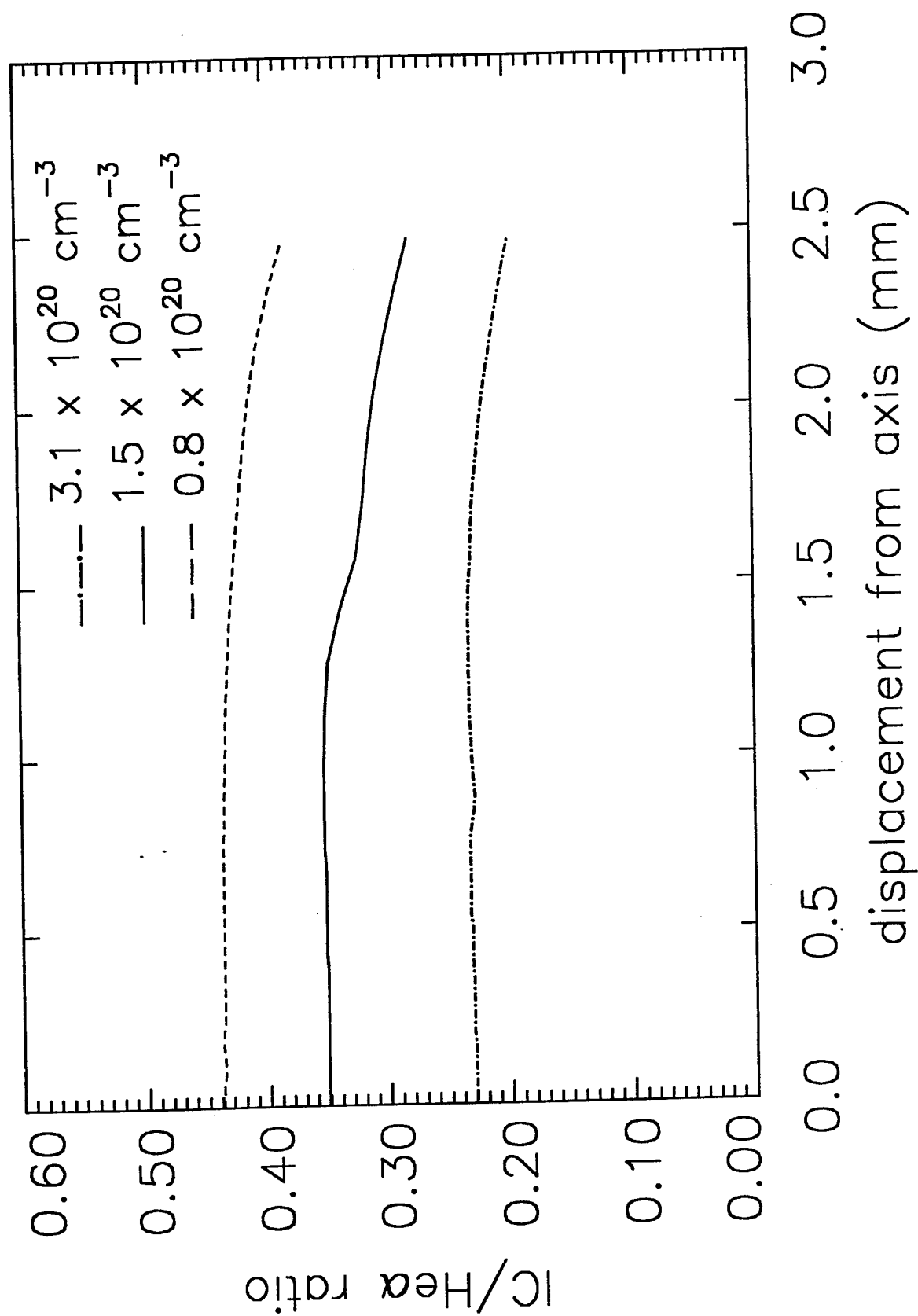


FIG. 6

### III. AN EFFICIENT NON-LTE RADIATION TRANSPORT MODEL SUITABLE FOR MULTIDIMENSIONAL HYDRODYNAMICS CALCULATIONS

#### I. Introduction

A straightforward approach to establishing a theoretical relationship between the initial asymmetries or the Rayleigh Taylor (RT) instabilities of a z-pinch and its ability to efficiently radiate K-shell photons would be to perform two-dimensional (2D) or three-dimensional (3D), time dependent, non-local thermodynamic equilibrium (non-LTE), full radiation transport, magneto-hydrodynamic (MHD) calculations. However, this capability has never been demonstrated by the z-pinch community because the computer requirements for performing the zone-to-zone coupling needed to solve the equation of radiative transfer in a 2D or a 3D plasma are severe. In the past, our 2D MHD model, PRISM,<sup>1</sup> which stands for Plasma Radiating Imploding Source Model, inadequately modeled the radiation field by assuming either that the plasma was optically thin or that a local escape model could be used to model some of the photon self-absorption physics. Another model widely used by the z-pinch community, the LTE radiative diffusion model, is also inadequate for modeling the radiation physics of plasma radiating source (PRS) loads designed for K-shell emission because neither the diffusion approximation nor the LTE assumption are valid for K-shell plasma conditions produced by present day Z-pinch.

The transport of radiation within an optically thick plasma is both a nonlinear and a nonlocal problem. The source functions and absorption coefficients throughout the plasma determine the amount of radiation that escapes the plasma as well as the local radiation energy densities. The source functions, in turn, depend on these densities through the photoexcitation and ionization processes they stimulate, which influences the ion and excited state population densities in the plasma. The transport problem is solved exactly only when the radiation field and populations are determined self-consistently. For these reasons the optically thin and radiative diffusion models are not viable candidates for modeling radiation transport in multi-dimensional, K-shell emitting plasmas. We have therefore developed a model that retains the nonlocal and nonlinear nature of the transport problem but only approximates the exact solution by sacrificing some of the self-consistency inherent in an exact solution to the transport equation. This model is called the Tabulated Collisional-Radiative- Equilibrium (TCRE) model.

This model is described in Section II along with three other models with which it is compared later in the paper. In Section II.a, a Global Collisional-Radiative-Equilibrium (GCRE) model is discussed. This model gives accurate solutions to the exact transport problem, and it therefore serves as a benchmark for testing the TCRE model. Unfortunately, the self-consistency demanded by the GCRE model makes it computationally prohibitive for use in multi-dimensional calculations on most computer platforms at this time. In Section II.b, a less accurate “*on-the-spot*” model that is self-consistent, but which has a simplifying treatment of the nonlocality problem that is also employed in the TCRE model, is described. The self-consistency demanded by this model also makes it computationally prohibitive. The TCRE model is described in Section II.c. This section is concluded with a brief mention of an optically thin model in Section II.d. Results obtained from 1D, cylindrical geometry, z-pinch calculations using the TCRE model are compared in Section III with 1D radiation transport calculations<sup>2</sup> incorporating the three other models discussed in Section II. The TCRE model is found to produce results in reasonable agreement with the GCRE model. In Section IV, the TCRE model, as implemented in the 2D PRISM code, is employed to preliminarily investigate argon Z-pinch experiments similar to those performed on the Z-machine at Sandia National Laboratories.<sup>3</sup> These 2D calculations employ the measured initial gas distribution at the cathode (the axial dependence of the gas distribution is ignored) and the K-shell output is computed as a function of load mass. Comparisons are made with 1D model results of these same experiments to examine the rôle that the Rayleigh Taylor instability plays in affecting the production of K-shell emission. This work is summarized in Section V.

## II. Models for Radiation Transport and kinetics

The radiation field in a plasma alters the atomic level populations through photo-pumping while the populations determine the field through emission and absorption processes. Therefore radiation transport and population kinetics are coupled and can only be solved in a unified approach. The transport equation for the radiation intensity  $I_\nu(\vec{r}_o, t, \hat{\Omega})$  at frequency  $\nu$ , at position  $\vec{r}_o$ , at time  $t$ , traveling in the unit direction  $\hat{\Omega}$ , is

$$\hat{\Omega} \cdot \vec{\nabla} I_\nu + \kappa_\nu I_\nu = j_\nu, \quad (1)$$

where  $\kappa_\nu$  is the frequency dependent absorption coefficient in units of inverse length and  $j_\nu$  is the emission coefficient at frequency  $\nu$  in units of energy per unit volume, per unit time, per unit



frequency, per steradian. The finite light transit time across the medium has been neglected in eqn.(1), as is appropriate for Z-pinchs. Integrating  $I_\nu$  over all directions at a canonical position  $\vec{r}_o$  gives the mean intensity  $J_\nu(\vec{r}_o) = (1/4\pi) \int I_\nu d\Omega$ . For the population kinetics consider a simple atomic level model with ground level ionization stages  $j$  and  $j + 1$ , and stage  $j$  having a single excited state  $k$ . The number density,  $n_k(\vec{r}_o, t)$ , in the excited state  $k$  of the  $j$ 'th ionization stage at position  $\vec{r}_o$  and time  $t$ , is calculated from

$$\begin{aligned} \frac{\partial n_k}{\partial t} = & n_e n_j C_{j,k} - n_e n_k D_{k,j} + n_e n_e n_{j+1} B_{j+1,k} - n_e n_k C_{k,j+1} + n_e n_{j+1} R_{j+1,k} \\ & - n_k \int \sigma_\nu^{k,j+1} \frac{J_\nu}{h\nu} d\nu + n_j \int \sigma_\nu^{j,k} \frac{J_\nu}{h\nu} d\nu - n_k A_{k,j} . \end{aligned} \quad (2)$$

The electron collisional excitation rate  $C_{j,k}$  is from the ground state of ion  $j$  to the excited state  $k$ , and  $D_{k,j}$  is the corresponding de-excitation rate. Three-body recombination from the next higher ionization state is given by  $B_{j+1,k}$ , and  $C_{k,j+1}$  is the electron ionization rate. The remaining four terms represent radiative processes.  $R_{j+1,k}$  is the radiative recombination rate. Dielectric recombination (not explicitly displayed) can be included with the same functional form as the  $R$  term. The frequency integrals are over the photo-ionization cross-section  $\sigma_\nu^{k,j+1}$  and the photo-excitation cross-section  $\sigma_\nu^{j,k}$ . These cross-sections include stimulated emission processes. The transition probability  $A_{k,j}$  accounts for radiative decay of the excited state. The populations from eqn.(2) are coupled to the radiation field of eqn.(1) through the expressions for the emission and absorption coefficients. For the line emitted by the excited state  $k$  and absorption by the ground state  $j$  one has

$$j_\nu = \frac{1}{4\pi} n_k h\nu_{k,j} A_{k,j} \phi_\nu^{k,j} \quad \text{and} \quad \kappa_\nu = n_j \sigma_\nu^{j,k} , \quad (3)$$

where  $h$  is Planck's constant and  $\phi_\nu^{k,j}$  is the normalized line profile function:  $\int \phi_\nu^{k,j} d\nu = 1$ . The radiative power density, the net radiation energy lost or gained per unit volume per unit time from each point in the plasma, is

$$\Lambda = 4\pi \int (j_\nu - \kappa_\nu J_\nu) d\nu . \quad (4)$$

This expression can be positive or negative depending on the position in the plasma and enters as a loss or gain term in the electron energy equation, respectively. The integral of  $\Lambda$  over the whole plasma volume is the emitted radiated power from the plasma.

### a. Global Collisional Radiative Equilibrium

Four models are employed in this paper to solve the above coupled system of equations describing the radiation field and the atomic level populations. The assumptions of each approach will be described to clarify the essential differences. The first approach is the Global Collisional Radiative Equilibrium (GCRE) model in which the population kinetics of eqn.(2) are solved in the steady-state. This model assumes that the dynamic timescale for plasma motion is long compared to the timescale for collisional or radiative processes, which is accurate for most K-shell x-ray sources. This assumption is not however intrinsic to the model and other work has included time-dependent ionization for studies involving the production of high energy x-rays.<sup>4,5</sup> Other than the condition of steady-state, the complete non-linear coupling between the transport and the kinetics, which enters through the  $J_\nu$  terms in eqn.(2), is included and comprises the CRE component of the model. From the solution to eqn.(1) the photons which lead to photo-pumping (ionization or excitation) can arise from different parts of the plasma than the position  $\vec{r}_o$ . This leads to a non-local spatial coupling between any two positions, i.e., zones in a numerical simulation. Photons emitted from position  $\vec{r}_o$  and absorbed at a different position  $\vec{r}_1$  alter the populations and emissivity at the latter point, which in turn affects the populations at the originating position  $\vec{r}_o$  due to absorption of photons from  $\vec{r}_1$ . This feedback can be accounted for by calculating a matrix of radiative coupling coefficients connecting each zone to every other zone for each frequency. In a full dynamic simulation, the solution for the populations and radiation field at a particular timestep is then iterated while conserving electron thermal plus excitation/ionization energy in each zone separately. This procedure provides a self-consistent solution for both the radiation field and the level populations.

In some cases the matrix of coupling coefficients at each frequency can be replaced by a similar matrix for each emission line. In essence the set of frequencies covering a line is integrated over and the matrix components provide the probability that a line photon emitted from  $\vec{r}_1$  will transit the plasma and be absorbed at  $\vec{r}_o$ . Apruzese<sup>6-8</sup> provides frequency and angle averaged formulas for the line-profile-averaged transit probabilities using Lorentz, Doppler, or Voigt line profiles. A similar procedure can be used for bound-free edges arising from photo-ionization.<sup>9</sup> The advantage of the transit probability approach over that of multi-frequency is a reduction in the size of the matrix of coupling coefficients since typically 10-30 frequencies must be used to cover each line. In either case, however, the adjective "Global" as part of the model designation

emphasizes the non-local character of the solution scheme coupling the the radiation transport of eqn.(1), the level kinetics of eqn.(2), and the emissivity and absorption coefficients of eqn.(3). The GCRE model has been used to calculate the radiative emission from a Z-pinch implosion in much of the work by the Radiation Hydrodynamics Branch at the Naval Research Laboratory during the last twenty years, see, e.g. references 4-10. In their papers the approach is referred to as CRE. All of the dynamic calculations of Z-pinch implosions which employ GCRE have been limited to 1-D but include many excited states per ionic stage. The above GCRE approach in 2-D, which requires a matrix of radiative coupling coefficients between all zones at each emission feature is at present computationally prohibitive for most platforms.

### b. "On-the-Spot"

A second model employs the "on-the-spot" approximation of Holstein<sup>11</sup> and Osterbrock<sup>12</sup>. In this approximation if a photon is absorbed anywhere in the plasma it is assumed to be absorbed in the emitting zone. The physical basis of this approximation is that most photons that do not escape the plasma are those emitted in the highly opaque cores of spectral lines and are therefore absorbed nearby. It is most accurate in the extreme limits of either a highly opaque or optically thin plasma. In the present implementation of this approximation the steady-state condition is again assumed, photo-ionization in eqn.(2) is neglected, and for each emission line one determines the probability that a photon emitted from position  $\vec{r}_o$  will escape all the way to the edge of the plasma, i.e., the probability-of-escape  $\mathcal{P}$ . Holstein<sup>11</sup> first developed an expression for the mono-directional escape probability for a completely frequency redistributed Doppler line profile at large optical depth. In a multi-dimensional plasma simulation one requires an average of this escape probability over all possible directions. For the line emission from level  $k$  down to  $j$ :

$$\mathcal{P}_{k,j}(\vec{r}_o) = \frac{1}{4\pi} \int \int \phi_{\nu}^{k,j} e^{-\tau_{\nu}^{k,j}(\hat{\Omega})} d\nu d\Omega, \quad (5)$$

where the the optical depth for the  $k$ -to- $j$  transition  $\tau_{\nu}^{k,j}$  covers the path from  $\vec{r}_o$  to the edge of the plasma along the direction  $\hat{\Omega}$ . A ray trace method is employed to calculate  $\tau_{\nu}^{k,j} = \sum_m \kappa_{\nu}^{k,j}(\vec{r}_m) \delta s_m$ , where  $\delta s_m$  is the path length through zone  $m$  in the  $\hat{\Omega}$  direction and  $\kappa_{\nu_{k,j}}(\vec{r}_m)$  is the absorption coefficient in that zone. The angular integral in eqn.(5) is calculated in 3-D by choosing a discrete set of ordinates with appropriate weights. The probability-of-escape is

used to combine the last two terms of eqn.(2) leading to

$$\begin{aligned} \frac{\partial n_k}{\partial t} = 0 = & n_e n_j C_{j,k} - n_e n_k D_{k,j} + n_e n_e n_{j+1} B_{j+1,k} - n_e n_k C_{k,j+1} \\ & + n_e n_{j+1} R_{j+1,k} - n_k A_{k,j} P_{k,j} . \end{aligned} \quad (6)$$

When the plasma is optically thick in a particular line ( $\mathcal{P} < 1$ ), a fraction  $(1 - \mathcal{P})$  of the photons emitted from position  $\vec{r}_o$  are reabsorbed and, consequently, the radiative decay rate is effectively reduced to a fraction  $\mathcal{P}_{k,j}$  of its intrinsic atomic value. The computational advantage of the “on-the-spot” approximation is the absence of a matrix of radiative coupling coefficients since one needs only to compute and store the escape probabilities to the plasma edge and not to all zones within the plasma. This is a simplification for radiation transport in multi-dimensional simulations. However, an iterative procedure between the radiation field of eqn.(1) and the population kinetics in eqn.(6) is still employed in this second model: the escape probability of one line at some position depends on the level populations and escape probabilities of other lines at all other positions in the plasma through the absorption coefficient  $\kappa$  of eqn.(3). Since a photon either is absorbed at its point of origin or escapes the plasma, the expression for the volumetric radiative loss term in eqn.(4) is replaced by

$$\Lambda = \sum 4\pi j_{k,j} P_{k,j} , \quad (7)$$

where the sum includes all emission lines.

### c. Tabular Collisional Radiative

The third model retains the non-local character of radiation transport inherent in the first two approaches, includes the non-linear coupling between the radiation field and the level populations, but replaces the exact self-consistency of a dynamically iterative solution performed at each timestep with an approximate one needing no iteration. The main assumption of this model is that the line emissivity from a particular position  $\vec{r}_o$  is equal to that from a *uniform plasma* whose properties are given by the density, temperature, etc., at that position. The size of this uniform plasma and the probability-of-escape are mutually dependent. This assumption is valid for optically thick lines when the gradient length scale of the plasma parameters is large compared to the absorption length of a photon. For thin lines the gradient is unimportant and the photon escapes along any line of sight. In this model the transport and kinetics are solved using a set of pre-calculated tables from which  $j_{k,j}$  and  $\kappa_{j,k}$  are obtained.

To illustrate how the tables are established, consider a uniform 1-D plasma slab specified by its thickness,  $\delta x$ , total ion density,  $n_i = \sum_j n_j + \sum_k n_k$ , and the internal energy,  $E$ . Equations (1), (2), and (3) are solved self-consistently for a single zone in this ideal plasma geometry by adjusting the electron temperature  $T_e$  and level populations until  $E = (3/2)n_e k_B T_e + \sum n_j \epsilon_j + \sum n_k \epsilon_k$ , where  $n_e$  is the electron density determined from the ion densities  $n_j$ , and  $\epsilon_j$  ( $\epsilon_k$ ) is the ionization (excitation) energy per particle. For each transported line  $j_{k,j}$ , there is a unique relation between  $\delta x$  and the probability-of-escape  $\mathcal{P}_{k,j}$  from the slab. This facilitates the construction of Radiative Equation of State (REOS) tables of electron temperature  $T_e$ , mean charge state  $\bar{Z}$ , emissivity  $j_{k,j}$ , and absorption coefficient  $\kappa_{j,k}$ , as a function of  $(n_i, E, \mathcal{P}_{k,j})$ . In practice at each timestep of a simulation the magnetohydrodynamic component of a code supplies  $n_i$  and  $E$  for every zone. Then the probability-of-escape is computed from eqn.(5) and the REOS Tables are searched for the corresponding values of  $(T_e, \bar{Z}, j_{k,j}, \kappa_{j,k})$  for each transported line from every zone whenever the radiation field is updated. In this manner the tabulated  $\mathcal{P}_{k,j}$  are matched to the probabilities-of-escape for the entire plasma, not the local numerical zone. The procedure is summarized in Fig.1. We designate this approach as the Tabular Collisional Radiative Equilibrium (TCRE) model.

The inconsistency which arises in the TCRE model stems from the use of tabular data based on a uniform medium in place of dynamically coupling the transport and kinetics by an iterative approach as described in the GCRE and “on-the-spot” models above. This inconsistency also leads to a temporal offset in the spatial coupling of populations between distant zones resulting from the time interval between radiation calls calculating the escape probabilities. The radiation field is typically updated on a much longer time scale than the hydrodynamic time scale. An inconsistency due to the non-iterative tabular look-up might be expected to arise from two different transported lines in different ionization stages, which have different probabilities-of-escape. This approach might give different values of  $T_e$  and  $\bar{Z}$  in the same zone based on the REOS table look-up. However, it is found that in the absence of bound-free opacity,  $T_e$  and  $\bar{Z}$  are for all practical purposes dependent primarily on  $n_i$  and  $E$ . The weak dependence of  $T_e$  and  $\bar{Z}$  on  $\mathcal{P}_{k,j}$  that does exist is largest at low ion density and negligible at higher ion density. This point is illustrated in Figs.2 and 3, where  $T_e$  and  $\bar{Z}$  are plotted as functions of  $E$  and  $\delta x$  for an argon plasma with ion densities of  $7.0 \times 10^{17}$  and  $7.6 \times 10^{20} \text{ cm}^{-3}$ , respectively. The consequences of not iterating are described in the results section.

In addition to the *uniform plasma* and “on-the-spot” approximations of the TCRE model there are other features worth noting. First, only one excited level in each ionization stage is included in the 1-D REOS tables as a representative line and is transported in the multi-dimensional plasma. This level is chosen to correspond to the strongest, most opaque resonance line. The emissivities of other lines emanating from that ionization stage are scaled from the resonant line using the uniform plasma approximation and are added to the emissivity of the representative line. Secondly, at present only line opacity is considered in the escape probabilities. Finally, opacity effects are included in the bremsstrahlung radiation emissivity but not for the recombination (free-bound) emissivity.

In summary, the TCRE model retains the advantages of the escape probability method developed for 1-D plasmas, and, as we will show, provides a reasonably accurate, computationally efficient, multi-dimensional method for coupling radiation transport and atomic level kinetics.

#### d. Optically Thin

A fourth model is considered in the paper for comparison purposes. It treats the radiation as optically thin and ignores transport effects altogether. This model simply but incorrectly assumes that all created photons escape the plasma and, hence, the  $\mathcal{P}$  term in eqn.(6) is set to unity. It is included to demonstrate the extreme differences which arise in dynamical simulations of Z-pinchs employing this assumption as compared to any other treatment of transport.

### III. Model Comparisons

The accuracy of the TCRE model is assessed by comparing the results of 1D Lagrangian MHD calculations that employ this model against results obtained using the GCRE model. Both models use the same 1D, cylindrical geometry, ray trace scheme.<sup>7</sup> The K-shell radiative yield, the total radiative yield, stagnation profiles for  $n_i$  and  $T_e$ , and computation times are compared for several typical Z-pinch calculations. These include  $150 \mu\text{g}/\text{cm}$  and  $500 \mu\text{g}/\text{cm}$ , uniform fill, 3.5 cm radius, argon loads that are imploded using a linearly ramped current profile that is terminated when the energy-per-ion coupled to the load exceeds an  $\eta^*$  value of 2.  $\eta^*$  is the coupled energy-per-ion divided by the minimum energy-per-ion needed to ionize to the K shell.<sup>13</sup> For argon this minimum energy is 40 keV per-ion.<sup>14</sup> In addition, comparisons are made for  $1125 \mu\text{g}/\text{cm}$  and

1857  $\mu\text{g}/\text{cm}$ , 2 cm long, titanium wire array loads that have initial array diameters of 4.5 cm and 3.5 cm, respectively. These loads are imploded using a circuit model for the Z machine at Sandia National Laboratories and have  $\eta^*$  values around 2.

Table I compares the total and K-shell yields as calculated for the above loads using four different radiation models, the models are: (1) TCRE, (2) “*on-the-spot*”, (3) GCRE, and (4) the optically thin. The 1D calculations are identical except for the radiation model. In comparison to the other models, the optically thin model predicts too much radiative energy escaping the z-pinch. For the titanium loads, the masses are large enough that the optically thin model radiates the energy so efficiently that the resulting overcooled plasma can barely ionize into and radiate from the K shell. This comparison emphasizes the importance of photon trapping.

Since the TCRE model is inherently the “*on-the-spot*” model with the exception that the *uniform plasma* approximation is also implemented, a comparison between the TCRE and “*on-the-spot*” models is a good indicator of how much the *uniform plasma* approximation is adversely affecting the TCRE calculation. In terms of K-shell and total yields, Table I shows that for these typical z-pinch loads the *uniform plasma* approximation is very good.

The Table I comparison of the TCRE, “*on-the-spot*”, and GCRE models shows that, with the exception of the K-shell emission of the 1857  $\mu\text{g}/\text{cm}$  titanium load, the models are in good to excellent agreement. One reason why model deficiencies are likely to show up for a load such as the 1857  $\mu\text{g}/\text{cm}$  titanium load is that the K-shell emission becomes very model sensitive for loads that have values of  $\eta^* < 2.0$ . A value of  $\eta^*$  near unity implies that there is barely enough energy to ionize into and radiate from the K shell, and its value is 1.5 for this titanium load. Titanium experiments performed on the Z machine also exhibited a decline in K-shell yield in this  $\eta^*$  regime.<sup>15</sup>

Based on the good K-shell yield agreement between the TCRE model and the “*on-the-spot*” model for the 1857  $\mu\text{g}/\text{cm}$  titanium load and the disagreement between the “*on-the-spot*” and GCRE model, it is reasonable to speculate that the major deficiency of the TCRE modeling of these load is the use of the “*on-the-spot*” approximation. Therefore, in the future, it may be worthwhile to improve the TCRE model by using an escape probability that is based on a more accurate transit probability than that calculated using the “*on-the-spot*” approximation.

The ion density and electron temperature profiles produced by the TCRE, “*on-the-spot*”, and GCRE models were generally in good agreement for the four tested loads. The greatest deviation

occurred for the  $500 \mu\text{g}/\text{cm}$  argon load. The profiles for this load are shown in Figures 4 and 5 for the ion density and electron temperature, respectively. The time profile of the K-shell radiative power is also shown for this load in Fig. 6. Even the profiles for the  $1857 \mu\text{g}/\text{cm}$  titanium load, which had the largest model disagreement in terms of predicted K-shell yield, showed generally good profile agreement. This is illustrated in Figures 7-10, respectively, for the ion density, electron temperature, total radiative power, and K-shell power profiles. For clarity, the "*on-the-spot*" results are omitted from these figures. They lie between the TCRE and GCRE results. In all cases there were significant spatial and temporal differences between the profiles generated under optically thin conditions and the profiles generated using any of the other models.

Table II shows a typical example of the computer times that the GCRE, TCRE, and "*on-the-spot*" models require to perform a calculation. Specifically the timing results for the  $1857 \mu\text{g}/\text{cm}$  titanium load calculation are displayed. The time spent transporting the radiation dominates the total calculation time for the GCRE and "*on-the-spot*" models, whereas, the radiation computation time is negligible for the TCRE model. The radiation calculation was at least 1000 times faster for the TCRE model than for either the GCRE or "*on-the-spot*" models. Note, these calculations were performed using a 500 MHZ, Pentium III personal computer.

In the 2D calculations discussed below, the radiation computation time for the TCRE model is about one third of the total computation time. The reason this time is relatively longer in 2D than 1D is because of the 2D ray trace. For a fixed number of rays the computation time associated with the 2D ray trace scales approximately with the square of the number of zones. Furthermore, the number of rays required to adequately resolve the radiation field is much greater in 2D (typically 50 to 100 rays are needed).

#### IV. Two-Dimensional TCRE Calculations

The main purpose of this section is to demonstrate that the TCRE model can be readily adapted to an existing 2D code, namely PRISM, and to present some 2D results. However, we also consider some modeling issues in 1D and 2D that can have as profound an effect on results as the choice of radiation model. A proven method of increasing understanding and improving models is to compare experimental data with model calculations. By improving the radiation models used in the calculations one can better focus on other physics and numerical issues to resolve differences



between experimental and theoretical results.

A comparison is made between 1D and 2D model results for K-shell radiative yields obtained from argon gas puff calculations that were intended to simulate experiments performed on the Z machine at Sandia National Laboratories. These gas puff calculations are for 2 cm length, 7 cm diameter, double puffs of 500, 1000, 1500, 2000, and 2500  $\mu\text{g}/\text{cm}$ . The mass distribution of gas used in these calculations is taken from the measured gas distribution obtained from interferometry measurements performed at the Naval Research Laboratory,<sup>16</sup> see Figure 11. A circuit model of the Z machine is used to drive the theoretical implosions.

The mass distribution is initially uniform along the  $z$  direction in the 2D calculations; however, when the outer radius of the pinch has imploded to a radius of less than 3 cm a density and velocity perturbation is applied. The initial perturbation wavelength  $\lambda$  is chosen as 0.5 cm, which is a typical disruptive wavelength. It is a non-compressible perturbation characterized by: (1)  $\rho' = \rho_o \times (0.25) \times \cos(2\pi z/\lambda)$ ; where the mass density  $\rho$  equals  $\rho_o$  (initial mass density)  $+\rho'$  and (2)  $u' = -u_o \times (0.25) \times \cos(2\pi z/\lambda)$ ; where the radial velocity  $u$  equals  $u_o$  (initial radial velocity)  $+u'$ . When the perturbation is turned on it is limited to zones near the outer plasma radius because it is only applied when  $|u| > 0.1 \times |u_{max}|$ . Note, the choice of perturbation level and turn-on time is somewhat arbitrary, which is in the spirit of this preliminary investigation to look for general trends made apparent by the 2D modeling of Rayleigh-Taylor instability growth. Figure 12 shows the 2D radiative power density profile for a 2000  $\mu\text{g}/\text{cm}$  load at 30 ns after the perturbation turn-on time. Notice, that this figure shows that the radiative power is larger at the axial boundaries, which is a consequence of their higher photon escape probabilities.

The K-shell yield comparison is made for the following models: (1) 1D Lagrangian MHD with GCRE radiation transport, (2) 1D Lagrangian MHD with TCRE radiation transport, (3) 1D Lagrangian MHD with optically thin radiation, (4) 1D Eulerian MHD (PRISM code) with TCRE transport and (5) 2D Eulerian MHD (PRISM code) with TCRE transport. The 1D Lagrangian calculations employ 80 radial zones, the 1D PRISM calculation employs 200 radial zones and the 2D PRISM calculation uses 200 radial zones and 40 axial zones. The only substantial difference between applying the TCRE model in 2D as opposed to 1D is that the ray trace method used to calculate the “*on-the-spot*” escape probabilities is more complicated. The 2D method used here was developed by Chong<sup>17</sup>. Nearly the same K-shell yield and total yield results (within 10

percent) are attained with the 1D Eulerian code when it is run with either the same ray trace scheme utilized in the 1D Lagrangian calculations or with the 2D ray trace method. The K-shell yields as a function of argon mass load are plotted for these five models in Figure 13.

The 1D Lagrangian GCRE K-shell yield results curve (1) of Fig. 13 is nearly identical to the 1D Lagrangian TCRE curve (2). This agreement and the fact that the  $n_i$  and  $T_e$  stagnation profiles produced by these two models are also in good agreement (not shown), provide strong evidence that the TCRE model is modeling opacity and optical pumping effects in accord with the GCRE model. Therefore the TCRE model should also be suitable for modeling these effects in 2D. The substantial differences between the GCRE curve (1) results and the optically thin results of curve (3) again illustrate the importance of including detailed and accurate radiation models in Z-pinch calculations.

Comparing the 1D Eulerian results of curve (4) with the 1D Lagrangian results of curve (2) reveals that there are large inherent numerical differences when implosion calculations are performed in a Lagrangian versus an Eulerian reference frame. In all fairness to the Eulerian model, there was probably inadequate resolution in the radial direction to converge its results. Nevertheless, the point needs to be made that model characteristics other than the choice of radiation treatment can affect results. In particular, model reference frame and zoning can have a strong influence. Minimizing some of the model dependencies by benchmarking a calculation to a specific experiment and then analyzing the rest of the experiments in the series under the conditions of the benchmark is a useful technique for studying 1D and 2D experimental trends.<sup>13,18,19</sup> This benchmarking has involved alterations in transport coefficients, perturbation levels, perturbation turn-on times, and radiation dilution factors.

The 2D Eulerian results of curve (5) when compared with the 1D Eulerian results of curve (4) indicate that the presence and growth of R-T instabilities in the experiments has the potential to somewhat degrade the K-shell yields. However, in this preliminary investigation, a comparison of these curves with the 1D Lagrangian results of curve (2) again emphasizes that the numerical algorithm and zoning can play at least as large a role as R-T instabilities in affecting calculated K-shell yields.

## V. Summary

A computationally efficient, multi-dimensional, transport method suitable for modeling Z-pinch plasmas that are in collisional radiative equilibrium has been developed and demonstrated in 1D and 2D calculations. This method is superior to diffusion methods because: (1) the source function is based on a self-consistent non-LTE calculation, not an *ad hoc* assumption that it is Planckian, (2) the optically thin radiation is allowed to escape, not subjected to an inappropriate diffusion equation, and (3) accurate line-by-line escape probabilities are used, not diluted as in diffusion, by frequency groups that mix line and continuum opacities.

The basis of this TCRE model is an approximation that states: a localized region of plasma with ion density  $n_i$ , electron internal energy  $E$ , and escape probability  $\mathcal{P}$  for a given line photon will have the same line emission coefficient and absorption coefficient as that given by a uniform plasma having identical  $n_i$ ,  $E$ , and  $\mathcal{P}$ . This approximation allows one to utilize existing 1D escape probability based results for the solution of the radiative transfer equation to approximate a solution in two or three dimensions. The TCRE model is very efficient because the 1D transport results that it is based upon are tabulated. This method is at least a thousand times faster than the time required for the full transport calculation.

The current implementation of the TCRE model is in reasonably good agreement with the GCRE calculation over a wide range of Z-pinch titanium and argon plasma conditions, even when sharp gradients in temperature and density are present. We have not encountered conditions where the TCRE approach gives poor results. However, there is missing physics in the TCRE model which must be added in the future to guarantee its continued robustness. For instance, continuum opacity is not included in the calculation of the escape probabilities, nor can time-dependent ionization dynamics be treated. As Z-pinch drivers become more energetic and powerful, simulation of their plasmas will increasingly require that these effects be included in any realistic modeling. Another potential weakness of TCRE is that the present calculations have shown that for plasmas just barely energetic enough to ionize into the K shell, the “*on-the-spot*” approximation begins to break down. We expect to address these issues as further development of the TCRE approach proceeds.

It must be noted that developing a reliable link between 1D Lagrangian and 2D Eulerian via 1D Eulerian descriptions of a radiating plasma is not simply a technical issue of numerical simulations. Rather, it has a direct practical significance for the development of plasma radiation sources (PRS). The full transport (GCRE) 1D Lagrangian calculations describe, to the best of our knowledge, the

radiation performance of PRS under the "best case" conditions where instability of the plasma flow is completely suppressed. Such modeling is fully adequate for studying the effect of radial load structures on the K-shell radiation yield, e.g., to evaluate the contribution of this effect apart from the axial dependence of the radiated power especially in gas-puff loads. In two dimensions, the effects of structure and stability become inseparable. A 2D Eulerian RMHD simulation allows inclusion of both effects, but without accurate radiation transport it lacks a reliable reference point with which to evaluate the degree of hydrodynamic modeling inaccuracy. One reference point is provided by the GCRE Lagrangian 1D model. Combined use of both models will allow us to better address the major issues of PRS load design and optimization. For instance, if it is established that under certain load conditions the K-shell yield is sensitive mainly to the radial density/composition structure of the load, then the instability is tolerable, and we should optimize the radial/composition structure, e.g., through gas puff nozzle design. On the other hand, if the key factor turns out to be the RT instability of implosion, then this is the issue to be addressed by structuring the load for the specific purpose of mitigating this instability, e.g., by adding a weak axial magnetic field.

## References

- [1] F. L. Cochran, J. Davis, and A. L. Velikovich, *Phys. Plasmas* **2**, 2765 (1995).
- [2] J. W. Thornhill, K. G. Whitney, and J. Davis, *J. Quant. Spectrosc. Radiat. Transfer* **44**, 251 (1990).
- [3] R. B. Spielman, S. F. Breeze, C. Deeney, M. R. Douglas, F. Long, T. H. Martin, M. K. Matzen, D. H. McDaniel, J. S. McGurn, T. J. Nash, J. L. Porter, L. E. Ruggles, T. W. L. Sanford, J. F. Seamens, W. A. Stygar, J. A. Torres, D. M. Zagar, D. O. Jobe, D. L. Peterson, R. W. Shoup, K. W. Struve, M. Mostrom, P. Corcoran, and I. Smith, Paper O-4-3 in *Proceedings of the 10th International Conference on High-Power Particle Beams*, Prague, Czech Republic, 10-14 June 1996, edited by K. Jungwirth and J. Ullschmied, pp. 150-153. Copies of the conference proceedings can be ordered from BEAMS 96, Institute of Plasma Physics, Czech Academy of Sciences, Za Slovankou 3, 182 00 Prague, Czech Republic.
- [4] J. Davis, R. W. Clark, J. L. Giuliani, Jr., and J. W. Thornhill, in *Atomic Processes in Plasmas, 11<sup>th</sup> Topical Conference* (Auburn, Alabama, March 23-26, 1998), edited by E. Oks and M. S. Pindzola (American Institute of Physics, Woodbury, NY, 1998)pp. 199-215.
- [5] J. Davis, J. Giuliani, Jr., R. Clark, J. Apruzese, J. Thornhill, K. Whitney, A. Dasgupta, A. Velikovich, Y. Chong, L. Rudakov, R. Terry, P. Kepple, in *Atomic Processes in Plasmas, 12<sup>th</sup> Topical Conference* (Reno, Nevada, March 19-23, 2000), edited by R. Mancini and R. A. Phaneuf (American Institute of Physics, Melville, NY, 2000)pp. 69-80.
- [6] J. P. Apruzese, J. Davis, D. Duston, and K. G. Whitney, *J. Quant. Spectrosc. Radiat. Transfer* **23**, 479 (1980).
- [7] J.P. Apruzese, *J. Quant. Spectrosc. Radiat. Transfer* **25**, 419 (1981).
- [8] J. P. Apruzese, *J. Quant. Spectrosc. Radiat. Transfer* **34**, 447 (1985).
- [9] R.W. Clark, J. Davis, J.P. Apruzese, and J.L. Giuliani, *J. Quant. Spectrosc. Radiat. Transfer* **53**, 307 (1995).
- [10] J. P. Apruzese, *Computer Applications in Plasma Science and Engineering*, (Springer-Verlag, New York, Inc., 1991), p. 359.
- [11] T. Holstein, *Phys. Rev.* **72**, 1212 (1947).

- [12] D. E. Osterbrock, *Astrophysics of Gaseous Nebulae*, (W. H. Freeman and Company, San Francisco, 1974), p. 19.
- [13] J. W. Thornhill, K. G. Whitney, C. Deeney, and P. D. LePell, *Phys. Plasmas* **1**, 321 (1994).
- [14] K. G. Whitney, J. W. Thornhill, J. P. Apruzese, and J. Davis, *J. Appl. Phys.* **67**, 1725 (1990).
- [15] C. Deeney, C. A. Coverdale, M. R. Douglas, T. J. Nash, R. B. Spielman, K. G. Whitney, J. W. Thornhill, J. P. Apruzese, R. W. Clark, J. Davis, F. N. Beg, and J. Ruiz-Camacho, *Phys. Plasmas* **6**, 2081 (1999).
- [16] Y. Song, P. Coleman, B. H. Failor, A. Fisher, R. Ingermanson, J. S. Levine, H. Sze, E. Waisman, R. J. Commisso, T. Cochran, J. Davis, B. Moosman, A. L. Velikovich, B. V. Weber, D. Bell, and R. Schneider, *Rev. Sci. Instrum.* **71**, 3080 (2000).
- [17] Y. K. Chong, T. Kammash, and J. Davis, in *Dense Z Pinches, 4<sup>th</sup> International Conference* (Vancouver, Canada, 28-30 May 1997), edited by N. Pereira, J. Davis, and P. E. Pulsifer (American Institute of Physics, Woodbury, NY, 1997) pp. 277-282.
- [18] D. L. Peterson, R. L. Bowers, J. H. Brownell, A. E. Greene, K. D. McLenithan, T. A. Oliphant, N. F. Roderick, and A. J. Scannapieco, *Phys. Plasmas* **3**, 368 (1996).
- [19] J. H. Hammer, J. L. Eddleman, P. T. Springer, M. Tabak, A. Toor, K. L. Wong, G. B. Zimmerman, C. Deeney, R. Humphreys, T. J. Nash, T. W. L. Sanford, R. B. Spielman, and J. S. De Groot, *Phys. Plasmas* **3**, 2063 (1996).

Fig. 1. Schematic diagram of the Tabulated CRE transport model.

Fig. 2. Electron temperature ( $T_e$  (eV)) and effective charge ( $Z$ ) as a function of electron internal energy and plasma thickness  $\Delta r$ . The argon ion density  $n_i$  is  $7.0 \times 10^{17} \text{ cm}^{-3}$ .

Fig. 3. Electron temperature ( $T_e$  (eV)) and effective charge ( $Z$ ) as a function of electron internal energy and plasma thickness  $\Delta r$ . The argon ion density  $n_i$  is  $7.64 \times 10^{19} \text{ cm}^{-3}$ .

Fig. 4. Ion density ( $n_i$ ) radial profile at the time of peak argon K-shell emission for a variety of radiation transport models. Results are for a  $500 \mu\text{g/cm}$  argon load.

Fig. 5. Electron temperature ( $T_e$ ) radial profile at the time of peak argon K-shell emission for a variety of radiation transport models. Results are for a  $500 \mu\text{g/cm}$  argon load.

Fig. 6. Time evolution of the K-shell power for a variety of radiation transport models. Results are for a  $500 \mu\text{g/cm}$  argon load.

Fig. 7. Ion density ( $n_i$ ) radial profile at the time of peak titanium K-shell emission for a variety of radiation transport models. Results are for a  $1857 \mu\text{g/cm}$  titanium load.

Fig. 8. Electron temperature ( $T_e$ ) radial profile at the time of peak titanium K-shell emission for a variety of radiation transport models. Results are for a  $1857 \mu\text{g/cm}$  titanium load.

Fig. 9. Time evolution of the total radiated power for a variety of radiation transport models. Results are for a  $1857 \mu\text{g/cm}$  titanium load.

Fig. 10. Time evolution of the K-shell radiated power for a variety of radiation transport models. Results are for a  $1857 \mu\text{g/cm}$  titanium load.

Fig. 11. Initial ion density distribution used in 2D PRISM double puff calculations to preliminarily investigate argon experiments performed on the Z machine at Sandia National Laboratories.

Fig. 12. Spatial profile of the total radiative power  $30 \text{ ns}$  after the perturbation is turned on. Result is for a  $2000 \mu\text{g/cm}$  argon double puff load driven by a Z machine circuit model.

Fig. 13. Comparison of K-shell yields as calculated from 1D and 2D models of argon gas puff experiments performed on the Z machine. Calculations are performed for mass loads of 500, 1000, 1500, 2000, and 2500  $\mu\text{g}/\text{cm}$ .



Table I. Radiation transport model comparison of total and K-shell radiative yields in (kJ/cm) for different Z-pinch loads. The K-shell radiative yields are in parenthesis.

Radiation Transport Model	Argon 150 $\mu\text{g/cm}$	Argon 500 $\mu\text{g/cm}$	Titanium 1125 $\mu\text{g/cm}$	Titanium 1857 $\mu\text{g/cm}$
TCRE	12 (3)	87 (28)	262 (70)	366 (42)
On-the-Spot	10 (3)	81 (28)	258 (73)	370 (39)
GCRE	10 (3)	74 (23)	263 (69)	395 (26)
Optically Thin	23 (3)	100 (30)	400 (20)	600 (4)

Table II. Radiation transport model comparison of computer timings for the 1D 1857 mg/cm titanium wire array calculation.

Radiation Transport Model	Total calculation time (cpu - seconds)	Radiation transport calculation time (cpu - seconds)
GCRE	29270	26286
"On-the-spot"	19280	16296
TCRE	2984	11

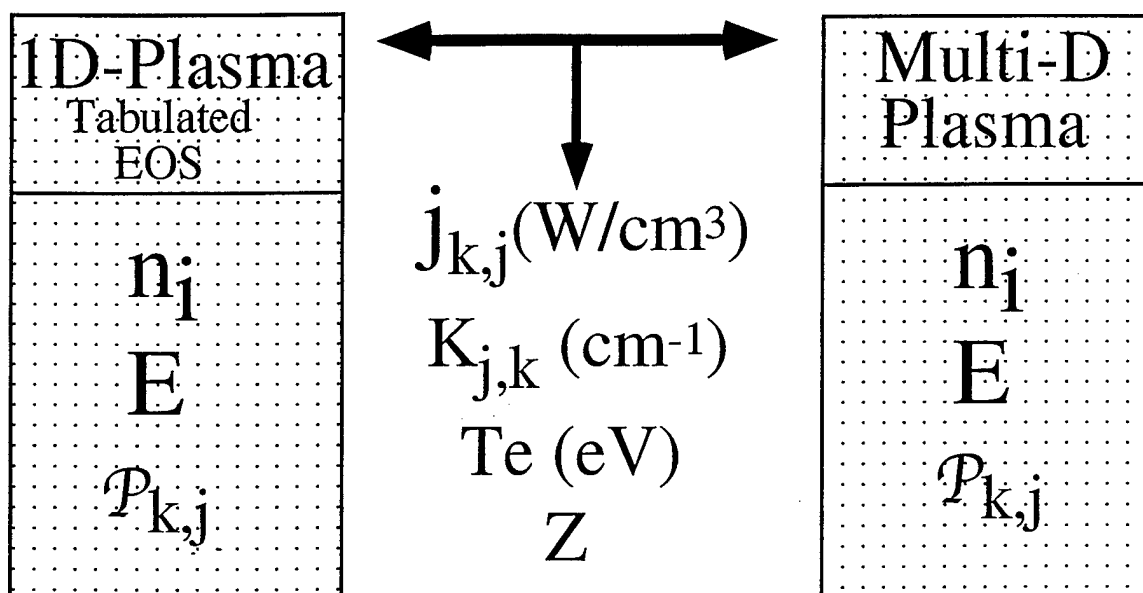


Fig. 1

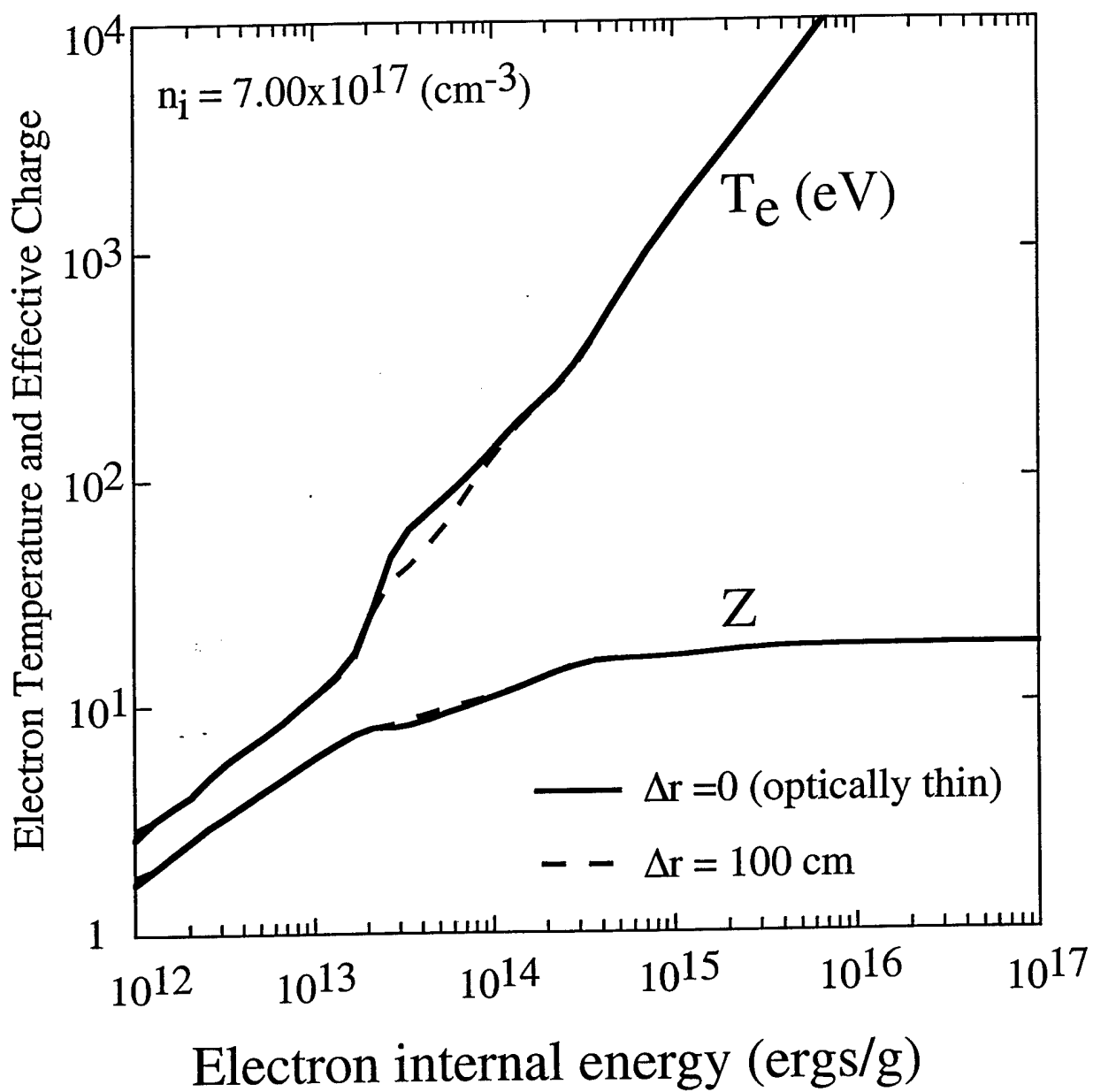


Fig. 2

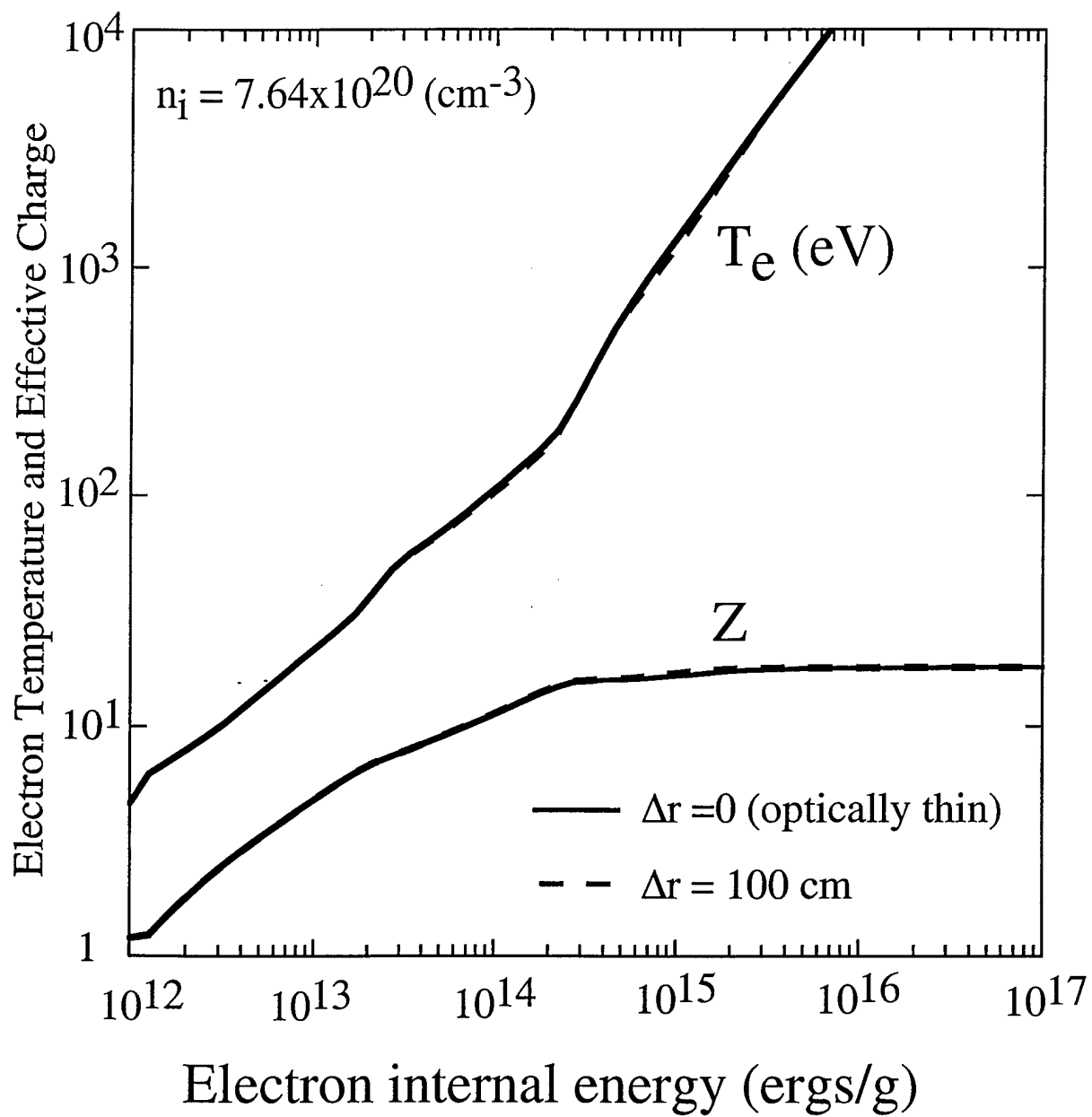


Fig. 3

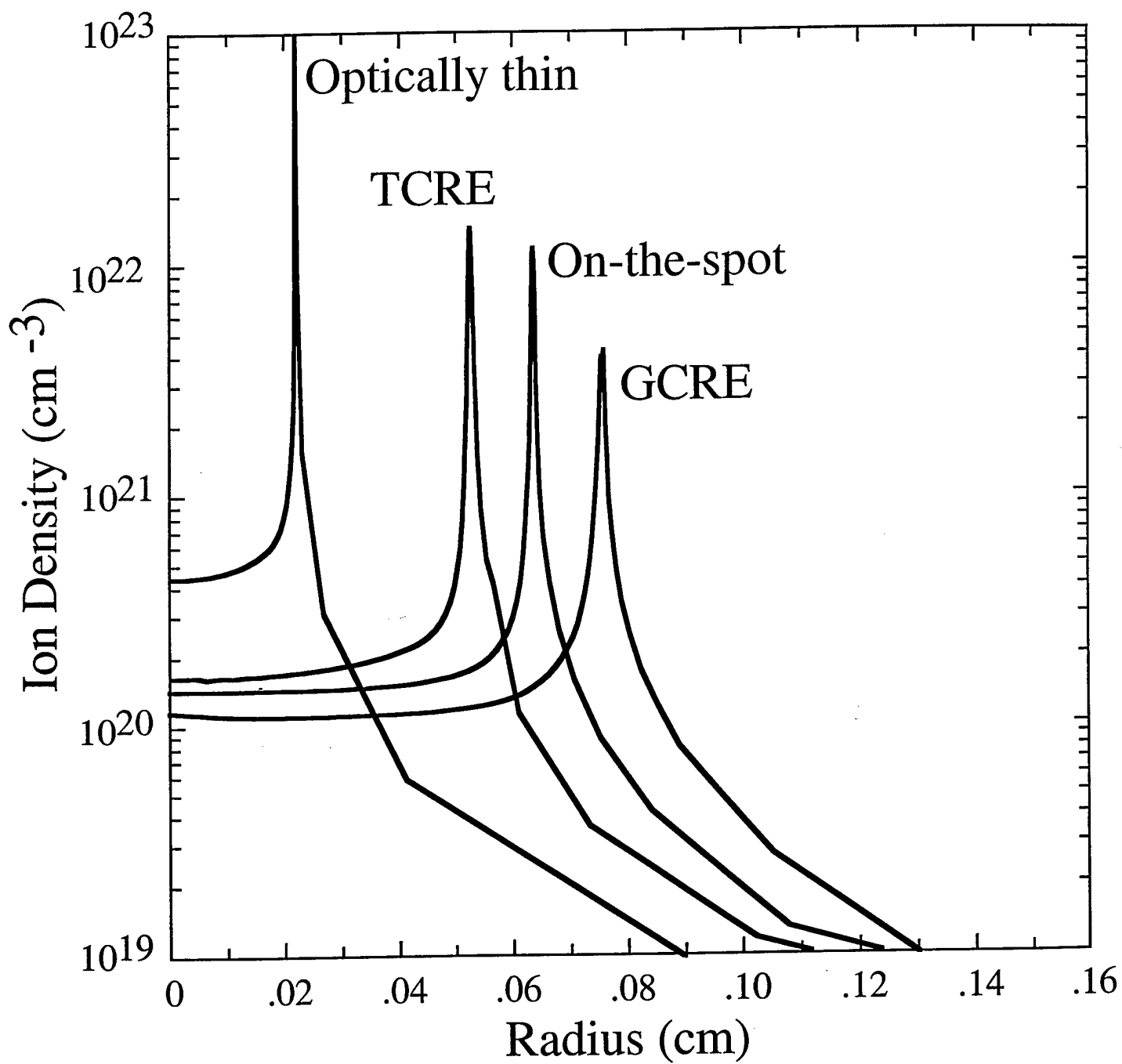


Fig. 4

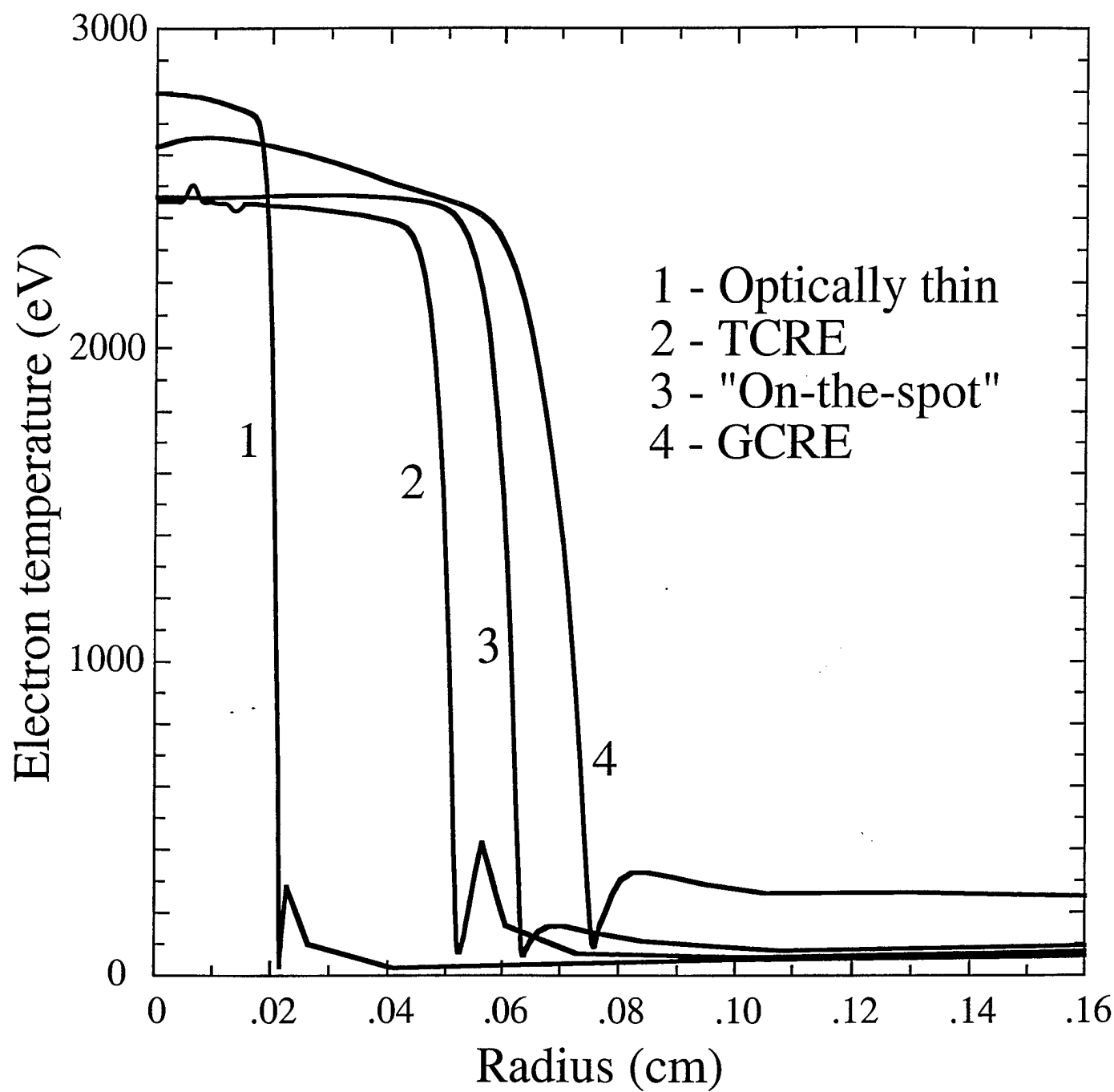


Fig. 5

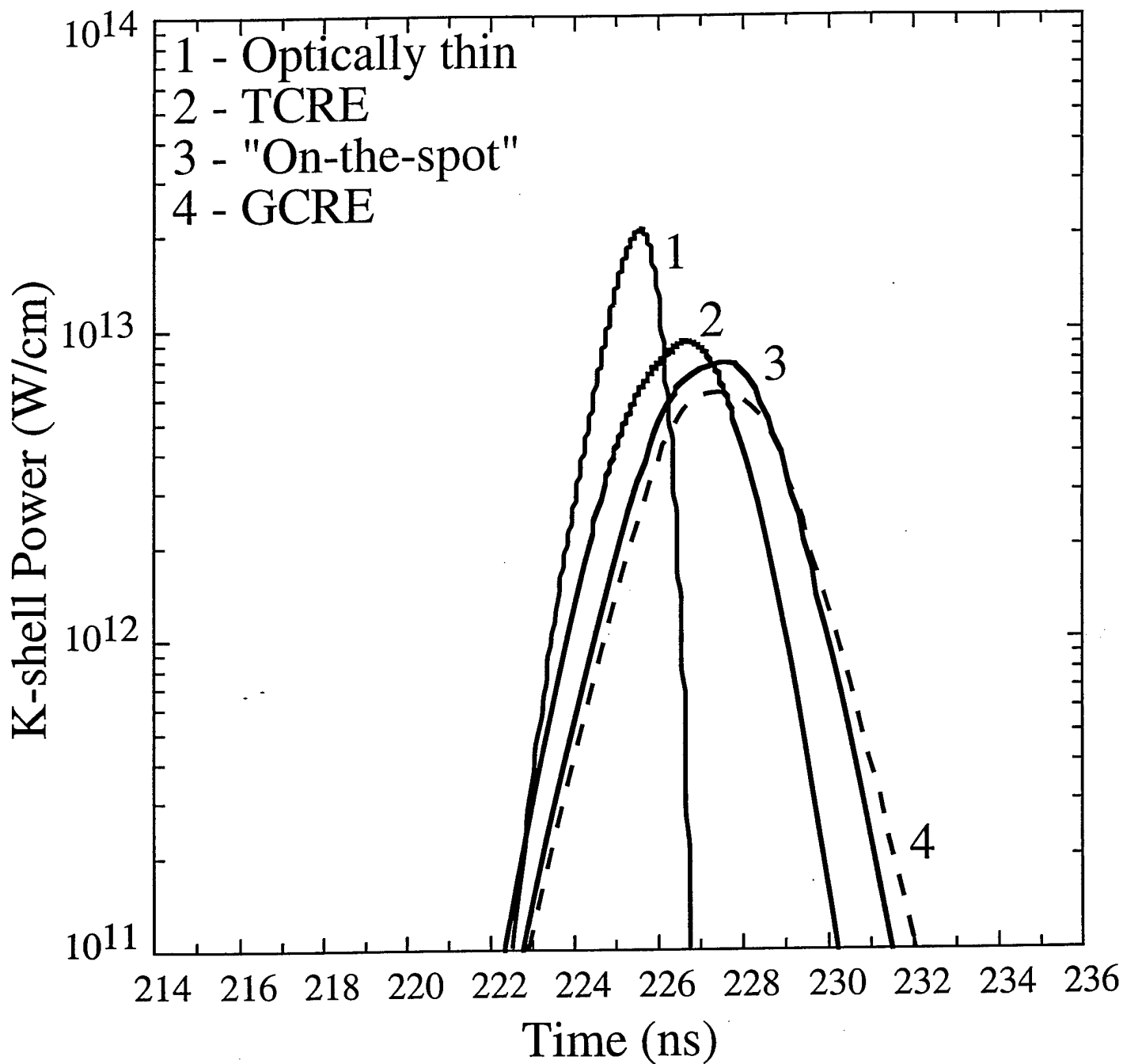


Fig. 6



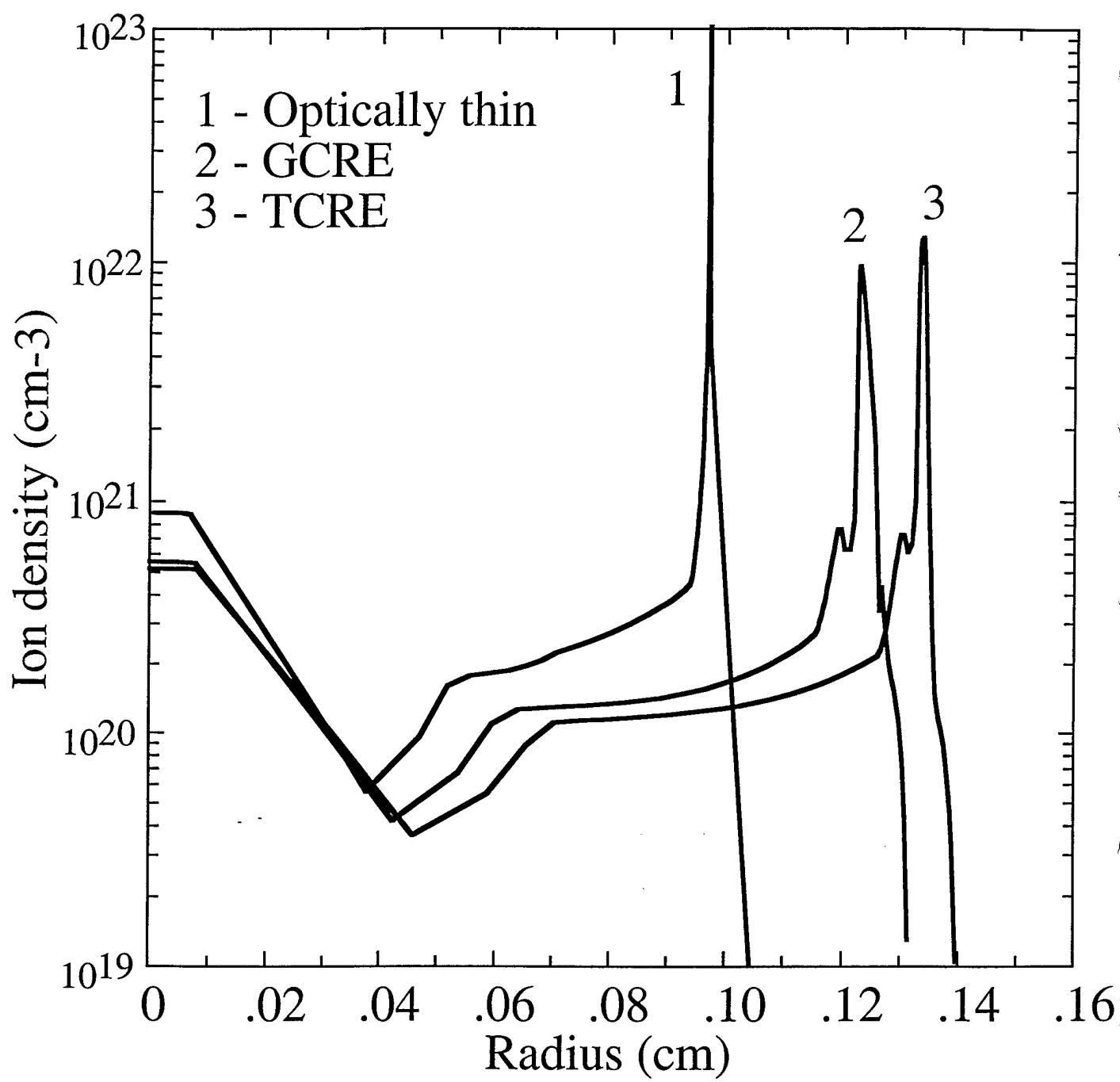


Fig. 7

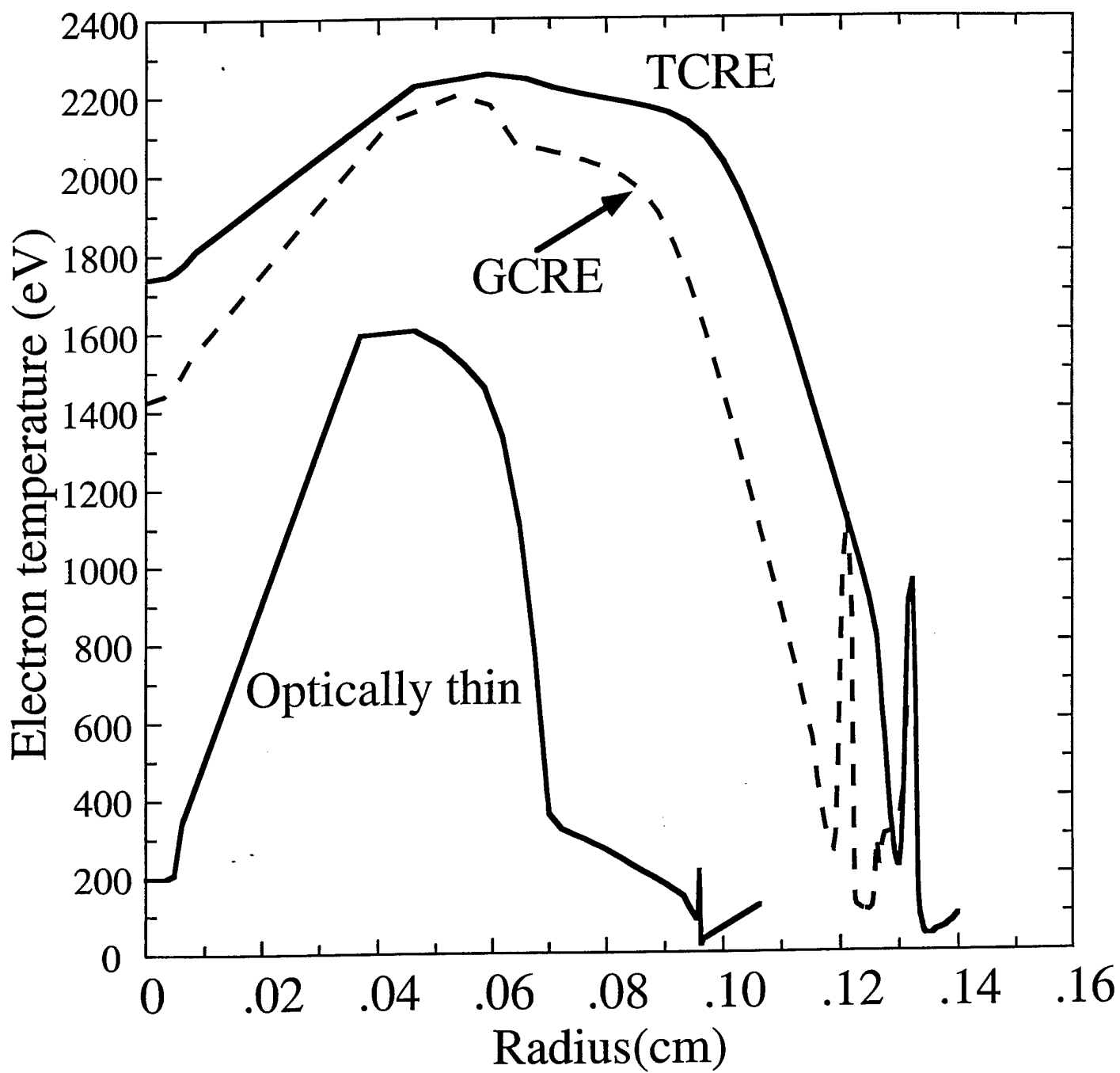


Fig. 8

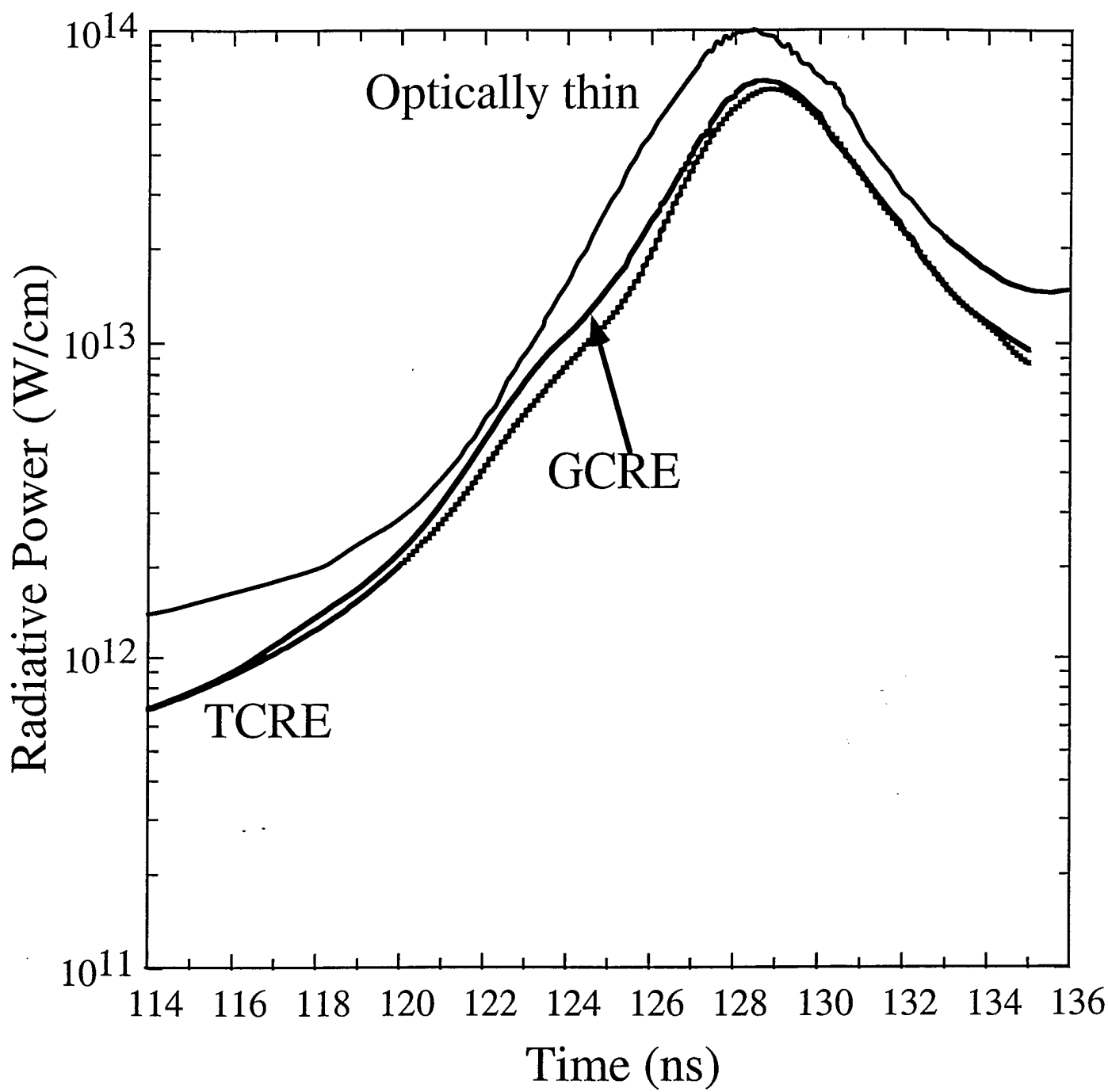


Fig. 9

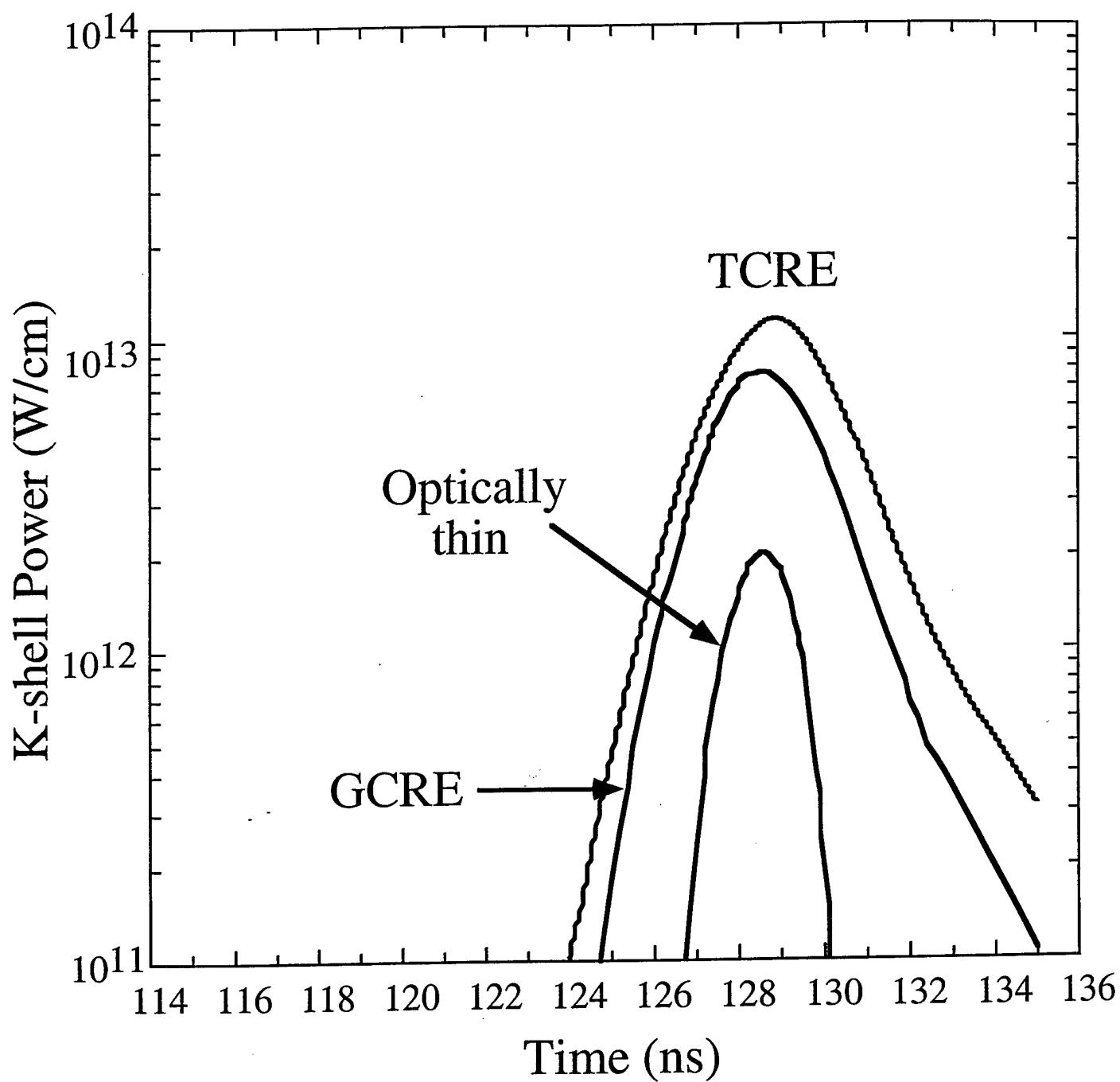


Fig. 10

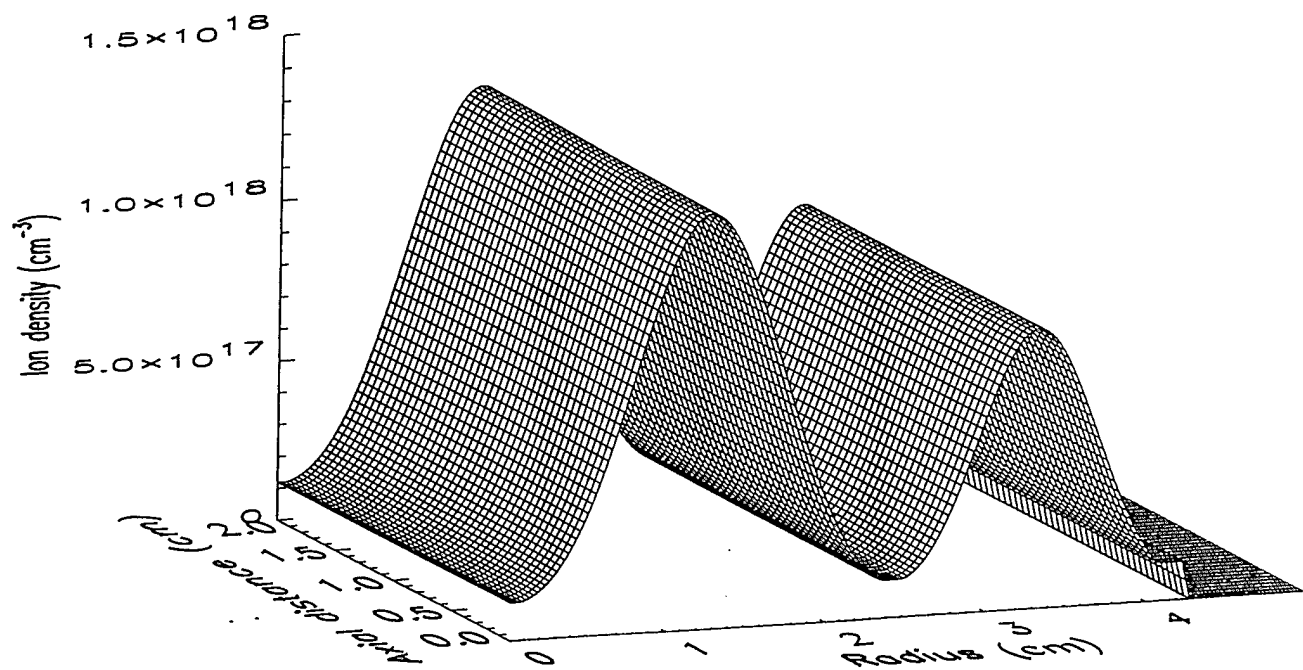


Fig. 11

## IV. Wire Load Dynamics and Modeling

### for DTRA Plasma Radiation Sources

Wire loads have shown a productive and reliable path to record high PRS radiative yields and powers. The technology offers a heretofore unknown level of control over pinch impedance history, load material variations, and assembly processes. As an element of the DTRA simulator program, the research and development effort focused on a fundamental, predictive and versatile understanding of these loads is described here.

An early insight into the operation of a wire load, in either a single or nested array, was provided by the advent of the Wire Dynamic Model (WDM) wherein the wire elements are treated as distinct circuit elements. The model has successfully described mass and current interchange in nested array loads over a current domain of 0.1 to 20 MA and the mass ranges that go with that for implosion times from 100 to 300ns. The behavior of bias inductance and wire resistance has been investigated experimentally and model generalizations to treat those variations are discussed here.

On the other hand a closer examination of wire implosion dynamics and initiation processes reveals a rich set of phenomena that are not so well understood. One such feature is the axial precursor of a wire array which forms on axis as array material is sloughed off and forced inward by magnetic pressure. The precursor is remarkably stable and settles into a steady state radius which is apparently characteristic of the the material and its radiation properties. A second such feature is the generation of a wire corona plasma which feeds the precursor and controls the inertia of the parent wire array as the implosion progresses. A third related feature is the process by which a wire array "closes" electrically and the relative fraction of current that is carried in the denser portions of the wire plasma at the time this closure obtains.

A fair amount of research to date appears to indicate that tenuous plasma dynamics is a noticeable to dominant contributor to the wire array implosion physics over the operational range of wire masses, interwire gaps, and deliv-

ered current per wire. It is also clear that the quality of equation of state and resistivity data plays a major role in the quality of theoretical prediction of the wire array physics.

Treating the tenuous plasma stresses conventional MHD codes nearly to (or argueably past) the point of validity as such thin material either streams around the interior wires of a nested array or builds a precursor column. The corona plasma experiences a wide dynamic range in ionization, perhaps radiatively driven, and conductivity as well. A final topic of research discussed here, the evolution of the WDM toward a true fluid particle model, is motivated primarily by the requirement to understand and to control (or perhaps even exploit) these load details for the optimization of the radiation product.

While the results of this effort are somewhat formal in nature, the required elements for a complete model are now in hand and some important properties of the theory are demonstrated. At present the model can be characterized as a Drift Kinetic Fluid Particle Hydrodynamics (DKFPH) which will span densities characteristic of dense pinch regions and corona with the same algorithm. The new fluid elements can be equipped with any desired equation of state, transport coefficients, and modern radiation treatments. A systematic particle management scheme is derived from straightforward thermodynamic considerations.

## 1 Applications Improving the WDM

The Wire Dynamic Model is a special case of a full fluid MHD picture in that (i) the wires are represented only as particles, while (ii) the dissipative or collisional effects in these wires are treated in a spatially averaged way, and (iii) the external forces are developed by an inductive and resistive lumped circuit description that presumes a known spatial concentration of electrical conductivity. These specializations are mostly of historical significance and are sequentially being replaced by more complete physics. However, the systematic perturbation about such valuable results has enabled the retention of an application ready version while the better implementations are developed.

In the following sections are discussed several new results which were added to the WDM during the program year, some are primarily formal while others are focused on particular experiments.

## 1.1 Energy Conservation and the Circuit Model

A definitive treatment of Poynting's theorem for the wire ensemble was not available once sticky, interacting wires were brought into play. The changes wrought by a better treatment are reflected in a more robust conservation of energy and the ability to capture the trade between inductive and resistive current division that is being observed in the laboratory.

For the WDM viewed as a "Biot-Savart gas" the direct interaction among an ensemble of current elements is equivalent to a potential energy defined by the array inductance and the velocity dependent drag forces are derivable from a Rayleigh dissipation function. Within the ensemble are symmetry groups of multiplicity  $S$ , e.g.

$$\mathcal{I} = \sum_{i=1}^{\mathcal{N},S} \mathcal{I}_{i,s} = \mathcal{I} \sum_{i=1}^{\mathcal{N}} S \alpha_i ,$$

where  $\alpha_i$  is any  $S$ -wise invariant current fraction contained in any particular wire path represented by a series resistance and inductance. Once the trajectories of an ensemble of wire elements are followed,

$$\begin{aligned} \mu_i \ddot{x}_{is} = & \left( \frac{\mu_0 \mathcal{I}^2(t)}{2\pi} \right) \left( \sum_{p,j \neq i} \frac{\alpha_i \alpha_j}{\mathcal{R}_{ij}^{sp}} \dot{x}_{ij}^{sp} + \sum_{p \neq s} \frac{\alpha_i^2}{\mathcal{R}_{ii}^{sp}} \dot{x}_{ii}^{sp} \right) \\ & - \left( \sum_{p,j \neq i} \tau \left( \frac{\mathcal{R}_{ij}}{a_w} \right) (\dot{x}_{ij}^{sp}) + \sum_{p \neq s} \tau \left( \frac{\mathcal{R}_{sp}}{a_w} \right) (\dot{x}_{ii}^{sp}) \right) \end{aligned}$$

determines the motion and the time advanced impedances  $L_{ij}$ . The energy absorbed and the work expended against the drag forces can be viewed as deposited in two reservoirs, the inductive energy  $\mathcal{E}_\Phi = 1/2 \mathcal{I}^2(t) \alpha_i L_{ij} \alpha_j$  and the dissipation function,

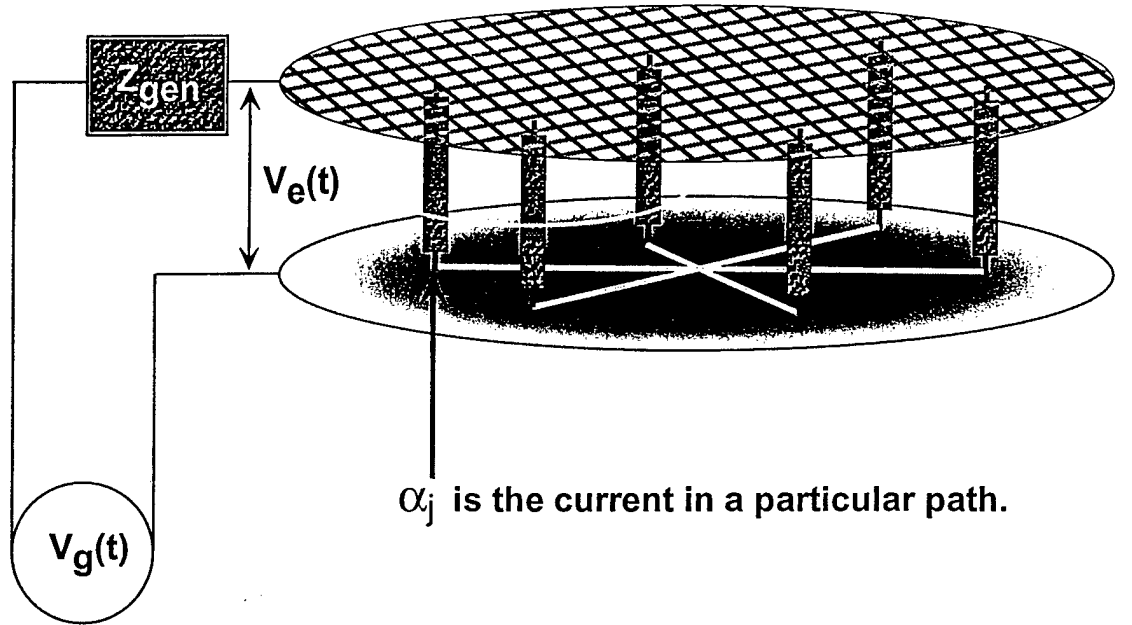
$$\mathcal{F}_{ij}(t - t_0) \equiv 1/2 \int_{t_0}^t \tau \left( \frac{\mathcal{R}_{ij}}{a_w} \right) (\dot{x}_{ij})^2 dt ,$$

with  $\mathcal{R}_{ij}$  a radial separation and  $a_w$  a wire size.

By construction then the sum of all  $\alpha_i$  is one. If we examine the voltage  $V_e(t)$  impressed at the entrance or feed of a wire array cage, then from the following figure, the resolution of the set  $\alpha_i$  and the total current  $\mathcal{I}$  admitted to the array are seen to be two distinct problems. From the view of the external generator  $V_g(t)$ , the array is a two terminal device and the energy into it must be the same for all sets  $\alpha_i$  that show the same net impedance.



WDM circuit elements can decompose into symmetry groups, with each element representing a resistance and inductance.



Maintaining equal voltage at each circuit element, the equations fixing the current fractions  $\alpha_i$  for any given  $V_e(t) = V_g(t) - Z_{gen}\mathcal{I}$  and  $\mathcal{I}$  can be written as,

$$V_e(t) = R_i(t)\alpha_i\mathcal{I} + \left( \frac{d}{dt} \mathbf{L}_{ij} \cdot \alpha_j \mathcal{I} \right),$$

and then integrated over the interval  $[\delta \equiv t_> - t_<]$  to eliminate the time derivative. Denote by  $\delta\Phi_e$  the change in flux over this interval, the matrix relation

$$\frac{\delta\Phi_e}{\mathcal{I}} \mathbf{u}_i = \delta R_j \mathbf{I}_{ij} \cdot \alpha_j + \mathbf{L}_{ij} \cdot \alpha_j$$

emerges, with  $\mathbf{I}_{ij}$  the diagonal identity matrix,  $\mathbf{u}_i$  a unit vector over the local group  $N$ . The common LHS to all these equations can be expressed as an

effective impedance at the entry point, viz.  $\delta Z_e \equiv \frac{\delta \Phi_e}{I}$  for any impressed voltage and current. One may also write  $L_e \equiv \delta Z_e$  to put the linear system in units of inductance. Normalized by the port inductance  $L_e$  the equations for the current fractions are simply,

$$L_e \mathbf{u}_i = (\delta R_j \mathbf{I}_{ij} + \mathbf{L}_{ij}) \cdot \alpha_j ,$$

and since the fractions must sum to one, the port inductance or impedance may be calculated independently of the particular value of voltage or current in the array of conduction paths. It is easy to show that in fact

$$L_e^{-1} \equiv \mathbf{u}_i \cdot (\delta R_j \mathbf{I}_{ij} + \mathbf{L}_{ij})^{-1} \cdot \mathbf{u}_j .$$

In the limit of vanishing inductance it is easy to see that the  $\alpha_i = Z_{||}/R_i(t)$  and that consequently they add up to unity.

In the general case the diagonal nature of the series resistances breaks the problem of energy transfer into a balance between the power building the electromagnetic energy density in the gap and the power brought forward of the generator impedance and series wire resistances. On the left hand side is the Poynting flow feeding the wire load, with power removed because the series resistors kill some magnetic flux,

$$\mathcal{I} \times (V_e(t) - \mathcal{I} \Sigma_i R_i(t) \alpha_i^2) = \frac{d}{dt} (\mathcal{E}_{field} + \mathcal{E}_{mech}) ,$$

which is balanced on the right by the total time derivative of field and mechanical energy. With the dissipation function defined above, we can integrate over the previously used time interval  $\delta$  to obtain the change in energy

$$\Delta \mathcal{E} \equiv (T_\delta - T) - \Sigma_{ij} \mathcal{F}_{ij}(\delta) + 1/2 (L_{a\delta} \mathcal{I}_\delta^2 - L_a \mathcal{I}^2) ,$$

with  $\delta$  indicating the forward time level for kinetic energy,  $T = 1/2 S \Sigma_i m_i v_i^2$ , and magnetic energy,  $1/2 L_a \mathcal{I}^2 = 1/2 \mathcal{I}^2 [\Sigma_{ij} \alpha_i \mathbf{L}_{ij} \alpha_j]$ . Of course here the  $\alpha_i$  are normalized to contain all the current in the  $i$ th wire of all the symmetry groups.

Time integrating the delivered power requires two special functions,  $C_1(\delta)$  and  $C_2(\delta)$ , easily developed from the "L/R" solution waveforms characterizing the feed. The result is dependent on the time interval only through the two coefficients and becomes

$$\mathcal{P}_\delta = C_1(\delta) V_g \mathcal{I} - C_2(\delta) \mathcal{I}^2 (Z_{gen} + \Sigma_i R_i \alpha_i^2) .$$

Combining this result with the expression for the change in field and mechanical energy leads to an algebraic constraint for the time advanced current  $\mathcal{I}_\delta$  as the solution of a quadratic equation, viz.

$$\mathcal{P}_\delta = (T_\delta - T) - \Sigma_{ij} \mathcal{F}_{ij}(\delta) + 1/2(L_{a\delta} \mathcal{I}_\delta^2 - L_a \mathcal{I}^2) .$$

The only required input is a voltage waveform  $V_g(t)$ . When carefully implemented this algorithm allows conservation of energy to essentially machine precision with very tight limits placed on the changes in wire velocity and position. The trade between energy convergence and runtime as such limits are relaxed is also very favorable. A relaxation scheme to converge the particle positions, velocities, and currents together is completely successful.

The accurate exchange of field and mechanical energy is a cornerstone of any further enhancements of the WDM that evolve it to a full fluid particle description. It has also made possible the accurate assessment of how important flux compression events are to the nested wire loads from the viewpoint of a filamentary current model.

## 1.2 Imperial College Experiments and the WDM

By way of review, the initial successes of nested arrays motivated an attempt at Imperial College to understand the transfer mechanisms for current and momentum from an experimental perspective.

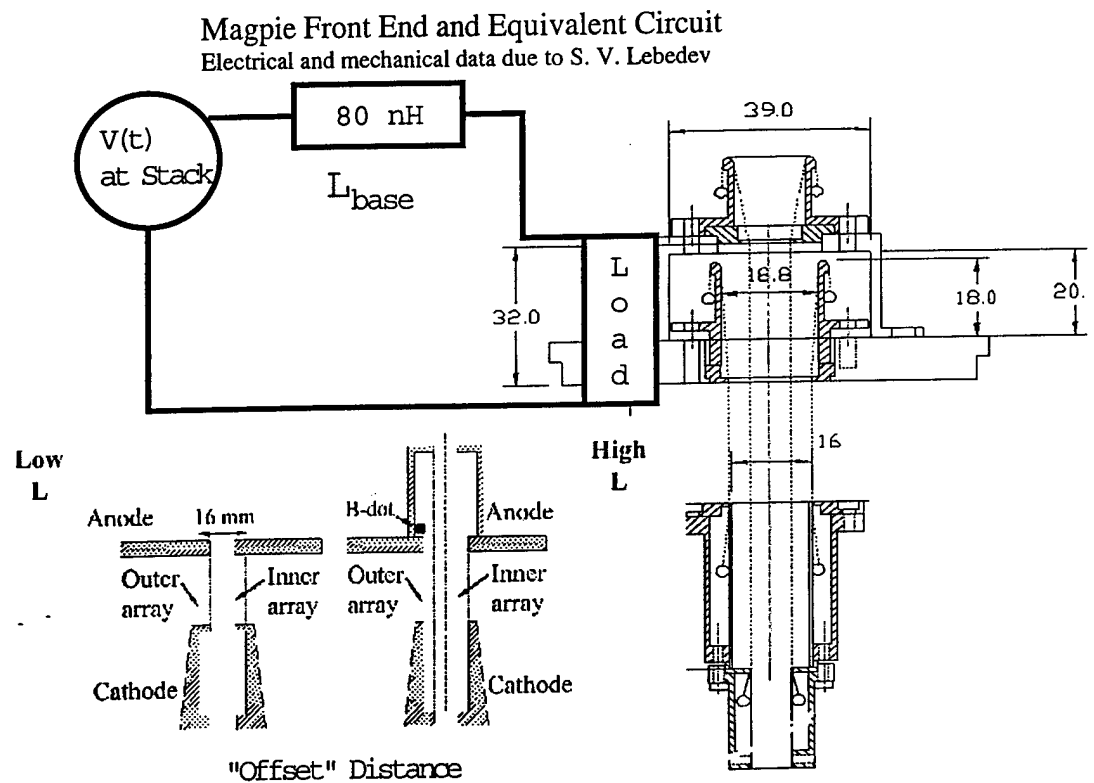
The nested array geometry was suggested as a means of obtaining a fast rising current on the interior (or target) array in J. Davis, *et. al.*, Appl. Phys. Lett. **70**(2), 13 Jan 97. The nested geometry was found to enhance x-ray power on the "Z" facility at 20 MA. The best yields and powers were seen with a target array lighter than the driver in C. Deeney, *et. al.*, PRL **81**(4883), 30 Nov 98. The Wire Dynamic Model showed that observed pinch dynamics on "Z" required mass interchange and current switching for correct modeling c.f. R. E. Terry, *et. al.*, PRL **83**(4305), 22 Nov 99.

Operating at a lower current (1 MA), detailed observations of nested array dynamics on MAGPIE show the mass interpenetration and show a shift in assembly time due to added inductance between the drive and target arrays. c.f. S. V. Lebedev, *et. al.*, PRL **84**(1708), 21 Feb 00. All lower current, lower number array implosions have been characterized by the formation of early plasma on axis. The implosion dynamics are strongly modified by this behavior — S. V. Lebedev, *et. al.*, PRL **81**(4152), 9 Nov 98, J. P. Chittenden,

*et. al.*, PRL 83(100), 5 July 99. Here we seek to examine these observations against the numerical model.

### 1.2.1 Comparing the Model Dynamics to Experiment

The experimental geometry is shown in this figure, with the offset inductance indicated.



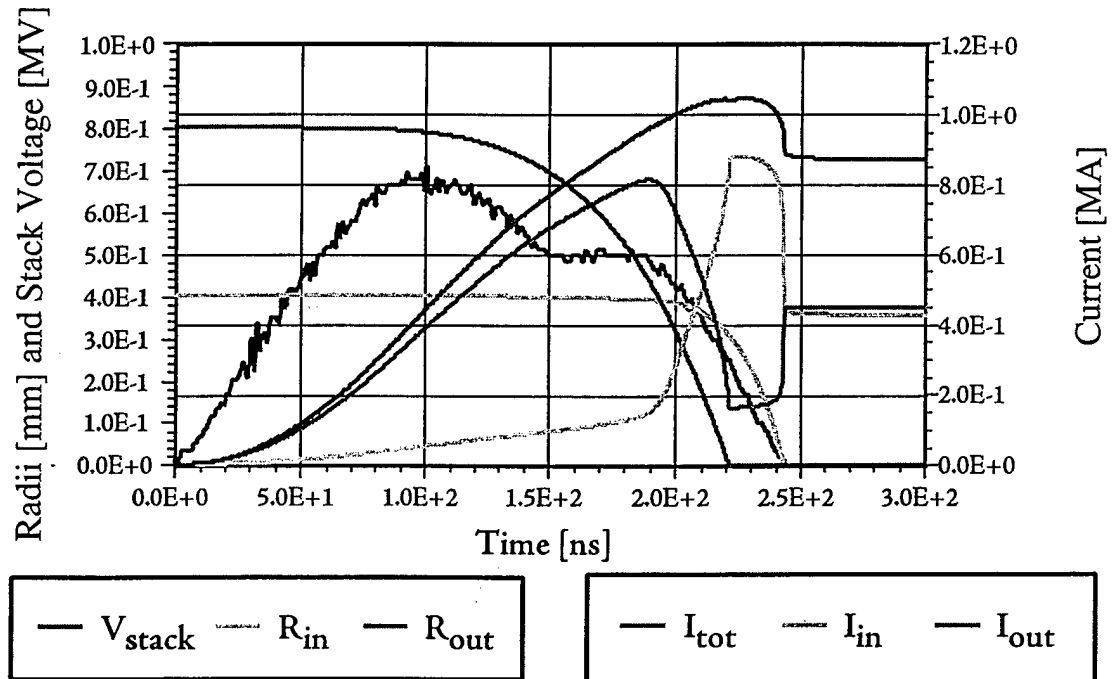
The relevant parameters for the simulation of implosion events in this device were taken as: i. array diameter of 8 mm Target and 16 mm Drive, ii. wire diameter of  $1.50 \cdot 10^{-3} \text{ cm}$ , iii. wire length of 23 mm + offset of  $0 \rightarrow 33 \text{ mm}$  in Target array, and iv. an array mass (D or T) of 0.1748 mg.

The WDM model was run against a series of test problems with varying offset length because the amount of conductor remaining in the circuit when the target wires break is unknown. The high and low inductance cases shown

below are on the extreme range of the study.

**Early Mass Shedding to a Precursor is Clearly Important** The WDM at fixed element mass fails to get the right strike time or trajectory shape before the current transfer. On the other hand, the mass shedding isn't important after the strike — we get a good trajectory calculation without it. The current transfer to the target array must therefore be much faster than the risetime in the main circuit.

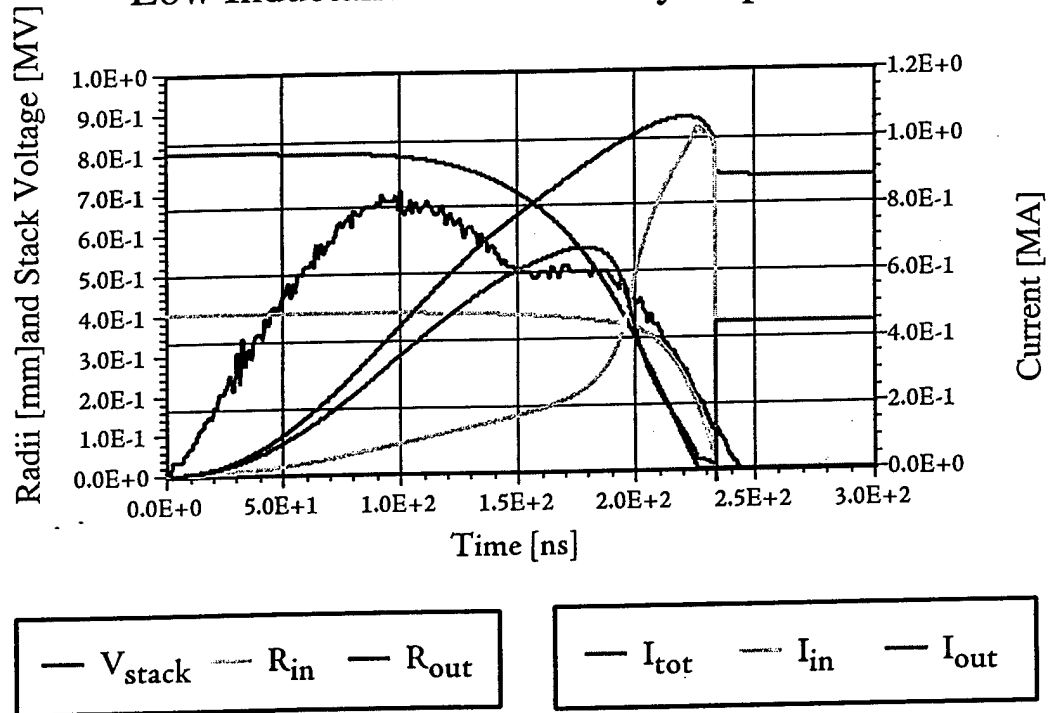
## High Inductance Nested Array Implosion



**Most of the Offset Inductance Remains in the Circuit** When the offset inductance is added, the best results are obtained when a full 33 mm of length is used. Moreover, this inductance appears to remain in the circuit after the strike — changes in this value for the offset length take the calculation away from the data.

Flux Compression is not important in MAGPIE True flux compression is signaled by a current partition fraction  $\alpha_j < 0$ . In modeling regular experimental cases for MAGPIE, such events are prolonged and noticeable only when an interior wire element rebounds from the origin — the “roach motel” effect. We can make the effect more pronounced during the rundown by examining azimuthally modulated cases which show strong filamentation modes, but it is still a fairly isolated behavior.

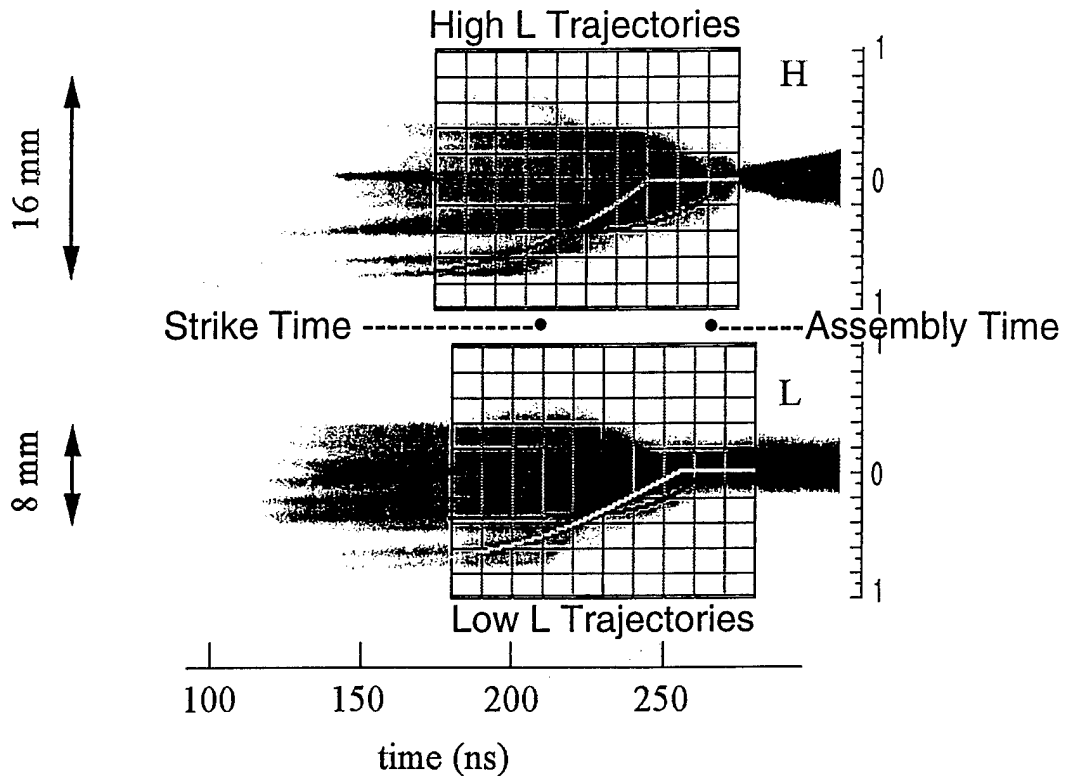
### Low Inductance Nested Array Implosion



Direct Momentum Transfer at Strike is Low In the experience to date, the use of “sticky” wires will cause strong divergence of our calculated trajectories from the observations. Apparently most of the drive array material moves through to the origin without pushing on the target array directly.

These observations are distilled into the best fit of model to experiment,

using only the value of expected offset inductance as the sweep parameter.



### 1.2.2 Conclusions

From the WDM analysis of this experiment several observations emerge.

**Mass Interchange and Current Switching** An understanding of these effects in nested array dynamics is critical to a correct account for array currents from 1 MA to over 20 MA.

**Flux Compression from a Rebounding Drive Array** The "roach motel" effect on rebounding drive plasma once it gets inside the target array may be an important design option to be examined by interior array wire number scans on bigger machines.

## 2 Precursor Plasmas in Steady State

It has been observed [Lebedev, et al] that heavier, sparse wire arrays do not simply implode under the influence of the injected current. The general behavior is the creation of corona plasma around a core of wire material, with the coronal plasma continually streaming into the center of the array, and impinging on the interior or target array. This core and corona morphology leads to two primary consequences.

First, the wire cores do not implode following the dynamics of isolated wire filaments. The mass shed to the corona plasma takes on the momentum transferred from the pulse power feed and leaves the core to be smoothly boiled away for a majority of the current pulse. Only after a significant fraction of the original mass is shed does the set of wire cores begin to implode.

Second, the coronal plasma forced to the interior generally forms a very regular, stagnant cylinder of progressively denser plasma that radiates away all the energy brought to it by the imploding jet. It is observed that the radius of the column depends strongly on the wire material used, but only weakly on time. No outwardly moving shock front is observed, but rather a progressively denser column.

### 2.1 The Central Column

The very regular behavior of the system naturally leads to the problem of a radiative calibration of the precursor plasma, viz. can the absolute radiative output be uniquely related to the flux contained in the input jet? Can the observed variation of stagnation radius with atomic number be explained?

As a starting point, we will consider first the construction of a simple steady state flow model which describes the transport of mass to the stagnant central column.

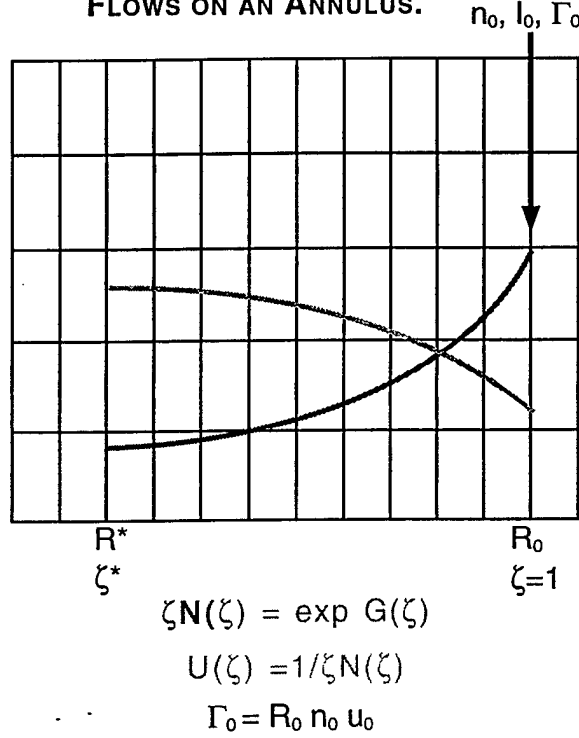
### 2.2 Geometry

As shown in the figure, the flow we seek to describe exists only on an annulus  $r_* \leq r \leq r_0$ . At the outer boundary there is a known flow speed  $u_0$ , density  $n_0$ , and entrained current  $I_0$  which is generally a small fraction of the current in the drive array that generates this inward streaming corona. The boundary mass flux  $\Gamma_0 \equiv r_0 u_0 n_0 = \Gamma(\zeta)$  is presumed fixed in time and space over the



annular domain, thus serving to define the interior flow profile  $U(\zeta)$  once the interior density profile  $N(\zeta)$  is known.

**FIG. 1 STEADY STATE ADIABATIC FLOWS ON AN ANNULUS.**



### 2.3 Model Statement

Mass continuity is satisfied by construction, viz.

$$\partial_t r_0^2 n(\zeta) = -\zeta^{-1} \partial_\zeta \Gamma(\zeta) = 0,$$

with  $\zeta = r/r_0$ . Momentum balance is to be established from density, current, and pressure profiles. The density form factor is just  $N(\zeta) = n(\zeta)/n_0$  such that  $N(1) = 1$ . The current is derived from a constant current density  $j_z = j_0 \cdot \mathcal{F} = (\sigma_0 E_{z0}) \cdot \mathcal{F}$ , with  $\mathcal{F}$  the ionization fraction and  $\sigma_0$  the dc conductivity based on electron neutral collisions at small  $\mathcal{F}$ . For low interior magnetic field and flow speeds, the transformation to the moving fluid frame

is a perturbation, as is the spatial dependence of  $E_{z0}$ . The pressure is derived from an adiabatic rule, viz.  $P(\zeta) = P_0 N^\gamma(\zeta)$ . These assumptions lead to a statement of momentum balance written as

$$-u \partial_\zeta u = \rho^{-1} \partial_\zeta P + \frac{B_\theta}{4\pi \rho \zeta} \partial_\zeta [\zeta B_\theta],$$

with  $B_\theta = 2I(\zeta)/cr_0\zeta$ ,  $I(\zeta) = I_0 \mathcal{F} \mathcal{I}(\zeta, \zeta_*)$ , and  $I_0 = \pi r_0^2 \sigma_0 E_0$ . Since the ambient electric field is assumed constant over the radial domain of interest, the current density thus will vary in accordance with the field in the radially moving frame that is seen outside of  $\zeta_*$ , viz.

$$\mathcal{J}(\zeta) \equiv \frac{j_z}{j_0 \mathcal{F}} = 1 - \frac{u_0 B_0}{c E_0} \frac{2\mathcal{F}}{\zeta^2 N(\zeta)} \int_{\zeta_*}^{\zeta} d\zeta_1 \zeta_1 \mathcal{J}(\zeta_1),$$

defines the current density form factor. Alternately, one may cast the equation into a form using the imbedded current form factor  $\mathcal{I}$ , that we defined above,

$$\mathcal{I}(\zeta, \zeta_*) = (\zeta^2 - \zeta_*^2) - 2\delta \mathcal{F} \int_{\zeta_*}^{\zeta} d\zeta_1 \frac{\mathcal{I}(\zeta_1)}{\zeta_1 N(\zeta_1)},$$

Using the current profile, let  $\zeta B_\theta = B_0 \mathcal{F} \mathcal{I}(\zeta, \zeta_*)$  with  $B_0 = 2I_0/cr_0$ , and set  $c_s^2 \equiv P_0/\rho_0$ . Next, writing  $v_{A0}^2 = B_0^2/4\pi\rho_0$ , and substituting  $u = u_0/\zeta N(\zeta)$  one finds that the pressure balance relation can be expressed in terms of only four distinct speeds, or equivalently three dimensionless ratios —  $\alpha \equiv c_s/u_0$ ,  $\delta \equiv \frac{u_0 B_0}{c E_0}$ , and  $\beta \equiv v_{A0}/u_0$ . In particular,

$$-\frac{u_0^2}{\zeta N(\zeta)} \partial_\zeta [\zeta N(\zeta)]^{-1} = \frac{c_s^2}{N(\zeta)} \partial_\zeta N^\gamma + v_{A0}^2 \mathcal{F}^2 \frac{\mathcal{I} \partial_\zeta \mathcal{I}}{\zeta^2 N(\zeta)},$$

and in order to cast the relation into a form defining  $\zeta N(\zeta)$  rather than  $N(\zeta)$  only, the following identity

$$\partial_\zeta \left( \zeta^{-\gamma} \exp(\gamma \mathcal{G}(\zeta)) \right) = \gamma \zeta^{-\gamma} \exp(\gamma \mathcal{G}(\zeta)) \left( \partial_\zeta \mathcal{G} - \frac{1}{\zeta} \right),$$

is useful. Expanding the velocity derivative and transforming to a new function  $\mathcal{G}(\zeta) = \ln[\zeta N(\zeta)]$ , yields a first order system of ordinary differential equations

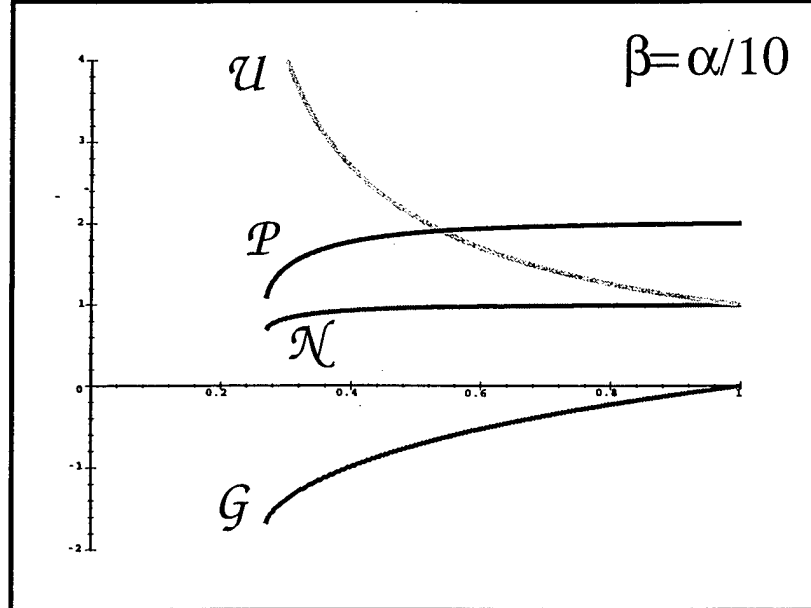
$$\partial_\zeta \mathcal{G} = \frac{-\alpha^2 \gamma \zeta e^{(\gamma+1)\mathcal{G}} + e^{\mathcal{G}} \zeta^\gamma \beta^2 \mathcal{F}^2 \mathcal{I} \partial_\zeta \mathcal{I}}{\zeta^{\gamma+1} - (\alpha \zeta)^2 \gamma e^{(\gamma+1)\mathcal{G}}},$$

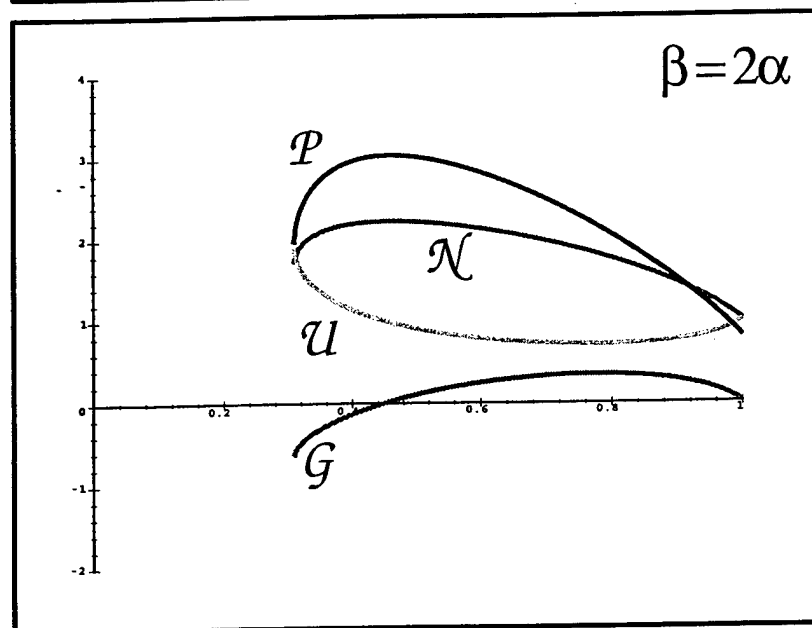
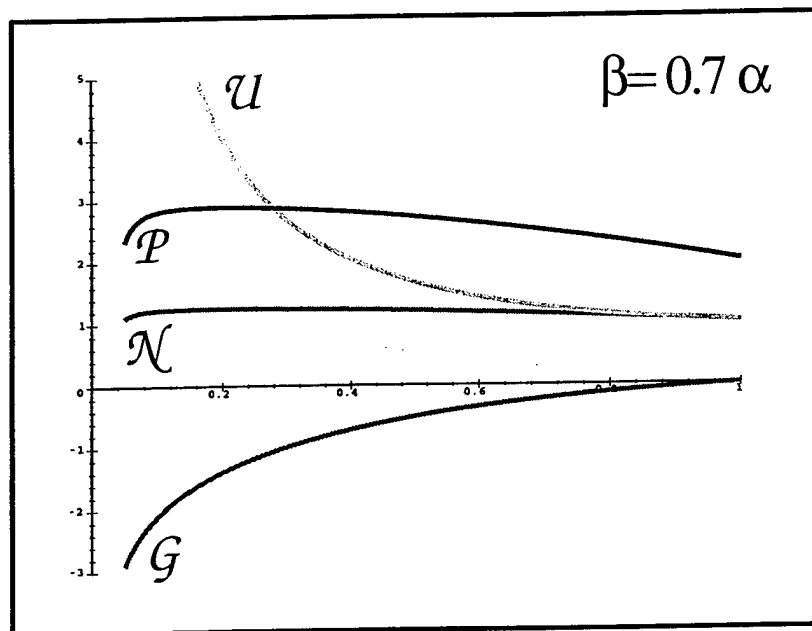
$$\partial_{\zeta} \mathcal{I} = 2 \left( \zeta - \mathcal{F} \delta \frac{\mathcal{I}}{\exp(\mathcal{G})} \right),$$

where we have collected all derivative terms to the left hand side. These equations are now to be solved subject to the boundary conditions  $\mathcal{G}(\zeta \rightarrow 1) = 0$  equivalent to  $N(\zeta \rightarrow 1) = 1$  since  $\exp[\mathcal{G}(\zeta)] = \zeta N(\zeta)$ , and  $\mathcal{I}(\zeta \rightarrow \zeta_*) = 0$ .

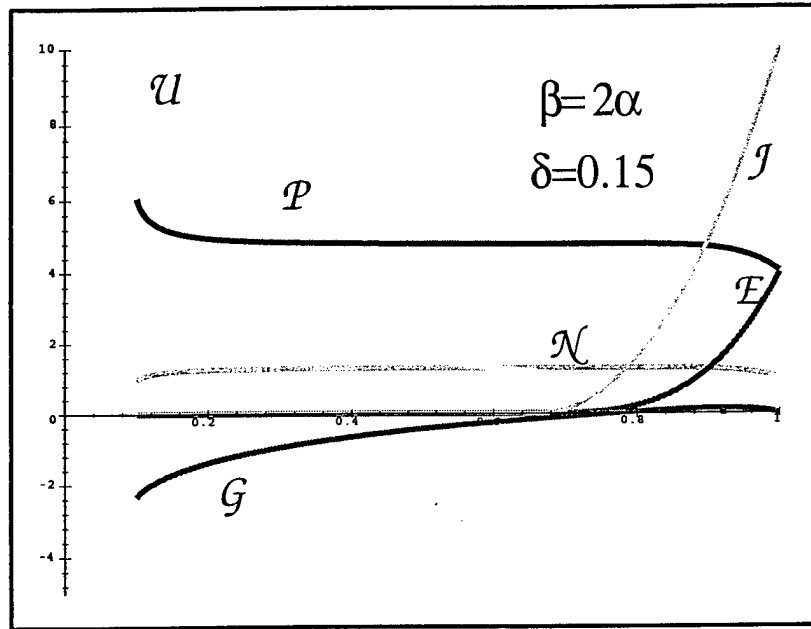
## 2.4 Model Solution

In the case that  $\delta \rightarrow 0$ , the current profile can be explicitly resolved and only a single ODE remains. Small  $\delta$  is an appropriate limit when  $\beta$  is also small, because the current plays a minor role in establishing the flow profile. In the three cases show below, the current is progressively increased and the pressure profile  $\mathcal{P}(\zeta)$  tends to peak toward the interior as a measure of the stress imposed by the magnetic field. The other profiles shown (density  $\mathcal{N}(\zeta)$ , flow  $\mathcal{U}(\zeta)$ , and  $\mathcal{G}(\zeta)$ ) are as defined above.





When the ordering  $\alpha > \beta > \delta$  is violated, the profiles are best calculated by the full pair of ODE's shown above. In a typical case, the usual condition of constant electric field in the lab is relaxed and a parabolic profile rises up from a selected scale radius of 0.6.



Here the current density  $J$  is extinguished at a scale radius of 0.6, while the imbedded electric field  $E$  rises to the value required to ensure that no reversal of current density is obtained in the solution. Once such a balance is struck the material coasts into the origin with a very flat density profile  $N$  and modest upturn of velocity  $U$  as it nears the stagnation zone.

Using a decaying electric field profile serves to contain the current to the exterior of the flow in keeping with observations that little or no kink mode instability is seen in the stagnation column.

## 2.5 Match Conditions at $\zeta_*$

Let  $\mathcal{G}_*$  be the value at the interior boundary. The required match to a stagnation flow region there is determined by the value and gradients of the fundamental solution curves.

$$\partial_\zeta \mathcal{G}_* = \frac{-\alpha^2 \gamma \zeta e^{(\gamma+1)\mathcal{G}_*}}{\zeta^{\gamma+1} - (\alpha\zeta)^2 \gamma e^{(\gamma+1)\mathcal{G}_*}},$$

$$\partial_\zeta \mathcal{I}_* = 2\zeta_*,$$

and the implied constructs from them:  $\mathcal{N}_* = \zeta_*^{-1} e^{\mathcal{G}_*}$ ,  $\mathcal{U}_* = e^{-\mathcal{G}_*}$ ,  $\mathcal{P}_* = 2\alpha^2 e^{\gamma\mathcal{G}_*} / \zeta_*^\gamma$ ,  $\mathcal{H}_* = e^{-2\mathcal{G}_*} + 2\alpha^2 e^{(\gamma-1)\mathcal{G}_*} / \zeta_*^{\gamma-1}$ , constituting the dimensionless form factors for density, velocity, pressure, and specific enthalpy as evaluated at the stagnation boundary.

At the stagnation boundary several conditions must coexist. First, the flow must change over from a steady flow in time and space to a homogeneous compression flow which collects material at the rate determined by the steady state number balance condition. Second, the mass accretion from the thin precursor to the much denser central column must conserve radially directed momentum density as that inelastic collision proceeds. Finally a power balance must be struck between the radiative losses and the stagnation enthalpy flux from the incoming steady state flow. Neither the first nor second condition constrains the location of the stagnation radius, but it is easy to see that the third determines it, and hence the implied column size, uniquely.

Turning now to the first two conditions, when the interior column density profile is essentially uniform the velocity profile will be linear in radius and characterized by a rate parameter that itself may be a function of time, viz.  $\mathcal{U}_c = -\dot{a}\zeta/2$ . Now the density will build according to the simple rule,  $\partial_t \mathcal{N}_c = (u_0 \dot{a} / r_0) \mathcal{N}_c$ . As fresh material is added in an inelastic collision process, the radial momentum density will be conserved (provided the collision is confined to a small radial domain and no external forces act). Equating the interior momentum density to the column momentum density, one has  $(\mathcal{N}_* + \mathcal{N}_c) \mathcal{U}_c = \mathcal{N}_* \mathcal{U}_*$ , which leads to a snowplow constraint on the recoil speed parameter,

$$\dot{a} = \mathcal{U}_* \frac{2}{\zeta_*} \frac{\mathcal{N}_*}{\mathcal{N}_* + \mathcal{N}_c},$$

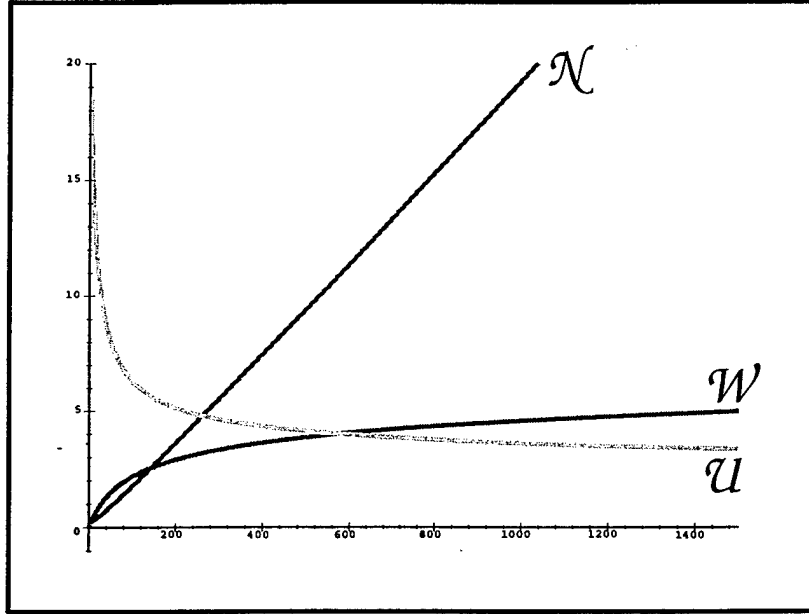
with the density evolving according to

$$\partial_t \mathcal{N}_c = \mathcal{U}_* \frac{2u_0}{\zeta_* r_0} \frac{\mathcal{N}_* \mathcal{N}_c}{\mathcal{N}_* + \mathcal{N}_c}$$

With the substitution  $\mathcal{W} = \ln(\mathcal{N}_c/\mathcal{N}_*)$ , the density is to be calculated as a solution to

$$\partial_t \mathcal{W} = \mathcal{U}_* \frac{2u_0}{\zeta_* r_0} \frac{1}{1 + e^{\mathcal{W}}}$$

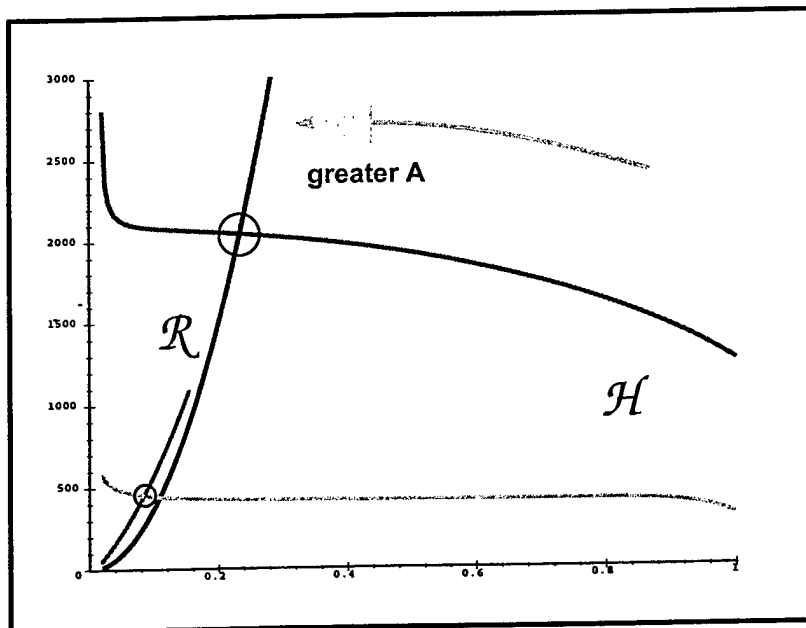
with the boundary condition  $\mathcal{W}(0) = 0$ . A typical solution is shown in the figure, with exponential growth giving rise to a quasi-linear phase after a few transit times  $r_0/u_0$ .



Within the column the radiation losses will scale as a quadratic to linear function of  $\zeta_* \mathcal{N}_c$  depending on the opacity, and the spectrally averaged emissivity will depend most sensitively on the column temperature and the atomic species. Hence if we write the radiated power per unit length in terms of the form factors above,  $\mathcal{P}_r = \epsilon(T_c, A)(\zeta_* e^{\mathcal{W}})^2$ . The function  $\epsilon(T_c, A)$  is also going to show a dependence upon the detailed column density profile and on the rate at which jet energy is thermalized (in the early part of the accretion), but such effects are less important than the scaling with atomic species.

Since the column will fill uniformly with time as the precursor pours into the center the radiative power might be expected to saturate in time after the material becomes more optically thick. In addition at later times that optical thickness will make the column more of a surface radiator and the density dependence will cease. However these limits are not expected in the case of the observations due to Lebedev, because the filling rate is small ( $r_0/u_0$  may be on the order of  $\mu s$ ) and the observed radiation is not that of a blackbody.

In any case two observations are now crucial to a description of the stagnant precursor column. First, every relation thus far derived places *no constraint whatever* on the parameter  $\zeta_*$ . The exterior steady state flows can show a wide range of interior end points as  $\alpha$ ,  $\beta$ , and  $\delta$  are varied. The collection of material to satisfy number balance can find a solution for any value of stagnation radius. Second, nothing in the steady state solution is strongly dependent upon the atomic species involved. Noticeable sensitivity to atomic species enters *only* through the radiation loss,  $\epsilon(T_c, A)$ .



If on the other hand one requires a power balance to be struck between the radiation loss and the incoming enthalpy flux, then the following relation emerges



$$\mathcal{R}\epsilon(T_c, A)(\zeta_* e^{\mathcal{W}})^2 = e^{-2\mathcal{G}_*} + 2\alpha^2 e^{(\gamma-1)\mathcal{G}_*} / \zeta_*^{\gamma-1},$$

which most assuredly does constrain  $\zeta_*$ . The scaling factor  $\mathcal{R}$  is just the ratio of the radiation power at  $\mathcal{N}_*$  and  $T_c$  to the input enthalpy flux  $r_0 u_0 h_0 = r_0 m_0 n_0 u_0^3 / 2$  before any radial acceleration of the fluid occurs. Generally  $\mathcal{R}$  is a large number and so the solution to this relationship for  $\zeta_*$  generally tends to occur at a small radius. Moreover, as indicated in the figure above that represents a typical case, larger atomic number forces a solution at lower radius.

In the cases shown above the upper pair is from a set of profiles with a constant electric field profile and no  $\delta$ . The lower is from the more realistic choice of parabolic electric field and modest  $\delta$ .

### 3 Precursor Investigations with Mach2

The active version used here was Mach 2.5b with some detailed enhancements due to M. Friese and M. Douglas. The Lee-More-Desjarlais resistivity model for Al was incorporated with a set of SESAME tables build from data due to M. Desjarlais.

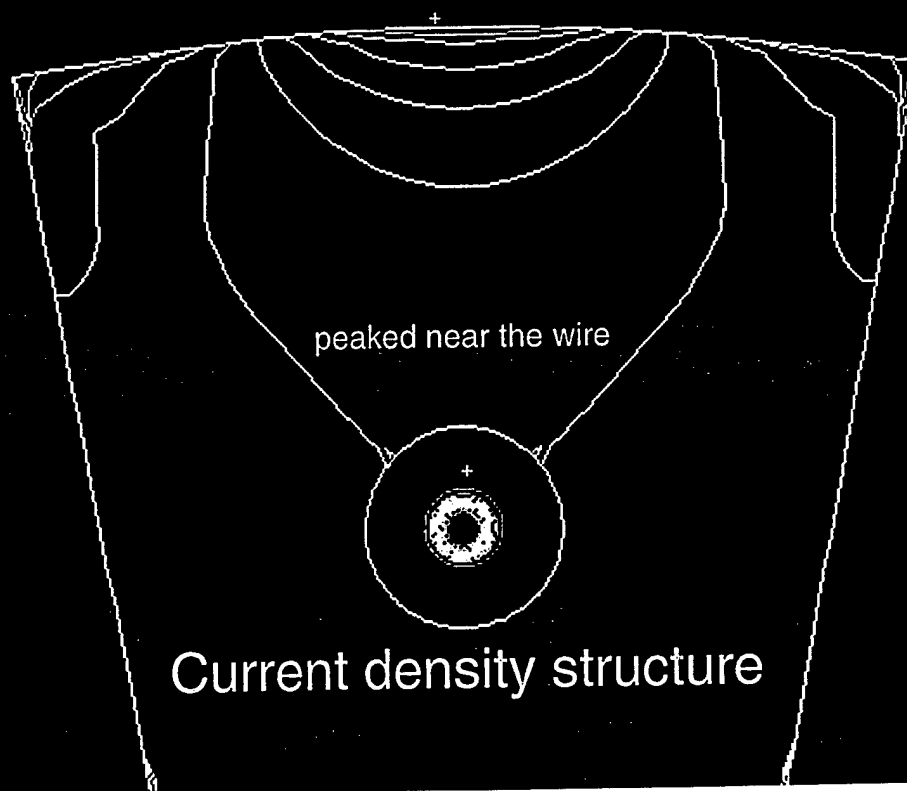
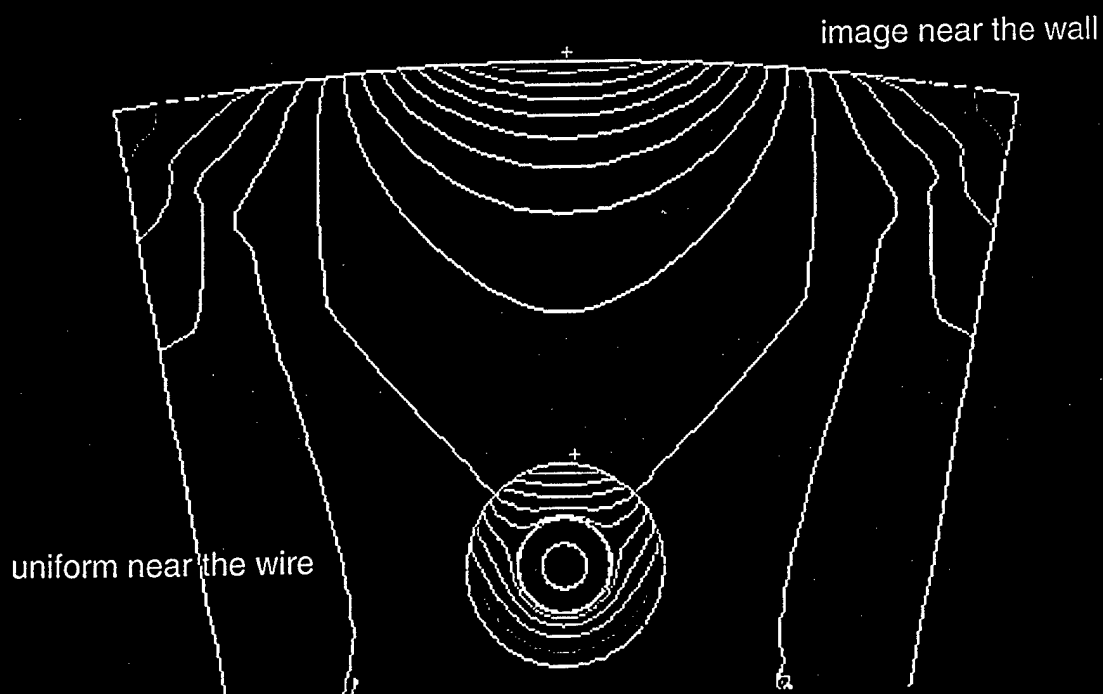
#### 3.1 Problem Statement

Here a single Al wire (at 2.0 cm radius) is presented with a scaled Saturn “log pulse” current waveform and must interact with a return current conductor at a fixed outer radius (2.5 cm). The lower radius of the problem (1 cm) is also set with a floating conductor boundary. Symmetric lateral boundary conditions are imposed appropriate to a wire count of 24 or so. The initial wire is set to 100  $\mu\text{m}$  radius to allow for plenty of material blowoff into a corona.

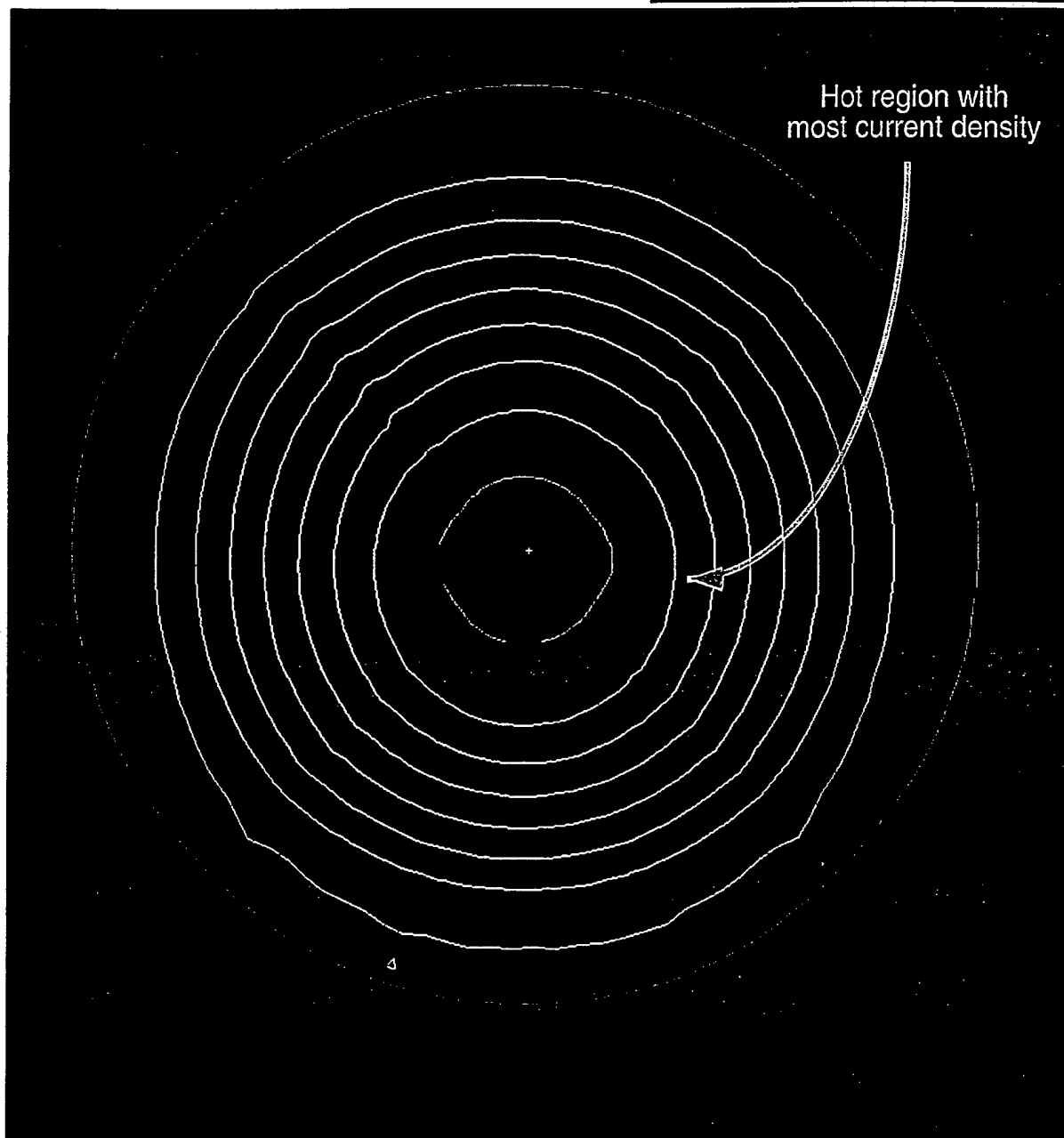
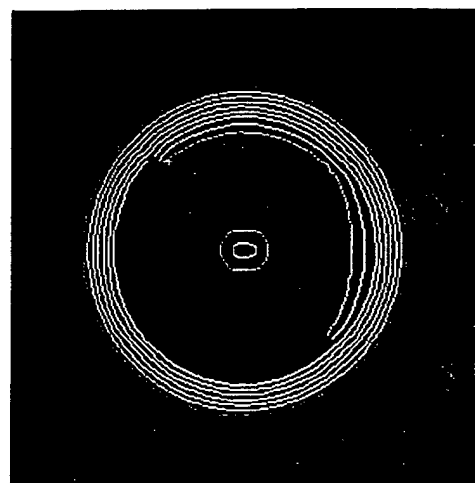
#### 3.2 Results

In keeping with observations from other workers, the wire tends to hold current very close and not achieve a sufficiently hot corona to set up an inward stream of material to feed a precursor. The magnetic pressure map shows that a corona would indeed drift to the center if it could form.

## Electric field structure



From a cold start the Al wire expands with the current density in the hot, dense region at about 3.4 eV. The exterior is about 0.7 eV.



## Magnetic pressure structure

gradient pushes on the wire

well would receive wire corona

## 4 Advances in Fluid Particle Methods

The general success of the wire dynamic model (WDM) leads naturally toward a whole class of methods based upon discrete conduction paths and fluid elements that can more easily accommodate the phenomena of mass interpenetration, current exchange, and multiple materials for radiation sources. It is clear that azimuthal structures play an important role in existing load designs and may in fact be important factors in new load designs that seek even better yields and more controlled performance from the plasma radiation sources.

The work described here is a first step in building the WDM into a fully configured radiative-hydrodynamic description for future load analysis and design. We describe the baseline elements for the method and the successful application of the new tools to the old and familiar problems with the result of some improved understanding.

### 4.1 Review of Fluid Particle Methods

A fluid particle method may be defined as any numerical technique that replaces the conventional cell and boundary description of a hydrodynamic problem with some mobile, countable set of solution elements that contain information pertinent to the collection and not just the mechanical characteristics of an elementary fluid constituent. Methods based on cellular automata are then close cousins, being distinguished from fluid particles by the immobile character of the automata. So also are finite element methods on a Lagrangian mesh, distinguished by the inability to mix and a requirement to specify the connectivity of the set. Fluid particles retain the grid independent motion familiar to plasma PIC methods, but add in the physical properties of the fluid they are to represent.

In recent times fluid particle methods have been attempted by a number of workers. Among the most notable variations on this theme we find.

#### *Finite Size Grid and Particle Hydrodynamics*

The original formulation due to Bateson and Hewett [JCP 144, 358-378(1998)] uses freely drifting particles only and focuses on particle annihilation and creation rules to track emerging features.

#### *Smooth Particle Hydrodynamics*

Developed originally by Monaghan, it is most common in astrophysics and has been successfully specialized by Lombardi, *et.al.* [JCP 152, 687-

735(1999)] to self gravity problems. The method uses PIC-like particles, but allows ambient forces to accelerate them.

#### *Distribution Function Methods*

Generally not particle methods in the strictest sense, they show a mix of Eulerian and Lagrangian technique. These methods can combine a wide variety of ambient forces and plasma properties, e.g. Huba and Lyon [J. Plasma Physics 61, 391, 1999] or Sonendruker, *et.al.* [JCP 149 687-735(1999)]. The distribution function is used primarily to support flux and source calculations for a FDTD advance of the MHD or Vlasov equations.

### 4.2 Drift Kinetic Grid and Particle Hydrodynamics

As a further development of such methods here we first generate a second order accurate solution of the Vlasov (or drift kinetic) operator over a sufficiently short time interval that the accelerations and mean drifts are known functions of space. The new solution is used as a particle basis, bringing several advantages to the method with respect to momentum transfer and flexibility in the handling of external or internal forces.

Moreover in contrast to Bateson and Hewett, the particle management scheme is based upon a systematic energy and entropy conserving decomposition of observables. Using exact projection factors the exchange of information from the particle set to any desired grid can be done to machine precision. Such a scheme hence preserves any desired set of observed initial distribution function moments to forward projected moments of the fluid particles that contain all the information needed to specify the source or sink terms and fluxes for new fluid and electromagnetic field quantities.

In contrast to earlier work we use fluid particles that are a bit more complex and represent subsets of the fluid that may be given any required properties as needed, viz. temperature, entropy, internal energy, chemical potential, electrical conductivity or even electrical charge.

### 4.3 Core Drift Kinetic Solution for GaPH

The primary strategy in the solution method is an operator splitting, wherein the particles track the free streaming processes and a periodic collection and redecomposition refines the source and sink terms for the external fields and collisional processes. Since a physical system always has both sets of processes going on at once the operator splitting must find a workable compro-

mise in space-time steps that retains an image of the system that is "good enough" by some set of measures.

The GaPH distribution function at any time level is advanced from a drifted, accelerated Maxwellian in a cartesian box  $h$  of one to three dimensions. The minimal box dimensions are determined from the fundamental scale lengths for the kind of fluid picture that is appropriate at any location in the problem domain, viz. mean free paths, Debye lengths, test particle deflection distances, and the like. The upper limit of a box size is just determined by the desired resolution or the available experimental resolution for a problem. The drift velocity  $C$  and acceleration  $A$  are then  $C_0^\infty \mathcal{R}^3$  functions of local position  $x$  within the box,

$$C = V + x \cdot \delta/h, a = A + x \cdot \alpha/h.$$

Each box of the problem is observed or expected to contain a fixed initial number of particles in a known mix of species. It is noteworthy that considerable freedom exists in breaking up a box of observables into the fluid particles we will use, because of the presumption that the box represents the functional limit of resolution at any local region of a problem.

The new building blocks are by construction exact solutions of the drift-kinetic equation for the acceleration fields specified, viz.

$$(\partial_t + v \cdot \partial_x + a \cdot \partial_v)f \equiv \mathcal{L}_0 f = 0.$$

First we can treat the case of one dimensional particles, since multidimensional ones are just formed as outer products. To extract the implied observables we need the following types of integrals over the drift kinetic solution in the velocity subspace.

$$\begin{aligned} \mathcal{O}_L(X, t) = & \left(\frac{N}{2h}\right) \frac{1}{U\sqrt{2\pi}} \int_{-h}^h \left(\frac{dx}{t}\right) \left(\frac{X-x}{t}\right)^L \\ & \times \exp\left(-\frac{1}{2} \left(\frac{((X - (A + \alpha x/h)t^2/2 - x)/t) - (V + \delta x/h)}{U}\right)^2\right) \end{aligned}$$

Integrating back in  $x$  is moving back in time along the characteristic, the original Gaussian velocity distribution spreads in  $x$  and  $v$  to give hydrodynamic motions. With accelerations added, the integrals are similar to those

of Bateson and Hewett, but now the ambient forces can adjust the particle trajectories as they evolve.

The base particle solutions contain three common factors which represent the dilation of the box (due to the shear in the velocity and acceleration), and the (asymmetric) movement of the box boundaries:

$$D(t) = \left(1 + \frac{t\delta}{h} + \frac{1}{2} \frac{t^2\alpha}{h}\right),$$

$$h_+(t) = h + (V + \delta)t + \frac{1}{2}(A + \alpha)t^2,$$

$$h_-(t) = -h + (V - \delta)t + \frac{1}{2}(A - \alpha)t^2.$$

The expected profile for number density (per unit length, area, or volume)  $n(X, t) \equiv \langle N \rangle / \ell$  is then:

$$n(X, t) = \frac{N}{2hD(t)} \left( \operatorname{erf} \left( \frac{(h_+(t) - X)}{\sqrt{2}Ut} \right) + \operatorname{erf} \left( \frac{(X - h_-(t))}{\sqrt{2}Ut} \right) \right),$$

while the momentum density profile  $P(X, t) \equiv \langle \rho v \rangle / \ell$  is seen to be:

$$P(X, t) = \frac{mN}{2hD^2(t)} \left( \operatorname{erf} \left( \frac{(h_+(t) - X)}{\sqrt{2}Ut} \right) + \operatorname{erf} \left( \frac{(X - h_-(t))}{\sqrt{2}Ut} \right) \right) \left( V + \frac{\delta X}{h} + \frac{1}{2}t \left( A + \frac{\alpha X}{h} \right) \right) + \frac{mNU}{\sqrt{2\pi}2hD^2(t)} \left( e^{(-1/2) \frac{(h_+(t) - X)^2}{U^2 t^2}} - e^{(-1/2) \frac{(X - h_-(t))^2}{U^2 t^2}} \right).$$

The enthalpy or total kinetic energy content profile  $H(X, t) \equiv \langle \rho v^2 \rangle / 2$  is given by:

$$H(X, t) = \frac{mN}{2hD(t)} \times \left( \operatorname{erf} \left( \frac{(h_+(t) - X)}{\sqrt{2}Ut} \right) + \operatorname{erf} \left( \frac{(X - h_-(t))}{\sqrt{2}Ut} \right) \right) \left( U^2 + \frac{\left( V + \frac{\delta X}{h} + \frac{1}{2}t \left( A + \frac{\alpha X}{h} \right) \right)^2}{D(t)^2} \right)$$



$$\begin{aligned}
& + \frac{mN}{\sqrt{2\pi}2hD^3(t)} U \left( V + \frac{1}{2} At + X \left( \frac{1}{t} + 2 \frac{\delta + \frac{1}{2} \alpha t}{h} \right) \right) (e^{(-1/2 \frac{(h_+(t)-X)^2}{U^2 t^2})} - e^{(-1/2 \frac{(X-h_-(t))^2}{U^2 t^2})}) \\
& - \frac{mN}{\sqrt{2\pi}2hD^3(t)} U (\delta + \frac{h}{t} + \frac{1}{2} \alpha t) (e^{(-1/2 \frac{(h_+(t)-X)^2}{U^2 t^2})} + e^{(-1/2 \frac{(X-h_-(t))^2}{U^2 t^2})}) ,
\end{aligned}$$

including both thermal and drift energies and the changes in these energies provided by the external forces. There are similar expressions for all velocity moments of the core distribution function solution, such as the heat flux vector or the pressure tensor.

Because the drift kinetic solution component is known exactly a complete specification of the influence that each fluid particle brings to any other region can be tabulated by projecting any observable moment over any remote domain of interest. The projection factors,

$$\begin{aligned}
\mathcal{P}_L(X_<, X_>, t) &= \left(\frac{N}{2h}\right) \frac{1}{U\sqrt{2\pi}} \int_{X_<}^{X_>} dX \int_{-h}^h \left(\frac{dx}{t}\right) \left(\frac{X-x}{t}\right)^L \\
&\times \exp\left(-\frac{1}{2} \left(\frac{((X - (A + \alpha x/h)t^2/2 - x)/t) - (V + \delta x/h))}{U}\right)^2\right)
\end{aligned}$$

are then the means for collecting information out of the particles to a fresh set of boxes so that the resolution of collisional processes and source terms can proceed. In contrast to finite difference methods the domain of support can never exceed the domain of influence for any selected time step. Moreover, summations of positive definite elements can never produce a negative particle or energy density.

#### 4.4 Conserved Quantities from the Moments

It is obvious from the structures quoted above that the moments of the drift kinetic particles show conservation of number, momentum, and energy over all space as the particle spreads out. If we evaluate the various  $\mathcal{P}_L(X_<, X_>, t)$  over the whole domain, the original particle number is independent of space and time,

$$N = \left(\frac{N}{2h}\right) \int_{-\infty}^{+\infty} dX \frac{1}{U\sqrt{2\pi}} \int_{-h}^h \left(\frac{dx}{t}\right) \exp\left(-\frac{1}{2}\left(\frac{(((X - (A + \alpha x/h)t^2/2 - x)/t) - (V + \delta x/h))}{U}\right)^2\right).$$

The momentum  $(\rho V)(X, t)$  contains the original momentum plus that added by external forces,

$$N\left(\frac{1}{2}tA + V\right) = \left(\frac{N}{2h}\right) \int_{-\infty}^{+\infty} dX \times \frac{1}{U\sqrt{2\pi}} \int_{-h}^h \left(\frac{dx}{t}\right) \left(\frac{X - x}{t}\right) \exp\left(-\frac{1}{2}\left(\frac{(((X - (A + \alpha x/h)t^2/2 - x)/t) - (V + \delta x/h))}{U}\right)^2\right).$$

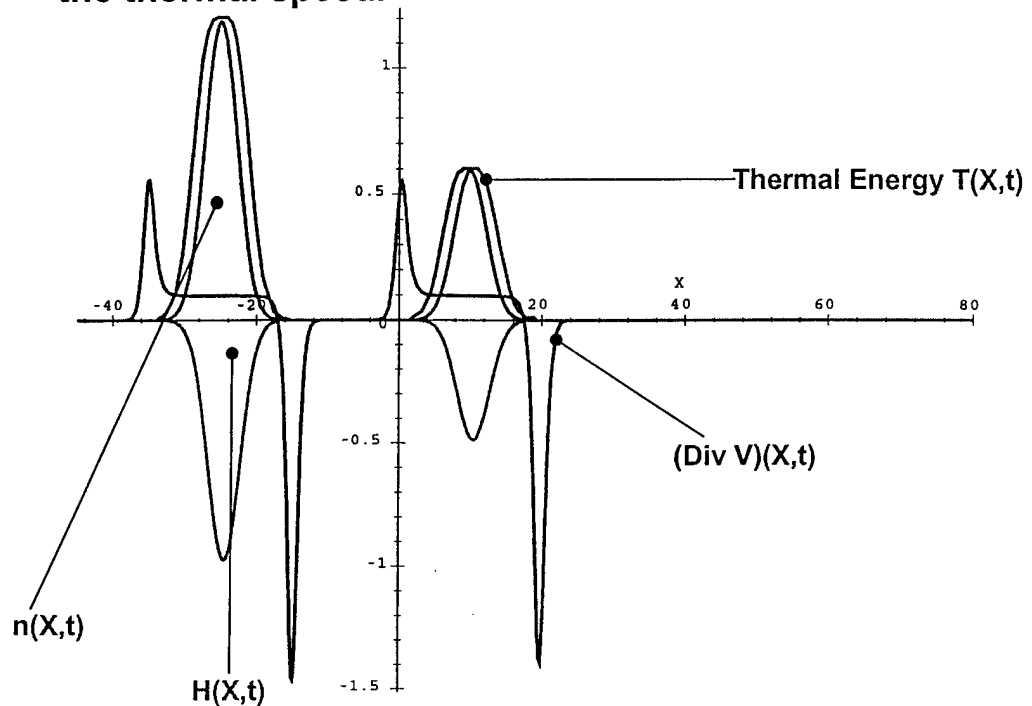
The enthalpy  $(\rho V^2/2 + \rho U^2/2)(X, t)$  contains the original energy plus that added by external forces and force gradients,

$$(mN/2)(U^2 + (\frac{1}{2}tA + V)^2 + \frac{1}{3}(\frac{1}{2}t\alpha + \delta)^2) = \left(\frac{mN}{4h}\right) \int_{-\infty}^{+\infty} dX \times \frac{1}{U\sqrt{2\pi}} \int_{-h}^h \left(\frac{dx}{t}\right) \left(\frac{X - x}{t}\right)^2 \exp\left(-\frac{1}{2}\left(\frac{(((X - (A + \alpha x/h)t^2/2 - x)/t) - (V + \delta x/h))}{U}\right)^2\right).$$

#### 4.5 Structure of a Drift Kinetic Fluid Particle

A first example shows two particles with an imbedded drift toward the right and a thermal speed about half this drift speed. Shown are the number density  $n(X, t)$ , and the enthalpy density  $H(X, t)$ . Also shown are fields derived from the momentum density  $P(X, t)$ . The implied velocity field,  $V \equiv P/mn$ , is used to obtain the equivalent thermal profile  $T(X, t) \equiv H(X, t) - 1/2(\rho V^2)$  and the divergence of velocity  $\nabla \cdot V(X, t)$ . The thermal profile has been scaled up to illustrate how it blooms out relative to the number density. Note that the divergence of velocity spikes negative on the leading side of the particle where density must increase as the drift brings material into a region. The divergence also spikes positive on the trailing edge of the particle as that region rarifies. The interior of the particle retains an essentially homogeneous deformation as it drifts. In this manner the continuity equation has been built into the particle action and, as shown above, explicitly conserves the total constituent number in the drift kinetic fluid particle (DKFP).

## Two Fluid Particles - the drift speed is about twice the thermal speed.

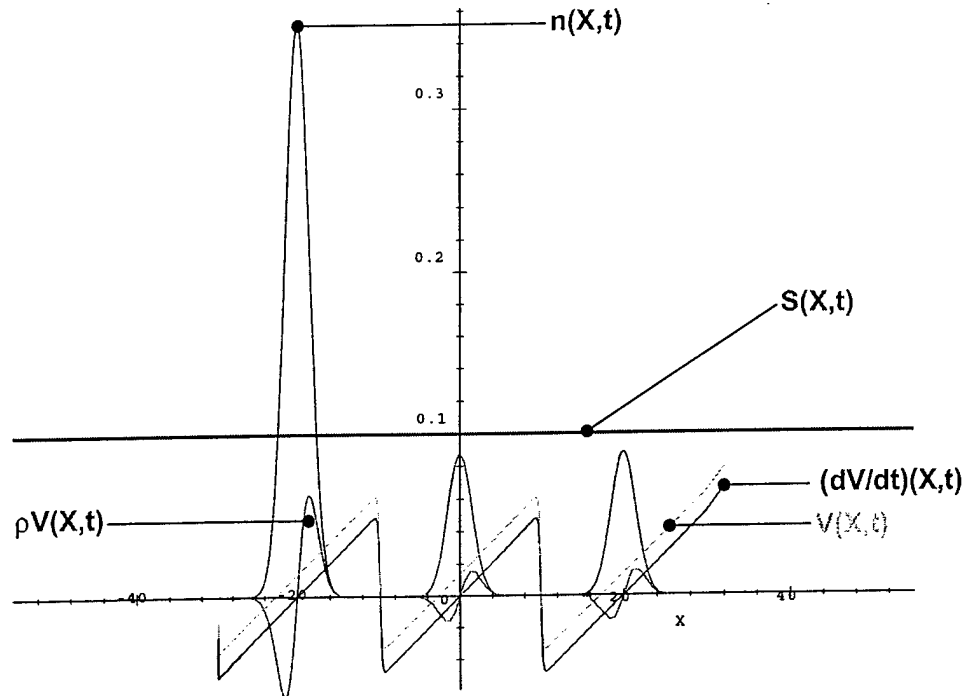


The "free" DKFP accelerates its drift speed according to the applied forces which generally will include ambient drag from its neighbor particles. These elements are free to pass smoothly through one another as would the molecules of a gas in the "molecular flow" regime. Note that the time origin and thermal speed are completely unconstrained at this level of the representation. Each element is a kind of partial pressure within the gas.

### 4.6 Dynamic Rules for the Momentum

Not only is number transport is essentially solved by construction, the momentum transport is as well, making it essentially redundant to ever compute a pressure gradient and use that to obtain forces among the DKFP. The reason is simply illustrated in the following figure, which portrays the velocity field and the acceleration field (in addition to the usual profiles) while three

Three Fluid Particles Collide - the acceleration and velocity fields are everywhere proportional, the similarity variable  $S(X,t)$  is everywhere constant.



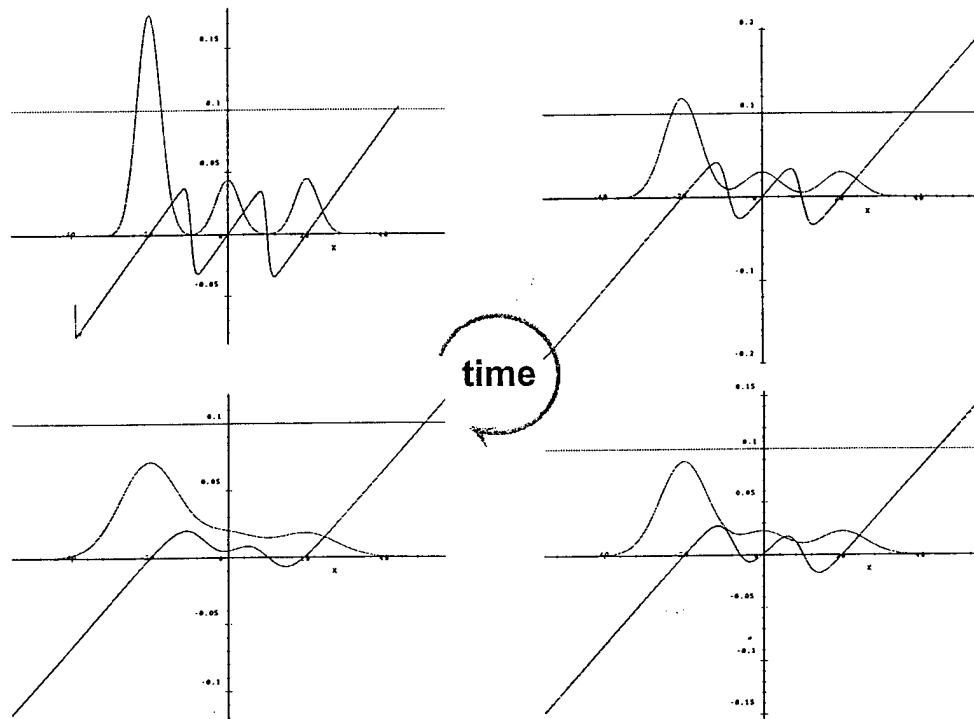
DKFP collide and blend into one another. Each is drifting with the same (null) velocity but subject to a boundary pressure gradient that drives them together over time. The similarity variable  $S(X,t)$  that plots as a straight line over all space and time is a measure of the strictly proportional nature of acceleration to velocity during the exchange of momentum among an arbitrary number " $N$ " of DKFP.

The fundamental theorem concerning the momentum transport as depicted above is therefore a sum, a decomposition of unity, viz.

$$-\frac{1}{N} \sum_{i=1}^N \left( \frac{tkT}{2D(t)} \left( \frac{\partial_X n(X,t)}{(nV(X,t) - n(X,t)(V + (\delta X/h) + (t/2)(A + \alpha X/h))/D(t))} \right) \right)_i = 1,$$

showing that each DKFP expands and blends with the *sum of all others* in a completely self-similar manner with the net drift motion subtracted out. So

**Three Fluid Particles Collide - over time a homogeneous deformation results while the similarity variable remains constant.**



even with regard to momentum transport the fundamental solution is built right in and requires no machinery to track boundaries or pressure gradients — the boundaries are reconstructed continually by the particle action.

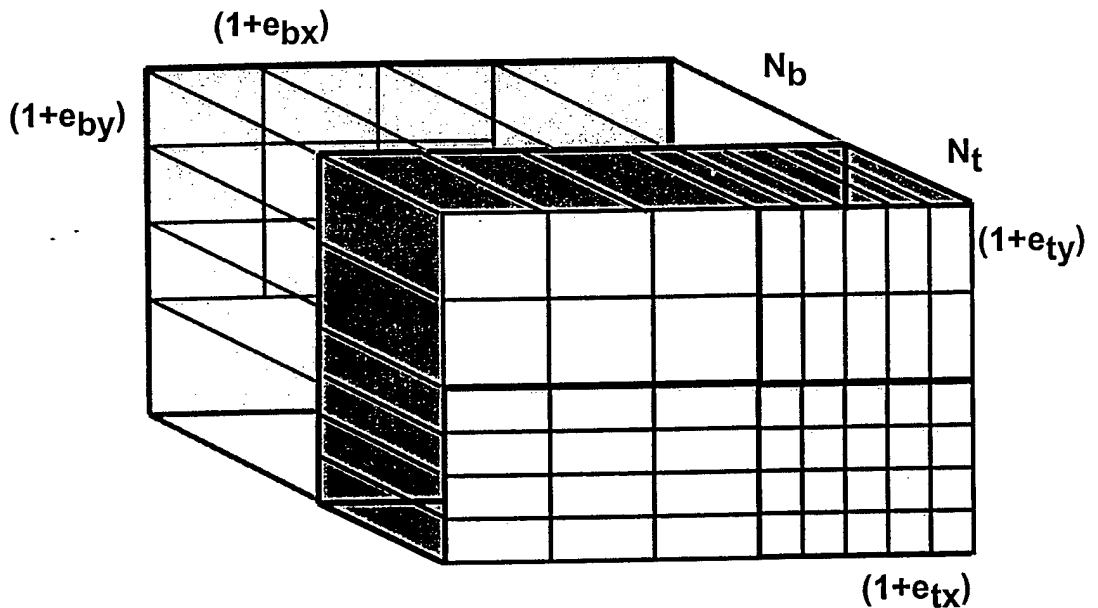
The subsequent figure follows the same process over time as the colliding particles advance toward a state of global homogeneous deformation. Note that the similarity variable remains strictly constant at one for each particle in the set on all space and time.

#### 4.7 Isentropic Rules for Decomposition

In order to represent a general fluid's behavior a systematic means of dividing an "observables box" into fluid particles is at least desirable and argueably required if one is to capture the thermodynamics of the system. Insofar as the decimation of an "h box" into particles is to be done at a moment in

time, as is their recapture to any fresh set of such boxes after a period of drift and interaction, the central thermodynamic variable of interest is the entropy of the system defined by the observable "h box". In the figure is shown a box containing  $N = N_b + N_t$  base particles and test particles. The test particles are more numerous but contain less material than the base particles. The spatial grid for the test particles is distorted differently than for the base particles. When the box is first divided into the two classes at *fixed* volume, each class is cooled to preserve the specific entropy which depends upon the product of number density and temperature to the 3/2 power. Each class can then be distorted into spatial packets of variable size (smaller packets are heated a bit, larger ones are cooled) in such a way that, if the particles were all recombined, the original entropy and internal energy are recovered over the whole box.

**Fluid Particles can decompose any observed set of density or velocity fields and preserve number, energy and entropy.**



The fundamental theorem concerning adiabatic particle decompositions

is similar to that for momentum in that it is posed as a decomposition of unity. Summing over the sets of base particles and test particles, the various distortion factors  $\epsilon_{bk}$  and  $\epsilon_{tk}$  are adjusted to preserve both the internal energy and entropy of the observable "h box". The adiabatic or isentropic nature of the transformation is built in by the power law variations but the net change in internal energy (for an ideal gas in this case) is a factor posed by the left hand side of

$$\sum_{i,j=1}^{L,K} \left( \frac{(N_b/N)^{5/3}}{((1 + \epsilon_{bi})(1 + \epsilon_{bj}))^{2/3}} \right) / LK + \sum_{i,j=1}^{I,J} \left( \frac{(N_t/N)^{5/3}}{((1 + \epsilon_{ti})(1 + \epsilon_{tj}))^{2/3}} \right) / IJ = 1 .$$

The decomposition required is achieved when a set of distortions is found such that the equality is satisfied. It is easy to see that if no test particles are selected, then the only solution is for vanishing  $\epsilon_{bk}$ . Yet when some test particles are used the  $\epsilon_{tk}$  must be chosen to boost their temperature back up a bit and balance the equation. The efficient multivariate solution for large numbers of base and test particles will clearly be a topic of future effort but problems of modest numbers are straightforward. Note that solutions here are *not* unique, but link the  $\epsilon_k$  in a regular way. Note also that the sum of the distortions must be zero since the size of the box remains invariant as the base or test particle parcels are compressed or stretched.

## V. HYDRODYNAMIC MODELING OF NESTED-PLASMA Z PINCHES

### I. Introduction

Issues related to the design and modeling of titanium, nested-plasma, Z-pinch loads are investigated in this report. Common to both sets of issues is the problem of determining initial conditions. They are established in experiments nonuniformly over the time it takes for nested loads to be broken down and totally ionized as the current rises, and, in computer calculations that are used to model these experiments, initial plasma conditions are arbitrarily chosen and taken to be uniform. A second issue of importance concerns the role of electron viscosity in diverting some of the ion thermal energy into K-shell x-rays in moderate atomic number Z-pinch. When electron viscosity is ignored in modeling calculations, all of the viscous energy goes into ion heating which, in turn, tends to divert more of the compression heating into the ions as well. However, the few measurements of line broadening that have been attempted to date often tend to imply substantially lower ion temperatures than are seen in calculations.

Viscous heating occurs when large gradients in fluid velocity, ion density, and electron temperature are generated as shock fronts form during the acceleration and deceleration phases of the pinch dynamics. The resolution of such structures in computer calculations generally requires many more computational zones than present-day computer resources can handle, even in one-dimensional (1-D) hydrodynamics calculations. For this reason, artificial viscosities are employed to model viscous heating since they allow smaller numbers of zones to be used that incompletely resolve the shock structures but still simulate viscous heating effects. However, even in small-zone-number calculations, large gradients can be generated that are only tens of electron mean free paths in length. In such gradients, other nonlinear contributions to the pressure tensor become important in addition to the classical pressure tensor contributions, which are proportional to velocity gradients. However, the impact of these additional terms on the pinch hydrodynamics are not evaluated in this work.

The pinch modeling that is reported on here utilized 1-D hydrodynamics calculations with a variety of initial conditions and zoning assumptions in order to determine some of the sensitivity of the hydrodynamic velocity, temperature, and density gradients to these assumptions. Since K-shell emissions depend on gradient structures, the dependence of these emissions on initial conditions is ultimately of interest. The modeling of plasma viscosity also presents a number of problems since (1) analytic shock front calculations must necessarily ignore the ionization dynamics and provide limited benchmarks against which to check a code calculation, (2) real viscosities are not used in computer codes for lack of zoning resolution, (3) electron viscosities only become important beyond certain levels of ionization in moderate to high atomic number plasma and then only under certain plasma conditions, and (4) accurate computer modeling of shock front generation in moderate atomic number plasmas requires good ionization dynamic and radiation transport models in addition to a large number of zones. Consequently, for the modeling described in this report, the standard form of artificial viscosity was used, but the heating it produced was divided between electrons and ions according to the ratio of their classical viscosities, a ratio that was recently computed analytically [K. G. Whitney, "Momentum and Heat Conduction in Highly Ionizable Plasmas", *Phys. of Plasmas*, **6**, 816 (1999)].



Two sets of calculations of titanium and krypton plasma implosions were carried out. In one set of calculations, the imploded loads were initially uniform fills of krypton and titanium plasmas at a temperature of 4 eV. These calculations were carried out using 60 zones, and the fills were driven by a linearly rising current pulse that was terminated when a prescribed energy input was achieved. The mass of the fill, its initial density, and the energy input were varied so that comparisons of the ion temperature profiles and K-shell yields and powers could be made with and without electron viscosity in the calculations. Fill masses between 10 and 1.25 mg/cm were used. A collisional-radiative equilibrium (CRE) ionization dynamics was employed; ultimately however, more accurate modeling of shock fronts will require time-dependent ionization since the passage of a shock causes rapid heating to occur that drives the ionization out of equilibrium. The results of the uniform-fill calculations are described in section II. Next, a nested titanium plasma geometry was set up in which an outer portion of the above described fill plasma was separated from the inner portion by moving the outer plasma out in radius, thereby creating a small mass of reduced density (by a factor of 10) between the inner and outer plasmas. This nested plasma load was again driven by a linearly rising current to pre-determined energy inputs. A mass of 1.25 mg/cm was used in a number of nested-plasma calculations, since it corresponds to an amount of plasma mass (and not necessarily wire mass) that can be imploded on the Z accelerator to velocities that are needed to effectively excite the K-shell of titanium. The results of these calculations, with and without electron viscosity, are described in section III. Finally, in section IV, the K-shell power and yield behavior of a series of calculations that correspond in essential ways to a series of titanium nested array shots that were conducted on the Z accelerator are discussed. These calculations use the same geometry as the section III nested plasma loads. The experiments were initiated using two sets of nested titanium wire arrays of varying total mass with a 2:1 mass ratio and a 2:1 radii ratio of outer to inner plasmas. These loads were accelerated to larger implosion velocities as the load mass was reduced. The nested plasma calculations described in section IV were carried out using the same masses and achieving approximately the same implosion velocities as in the Z experiments. Comparisons between these experiments and the corresponding calculations and some comments about future work are made in section V.

## II. Analytic Considerations

When B-field effects are ignored, the classical electron and ion pressure tensors,  $\Pi_e$  and  $\Pi_i$  respectively, are linearly proportional to the symmetrized and traceless version,  $(\nabla \mathbf{v}_f)_S$ , of the velocity gradient tensor:

$$\Pi_e = \eta_{e0}(\nabla \mathbf{v}_f)_S, \quad \Pi_i = \eta_{i0}(\nabla \mathbf{v}_f)_S.$$

Thus,  $\Pi_e/\Pi_i \equiv r = \eta_{e0}/\eta_{i0}$ , and, from the calculation of  $\eta_{e0}$  and  $\eta_{i0}$ ,

$$r \cong \frac{1.33Z(Z^2 + 2.820Z + 1.343)}{Z^3 + 4.434Z^2 + 5.534Z + 1.780} \left( \frac{m_e}{M_{ion}} \right)^{1/2} \left( \frac{T_e}{T_i} \right)^{5/2} Z^3.$$

This ratio is a function only of the degree of plasma ionization,  $Z$ , and the electron to ion temperature ratio. Also, since

$$\Pi_e + \Pi_i = \Pi_{artificial},$$

one can partition the artificial viscous heating between the electrons and ions using the above easily calculable ratio,  $\tau$ . This procedure represents the minimum step that can be taken in evaluating the role of electron viscosity in Z-pinch implosions.

The role expected can be discerned from an examination of the fluid equations for the electron and ion temperatures. These equations have similar forms when written in terms of the dimensionless viscosity coefficients,  $\hat{\eta}_{e0}$  and  $\hat{\eta}_{i0}$ , which are defined by

$$\eta_{e0} = \hat{\eta}_{e0} p_e \tau_e, \quad \eta_{i0} = \hat{\eta}_{i0} p_i \tau_i.$$

When written in terms of these coefficients, the temperature equations become

$$\left( \partial_t + v_r \partial_r \right) T_e + \frac{2}{3} \left( \frac{1}{r} \frac{\partial}{\partial r} (r v_r) - \hat{\eta}_{e0} \tau_e (\nabla \mathbf{v}_f)^2 \right) T_e = \text{e-i heating \& cooling terms,}$$

$$\left( \partial_t + v_r \partial_r \right) T_i + \frac{2}{3} \left( \frac{1}{r} \frac{\partial}{\partial r} (r v_r) - \hat{\eta}_{i0} \tau_i (\nabla \mathbf{v}_f)^2 \right) T_i = \text{e-i cooling,}$$

Both compressional and viscous heating enter these equations as variable exponential growth rates. Additional heating and cooling takes place locally due to electron-ion collisions and thermal conduction, while global cooling occurs because of radiation losses. These equations show that plasma compression acts to heat both electrons and ions at the same rate in the absence of viscous heating. However, when electron viscosity is ignored and all of the viscous heating is put into the ions, the exponential rate of ion heating exceeds the electron rate, which, in this case, is due to compression heating alone. Thus, the ions become significantly hotter than the electrons. This effect shows up in all computer code calculations that include ion viscosity only. The addition of electron viscosity should, therefore, reduce ion temperatures and raise electron temperatures slightly, which suggests the possibility of converting some of this energy into extra K-shell emission. However, this possibility will depend on the plasma conditions that are generated during the implosion, since the ratio,  $\tau$ , is substantially reduced when  $T_i$  is allowed to become much larger than  $T_e$ . Radiation cooling can become a drag on the electron temperature that acts on the ions only indirectly through electron-ion collisions. Thus, the ions can get hotter than the electrons when radiation losses are high and the electron-ion coupling is too weak. Under conditions of too low an ion density, the rerouting of ion thermal energy into K-shell emissions is inhibited.

### III. Uniform Fill Calculations

Since the ratio of electron to ion viscosity increases roughly as  $Z^{5/2}$  for K-shell emitters, two uniform-fill krypton calculations were carried out prior to uniform-fill titanium calculations to test for the influence of this Z-scaling. The mass of the krypton load was taken to be 10 mg/cm, its initial radius was 4 cm, and the energy input to the pinch corresponded approximately to an  $\eta^*$  of two. Results from these calculations are shown in Figs. (1)-(5). Because 60 zones were used in the calculations, the artificial viscosity was not enhanced. However, even with only 60 zones, very sharp gradients in temperature, density, fluid velocity, and fractional viscous heating were generated, as illustrated in Figs. (1) and (2) at two different times (60 and 80 ns) early in the implosion. Figs. (3)-(5) show comparisons between CRE calculations that were done with

and without electron viscosity. When included in the calculation, electron viscosity produced significant reductions in the ion temperature: illustrated in the ion temperature profiles of Figs. (3) and (4) at 80 and 113.5 ns respectively. In this particular calculation, reduced ion heating led to a 20% increase in K-shell energy output and produced close to 4 MJ. As Fig. (4) shows, all of the K-shell emission originated from the core of the compressed plasma. The outer portion of plasma, which contains a sizable amount of the plasma mass, emitted only in the L-shell. Prior to K-shell emission, the electron temperature profile (at 80 ns in Fig. (3)) shows only slight changes due to electron viscosity in contrast to the ion temperature profile since there are  $Z$  times as many electrons to be heated as ions.

When 10 mg/cm of a uniform-fill of titanium (at an initial radius of 2 cm) was substituted for the 10 mg/cm of uniform-fill krypton, similar, but smaller, reductions in ion temperature were seen. These reductions in the ion thermal energy again showed up as increases in K-shell emission. Figs. (6)-(11) illustrate this behavior. Figs.(6)-(8) contain histories of the K-shell power and energy outputs in three calculations carried out with and without electron viscosity. Figs. (9)-(11) contain profiles of the ion temperature at times just before peak compression (with and without electron viscosity) and of the average degree of ionization. The energy input to the plasma was systematically increased in these calculations. In Figs. (6) and (9), the energy input corresponded to  $\eta^* \cong 1.8$ , in Figs. (7) and (10), this input was doubled to  $\eta^* \cong 3.6$ , and, in Figs.(8) and (11), it was doubled again to  $\eta^* \cong 7.2$ . These doublings were accomplished by reducing the risetime of the current.

The results in Figs. (1)-(11) were not obtained through a systematic and thorough study of how electron viscosity affects moderate atomic number pinch implosions; hence, they only represent a first look at how the electron viscosity can influence K-shell emission and about how this influence depends on plasma conditions and on the atomic number of the plasma. Figs. (6)-(8) demonstrate that the percentage increase in K-shell output due to reductions in ion temperature will vary with plasma conditions and that, for the fill plasma chosen, it exhibits a maximum as a function of the input energy. Figs. (5)-(8) demonstrate that this percentage can go up as a function of atomic number as the  $Z$ -scaling of the ratio of viscosity coefficients suggests. Note also that, as the energy input in these titanium calculations was doubled, the core ion temperatures more than doubled, the core ionization levels approached K-shell burn-through, and, as a consequence, the K-shell yield at first doubled but then did not.

Since the  $Z$ -accelerator does not have the energy to drive 10 mg/cm loads, two sets of uniform-fill calculations were carried out to observe what happens when the imploded mass is progressively lowered. The mass of the titanium load was lowered by first increasing the initial density of the load by  $\sqrt{2}$  and then by reducing the initial radius of the load, preparatory to doing nested-plasma calculations. In one set, the load mass was reduced to 5 mg/cm (for  $\eta^* \cong 3.6$ ) and, in the other, to a mass of 1.25 mg/cm for an  $\eta^*$  of 2, which corresponds to a mass and energy input obtainable in  $Z$ -accelerator experiments. Results from these calculations are shown in Figs. (12)-(15). In each set of calculations, the inclusion of electron viscosity reduced the ion temperature [Figs. (14) and (15)]. Note that, by halving the mass of the load and, thus, the number of radiators, the K-shell energy output was halved even though the power output was not significantly reduced [compare Fig. (12) with Fig. (7)]. The energy radiated in the 1.25 mg/cm calculation [Fig. (13)] also went down in proportion to both the number of radiators and the input energy. Figs. (14) and (15) indicate a tendency for the plasma core to be over-ionized in these calculations, i.e., to be non-optimally compressed. Note, both in Figs. (6)-(11) and in Figs. (12)-(15), that ion temperatures generated

in the core region of the plasma increased considerably as the amount of K-shell emission that the plasma produced from this region increased. Thus, even though the electron viscosity brought ion temperatures down in these particular calculations, it could not keep them down. This tendency for the ions to overheat is detrimental to K-shell emission since it reduces plasma compression and radiation rates, and it stores energy in the ions that cannot be radiated away.

#### IV. Nested-plasma Calculations

The 1.25 mg/cm uniform-fill calculation was used as a stepping stone to the 1.25 mg/cm nested-plasma calculations that are described in this section. They, in turn, provided guidance for the five nested-plasma calculations that were made in correspondence with five nested-titanium, Z-accelerator, wire shots and that are described in the following section. Several of the 1.25 mg/cm calculations were made to evaluate the way zoning, mass distribution, and implosion velocity affect the formation of plasma gradients and their influence on x-ray outputs. The influence of electron viscosity on nested titanium-plasma implosions was also investigated. The nesting used in the calculations was done by dividing the 1.25 mg/cm uniform-fill plasma into two parts and by moving the outer part out in radius, by roughly a factor of two. Since one cannot have a perfect vacuum between plasmas in a computer calculation, the calculations were zoned so that the density between the inner and outer plasmas could be reduced by a factor of ten. Thus, the nesting used in these calculations only approximated certain of the essential features of the Z-accelerator experiments, and for the following additional reasons. One, the calculations described here are of the shell-on-fill rather than shell-on-shell variety. To remove plasma from the axis for shell-on-shell implosions requires, in principle, even greater numbers of zones and more computer time than were used in the shell-on-fill calculations. Two, the initial plasma conditions that must be chosen when modeling the experiments are essentially unknown and, at best, approximate. Shell-on-shell calculations have an addition parameter to play with, since the initial shell thicknesses are chosen somewhat arbitrarily. Three, the plasma densities generated early in the experiments are not only unknown but also non-uniform. In addition, the state of the inner titanium (wires or plasma) at the time of impact is unknown. Altogether, these problems imply that there is no rationale for attempting calculations that purportedly accurately simulate (rather than correspond) to current nested-wire experiments. The shell-on-fill calculations described here have the utility of demonstrating hydrodynamic behavior that promotes K-shell emission from moderate atomic number loads. Another of their benefits is that they suggest certain hydrodynamic behavior that might favor wire-on-foam experiments with pre-ionization over simple wire-on-wire experiments.

The seven cases listed in Table I were analyzed and compared in these initial calculations. In the first three cases, the initial plasma was kept unchanged, but the implosion was calculated employing different zoning schemes. In case 1, only 80 zones were used, 16 of which were allocated to the inner (nested) plasma. In cases 2 and 3, the total number of zones was increased to 100, and the number used to resolve the gradients generated in the inner plasma was 17 in case 2 and 27 in case 3. The dynamics of these nested-plasma implosions is illustrated in Fig. (16). It contains time histories of the shell boundaries of the outer plasma (in red) as they implode inward and impact the outer boundary of the nested plasma (in blue) at approximately 46.5 ns. The second blue curve in Fig. (16) shows the time history of the first cell boundary. Even though a perfect vacuum does not exist between the two plasmas in the calculation, the collision time is still fairly well defined. Note that the outer surface of the outer plasma bounces outward at the time when the

Table I. Nested-plasma Calculations

Case #	# Zones (Total)	# Inner Plasma Zones	Mass Ratio (Outer/Inner)	Inner Plasma Radius (mm)	$\eta^*$
1.	80	16	2:1	4.2	2
2.	100	17	2:1	4.2	2
3.	100	27	2:1	4.2	2
4.	100	35	1:1	4.3	2
5.	100	27	2:1	4.2	4
6.	100	31	2:1	2.2	2
7.	100	35	1:1	4.3	4

current drive is terminated. Three vertical lines are drawn in Fig. (16) at 47.8, 49.3, and 50.7 ns. They identify the three times in the implosion history at which the spatial profiles of temperature, density, and ionization are drawn in Figs. (17) and (18). These two figures illustrate that strong shocks are formed during the collision of the outer and inner plasmas. However, even within a 100 zone calculation, these shocks are poorly resolved. The profiles in Fig. (17) show how the temperature front moves ahead of the density front, leading, at the time of peak compression, to a less dense core plasma. Since K-shell x rays originate from this core plasma, any reductions in its density can seriously impact this emission. Fig. (18) shows that during shock formation the plasma is driven into the ground helium-like state of the K-shell, but that [Fig. (19)] actual K-shell emission does not begin until 52 ns just before the final compression and heating take place.

Two case 3 calculations were made, one with and one without electron viscosity. The addition of electron viscosity allowed an additional 20 kJ of K-shell x rays to be extracted from the plasma [Fig. (19)]. Fig. (20) shows the reason for this added emission. Two ion temperature profiles are drawn at the onset of K-shell emission. Without electron viscosity, the ions are much hotter than the electrons in the core region of the plasma as the emission begins. Consequently, the temperature ratio in the formula for  $\eta_{e0}/\eta_{i0}$  is reduced allowing some of the final ion heating to be averted and channeled instead into x rays.

Another variable that can be used in place of the radius when plotting profiles is  $m(r)$ , the plasma mass contained within a cylinder of radius,  $r$ :

$$m(r) \equiv 2\pi \int_0^r dr' r' \rho(r').$$

When  $\langle Z \rangle$  is plotted as a function of  $m(r)$  rather than of  $r$  at the time,  $t = 51.6$ , just as K-shell emission begins, one learns that only  $\sim 28\%$  of the plasma mass in this load has been primed to emit from the K-shell as the final compression stage of the implosion begins.

Cases 1-3 address the question, how does the number and location of the hydrodynamic zones in a computer calculation affect the plasma dynamics and plasma profiles that are calculated? Part of the answer is given in Figs. (21)-(23). The profiles shown in these figures were all calculated at the time of peak compression. The plasma compression was significantly reduced along with the

core density by going, in case 1 to case 2, from 80 to 100 zones, while the core electron temperature was increased, and the ratio of electron-to-ion temperature was reduced. The increased zoning of the inner plasma, in going from case 2 to case 3, led to increased gradient resolution in the core, which increased the core compression without changing its temperature or its electron-to-ion temperature ratio. Figs. (21)-(23) provide examples of how the computed hydrodynamics, which is driven by gradients, is a function of the zoning used for small zone number, since zoning determines the gradient structure of the plasma that can be computed.

Case 4 addressed the question, could mass shifting and larger, initial, inner-plasma densities increase the mass participation from the  $\sim 28\%$  level seen in Fig. (20)? In case 4, the increased inner density was achieved by shifting mass from the outer to the inner plasma and making the masses equal. In case 4, the plasma received the same input energy as case 3. Figs. (24) and (25) show that this mass and density shift did increase the amount of K-shell mass participation (drawn in Fig. (24) at the times of peak compression) as well as the K-shell yield by increasing the peak power output. Notice, however, that the power pulse was clipped following peak power. Thus, the energy output was limited for this particular load because, at  $\eta^* = 2$ , there was no more energy available to be radiated from the core, i.e., the mass participation and energy content of the core in this case did not increase enough. Both Figs. (19) and (25) contain a plot of the outer radius of the inner plasma. These curves convey information about the elasticity or inelasticity of the compressions and suggest that the L-shell radiation losses in case 4 were larger than those in case 3 (as they were by approximately 100 kJ).

Case 5 looked at the response of the case 3 plasma when the current was increased and the implosion was driven by twice the input energy of case 3. For this plasma configuration, however, a doubling of the input energy did not double the K-shell power or the energy output [see Fig. (26)]. The L-shell output for this case, however, was less than that of case 4. Note that the energy output in these calculations changes in proportion to the peak power output generated at the time of peak compression since the current is turned off prior to peak compression. At the start of the x-ray pulse in case 5, when 25% of the plasma is already beginning to radiate in the K-shell, the electron viscosity had acted to reduce the ion temperature [Fig. (27)]; however, the subsequently large x-ray output keeps the electrons cool as the ions are heated, resulting in little difference between the K-shell outputs with and without electron viscosity [Fig. (26)]. The increased energy output occurred as a result of the approximately 14% increase in mass participation that the extra energy input was able to promote. Fig. (28) demonstrates this result by comparing ionization levels as a function of  $m(r)$  at the time of peak emission for the case 3 and 5 plasmas. Fig. (29), when compared to Fig. (18), explains why this increase occurred. The added energy input puts more of the plasma into the helium-like ground state early on in the implosion, preparatory to its lighting-up during the final stages of compression.

The last two cases studied, 6 and 7, are illustrated in Figs. (30)-(32). In case 6 in contrast to case 4, the mass ratio of outer-to-inner plasma was kept at 2:1, while the initial density of the inner plasma was raised by decreasing its radius. The effect of increasing density by decreasing radius was to increase the power output (to that of case 5) but to decrease the energy output by clipping the power pulse even more severely than in case 4. That this clipping effect could be mitigated was demonstrated in case 7. The plasma in case 7 was the same as in case 4, but the energy input was doubled. Hence, case 7 is to case 4 as case 5 is to case 3. Figs. (19) and (26) show that doubling the energy input when the outer-to-inner plasma mass ratio is 2:1 does not double the energy output, while Figs. (25) and (31) show that doubling the energy input more than doubles

the output when the mass ratio is 1:1. Again, the large electron cooling that the K-shell output produced eliminated the possibility, in this case, of seeing extra K-shell output as a consequence of electron viscosity [Fig. (31)], even though a large difference in ion temperatures at the beginning of the K-shell pulse existed in the two calculations (with and without electron viscosity) [Fig. (32)]. Note also in Fig. (32) that the doubled energy input in case 7 increased K-shell mass participation to  $\sim 50\%$ .

## V. Variable Mass, Variable $\eta^*$ , Nested Calculations

Five different nested-titanium-wire experiments were carried out on the Z accelerator. For two of the five, 3 shots each were done. Table II contains the basic parameters of the 9 shots.

Table II. Experimental Parameters

Shot #	Outer Diam (mm)	Outer Mass $\mu\text{g/cm}$	Inner Mass $\mu\text{g/cm}$	Wire Gap Spacing (mm)	$\eta$
422	40	1246	623	0.9	1.6
423	45	1072	534	1.18	2.1
466	45	1072	534	1.18	2.1
468	45	1072	534	1.18	2.1
424	50	858	429	1.64	2.6
465	50	858	429	1.64	2.6
471	50	858	429	1.64	2.6
470	55	714	357	2.16	3.1
467	60	500	250	3.37	3.8

As mentioned earlier, two problems immediately arise in attempting to do calculations that closely simulate these experiments. One, different wire array diameters were used in the experiments, which produced large variations in wire gap spacing: from 0.9 mm in shot 422 to 3.37 in shot 467. The effect of gap spacings on the implosion dynamics cannot be modeled, but their effect in the experiments is known to be large. This problem arises because wire number cannot be increased indefinitely on a given machine as the array diameter is increased. An analogous theoretical zoning problem arises because the number of zones in a computer calculation must also be increased as the load radius is increased; however, the number of zones cannot be increased indefinitely due to limitations in computer resources. Two, because the wire explosion and merging dynamics is unknown, the initial conditions to be used in the computers calculations are basically unknown. In either 1-D or 2-D calculations, one can only roughly approximate them. For these two reasons, the calculations that were done were chosen to correspond with the experiments in the following way. Plasma-on-plasma collisions were modeled in a fixed geometry with roughly a 2:1 ratio in outer-to-inner plasma diameters in accord with the experiments. Also, the same masses were used as in the experiments, and they were imploded to roughly the same velocities as in the experiments. Results from these calculations are shown in Table III and in Figs. (33)-(47).

**Table III. Experimental/Calculational Comparisons**

Shot #	K-shell Yield (kJ)	Total Yield (kJ)	K-Mass Radiating (mg/cm)	Mass Fract %	Exp K-shell Yield, Main Pulse (kJ)	Exp Total Yield, Main Pulse (kJ)
422	188	1005	0.35	18.7	47.2	700
423	254	1037	0.37	23.1	54.5	672
466	254	1037	0.37	23.1	41	620
468	254	1037	0.37	23.1	45	598
ave	254	1037	0.37	23.1	46.8	630
424	269	870	0.36	27.9	56.2	578
465	269	870	0.36	27.9	55	874
471	269	870	0.36	27.9	68	650
ave	269	870	0.36	27.9	59.7	701
470	249	708	0.33	30.8	84	626
467	140	269	0.27	35.3	57	364

The first five figures, Figs. (33)-(37), show calculated K-shell power and energy outputs as a function of time as the load mass was progressively decreased and the load input energy-per-ion and implosion velocity was increased. The powers and yields at first increase achieving a maximum for the 1.29 mg/cm ( $\eta^* = 2.6$ ) load before falling again. This behavior is explained in Figs. (38)-(42). These figures contain plots of the ionization level of the plasma at the time of peak emission as a function of the mass enclosed in cylinders of radii,  $r$ . In all cases, the K-shell emission comes from the core of the plasma, which grows, at first, slightly in size and then diminishes slightly. The temperature and density profiles at the time of peak compression and emission (in Figs. (43)-(47)) explain the behavior seen in Figs. (38)-(42). As more energy-per-ion is imparted to the load, core temperatures are driven higher, leading to core overheating. Thus, core densities go down, reducing x-ray radiation rates. This behavior is indicative of strong shock wave convergence on axis.

## VI. Conclusions

One of the conclusions that can tentatively be drawn from the above comparisons is that substantial improvements in load performance are possible through load designs that better approximate the initial conditions used in the calculations. Of course, the calculations assume overly ideal initial conditions, i.e., they assume that plasmas are preformed and uniform in both density and temperature. Consequently, the calculations produce much larger K-shell energy outputs in a single high-power pulse than the experiments do. Experiments, on the other hand, are carried out in ways that make it impossible to create such ideal plasma initial conditions. Consequently, it is not entirely surprising that they produce up to a factor of five smaller K-shell outputs in the main pulse than calculations do. Some of this large difference can be attributed to the poorly understood and uncontrolled explosion dynamics of the wires. However, the calculations



suggest that generating more uniform plasmas initially could produce large payoffs in significantly improved K-shell x-ray outputs from moderate atomic number Z-pinchs. Under the assumption that approximate agreement between trends seen in the theoretical and experimental implosions is due to common features in their dynamics (even when their initial conditions have marked differences), one can also make tentative interpretations of the experimental data and, consequently, some proposals for experiments that could improve load performance.

One notable trend common to both the experiments and calculations is the appearance of a K-shell yield maximum. The calculations show that, as the load mass is lowered and the input energy or implosion velocity is raised, the core region is driven to higher temperatures and lower densities. In collisional-radiative equilibrium, which is assumed in the calculations, these trends lead to K-shell burn-through and lower power emissions, which may or may not be present in the experiments. In addition, as the load mass was reduced in the calculations, the amount of mass in the core that ended up radiating in the K-shell went slowly downward at first and then more rapidly downward (even as the mass fraction went steadily up [see Table III]). However, while the radiating mass moved from  $370 \mu\text{g/cm}$  to  $265 \mu\text{g/cm}$ , the mass that was initially in the inner plasma moved from  $623 \mu\text{g/cm}$  to  $250 \mu\text{g/cm}$ . One might wonder, therefore, whether there are advantages to designing loads in which only the amount of inner, nested, plasma that ends up radiating in the K-shell is shock heated. Table III also shows that L-shell losses are dependent primarily on the amount of mass in the outer plasma. Thus, there may also be an advantage to using only the amount of mass in the outer plasma that is needed to shock heat the radiating core, although load designs that promote emissions from the outer plasma may be desired. In the above calculations, these were L-shell titanium emissions, but in other calculations, perhaps K-shell aluminum emissions or L-shell molybdenum emissions could be generated in the outer plasma for improved simulation fidelity. Finally, further investigation is needed to determine the kinds of load designs that are needed to increase K-shell emissions by increasing the amount of core mass that can be made to participate in K-shell emission. These investigations have never been done for elements in the fourth row of the periodic table.

# Kr (10 mg)

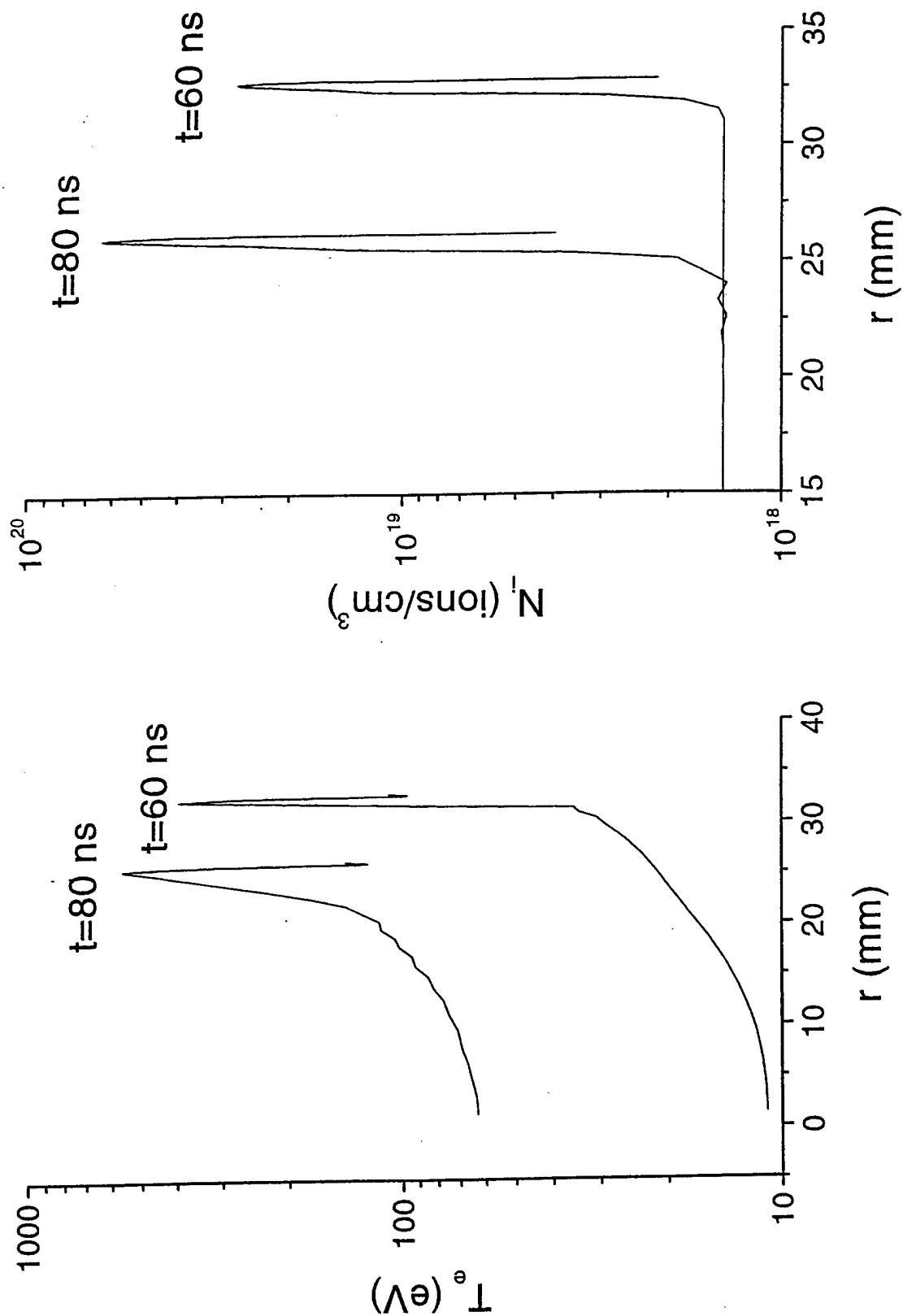


Figure 1

# Kr (10 mg)

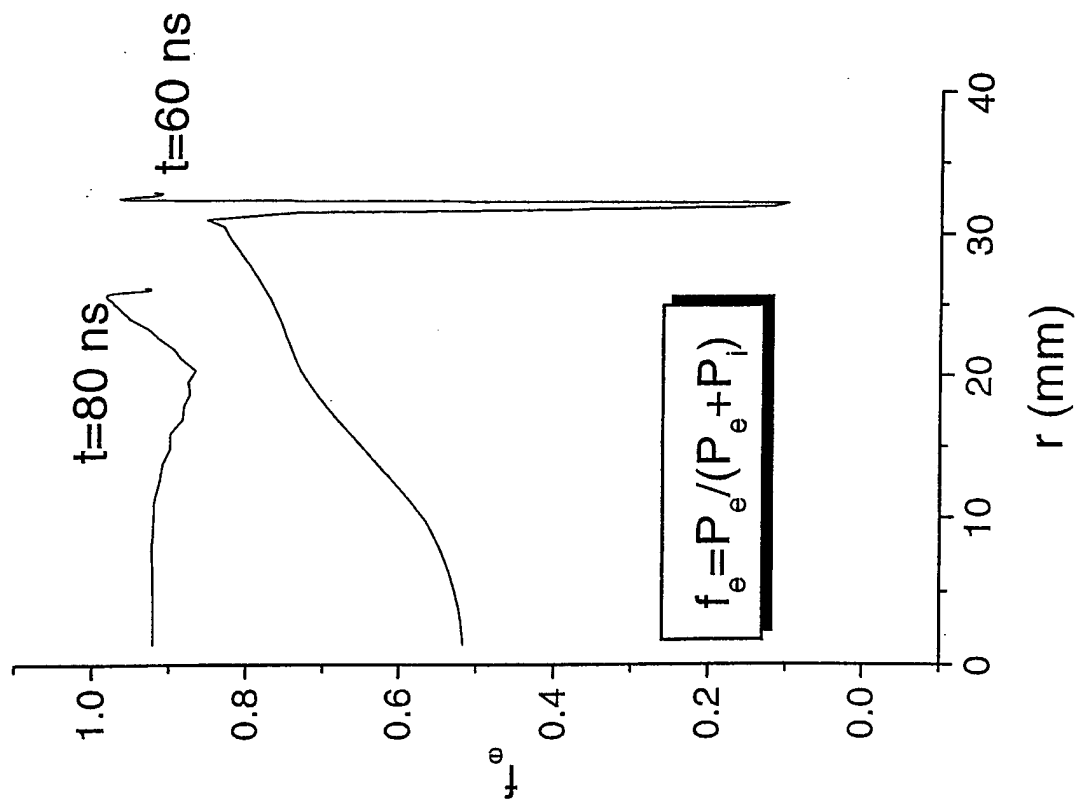
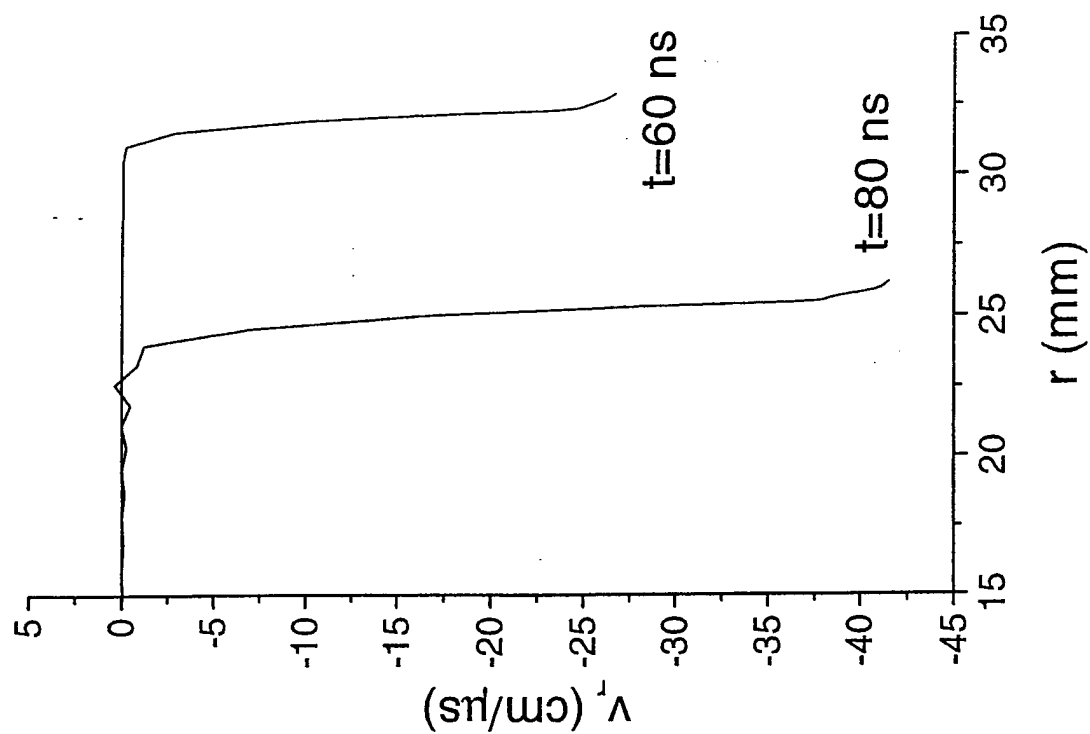


Figure 2

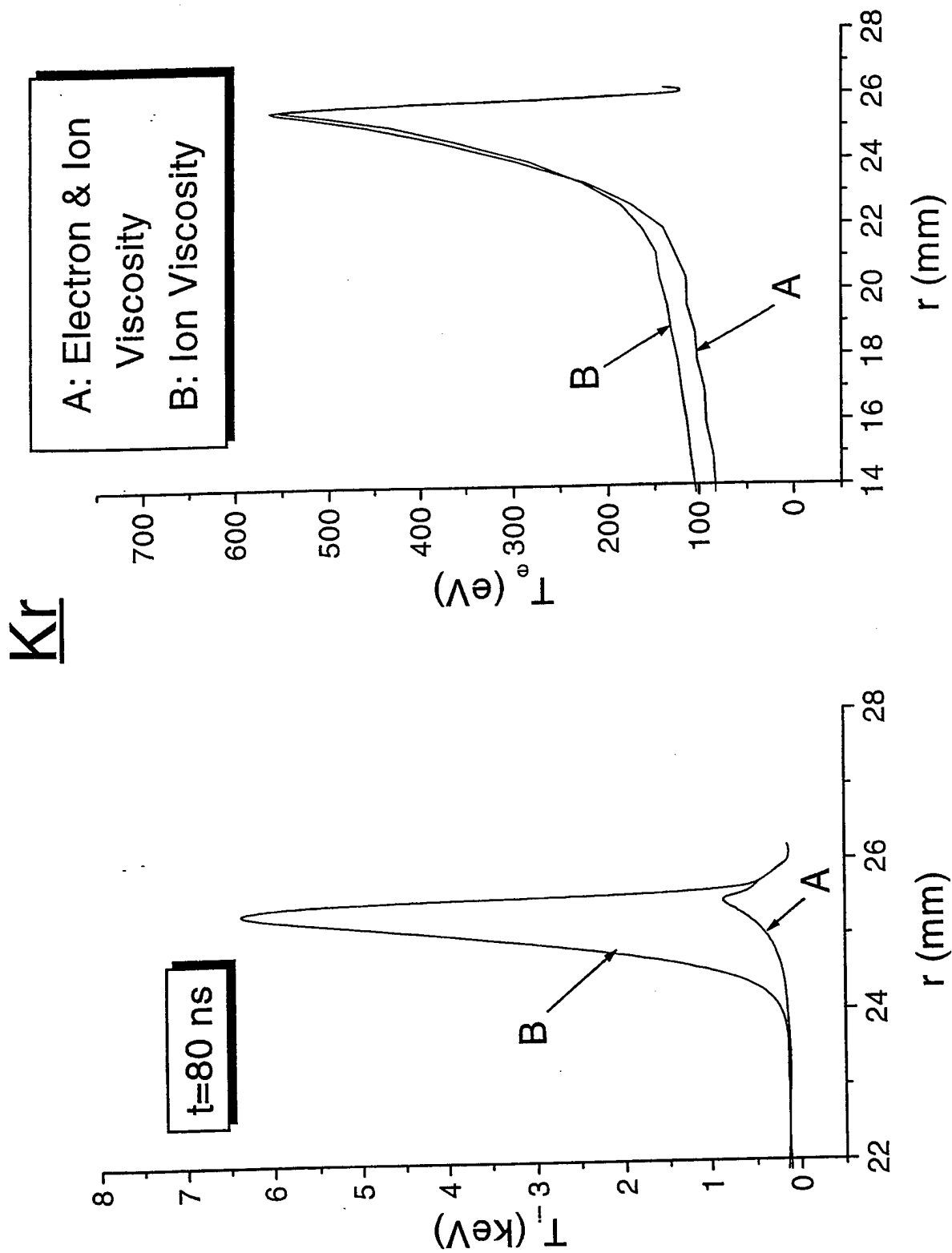


Figure 3

Kr (10 mg)

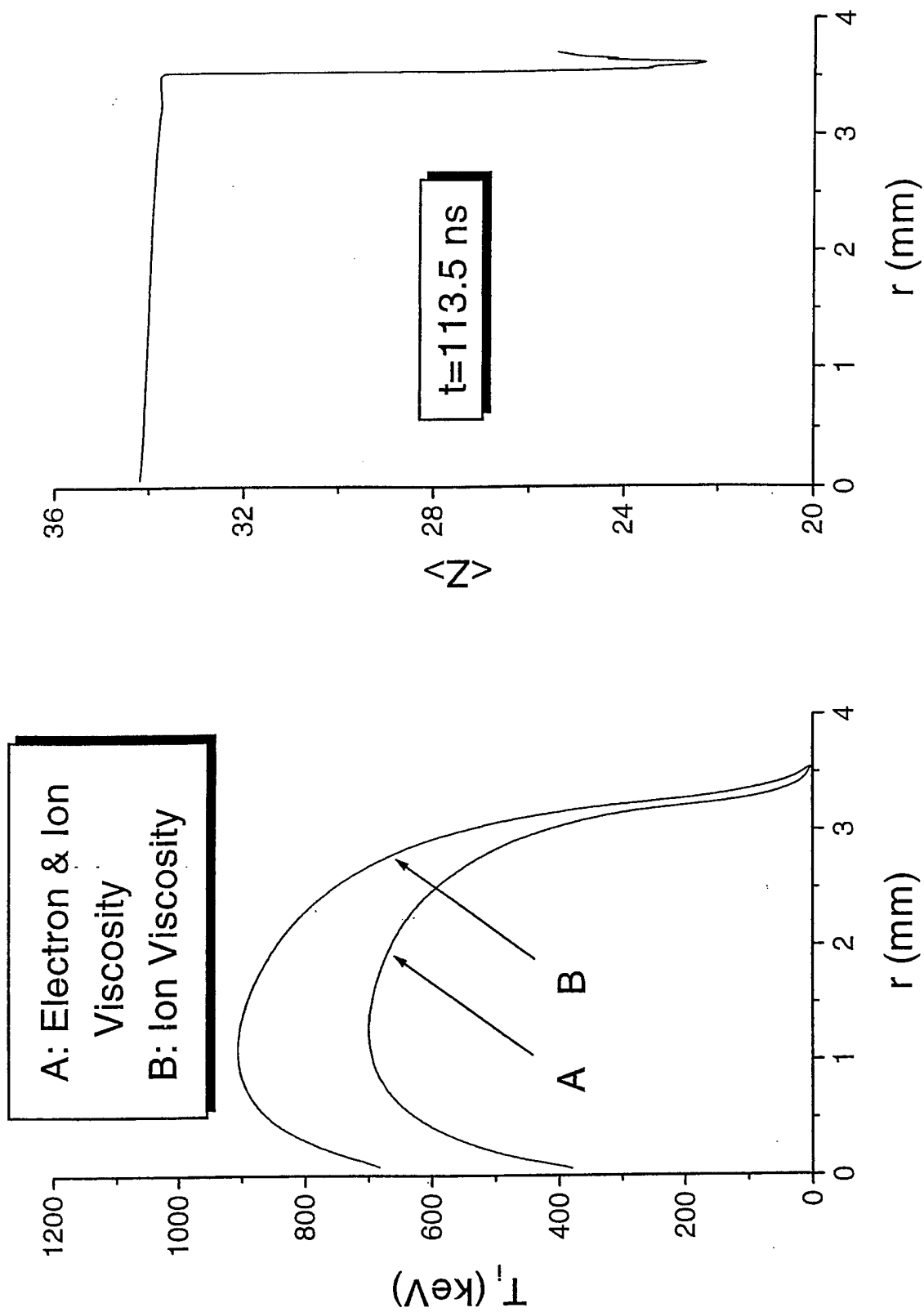


Figure 4

Kr (10 mg)

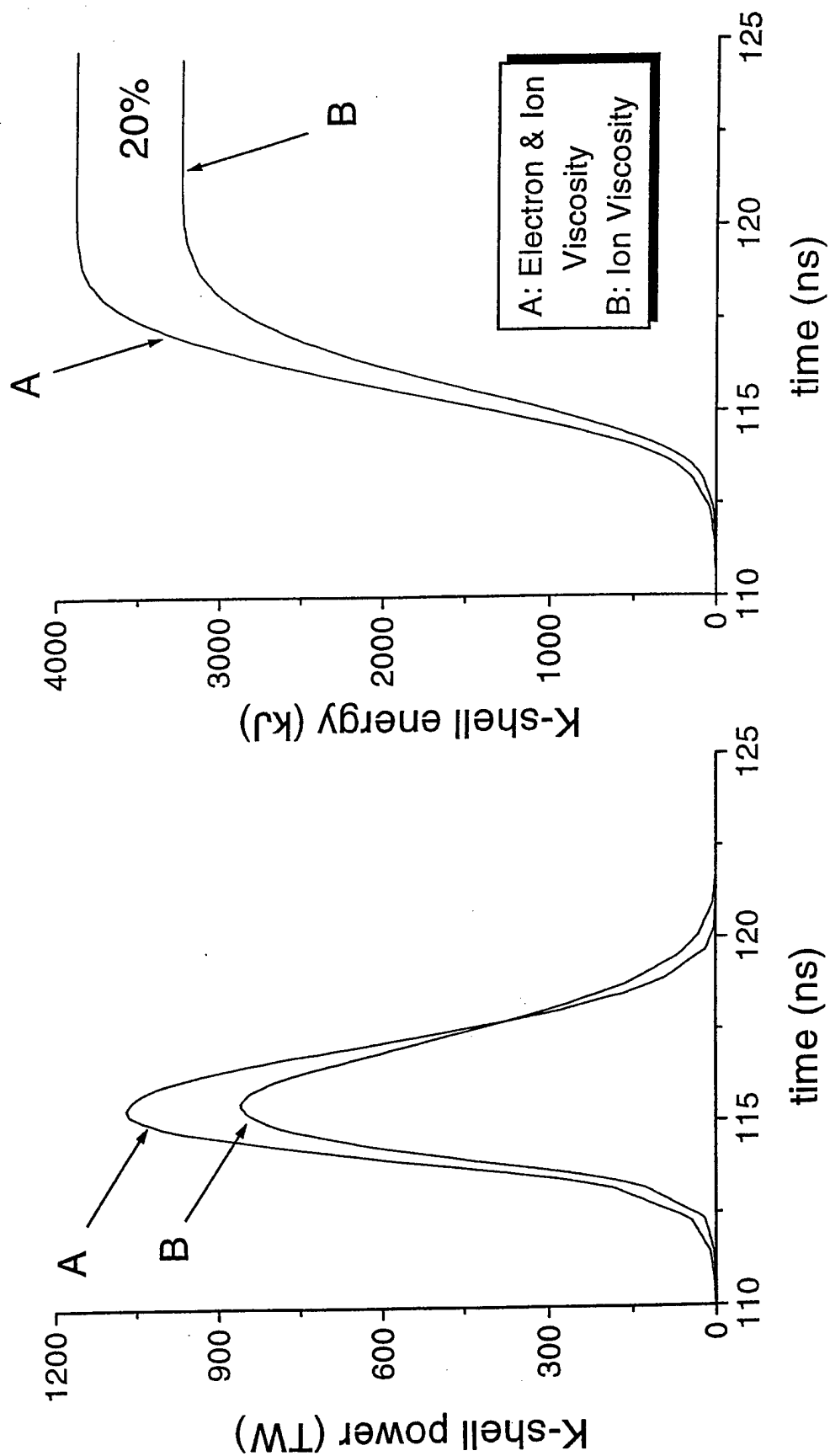


Figure 5

## II. $\text{Ti}$ (10 mg)

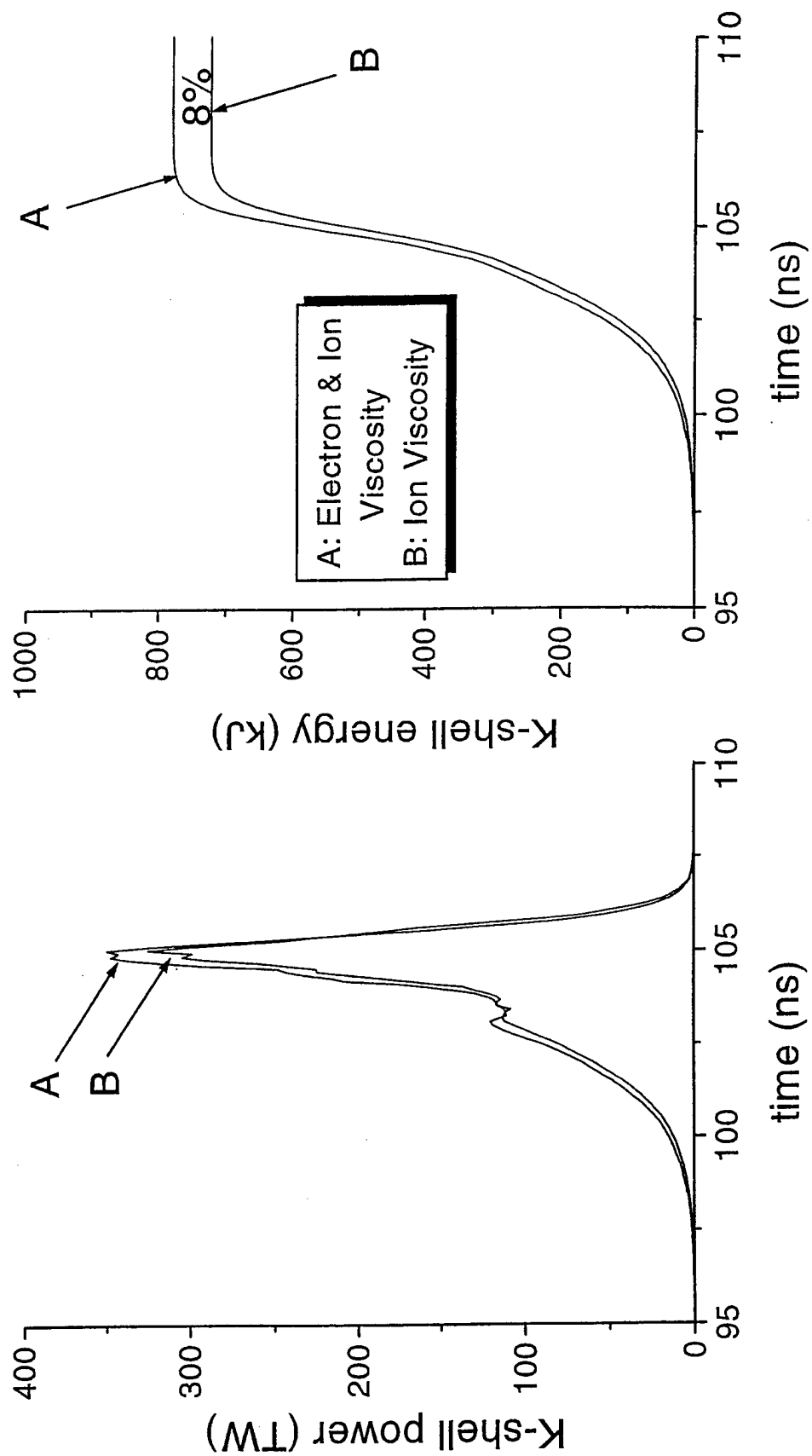


Figure 6

# I. Ti (10 mg)

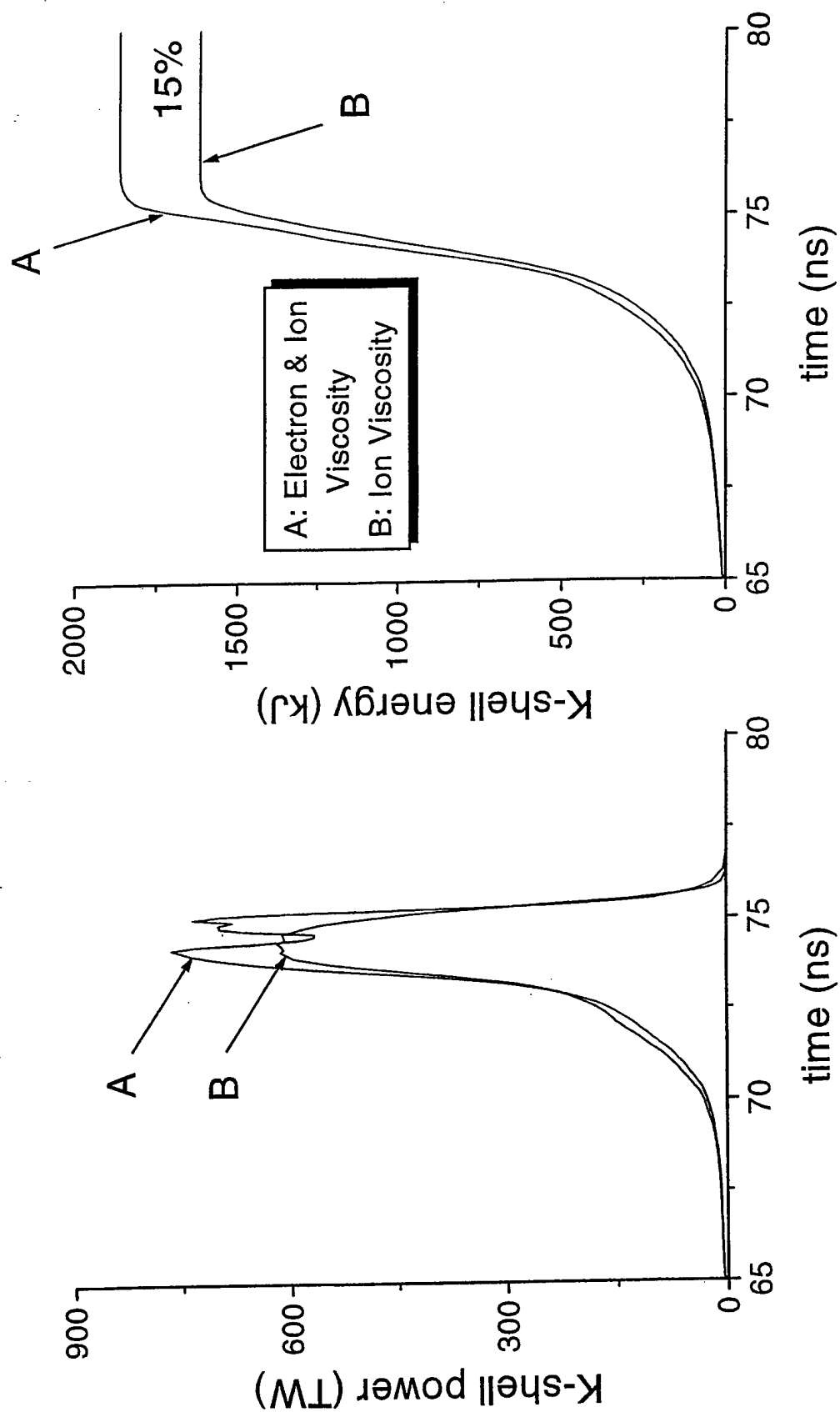


Figure 7



# Ti (10 mg)

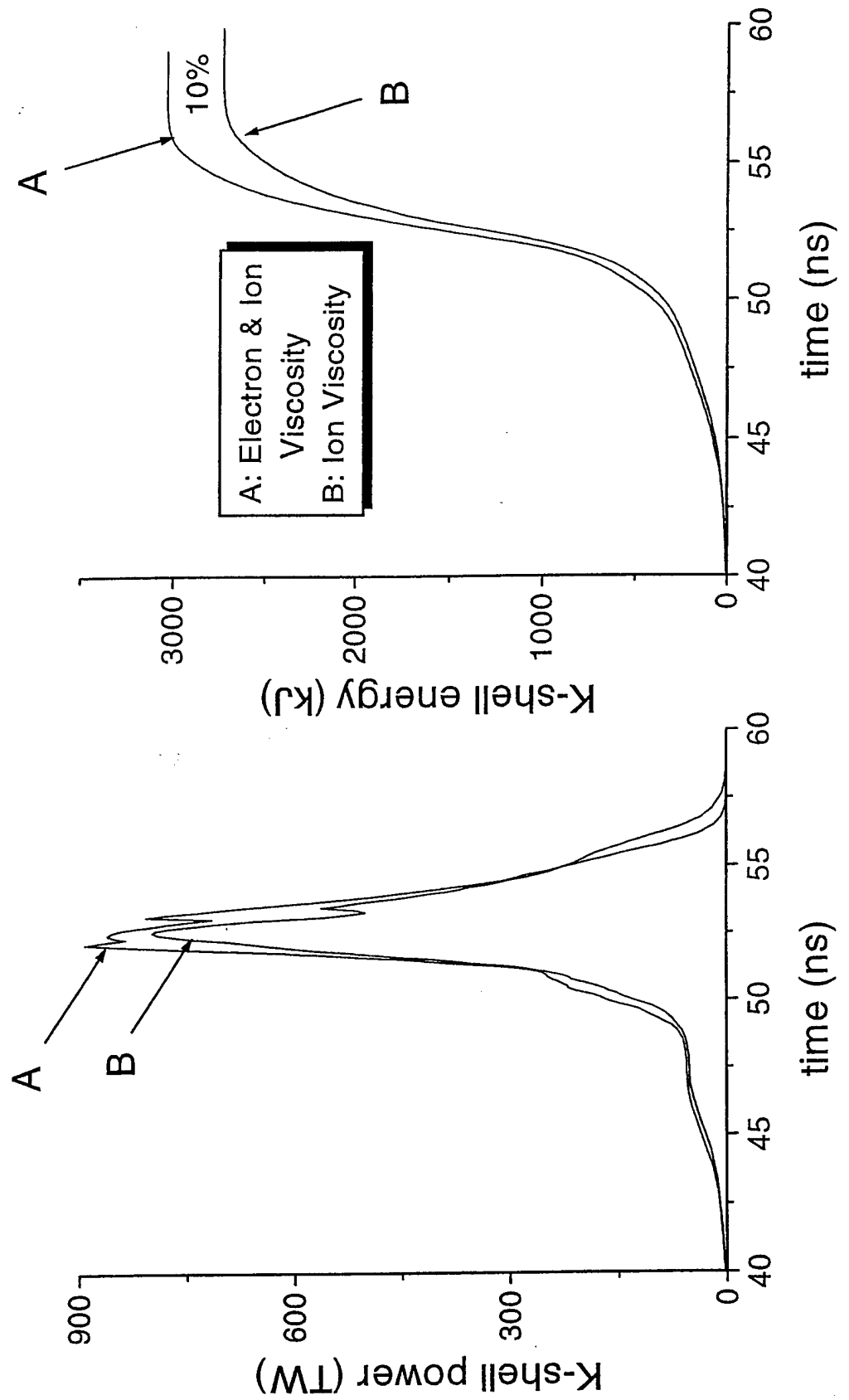


Figure 8

## II. $\text{Ti}$ (10 mg)

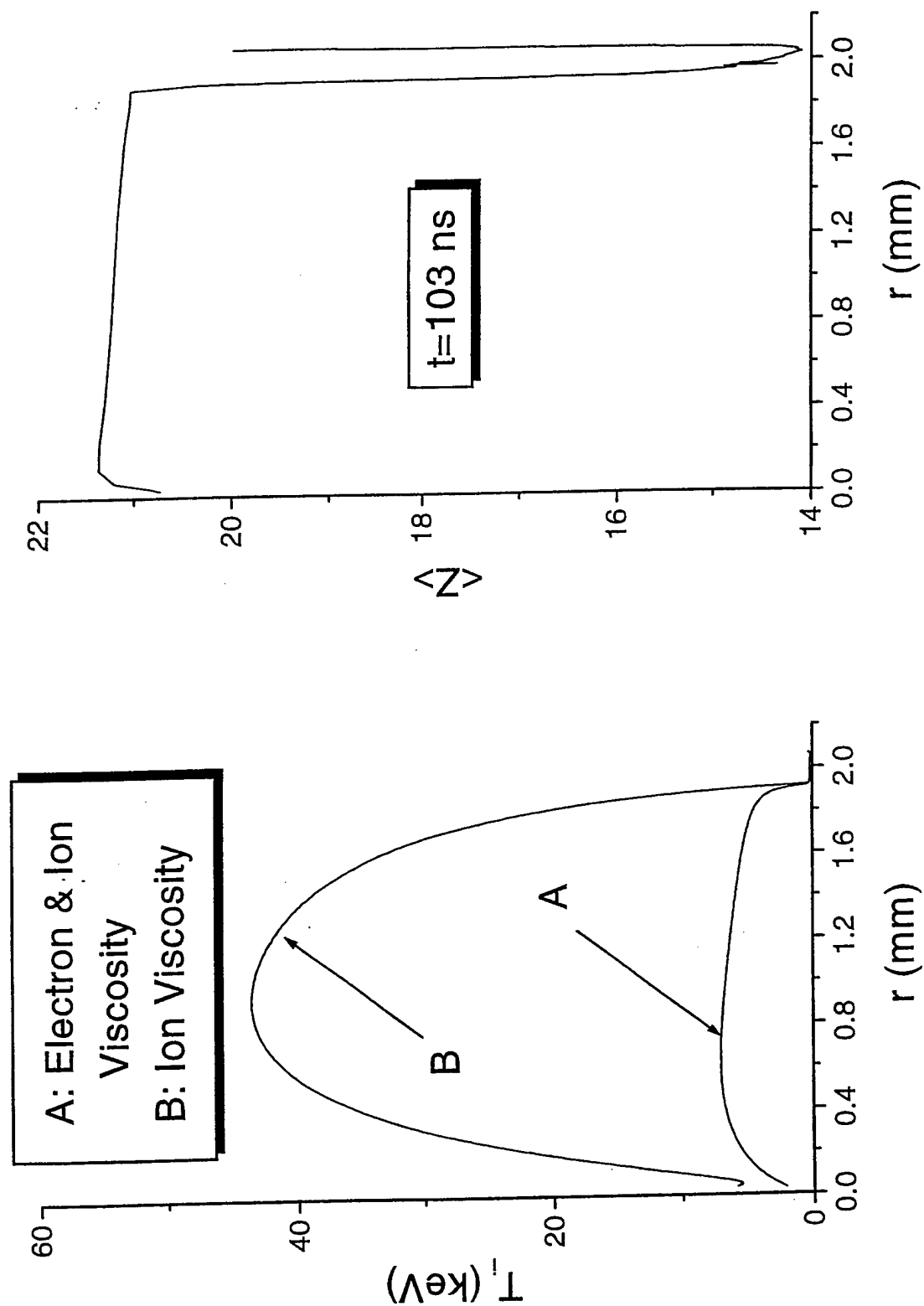


Figure 9

# I. $\text{Ti}$ (10 mg)

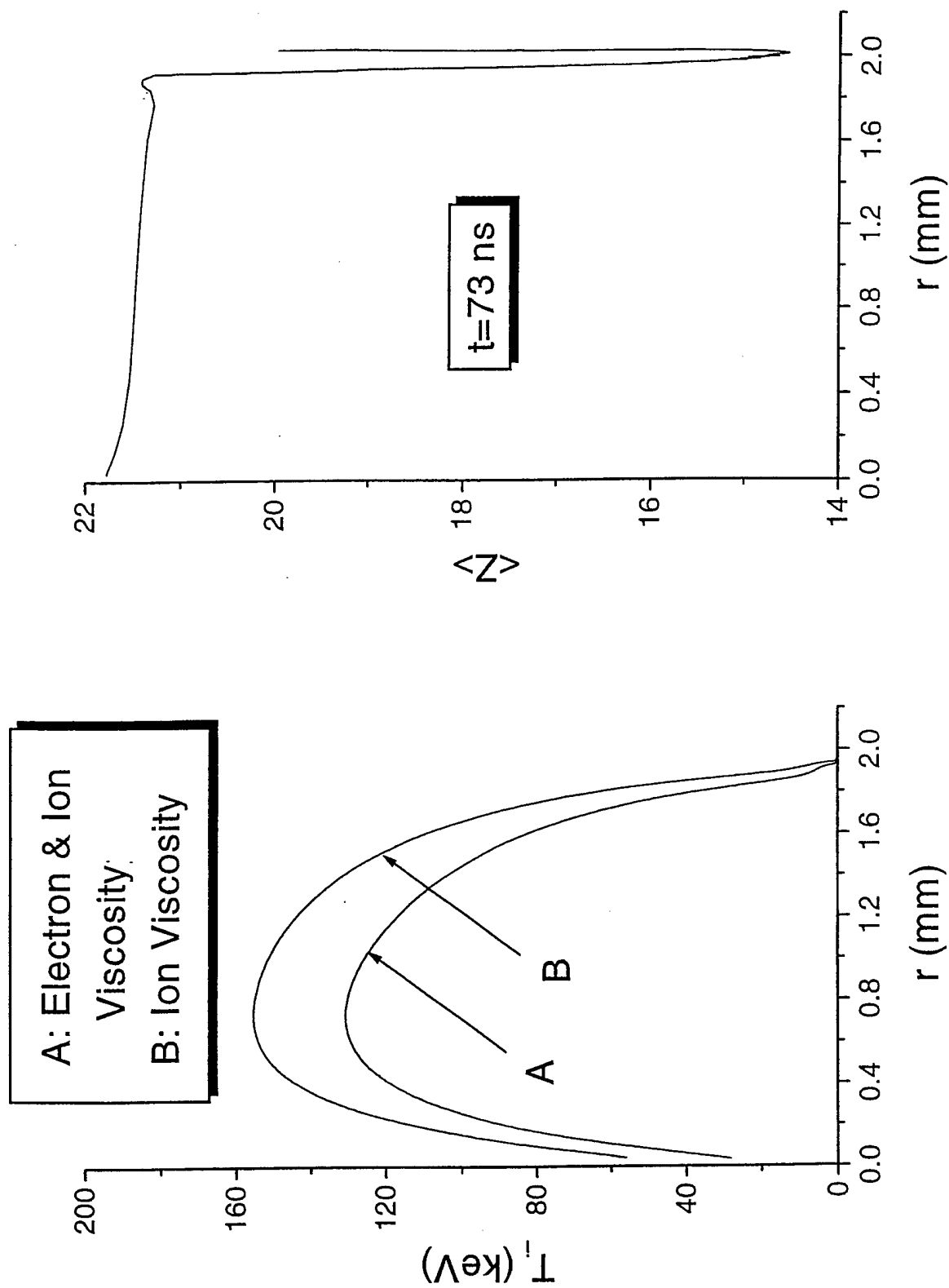


Figure 10

Ti (10 mg)

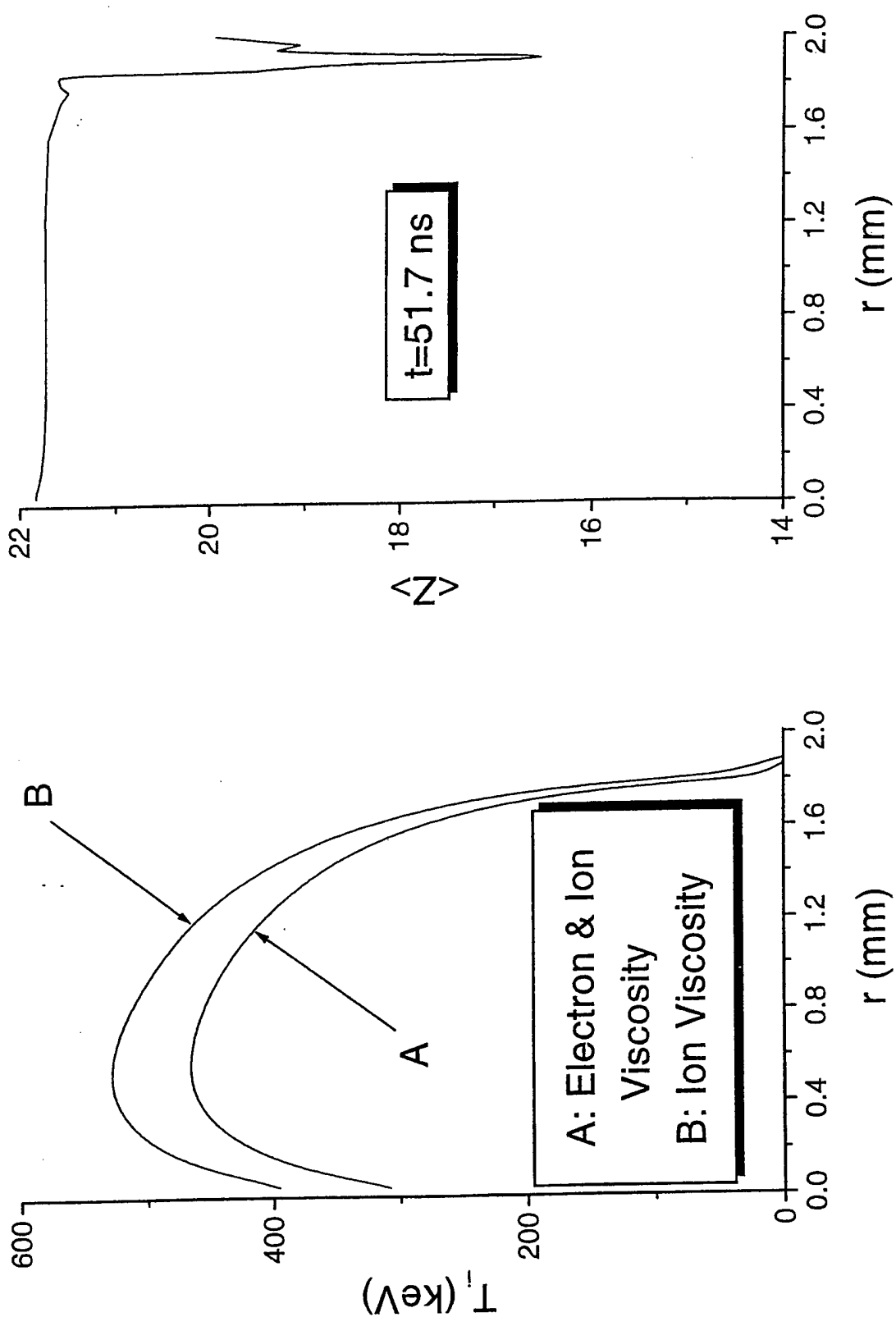


Figure 11

# Ti (5 mg)

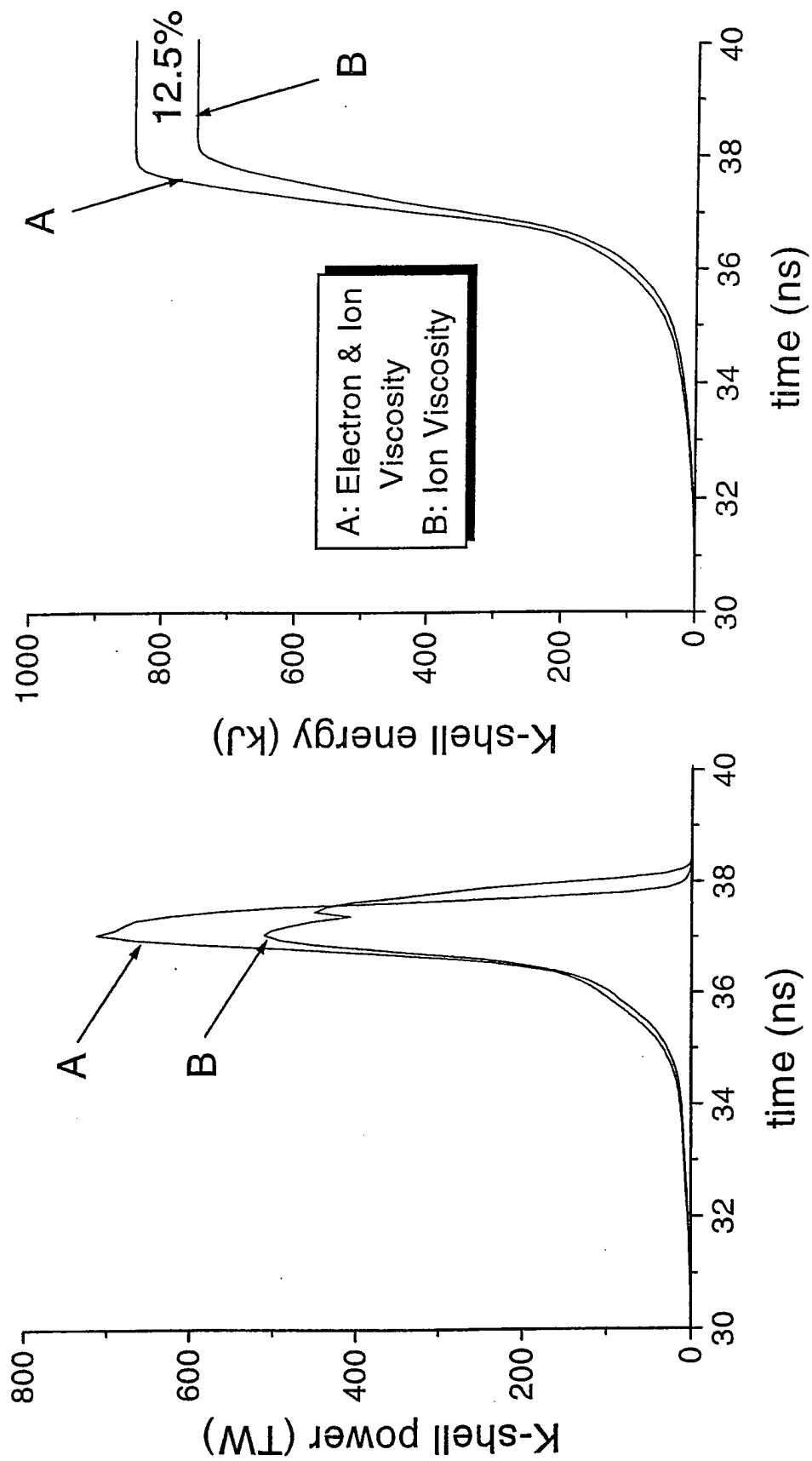


Figure 12

# Ti (1.25 mg)

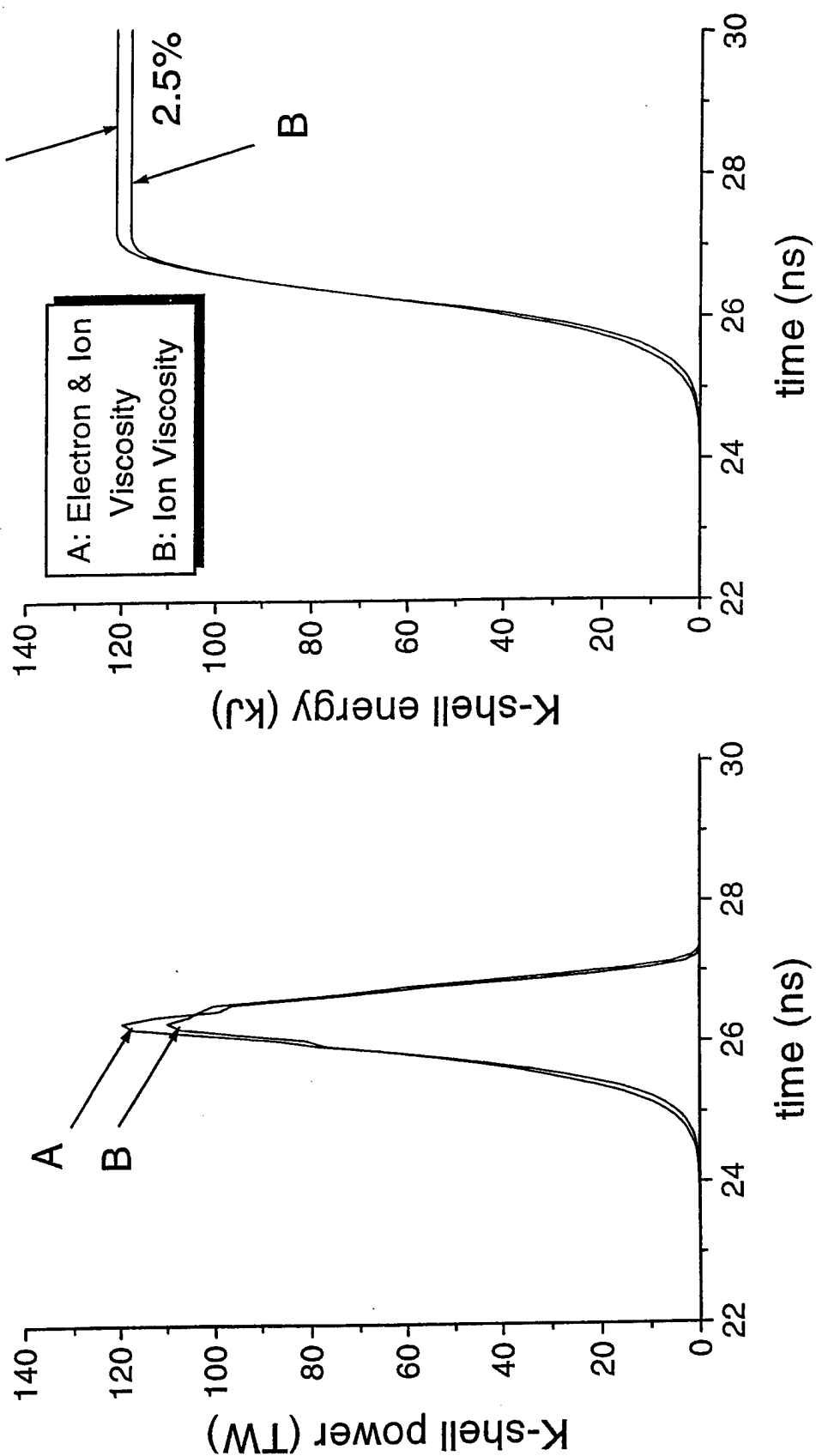


Figure 13

# Ti (5mg)

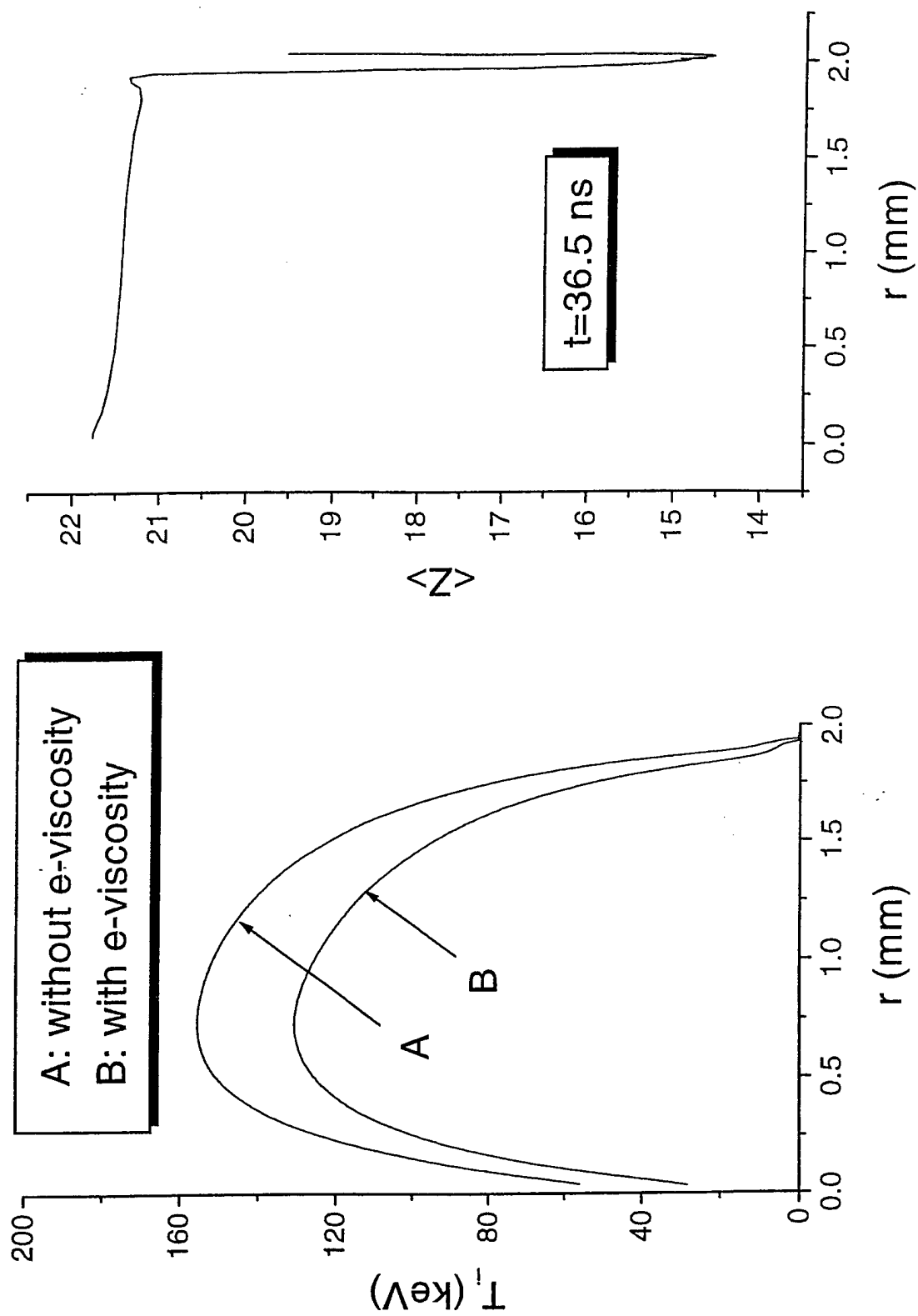


Figure 14

Ti (1.25 mg)

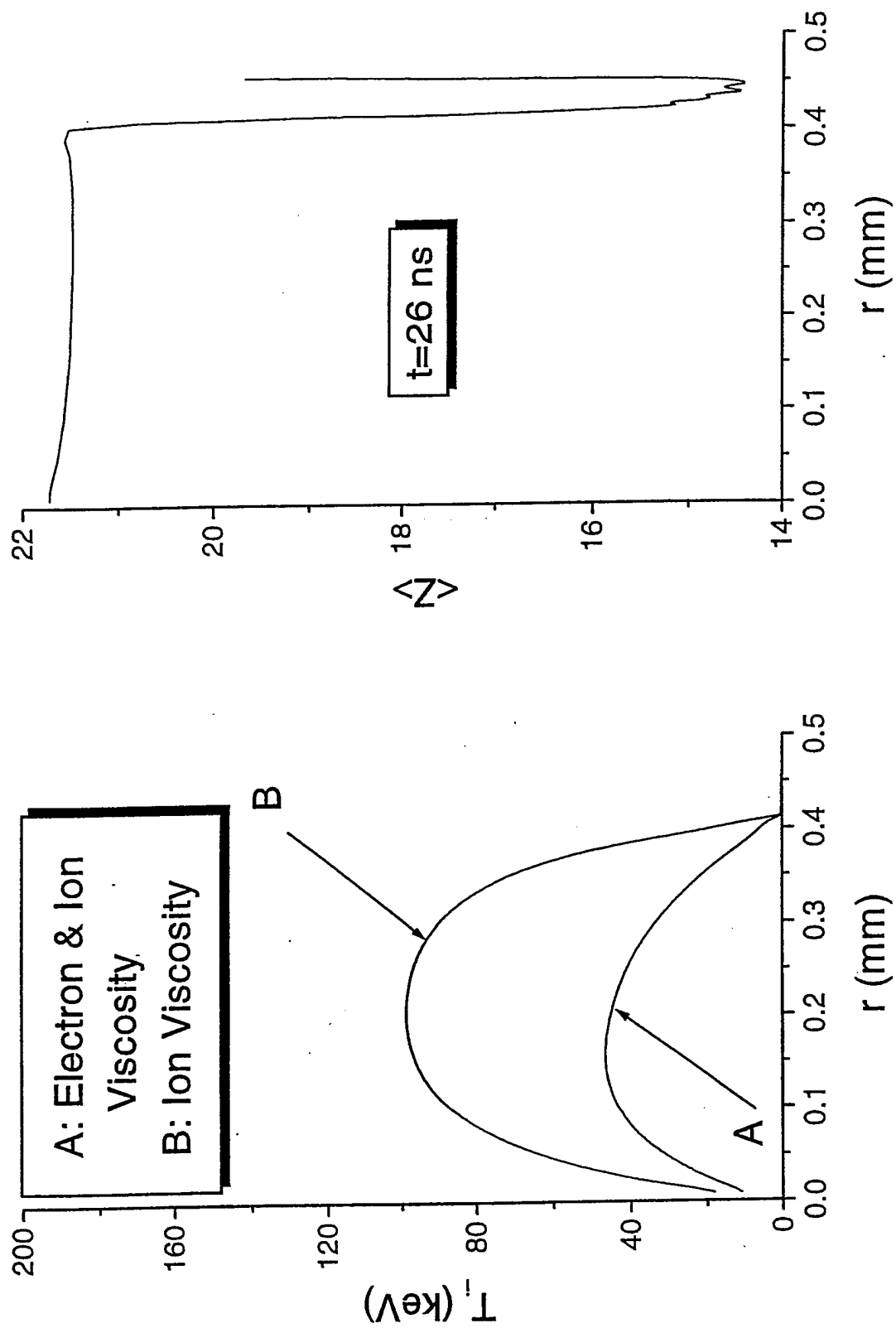


Figure 15



# Colliding Plasmas

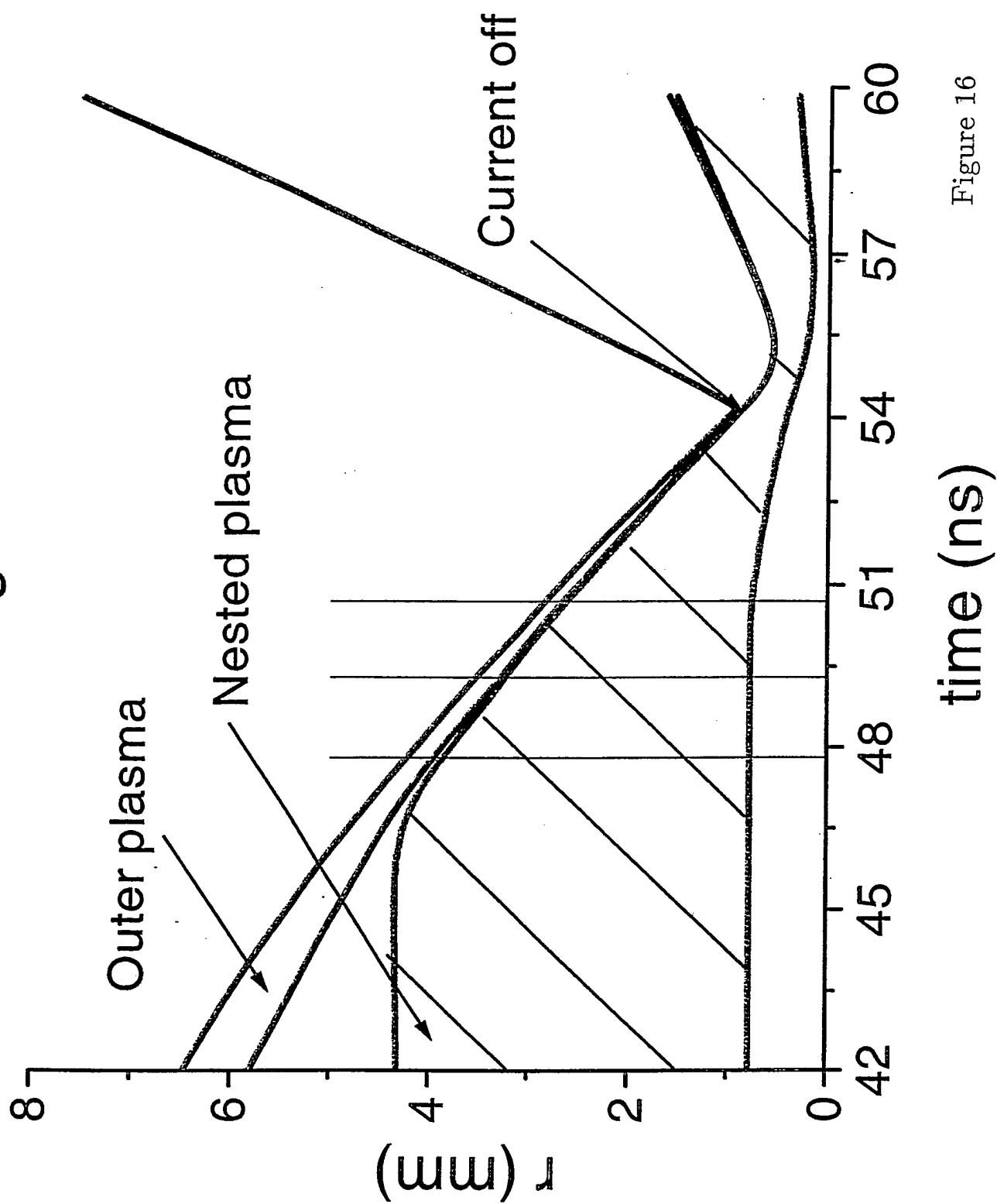


Figure 16

# Unresolved Shock Front Propagation

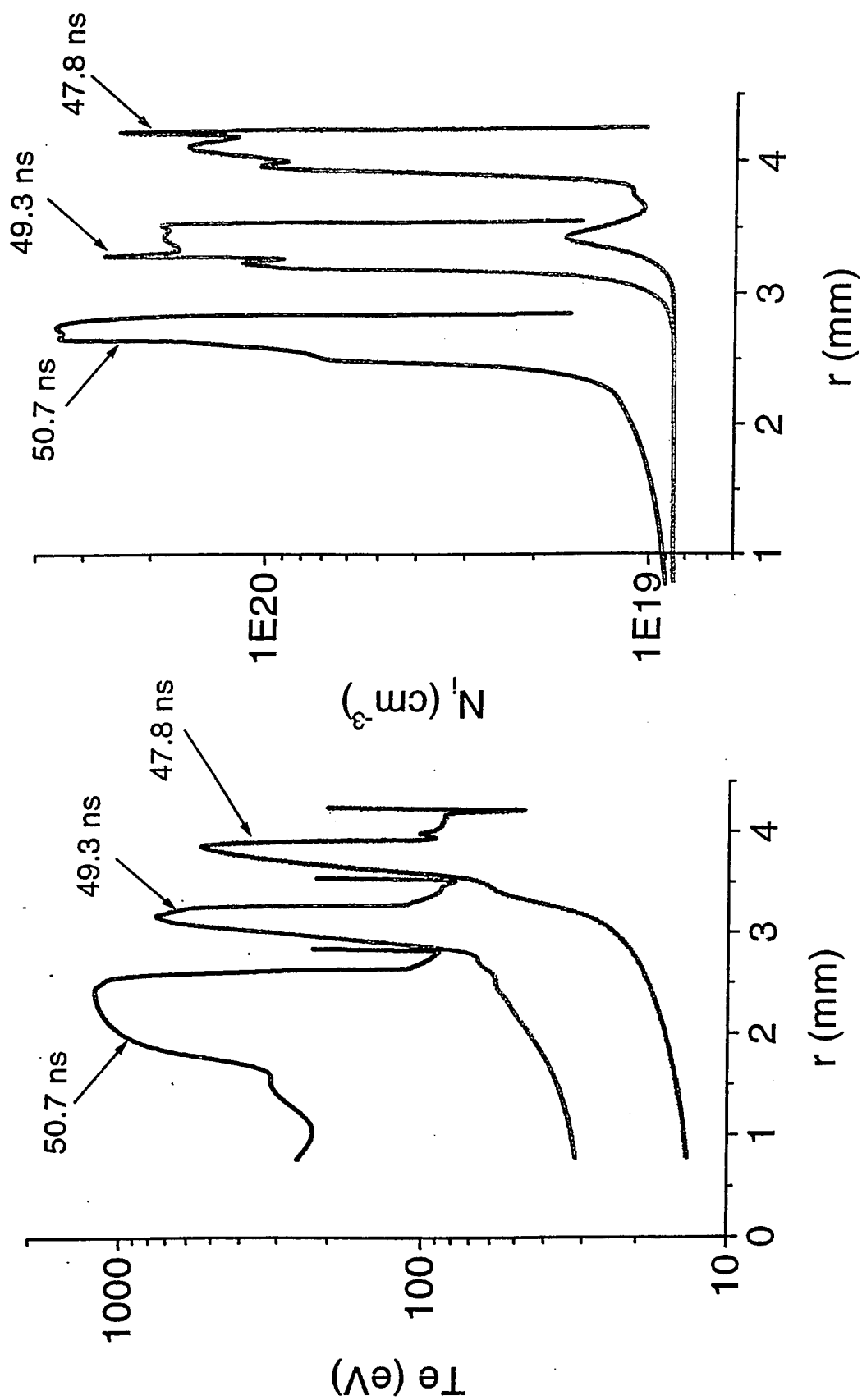


Figure 17

# Ionization Front Propagation

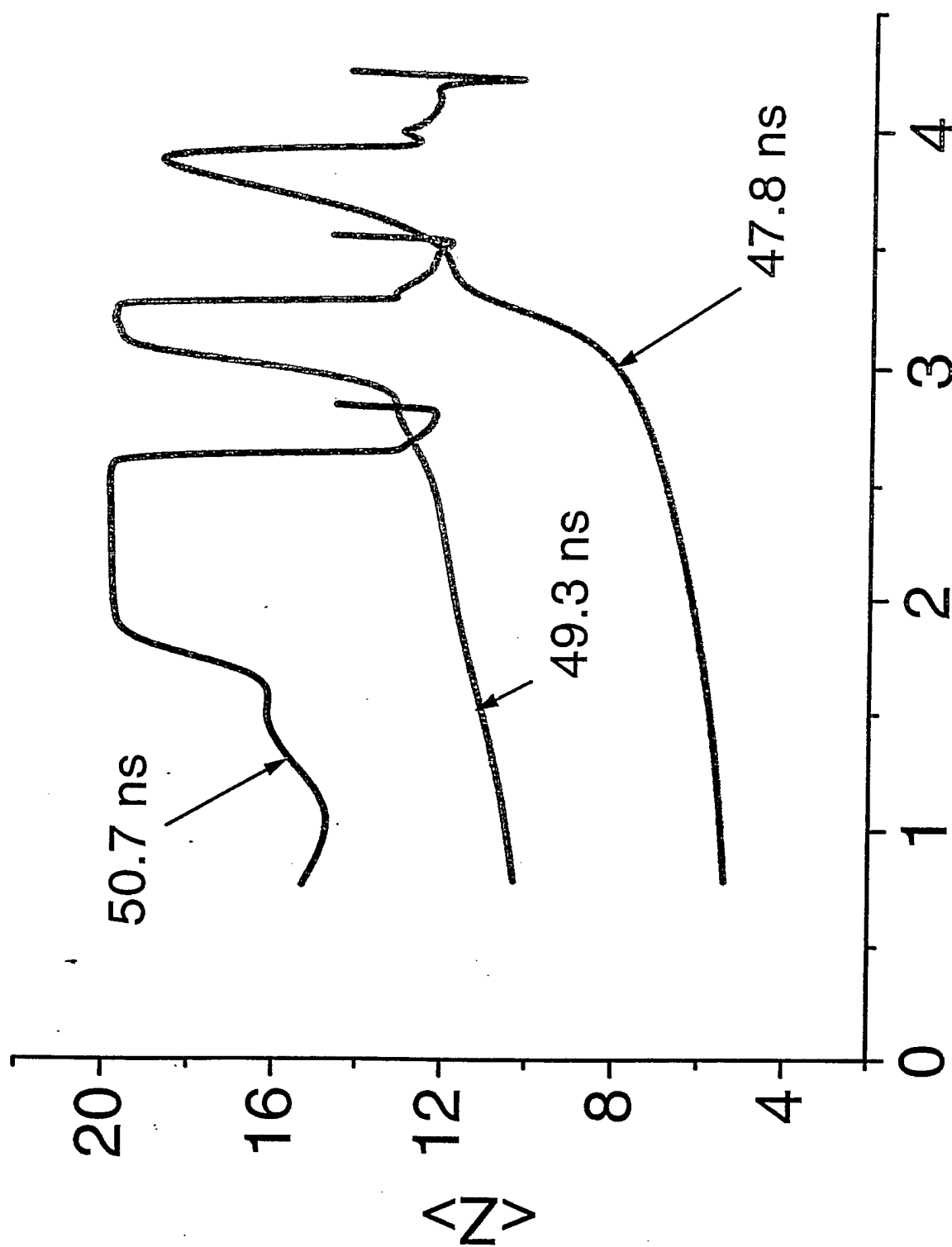


Figure 18

# Case 3 $\text{Ti}$ (1.25 mg, nested)

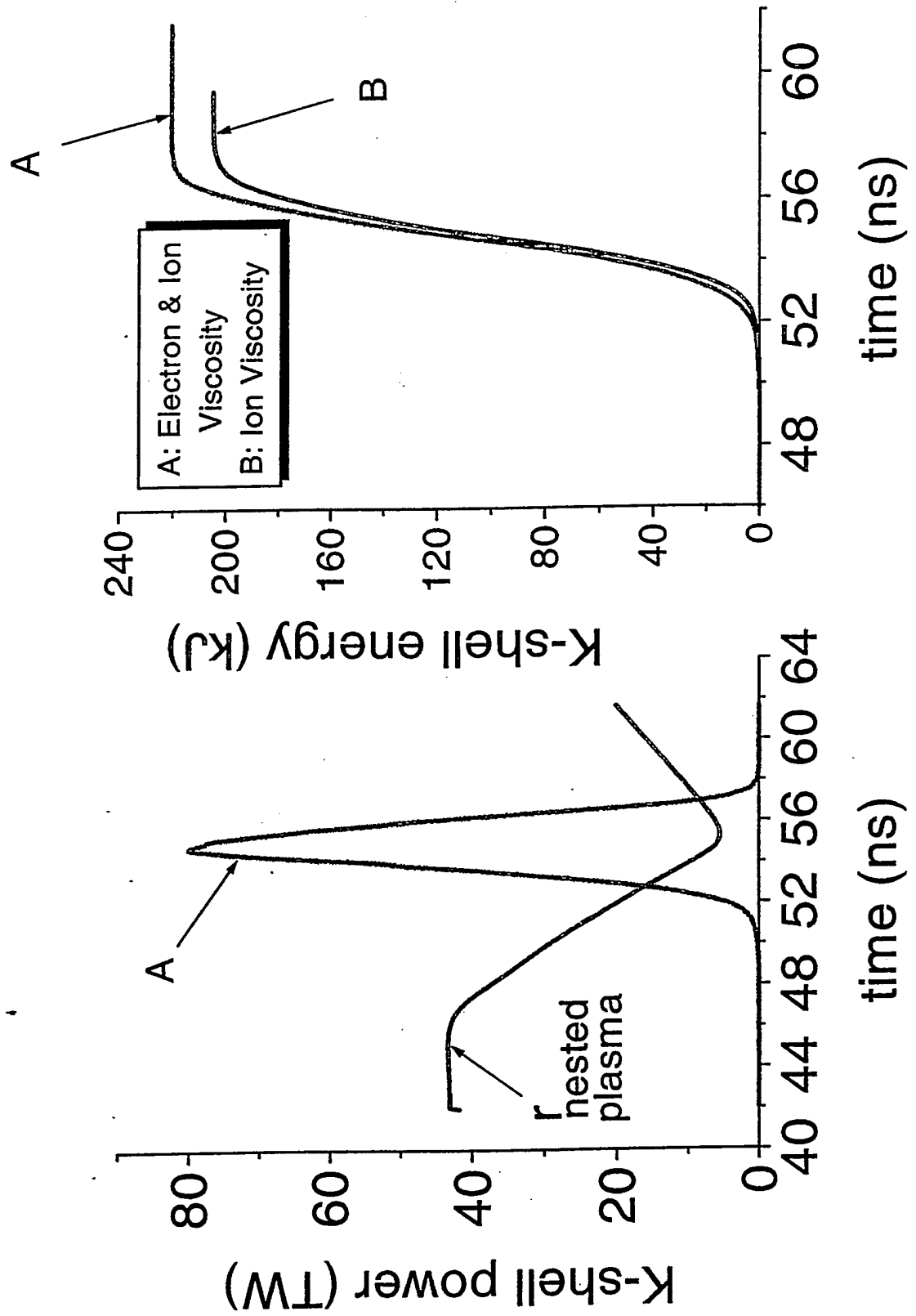
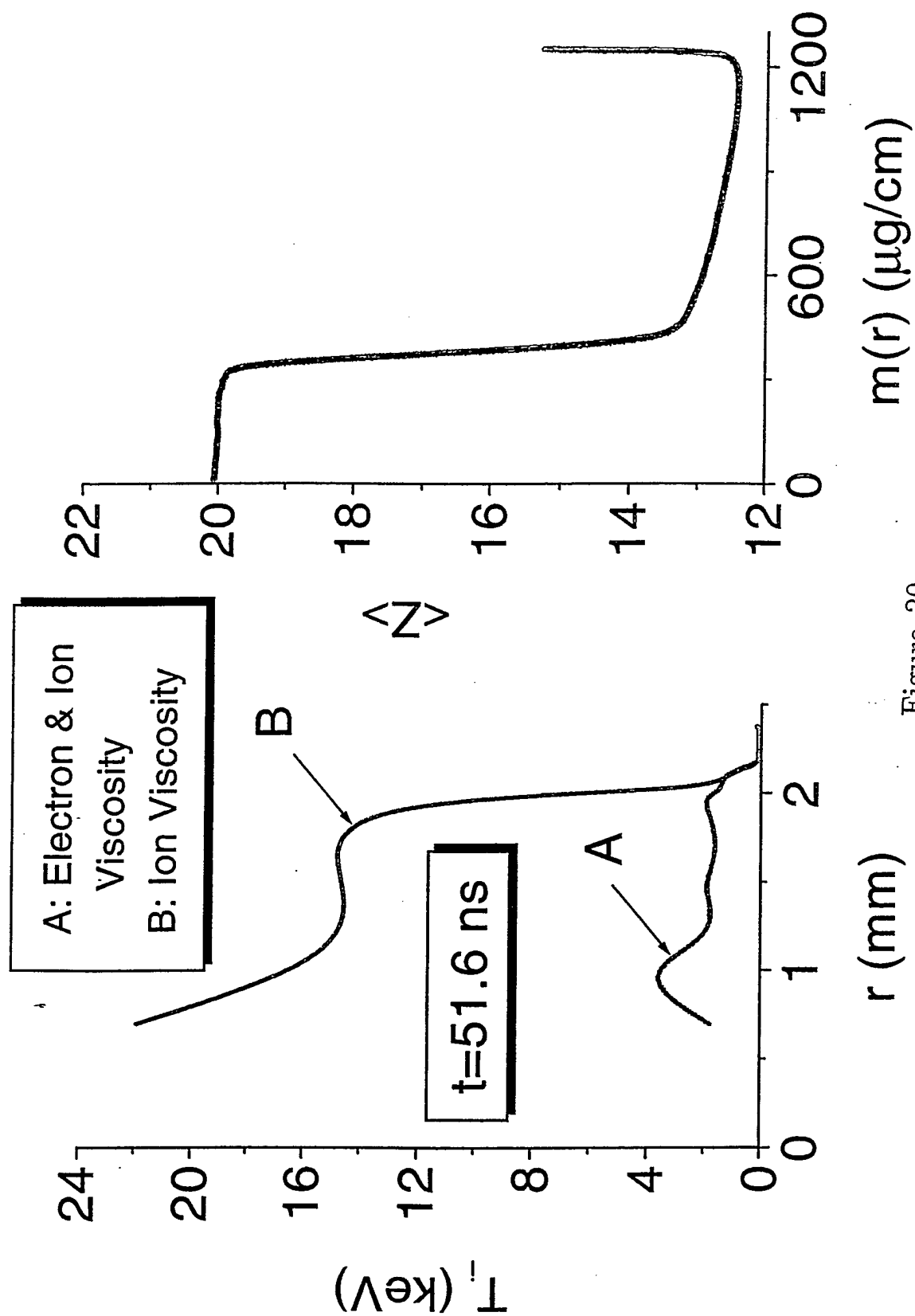


Figure 19

# Case 3 $\text{Ti}$ (1.25 mg/cm, nested)



# Case 1 (Ti 80 cells) (16 nested cells)

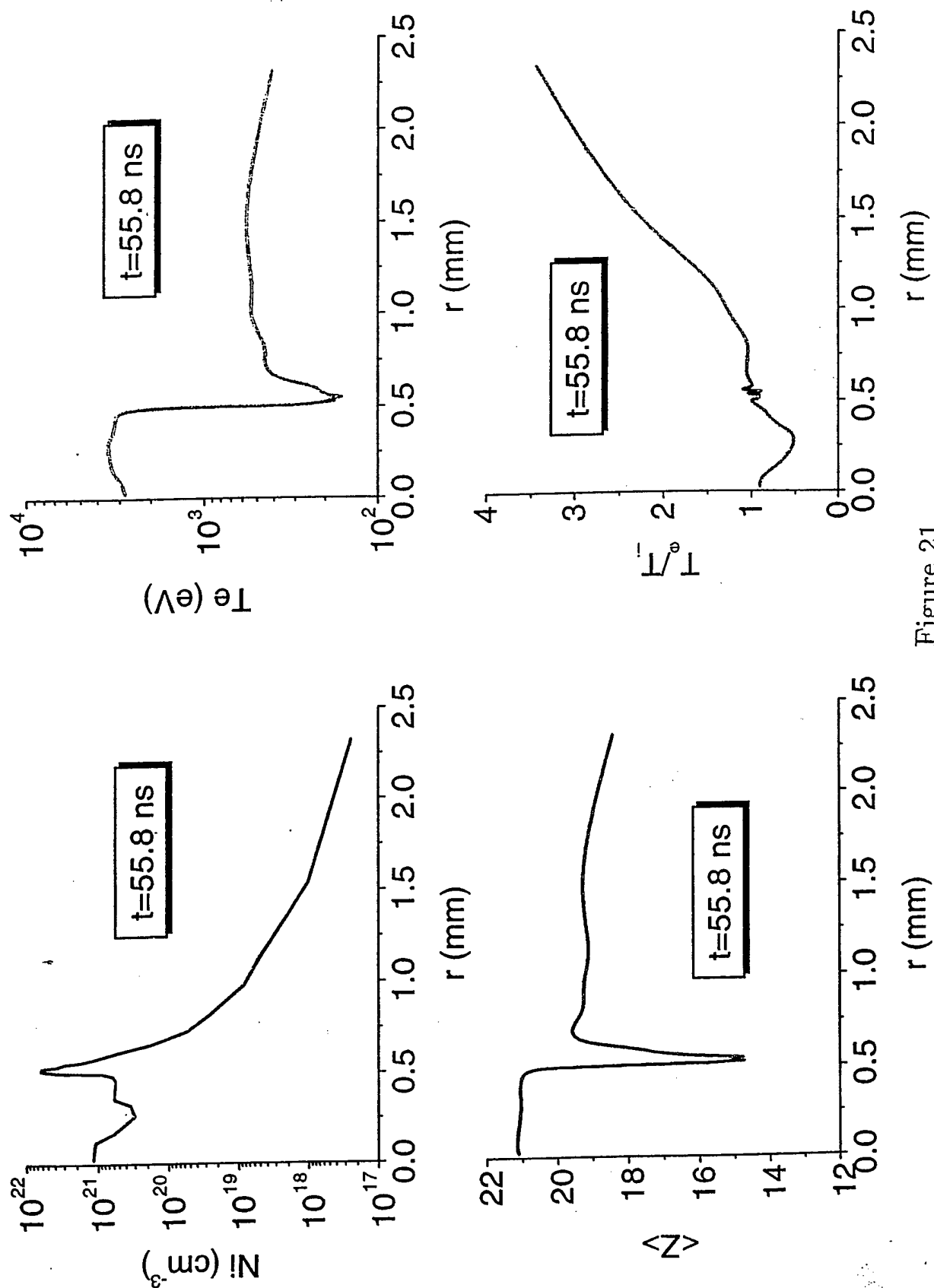


Figure 21

# Case 2 (Ti 100 cells) (17 nested cells)

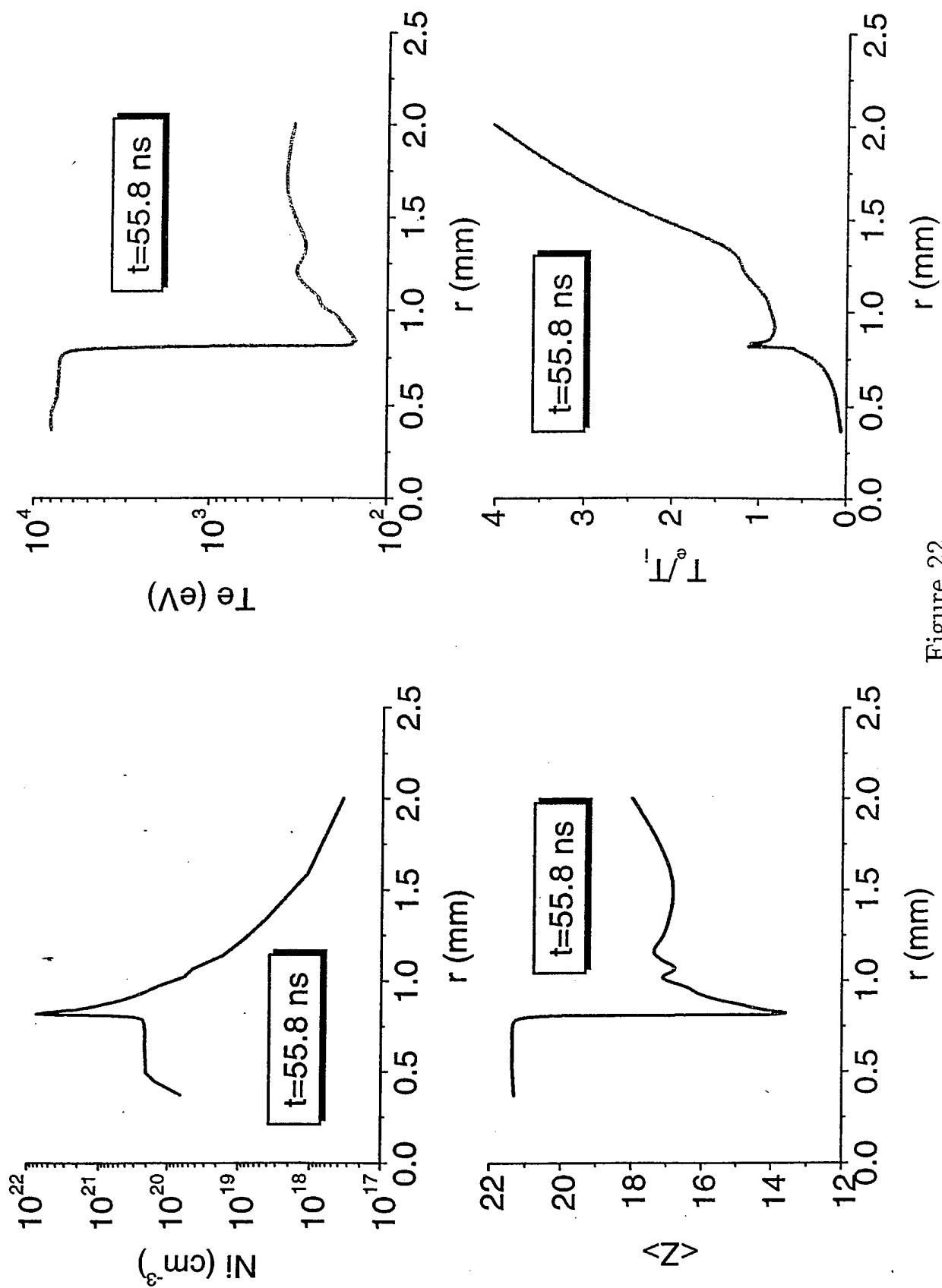


Figure 22

# Case 4 $\text{Ti}$ (1.25 mg, nested)

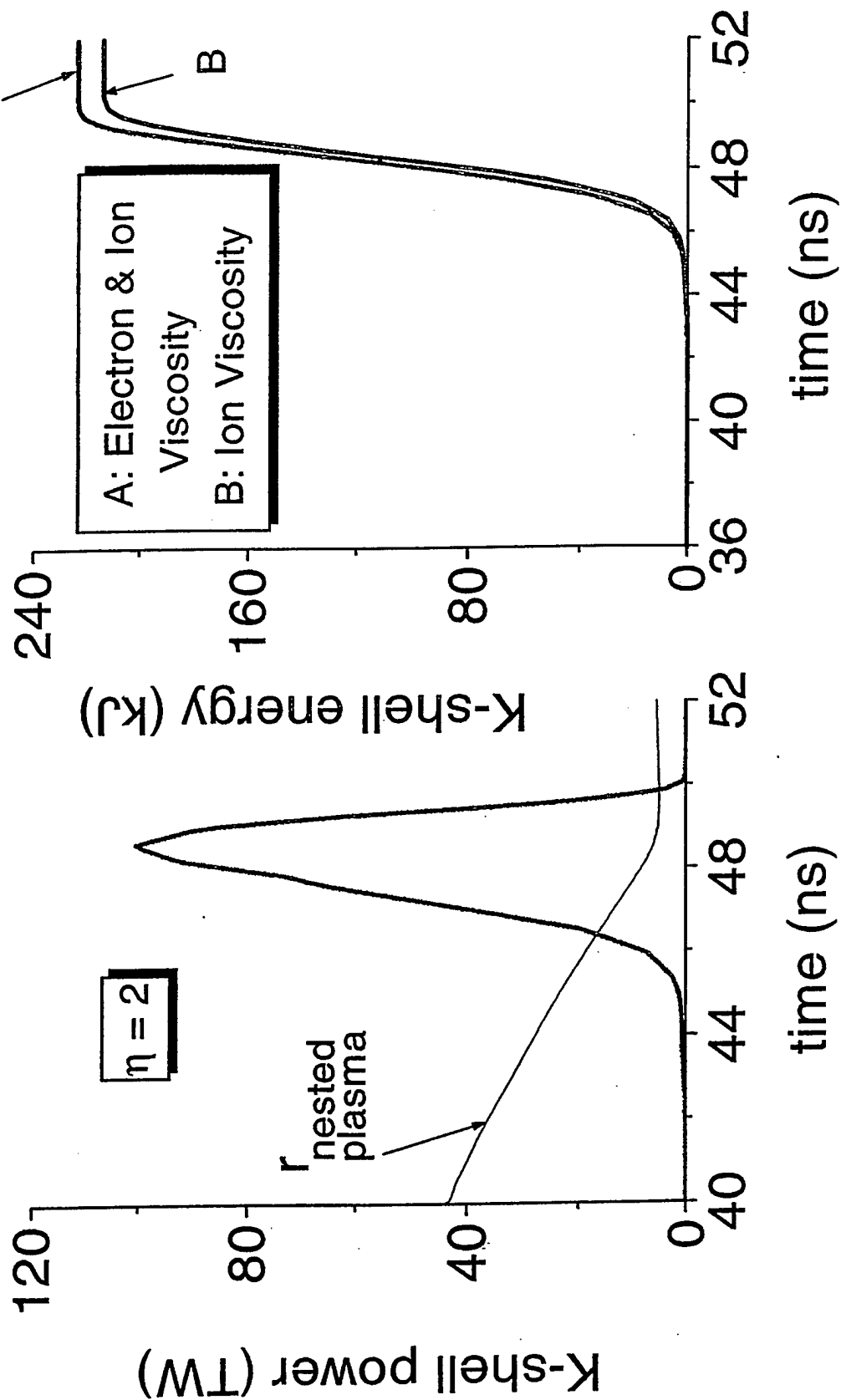


Figure 25



# Case 5 $\text{Ti}$ (1.25 mg, nested)

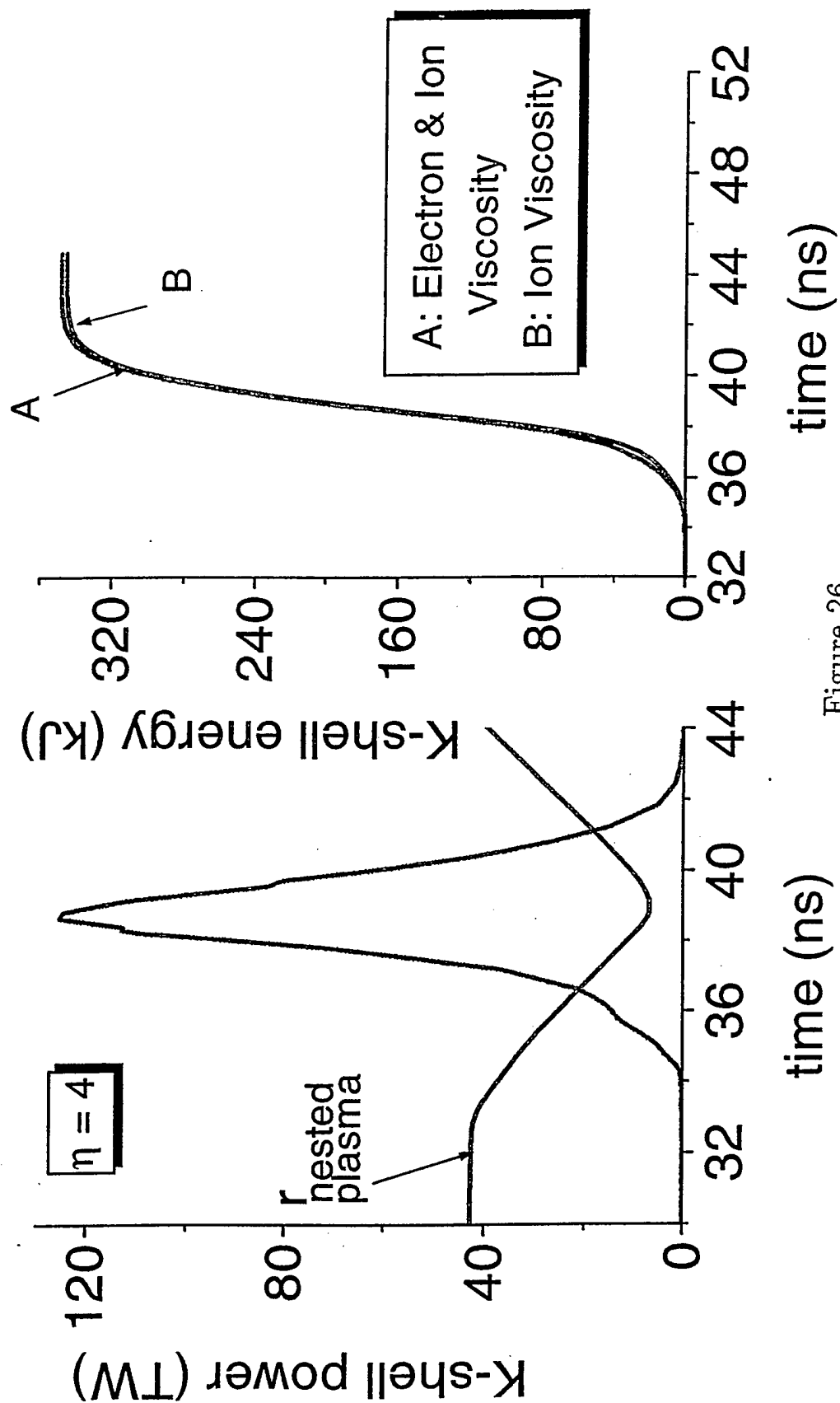


Figure 26

# Case 5 $\text{Ti}$ (1.25 mg/cm, nested)

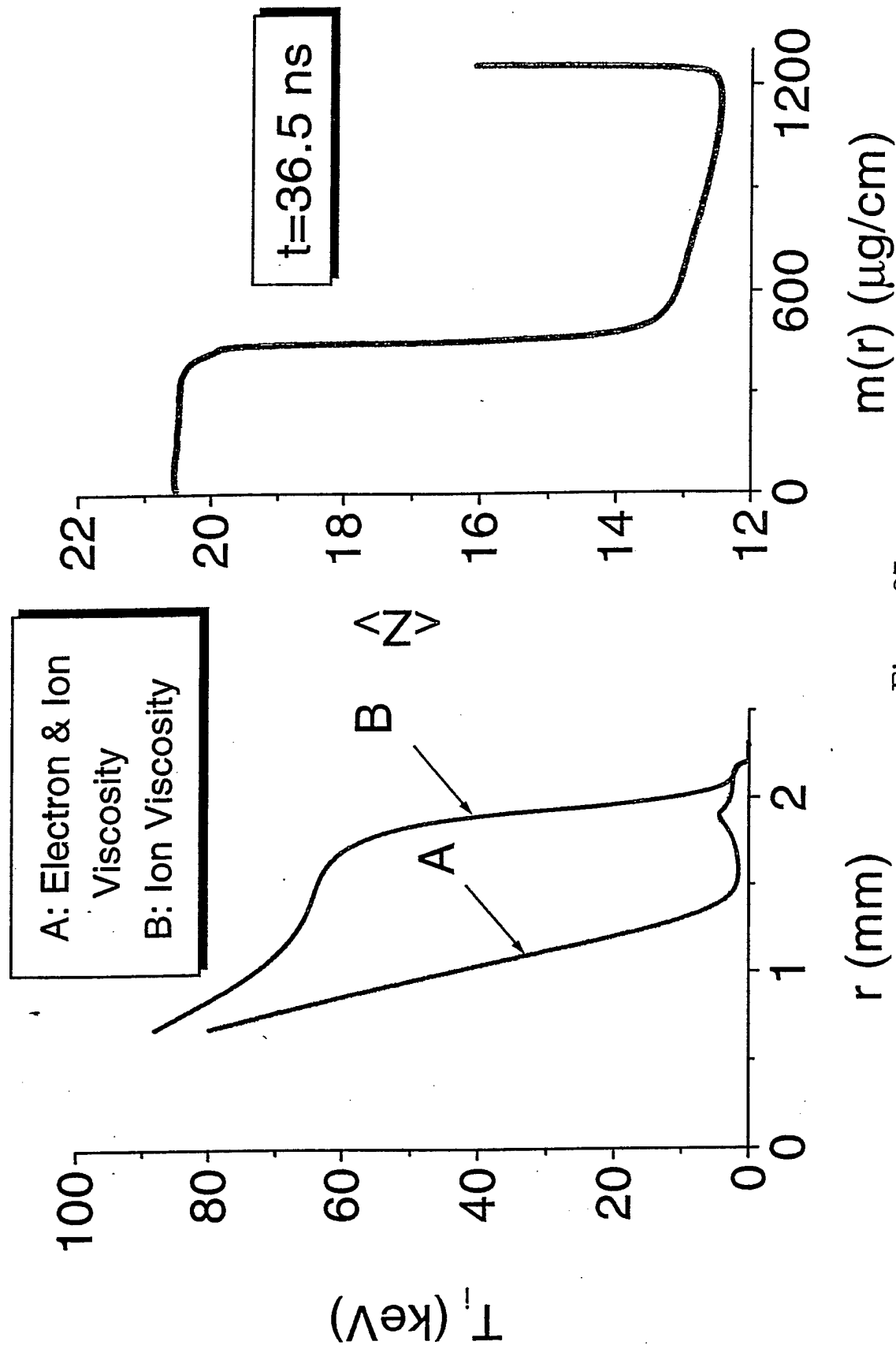


Figure 27

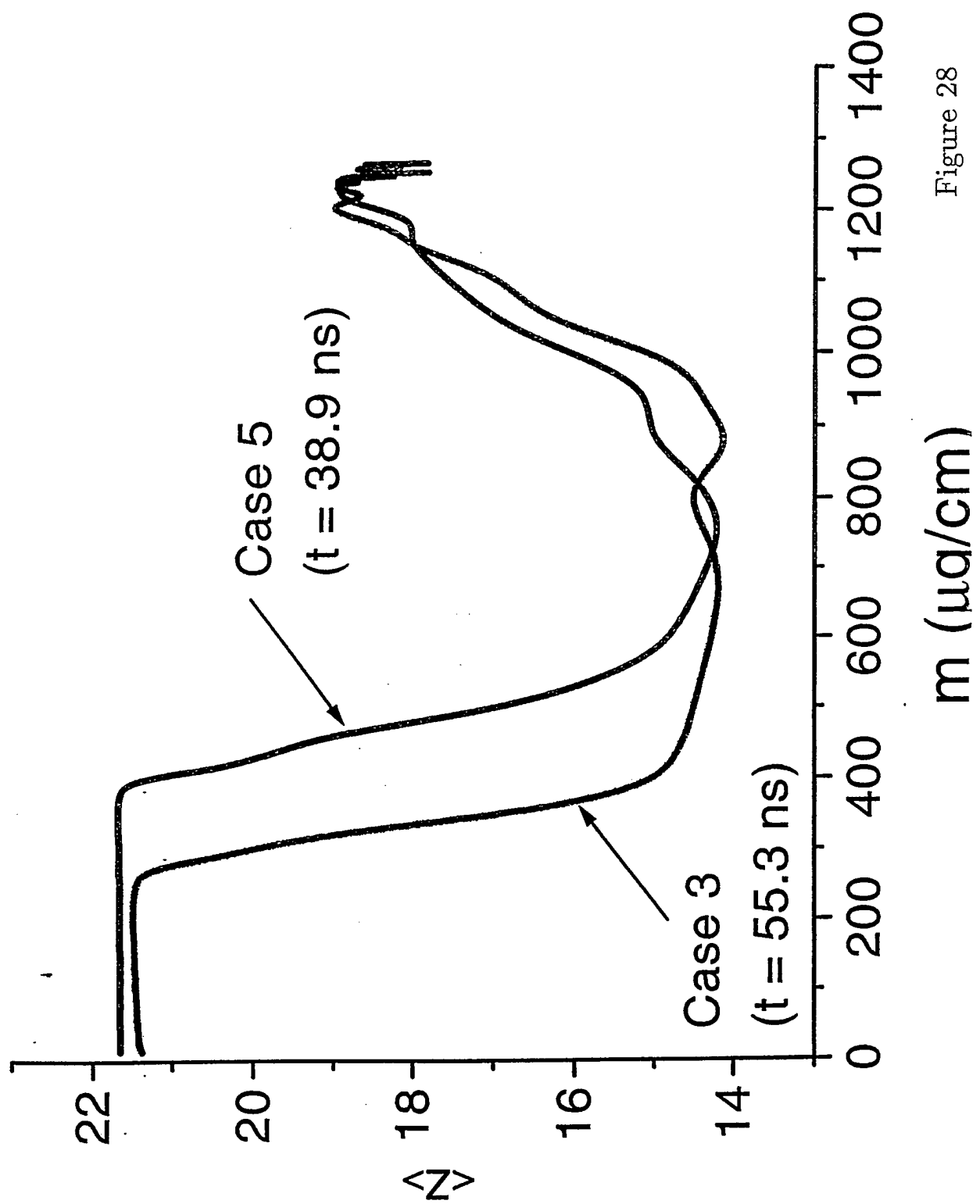


Figure 28

# Ionization Front Propagation

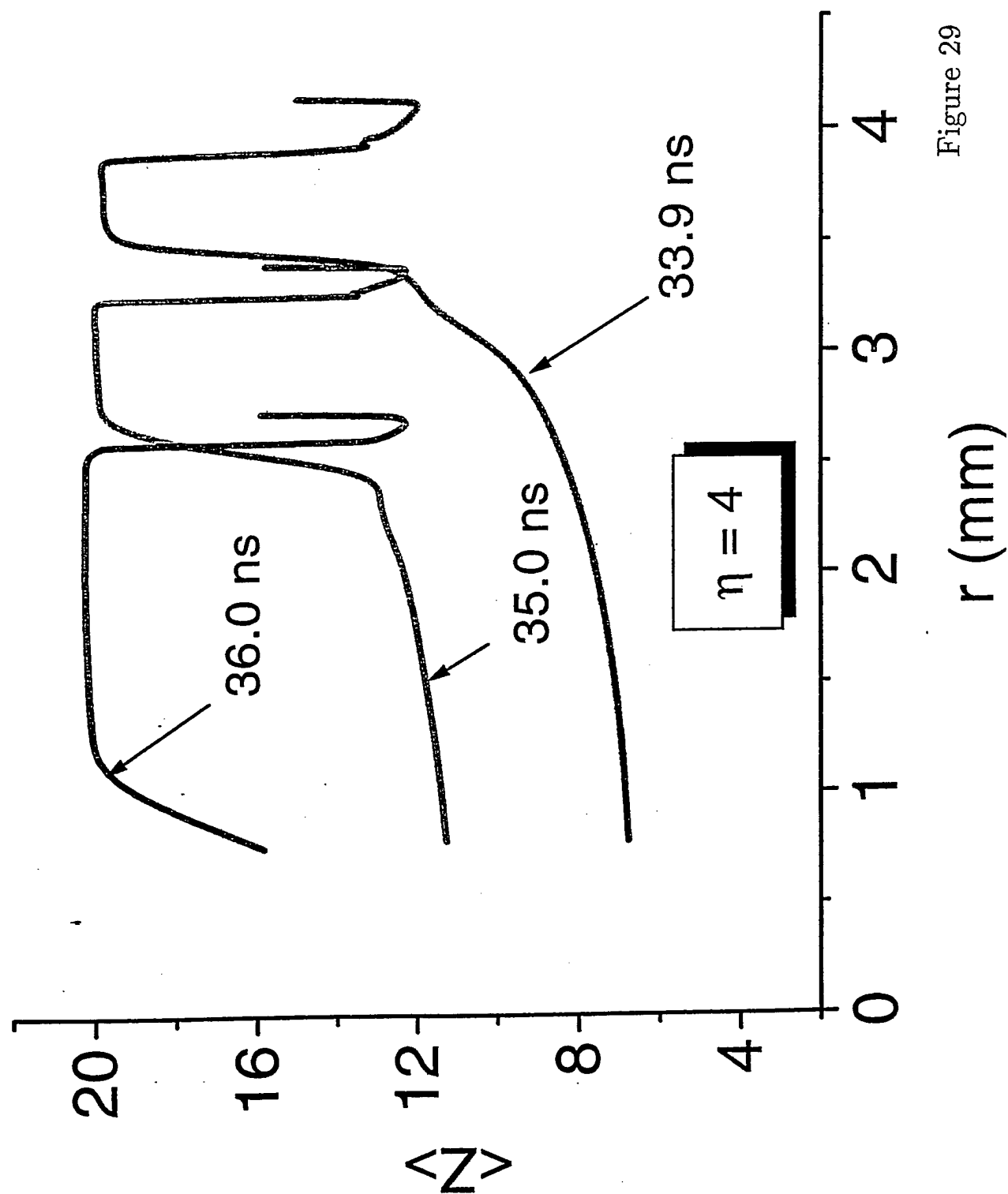


Figure 29

# Case 6: $\text{Ti}$ (1.25 mg, nested)

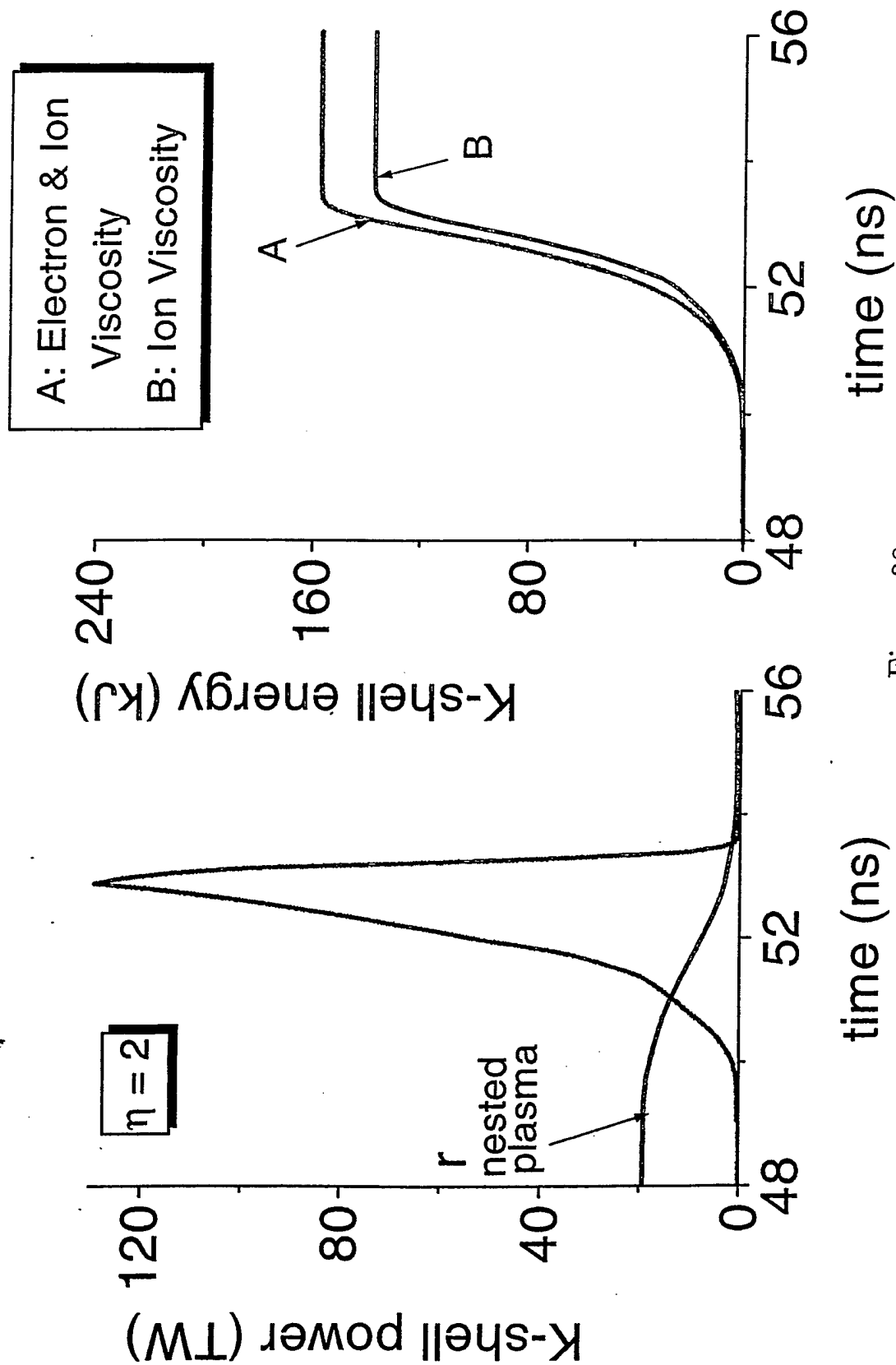


Figure 30

# Case 7: $\text{Ti}$ (1.25 mg, nested)

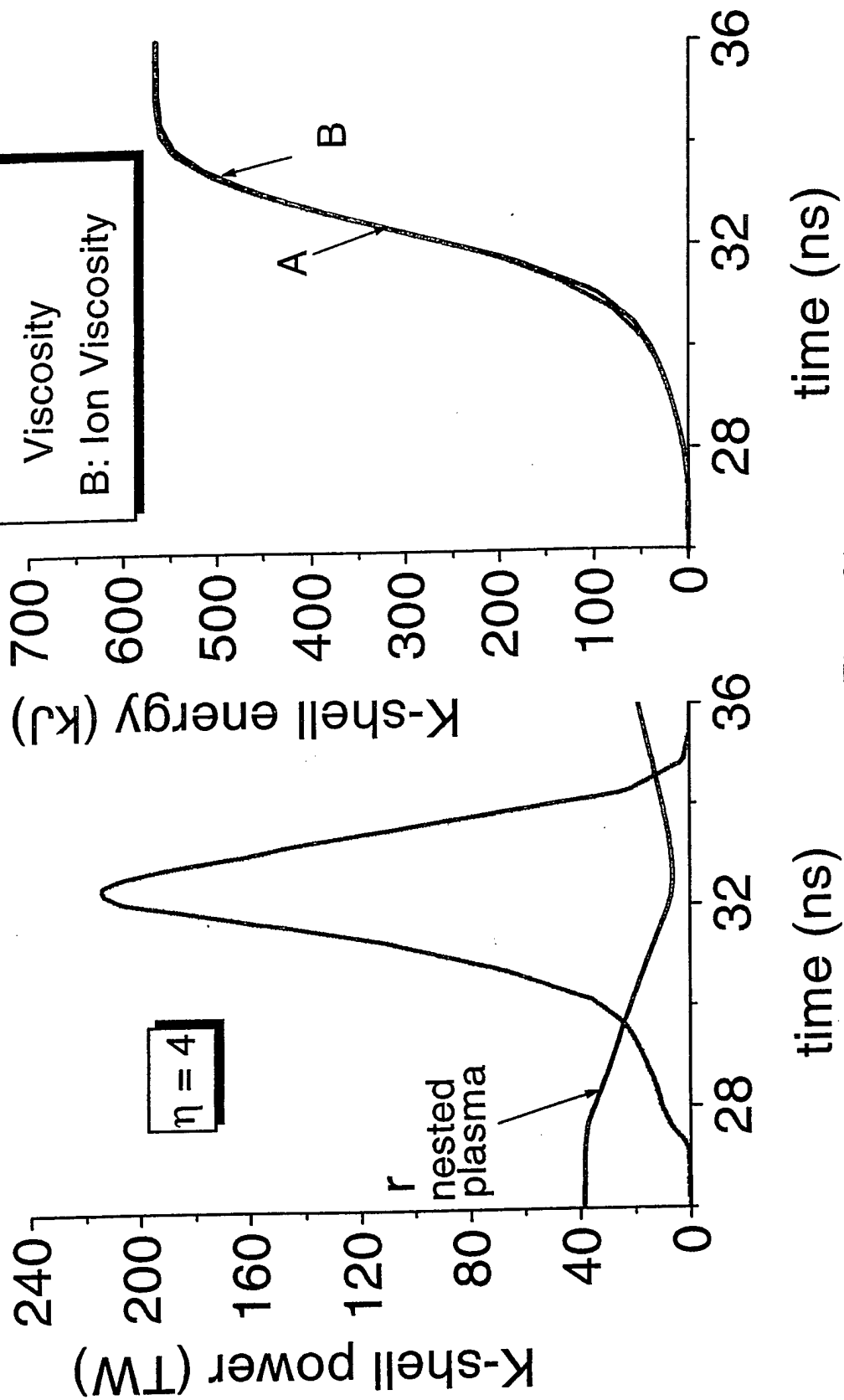


Figure 31

# Case 7 $\text{Ti}$ (1.25 mg/cm, nested)

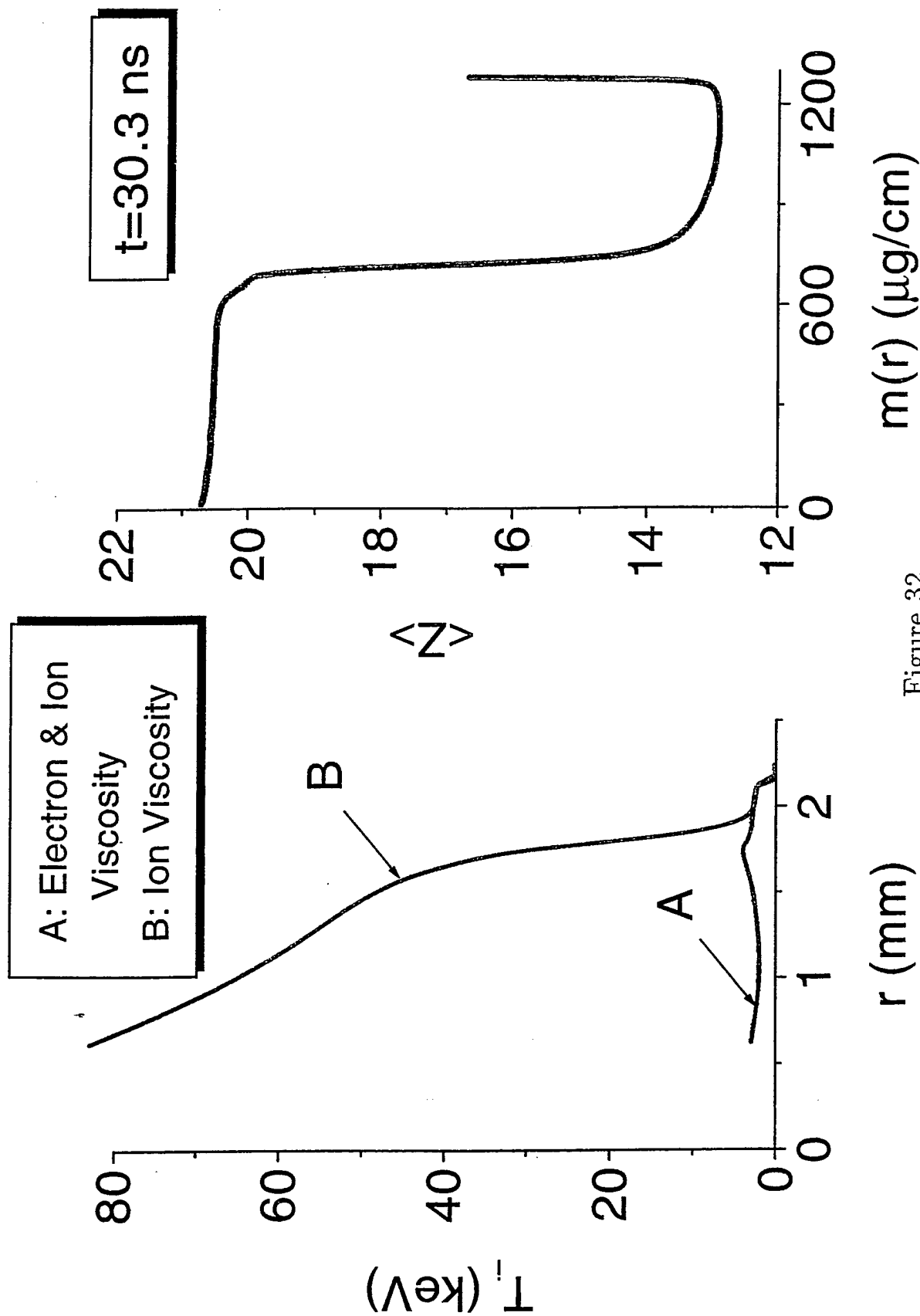


Figure 32

Ti (1.87 mg/cm, nested)

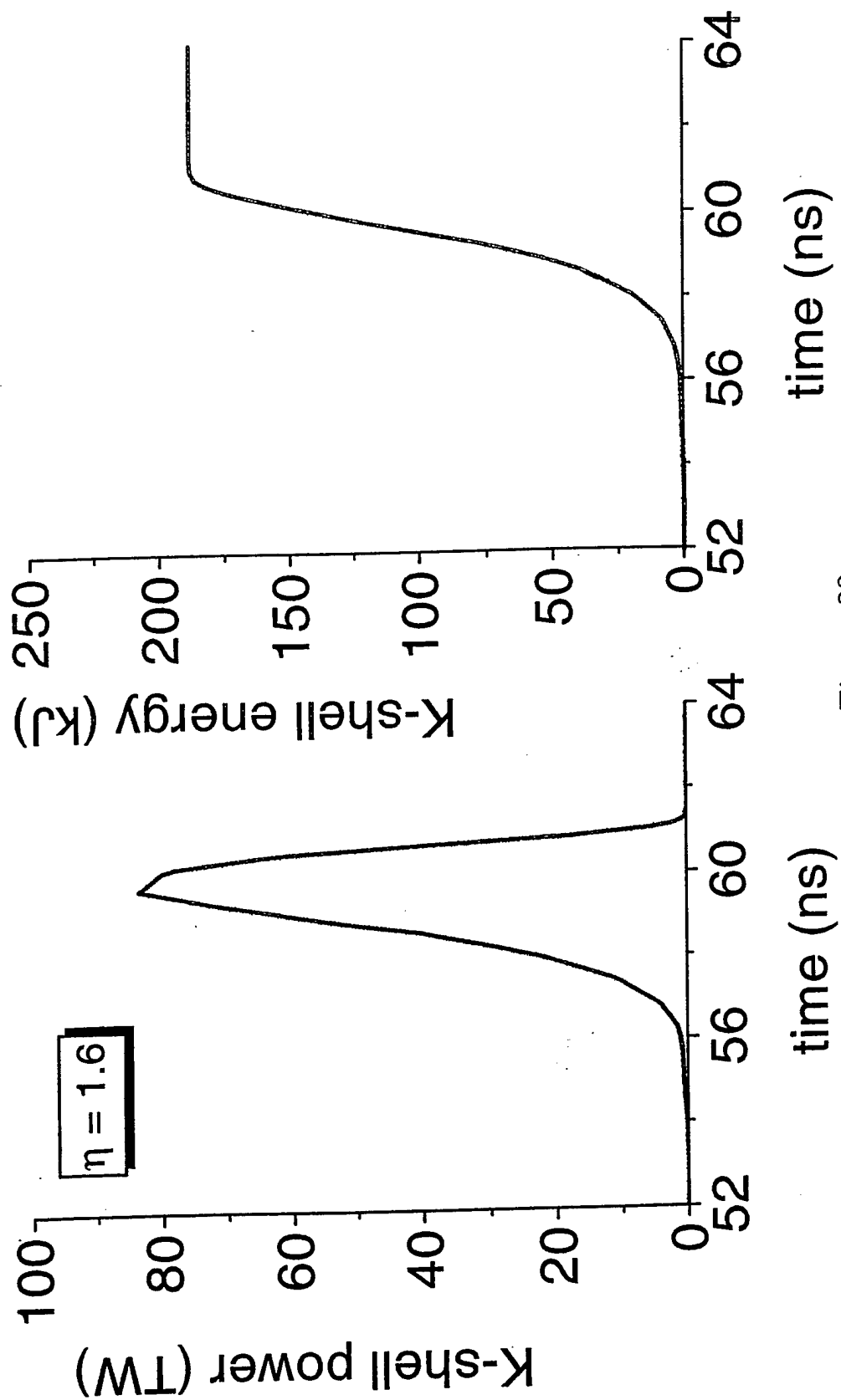


Figure 33



# Ti (1.6 mg/cm, nested)

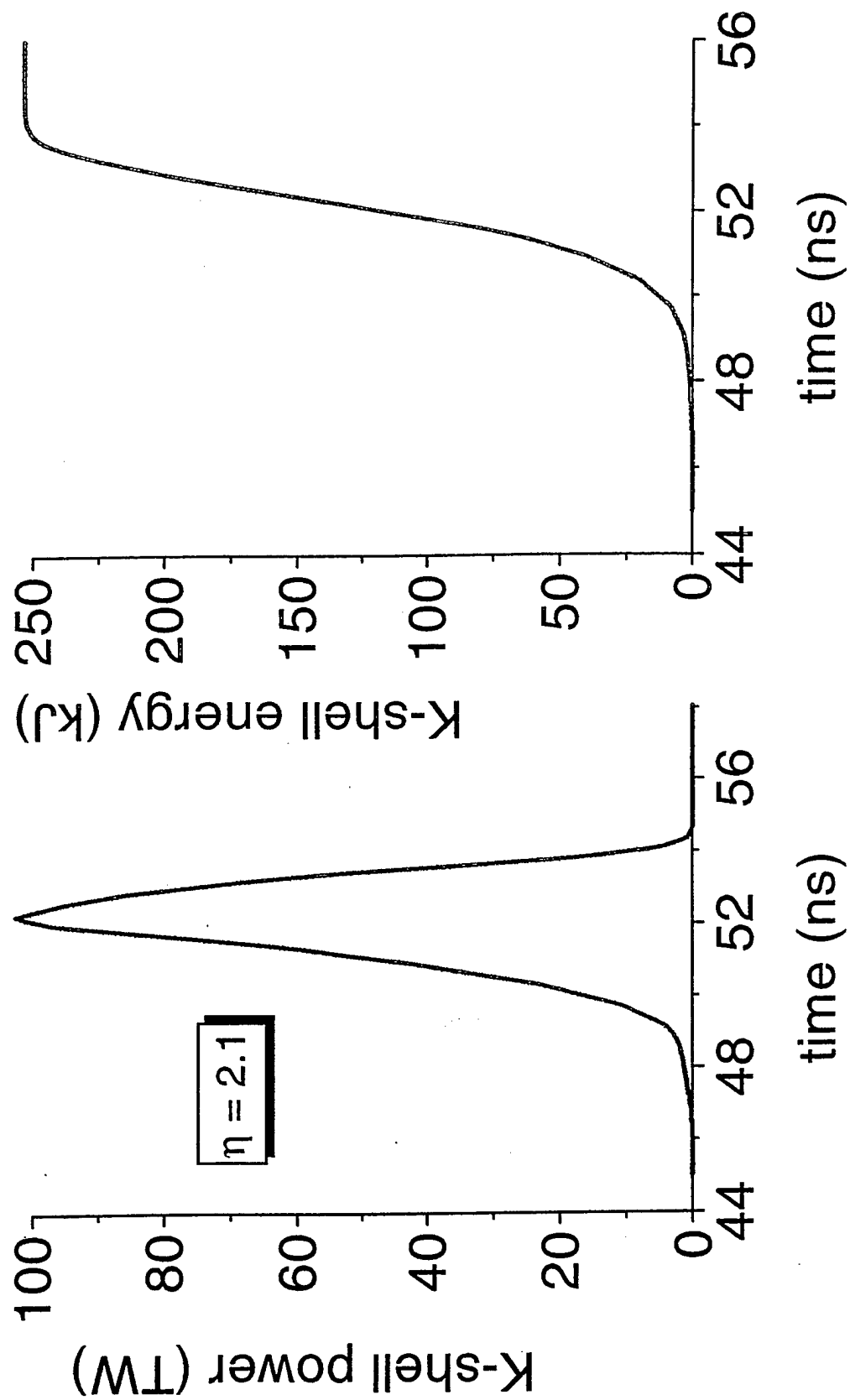


Figure 34

Ti (1.29 mg/cm, nested)

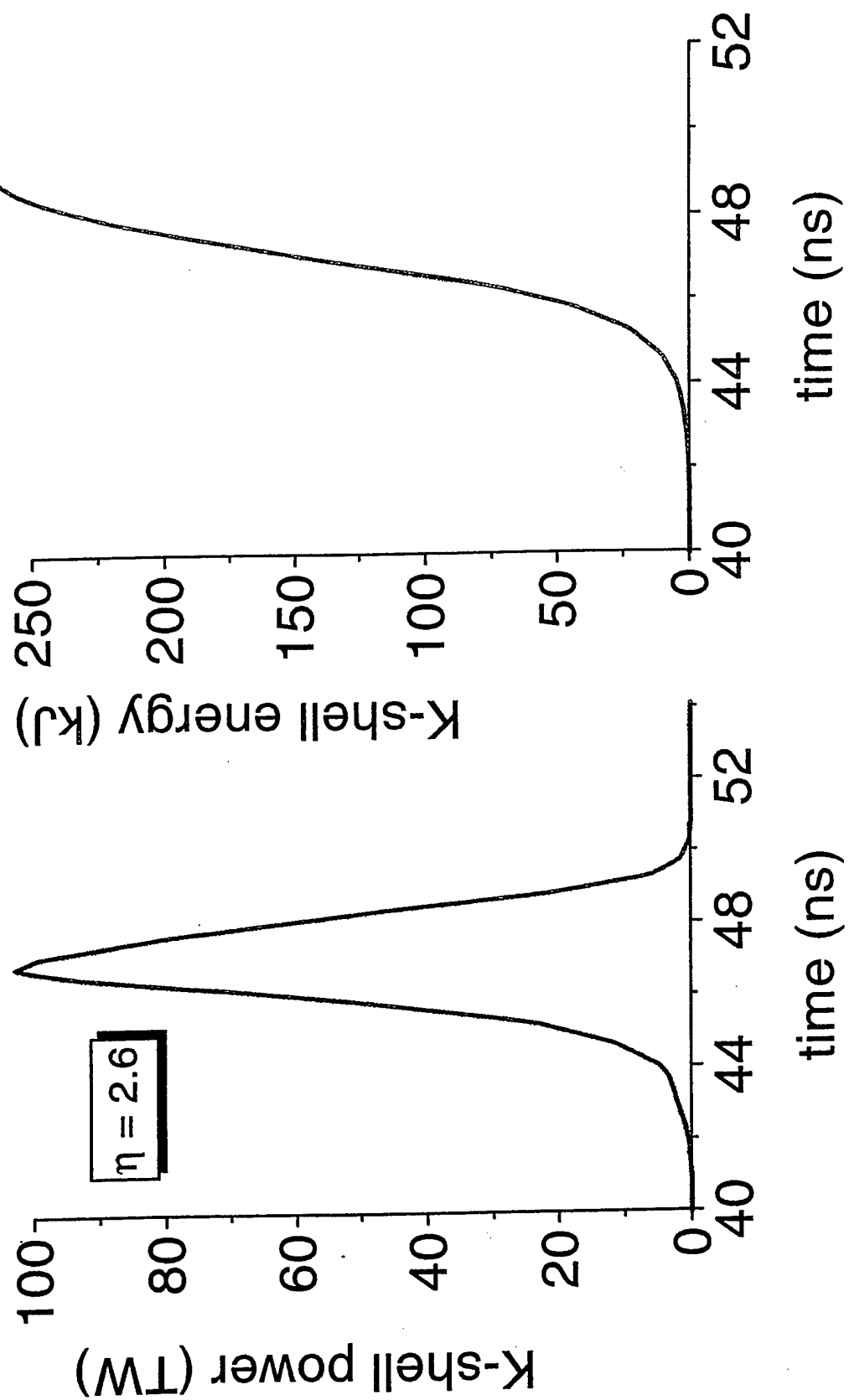


Figure 35

# Ti (1.07 mg/cm, nested)

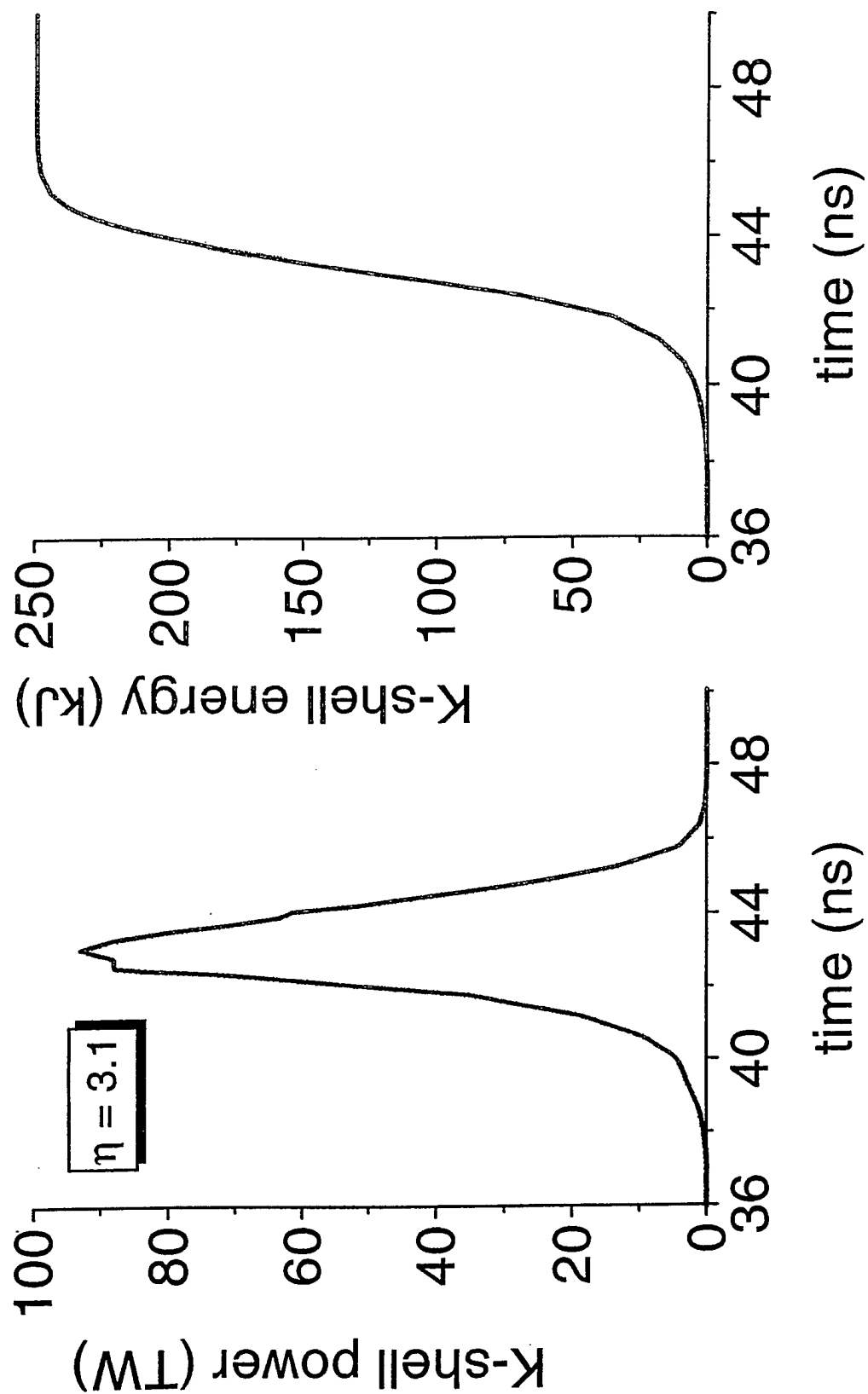


Figure 36

Ti (0.75 mg/cm, nested)

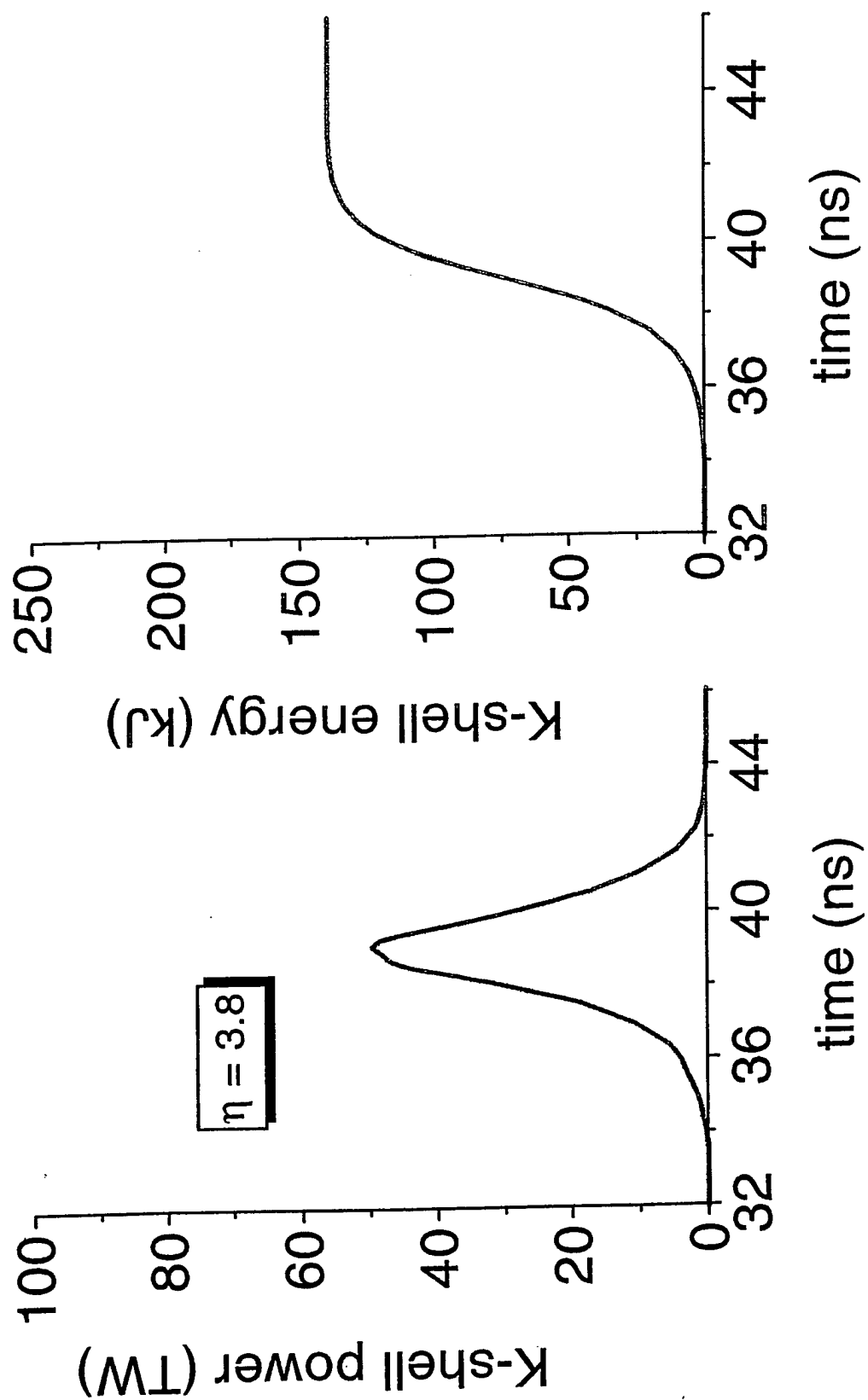


Figure 37

Ti: 1.87 mg/cm

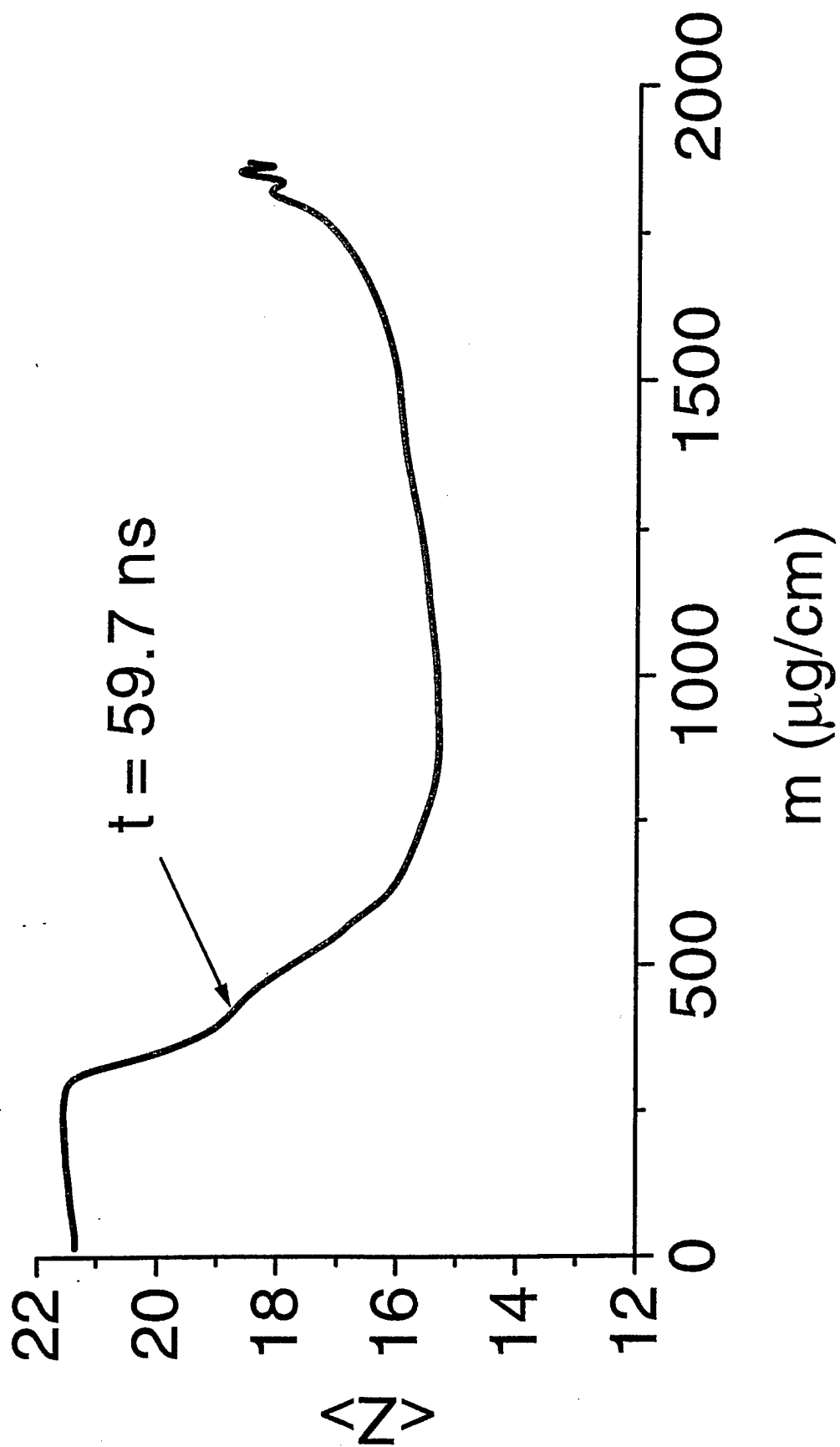


Figure 38

Ti: 1.6 mg/cm

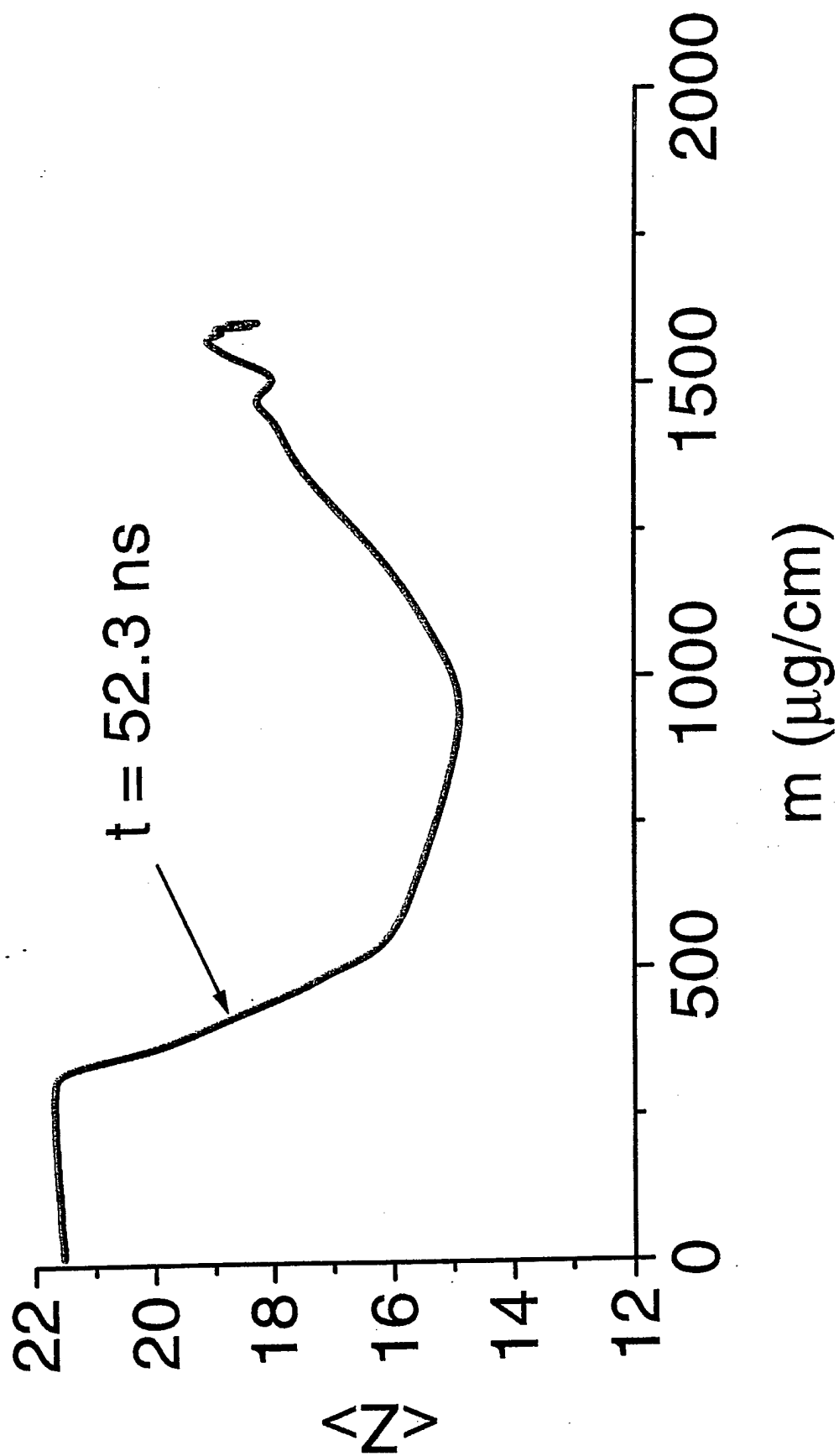


Figure 39

Ti: 1.29 mg/cm

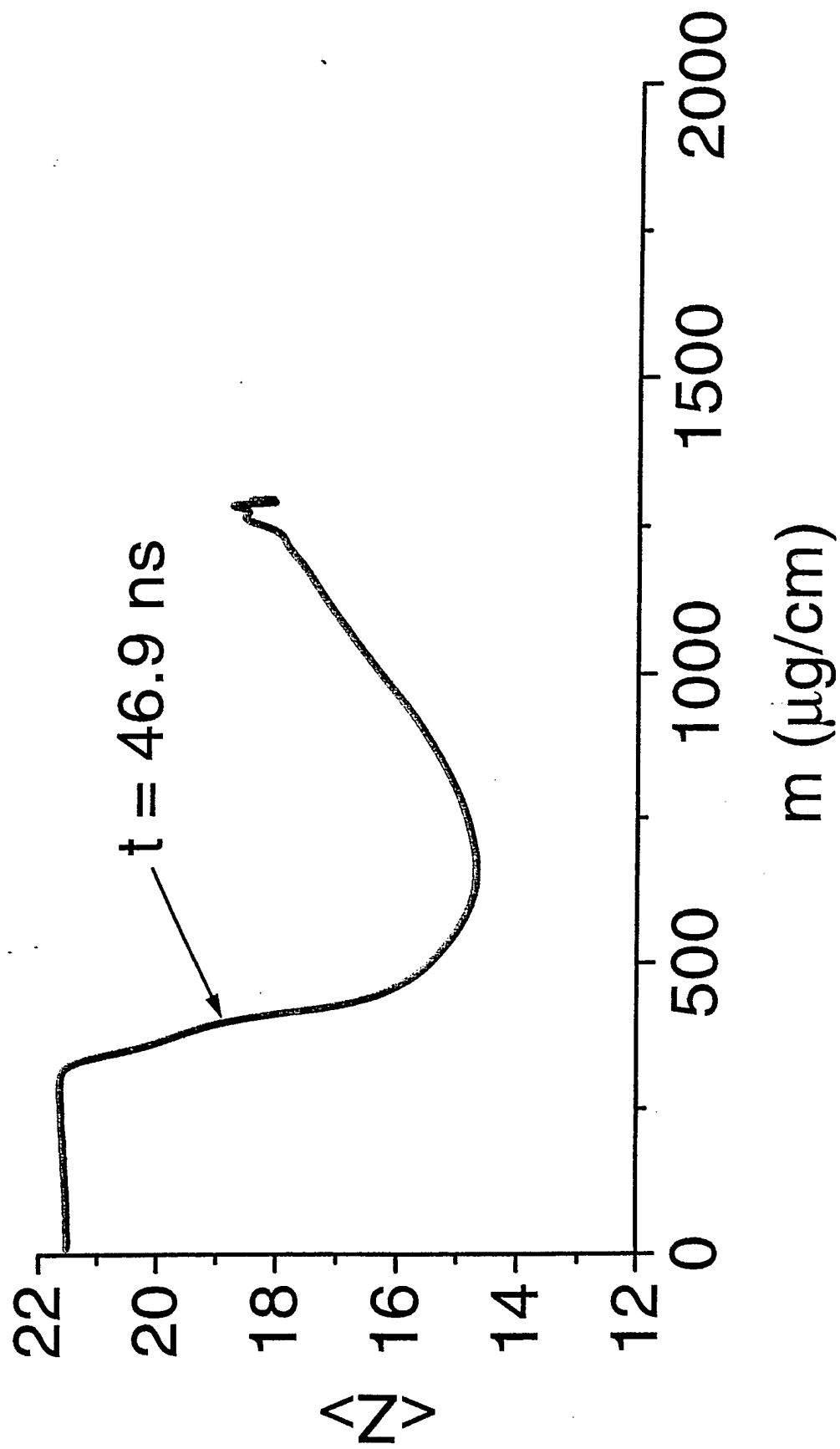


Figure 40

Ti: 1.07 mg/cm

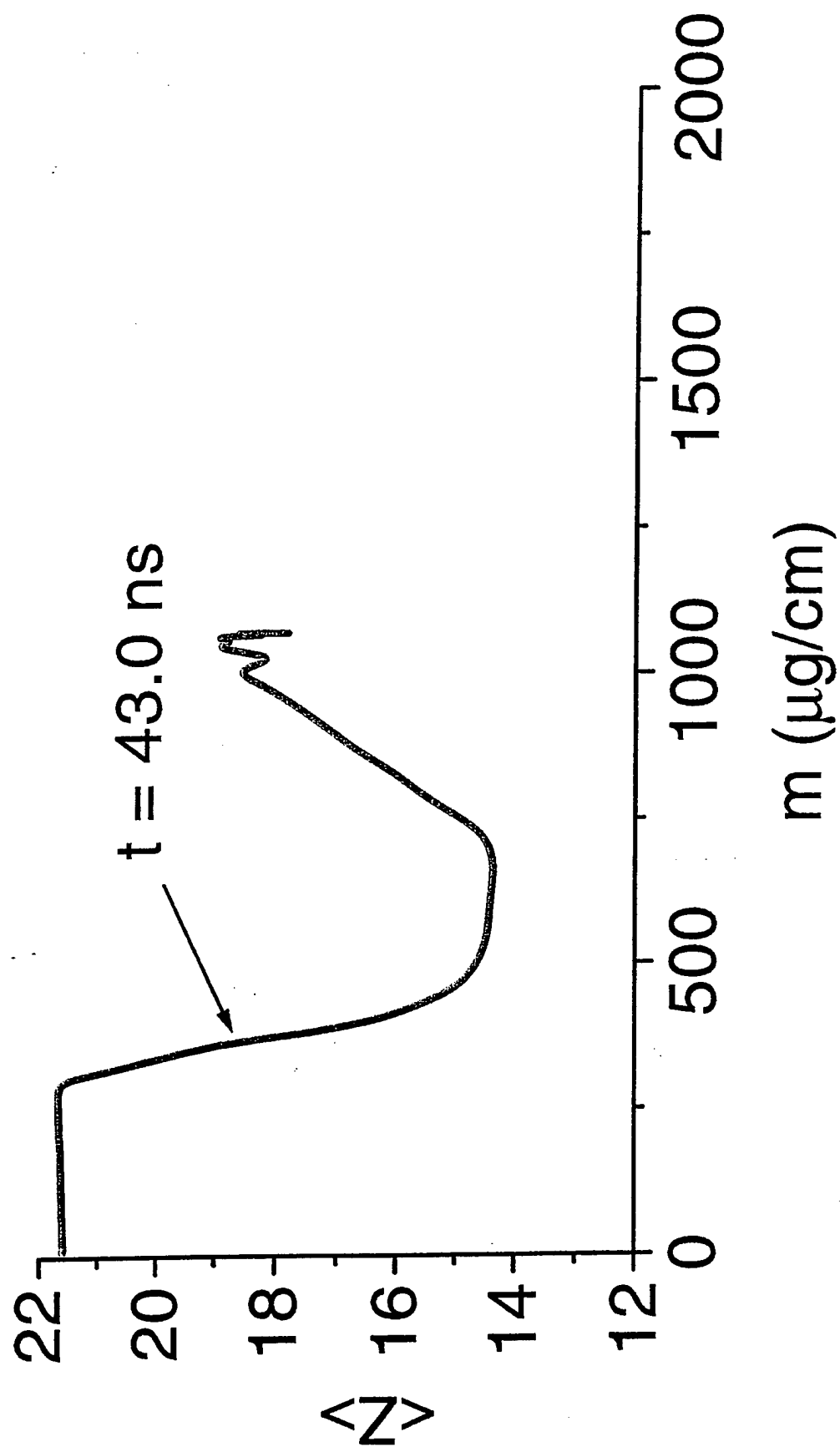


Figure 41



Ti: 0.75 mg/cm

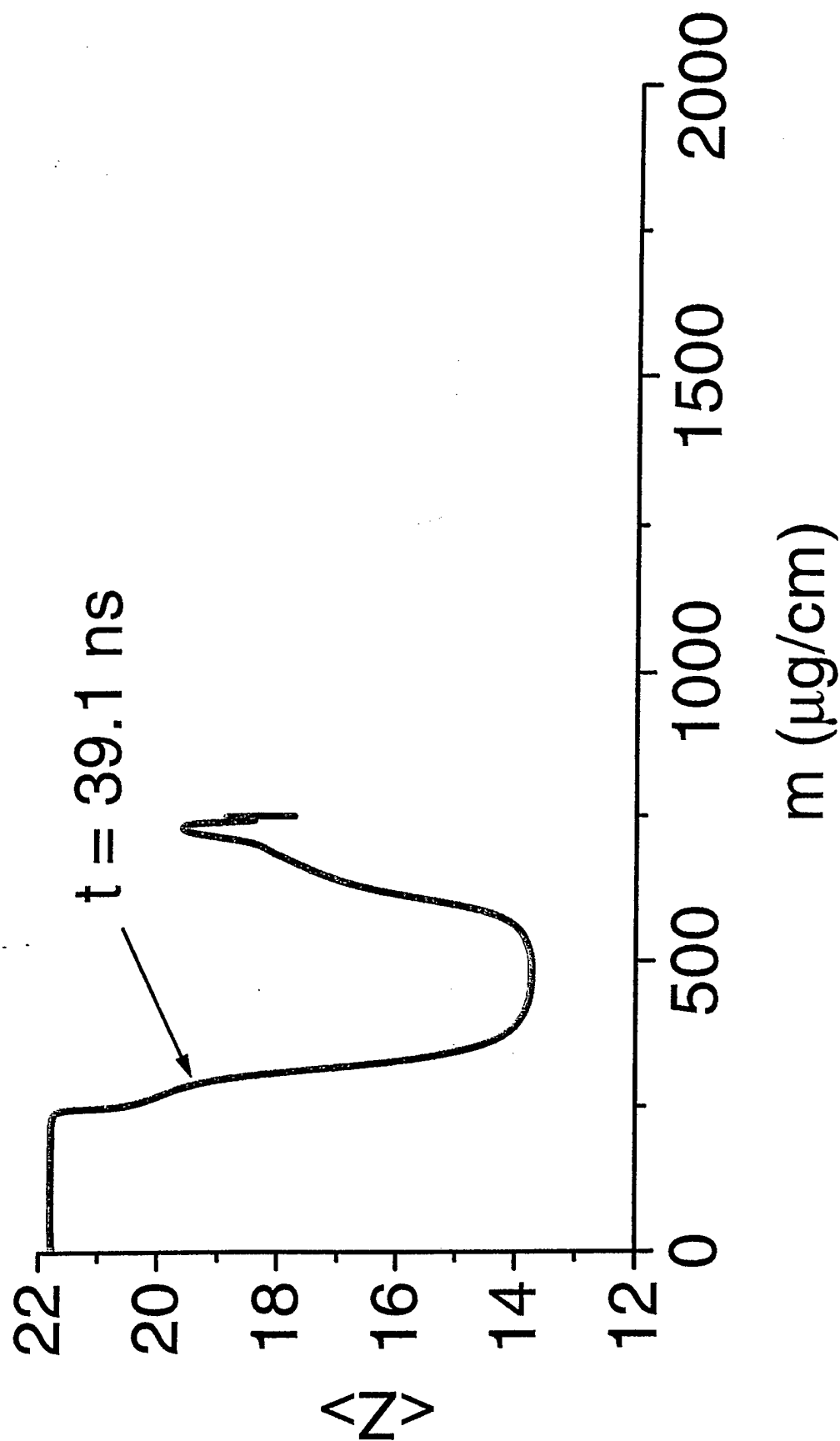


Figure 42

Ti:  $\eta=1.6$

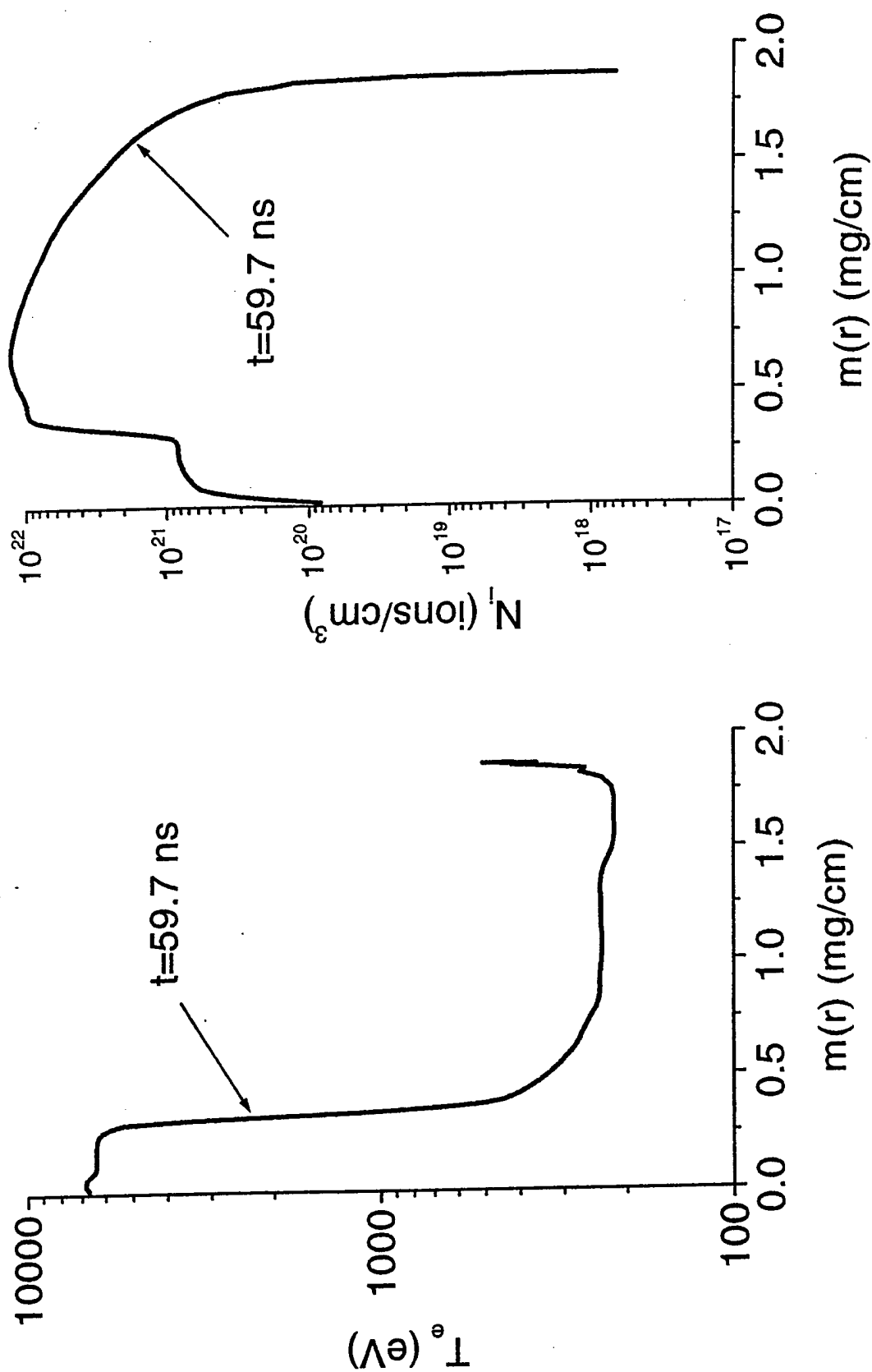


Figure 43

Ti:  $\eta=2.1$

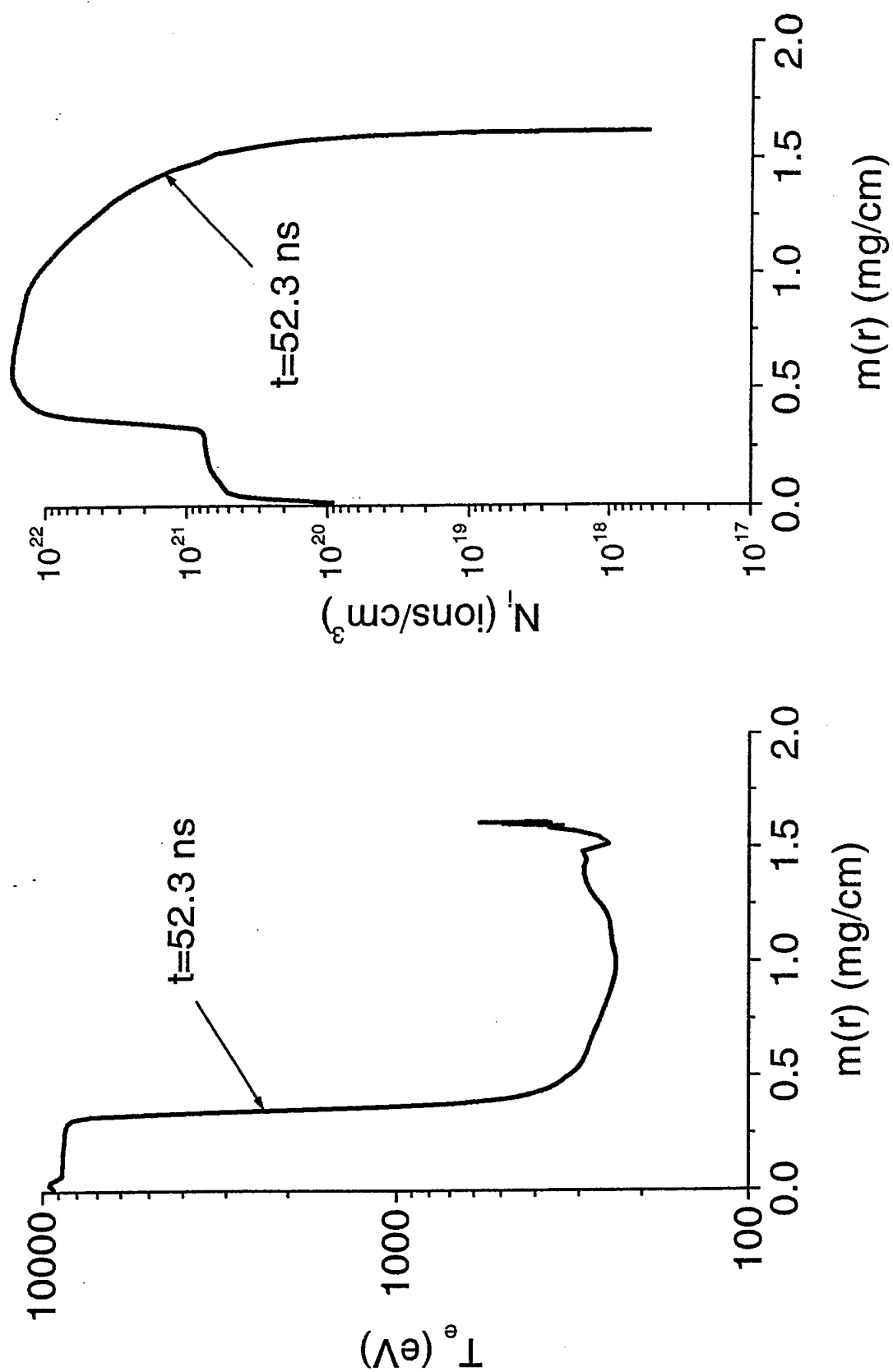


Figure 44

Ti:  $\eta=2.6$

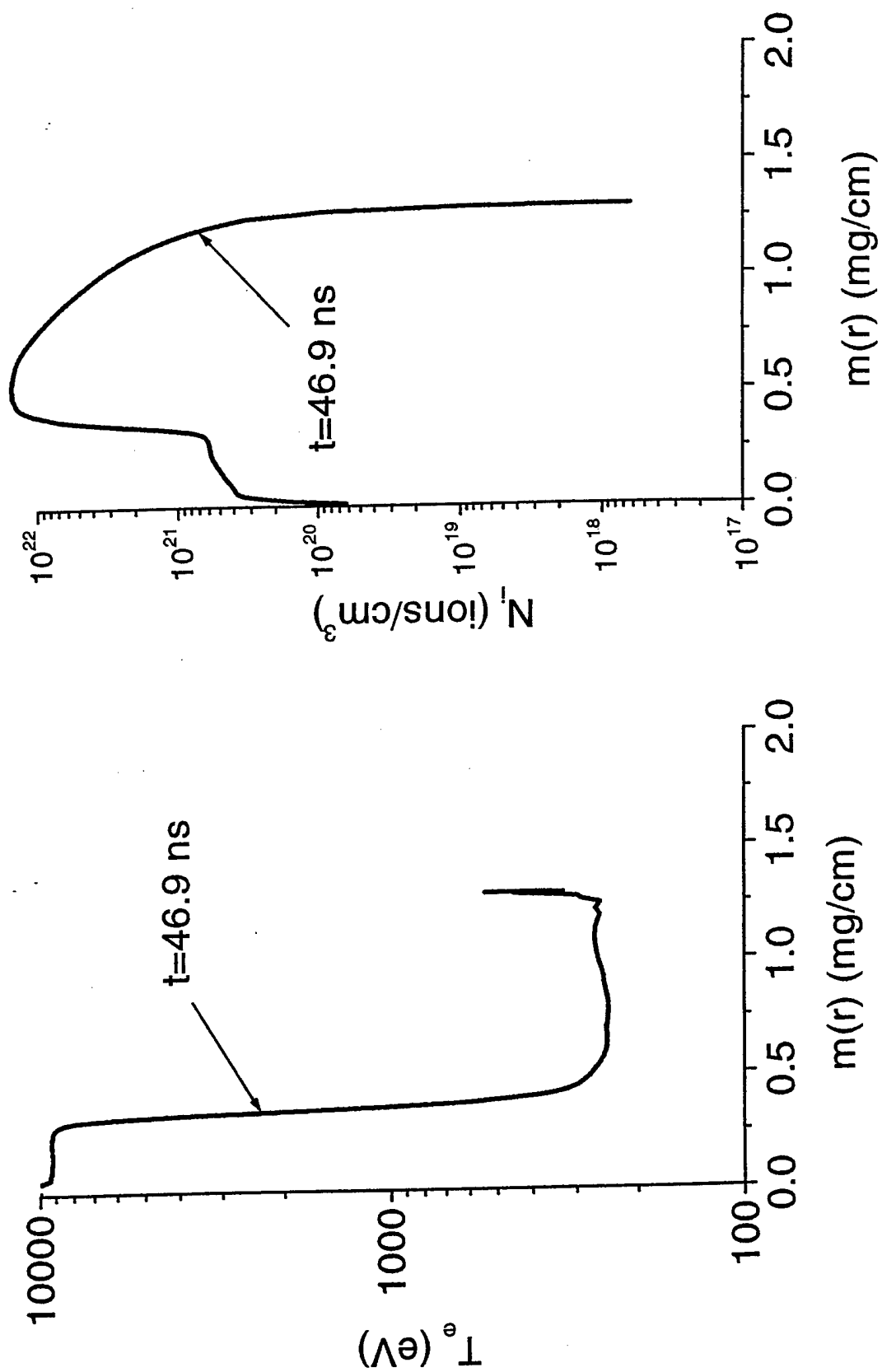


Figure 45

## Ti: $\eta=3.1$

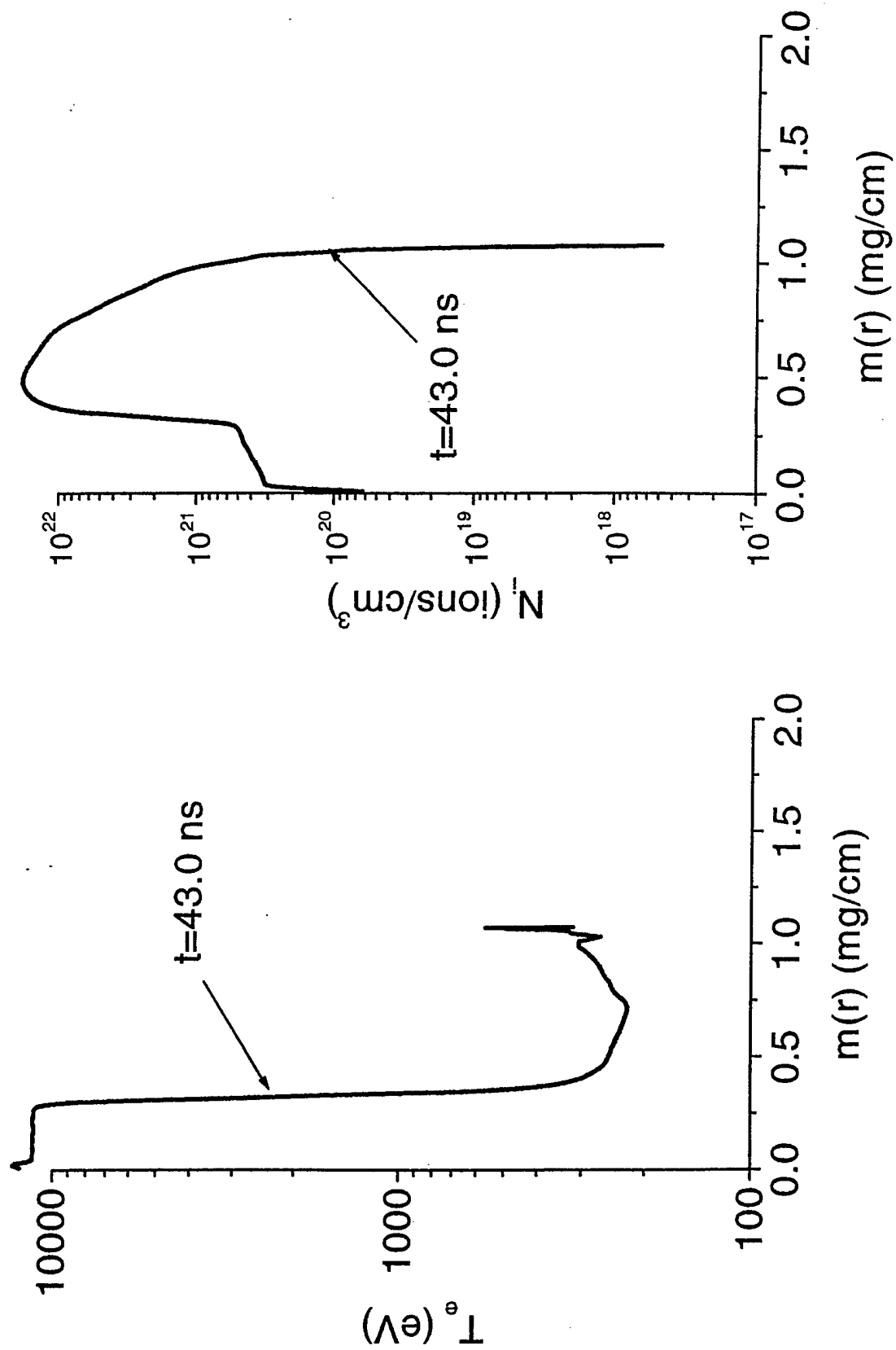


Figure 46

Ti:  $\eta=3.8$

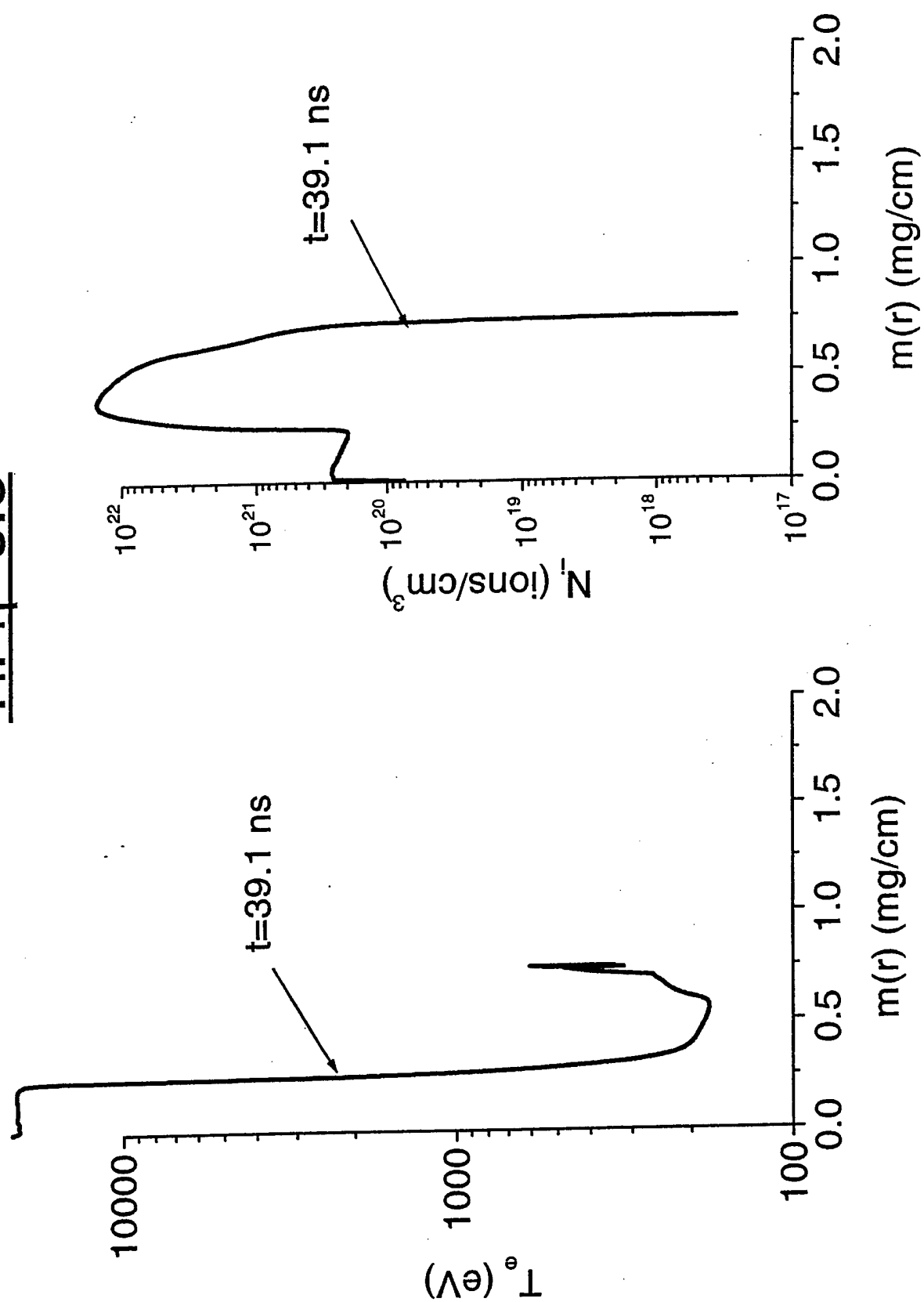


Figure 47

## VI. A role for electron viscosity in plasma shock heating

### I. Introduction

Shock heating of collisional plasmas is primarily due to viscosity that dissipates kinetic energy of the incident flow directly into heat in a so-called viscous sub-shock.<sup>1,2</sup> The length scale characteristic of the viscous sub-shock is of the order of the downstream ion mean free path,  $l_{ii}$ , which is typically much less than (the relevant) hydrodynamic scales of the surrounding flow. For this reason, the actual plasma viscosity is seldom, if ever, used in hydro simulations of high-density dynamic plasmas. Rather, various forms of an artificial viscosity are commonly used in Lagrangian codes in lieu of real viscosity. Conventional justification for this procedure is that viscosity is supposed to affect only the shock structure and its thickness, whereas the Hugoniot conditions that determine the shock compression and the shocked plasma's energy balance for a given shock intensity are known to be independent of the transport coefficients.<sup>1-3</sup> In hydro modeling, we are generally interested in large-scale phenomena; calculations are not intended to resolve structure on ion mean-free-path length scales (nor they are generally capable of resolving such structures). An artificial increase in the shock thickness seems to be a fair price to pay for reducing the computational effort and ensuring numerical stability by decreasing the number of computational grid points. This particularly holds true if the plasma states separated by the narrow shock front are accurately modeled when the true plasma viscosity is replaced in the simulation with some positive-definite artificial expression.

The consistency of this general approach, however, comes into question in some situations when shock waves in plasmas are modeled. A shock structure in a non-

magnetized plasma includes a long "tongue" of preheat ahead of the main viscous jump in pressure and velocity, which is due to electron thermal conductivity. The length scale of this "tongue" is of the order of  $(m_i / m_e)^{1/2} l_{ii} \gg l_{ii}$ , hence it is hydrodynamic rather than kinetic scale length.<sup>2</sup> Since hydro calculations must account for and be able to model some of the processes occurring within the shock width, less arbitrariness in the choice of kinetic coefficients is allowed. In particular, because the electron and ion temperatures of the plasma can be very different in shock-heated plasmas, separate energy balance equations for electrons and ions must be used. Then we have to decide into which of these two components of the plasma should the kinetic energy dissipated by the viscosity (artificial or otherwise) be deposited. Does it all go to the ions? Or should some part of it contribute to the direct heating of electrons?

For decades, it was conventionally assumed that the viscous dissipation heats only the ions, the electron viscosity being of little consequence. Even the classical paper by Braginskii<sup>4</sup>, where ion viscosity coefficients in fully ionized plasmas are given for all values of the ion charge  $Z$ , does not present the electron viscosity coefficients for  $Z > 1$ . Indeed, for  $Z = 1$  the ratio of electron to ion viscosity coefficients for an isothermal plasma,  $T_e = T_i$ , is very small, of order of  $(m_e / m_i)^{1/2}$ . The electron viscosity coefficient for arbitrary  $Z$  calculated in the same approximation as used by Braginskii<sup>4</sup>, was published only recently,<sup>5</sup> correcting the estimate of the above viscosity ratio to  $(m_e / m_i)^{1/2} Z^3$ . Therefore, for  $Z$  above 5, the electron viscosity exceeds the ion viscosity for equal electron and ion temperatures. In a number of plasma applications, including intense x-ray generation, shock compression and heating produce highly charged ions. For instance, in recent experiments with argon<sup>6</sup> ( $Z = 18$ ) and titanium<sup>7</sup> ( $Z = 22$ ) loads on



the “Z” generator at Sandia National Laboratories, substantial quantities of K-shell radiating helium- and hydrogen-like argon and titanium ions have been produced. Advancing further, to produce K-shell radiation from nickel, copper and krypton (Z varying from 28 to 36), we have to heat and shock-compress higher-still-Z plasmas. In these plasmas, the electron viscosity could considerably exceed the ion viscosity. Consequently, it must be taken into account and its contribution to electron heating estimated. This is the purpose of the present article.

This paper is structured as follows. In Section II, we an analytical solution of an idealized classical shock structure problem for a fully ionized high-Z plasma, where electron viscosity can significantly exceed the ion viscosity. Section III contains the results of one-dimensional (1D) hydrodynamic simulations that involve shock compressions of high-Z plasmas. Here, the contribution of electron viscosity is investigated numerically in a more realistic time-dependent setting. In Section IV we conclude with a discussion of some of the problems in need of future investigation.

## II. Electron viscosity in the plasma shock structure

### A. Comparison of electron and ion viscosity coefficients

The classical expression for the isotropic ion viscosity coefficient<sup>4</sup> is

$$\eta_0^i = \eta_{00}^i n_i T_i \tau_{ii} = \eta_{00}^i \frac{3m_i^{1/2} T_i^{5/2}}{4\pi^{1/2} \ln \Lambda e^4 Z^4}, \quad (1)$$

where  $n_i$ ,  $T_i$ ,  $\tau_{ii}$ ,  $Z$  and  $m_i$  are the ion number density, temperature (expressed in energy units), ion-ion collision time, charge, and mass, respectively,  $\ln \Lambda$  is the Coulomb

logarithm, and  $\eta_{00}^i$  is a dimensionless coefficient whose value is given in Ref. 4:

$$\eta_{00}^i = 0.96.$$

The electron viscosity coefficient calculated by Whitney<sup>5</sup> is expressed via the similar parameters referring to the electrons (with ion-ion collision time  $\tau_{ii}$  replaced by the electron-ion collision time  $\tau_{ei}$ ):

$$\eta_0^e = \eta_{00}^e(Z) n_e T_e \tau_{ei} = \eta_{00}^e(Z) \frac{3m_e^{1/2} T_e^{5/2}}{4(2\pi)^{1/2} \ln \Lambda e^4 Z}. \quad (2)$$

Here, the dimensionless coefficient  $\eta_{00}^e(Z)$  is a function of the ion charge,  $Z$ , given in Ref. 5:

$$\eta_{00}^e(Z) = \frac{1.81Z(Z^2 + 2.82Z + 1.343)}{Z^3 + 4.434Z^2 + 5.534Z + 1.78}. \quad (3)$$

For  $Z = 1$ , we obtain:  $\eta_{00}^e = 0.733$ , the value calculated by Braginskii.<sup>4</sup> From (1)-(3), we find the ratio of viscosity coefficients:

$$\frac{\eta_0^e}{\eta_0^i} = \left( \frac{m_e}{m_u} \right)^{1/2} \left( \frac{T_e}{T_i} \right)^{5/2} \frac{\eta_{00}^e(Z) Z^3}{\eta_{00}^i (2A)^{1/2}}, \quad (4)$$

where  $m_u$  is the atomic mass unit ( $m_u \cong m_{\text{proton}}$ ),  $A$  is the ion atomic weight. For a fully ionized plasma with not-too-high atomic number, one can approximate  $A \cong 2Z$ , to obtain<sup>†</sup>

$$\frac{\eta_0^e}{\eta_0^i} \cong \frac{1}{2} \left( \frac{m_e}{m_u} \right)^{1/2} \left( \frac{Z T_e}{T_i} \right)^{5/2} \frac{\eta_{00}^e(Z)}{\eta_{00}^i} = 1.17 \times 10^{-2} \left( \frac{\mathcal{E}_e}{\mathcal{E}_i} \right)^{5/2} \frac{\eta_{00}^e(Z)}{\eta_{00}^i}, \quad (5)$$

<sup>†</sup> In Ref. 5, where this ratio was first presented, a factor of 4/3 was inadvertently omitted from the expression for the ion pressure tensor. Here we present the corrected formula for the electron-to-ion viscosity ratio.

where  $\mathcal{E}_e$  and  $\mathcal{E}_i$  are thermal energy densities of the plasma components. To see why the ratio of viscosity coefficient depends on  $Z$  in this way, one can consult elementary kinetic theory.<sup>4</sup> Recall that the viscosity coefficient for any sort of particle is estimated to be of order  $nT\tau = nT/n'\nu_T\sigma$ , where  $n$  is the colliding particle number density,  $\nu_T = (3T/m)^{1/2}$  is the average thermal velocity,  $n'$  is the number density of the particles, against which the collisions occur. The collision time  $\tau$  is defined in terms of  $\sigma$ , the average cross section of such collisions. For charged particles,  $\sigma$  is proportional to the product of both charges squared times the Coulomb logarithm divided by the temperature squared. In high- $Z$  plasmas, there are  $Z$  more electrons than ions, and the electron mean free path is longer than the ion mean free path. Indeed, for ion-ion collisions,  $n = n' = n_i$ , and  $\sigma_{ii} \propto Z^4$ , which leads to (1). The electron-ion collision cross section  $\sigma_{ei}$  is less than  $\sigma_{ii}$  by a factor of  $Z^2$ ; additionally, electrons outnumber ions by a factor of  $Z$  ( $n = n_e = Zn_i$ ,  $n' = n_i$ ). The factor  $Z^3$  in (4) comes from this dependence on  $n, n'$ , and  $\sigma$ . Combining this factor with the factor  $A^{-1/2} \propto Z^{-1/2}$  coming from the ratio of thermal velocities, we arrive at Eq. (5). In high- $Z$  plasmas, most of the thermal energy typically is in the electron component, and we obtain from (5) that electron viscosity exceeds ion viscosity when  $\mathcal{E}_e/\mathcal{E}_i > 5$ . The ratio of viscosity coefficients vs.  $Z$  given by (4)-(5) is plotted on Fig. 1 for fully ionized plasmas with  $T_e = T_i$ . We see that  $\eta_0^e > \eta_0^i$  for  $Z > 5$  (carbon and higher). The ratio  $\eta_0^e/\eta_0^i$  exceeds  $Z$ , implying greater viscous heating per electron than per ion, for  $Z > 13$  (silicon and higher). For argon and higher- $Z$  plasmas stripped to helium- and hydrogen-like states, as in experiments of Refs. 6,7, the electron viscosity is substantially greater than the ion viscosity.

## B. Classical plasma shock structure with electron viscosity included

Let us find out how the presence of substantial electron viscosity affects plasma shock heating. For this purpose, we modify the well-known solution of a classical collisional plasma shock structure problem, originally studied in Refs. 8-10 (see also Section 2.1 of Ref. 2), to include the electron viscosity. In this Section, we consider a fully ionized plasma with constant ion charge  $Z$ , ignoring the ionization kinetics and thereby excluding contributions of ionization and excitation from the energy balance, as well as radiation effects, which are all significant in high- $Z$  non-fully-ionized plasmas. These are accounted for in the simulations that are reported in Section III. Additionally, we neglect the ion thermal conduction whose characteristic length scale in the shock structure we do not attempt to resolve. Here we limit ourselves to an idealized problem to single out and highlight specifically the magnitude of the effect of electron viscosity.

To find a steady-state shock structure, we conventionally pass to the reference frame where the shock front is stationary and write down the steady-state 1D fluid equations,<sup>4</sup> which in this case simply reduce to integrated form of conservation equations of mass, momentum, and energy<sup>1,2</sup>

$$nu = n_1 u_1, \quad (6)$$

$$nm_i u^2 + n(ZT_e + T_i) - \frac{4}{3}(\eta_0^e + \eta_0^i) \frac{du}{dx} = n_1 m_i u_1^2 + (1+Z)n_1 T_1, \quad (7)$$

$$\begin{aligned} \frac{1}{2}nm_i u^3 + \frac{5}{2}nu(ZT_e + T_i) - \kappa_e \frac{dT_e}{dx} - \frac{4}{3}(\eta_0^e + \eta_0^i)u \frac{du}{dx} \\ = \frac{1}{2}n_1 m_i u_1^3 + \frac{5}{2}(1+Z)n_1 u_1 T_1 \end{aligned} \quad (8)$$

and the heat balance equations for the ions

$$\frac{3}{2}nu \frac{dT_i}{dx} + nT_i \frac{du}{dx} = \frac{4}{3}\eta_0 \left( \frac{du}{dx} \right)^2 + Zn \frac{3m_e T_e - T_i}{m_i \tau_e}. \quad (9)$$

Here  $n$  is the ion number density (due to plasma quasi-neutrality, the electron number density  $n_e = Zn$ , and the velocity  $u$  is the same for both electrons and ions);

$\kappa_e = \kappa_0^e(Z)n_e T_e \tau_e / m_e$  is the electron heat conduction coefficient

( $\tau_e = 3m_e^{1/2} T_e^{3/2} / 4\sqrt{2\pi} \ln \Lambda e^4 Z^2 n$ , and the dimensionless coefficients  $\kappa_0^e(Z)$  are

tabulated in Ref. 4.) Subscript 1 refers to the values of the flow variables in the pre-shock uniform flow far upstream from the shock front, where all the gradients vanish; in

particular,  $u_1$  is the shock speed defined with respect to the plasma ahead of it. But the

flow variables also vanish in the post-shock state, far downstream, which we would

designate by subscript 2. The right-hand sides of Eqs. (6)-(8) must have the same values

whether they are expressed via the parameters characteristic of the pre-shock (subscript

1) or the post-shock (subscript 2) state. From this observation, we derive the relations

between the pre- and post-shock state parameters:

$$\frac{u_2}{u_1} = \frac{n_1}{n_2} = \frac{M_1^2 + 3}{4M_1^2} \equiv U_2, \quad (11)$$

$$\frac{T_2}{T_1} = \frac{(M_1^2 + 3)(5M_1^2 - 1)}{16M_1^2} \equiv \Theta_2, \quad (12)$$

where  $M_1 = u_1 \cdot [5(1+Z)T_1/3m_i]^{-1/2}$  is the Mach number characteristic of the shock wave.

These are, of course, conventional Hugoniot conditions for an ideal gas with  $\gamma = 5/3$ .

Since  $M_1 > 1$ , we have  $U_2 < 1$  and  $\Theta_2 > 1$ : the shock wave compresses and heats the plasma.

To obtain the shock structure solution, it is convenient to use normalized variables

$$U = \frac{u}{u_1}, \quad \Theta_e = \frac{T_e}{T_1}, \quad \Theta_i = \frac{T_i}{T_1}. \quad (13)$$

Then Eq. (6) is satisfied automatically if  $n_1/n$  equals  $U$  and Eqs. (7)-(9) are reduced to

$$U - 1 + \frac{3}{5M_1^2} \left[ \frac{Z\Theta_e + \Theta_i}{(1+Z)U} - 1 \right] - \Delta_v \frac{dU}{dx} = 0, \quad (14)$$

$$\frac{1}{2}(U^2 - 1) + \frac{3}{2M_1^2} \left( \frac{Z\Theta_e + \Theta_i}{Z+1} - 1 \right) - \Delta_v U \frac{dU}{dx} - \Delta_{Te} \frac{d\Theta_e}{dx} = 0, \quad (15)$$

$$\frac{3}{2} \frac{d\Theta_i}{dx} + \frac{\Theta_i}{U} \frac{dU}{dx} = \frac{5(1+Z)\eta_0^i}{3\eta_0^e + \eta_0^i} M_1^2 \Delta_v \left( \frac{dU}{dx} \right)^2 + \frac{\Theta_e - \Theta_i}{\Delta_r}, \quad (16)$$

where the length scale functions  $\Delta_v$ ,  $\Delta_{Te}$ , and  $\Delta_r$  of the variables  $U$ ,  $\Theta_e$ ,  $\Theta_i$  (and parameters  $M_1$ ,  $Z$ ), which are characteristic of viscosity, electron thermal conductivity and temperature relaxation, respectively, are defined as

$$\Delta_v = \frac{4\eta_0^e + \eta_0^i}{3m_i n_1 u_1}, \quad \Delta_{Te} = \frac{\kappa_e T_1}{m_i n_1 u_1^3}, \quad \Delta_r = \frac{m_i}{3Zm_e} u_1 \tau_e U. \quad (17)$$

We are interested in a solution of Eqs. (14)-(16) with the Hugoniot boundary conditions:

$$U, \Theta_e, \Theta_i \rightarrow 1 \text{ at } x \rightarrow -\infty; \quad U \rightarrow U_2, \quad \Theta_e, \Theta_i \rightarrow \Theta_2 \text{ at } x \rightarrow +\infty. \quad (18)$$

The upstream and downstream points at infinity, where all the derivatives vanish, correspond to singular points of the autonomous dynamic system (14)-(16). Therefore the solution sought for represents a singular trajectory that joins the two singular points (18).

The solution is obtained using the multiple-scale method, which is described in details in Refs. 2 and 10. The largest scale length turns out to be  $\Delta_{Te}$ , which is one associated with electron thermal conduction, and which is comparable to the temperature relaxation scale,  $\Delta_r$ . Consequently, by assuming that all the derivatives  $d/dx$ , are

$\sim 1/\Delta_{Te}$ , by neglecting the small terms of order of  $\Delta_v/\Delta_{Te}$ , and introducing a dimensionless length variable,

$$\Delta_{Te} = \Delta_{Tel} \Theta_e^{5/2}, \quad \xi = x/\Delta_{Tel}, \quad (19)$$

one can reduce the system (14)-(16) to an algebraic relation for  $\Theta_i$

$$\Theta_i = -Z\Theta_e + (Z+1) \left[ \Theta_e + \frac{5}{3}M_1^2 U^2 - \left( \frac{5}{3}M_1^2 + 1 \right) U \right] \quad (20)$$

and to the following two equations for  $U$  and  $\Theta_e$ :

$$\frac{dU}{d\xi} = \Theta_e^{-5/2} \frac{3Z(U-1)(U_2-U) + s \frac{\Theta_e}{U^2} \left[ \Theta_e + \frac{5}{3}M_1^2 U^2 - \left( \frac{5}{3}M_1^2 + 1 \right) U \right]}{-Z \frac{\Theta_e}{U^2} + \frac{5}{6}(Z+1)(-8M_1^2 U + 5M_1^2 + 3)}, \quad (21)$$

$$\frac{d\Theta_e}{d\xi} = 2\Theta_e^{-5/2}(U-1)(U_2-U), \quad (22)$$

where  $s = 27\kappa_{e0}(Z)Z^2/25(1+Z)^2 M_1^4$ .

An asymptotic analysis of the system (21)-(22) in the vicinity of its singular points, 1 and 2 [see (18)] reveals that the singular point 1 is a saddle points for any  $M_1 > 1$ . Consequently, a unique phase trajectory on the phase plane  $(U, \Theta_e)$  approaches this singular point (1, 1) at  $\xi \rightarrow -\infty$  from the domain of higher temperatures and densities. A shock structure solution would exists and be physically meaningful (stable, evolutionary<sup>2</sup>) if the same phase trajectory can be found to approach to the singular point 2  $(U_2, \Theta_2)$  at  $\xi \rightarrow +\infty$ . This is the case when the singular point 2 is a node attracting at  $\xi \rightarrow +\infty$  all the trajectories that pass in its vicinity. These latter conditions holds for weak shock waves, defined by the inequality

$$M_1 < M_{cr} = \left[ \frac{9Z+10}{5(Z+2)} \right]^{1/2}. \quad (23)$$

The structure of a weak shock wave is determined by electron thermal conduction, viscosity playing no role at all. Expression (23) for a critical Mach number is a simple generalization of Shafranov's result<sup>9</sup> (which was derived for  $Z = 1$ , implying  $M_{cr} = \sqrt{19/15} = 1.125$ ) to arbitrary  $Z$ . Weak shock profiles for high- $Z$  plasmas are no different from those discussed in Refs. 9-11, 2 (in particular, electron and ion temperatures are very close throughout the shock), and we will not describe them any further here. Rather, we are interested in the strong-shock case, where electron viscosity does make a difference.

For  $M_1 > M_{cr}(Z)$ , the downstream singular point 2 is a saddle point, too. In other words, only one phase trajectory approaches it as  $\xi \rightarrow +\infty$  from the domain of lower temperatures and densities, and this is not the same trajectory that approaches the downstream singular point 1 in the limit  $\xi \rightarrow -\infty$ . As a consequence, the shock structure defined by (20)-(22) contains a "viscous sub-shock", which, to zeroth order in  $\Delta_v / \Delta_{Te}$ , is simply a zero-thickness discontinuity, a jump from the former trajectory to the latter. If the length scale of the jump is  $\Delta_v$ , then  $d/dx \sim 1/\Delta_v$ . In this case, Eq. (15) ensures that electron temperature in the viscous sub-shock is essentially constant<sup>9, 10</sup> due to the smallness of the ratio  $\Delta_v / \Delta_{Te}$ .

To obtain the Hugoniot conditions for the viscous sub-shock, one can neglect the thermal relaxation term in the right-hand side of Eq. (16) (its order is determined by the



small ratio  $\Delta_v / \Delta_r$ ). Then, assuming constant electron temperature  $\Theta_e = \Theta_{ea}$  and

simplifying this equation with the aid of (14), we reduce it to

$$\frac{d\Theta_i}{dU} = \frac{2}{3(\Theta_i^{5/2} + \mu\Theta_{ea}^{5/2})} \left\{ \left[ \frac{5M_1^2}{3}(Z+1)U - \left( \frac{5M_1^2}{3} + 1 \right) (Z+1) + Z \frac{\Theta_{ea}}{U} \right] \Theta_i^{5/2} - \mu \frac{\Theta_i \Theta_{ea}^{5/2}}{U} \right\}, \quad (24)$$

where  $\mu$  denotes the right-hand side of Eqs. (4) or (5) at  $T_e = T_i$ . Equation (24) is to be

integrated, from the point with the initial condition  $\Theta_i = \Theta_{ia}$  at  $U = U_a$  to the point

$U = U_b$ ,  $\Theta_i = \Theta_{ib}$  where the velocity derivative in the left-hand side of Eq. (14) vanishes.

At this latter point,

$$U_b - 1 + \frac{3}{5M_1^2} \left[ \frac{Z\Theta_{ea} + \Theta_{ib}}{(1+Z)U_b} - 1 \right] = 0. \quad (25)$$

Points  $a$  and  $b$  are thus related by the Hugoniot condition for the viscous sub-shock.

In an analysis in which electron viscosity is neglected by setting  $\mu = 0$ , one can

explicitly integrate Eq. (24). Then, by substituting the result of the integration into (25),

one can reduce the subshock Hugoniot condition to a single transcendental equation:<sup>10</sup>

$$(U_a - U_b)(1 + U_2 - U_a - U_b) - \frac{3Z\Theta_{ea}}{10M_1^2(Z+1)} \ln \frac{U_a}{U_b} = 0. \quad (26)$$

The structure of a shock with electron viscosity included is calculated similarly to

Refs. 9, 10. We start in the vicinity of singular point 1 and, on the phase plane  $(U, \Theta_e)$ ,

plot the only trajectory of the system (21)-(22) that is outgoing from point 1 at  $\xi \rightarrow \infty$  to

the domain of higher temperatures and pressures. This part of the solution represents the

electron pre-heat zone ahead of the viscous shock. For each point  $a$  on this trajectory, we

find the corresponding point  $b$ , which is connected to it by the Hugoniot relation for the

viscous sub-shock, as explained above. As the point  $a$  moves along the pre-heat trajectory, it maps out a locus of the corresponding points  $b$  on the phase plane (Fig. 2). The shock structure equations permit a viscous subshock transition (occurring at constant electron temperature, i.e. a horizontal segment on Fig. 2) from any point  $a$  to each corresponding point  $b$ . However, only one  $b$  point lies on the solution trajectory. Starting from the correct point  $b$ , the solution to Eqs. (20)-(22) must approach the downstream singular point 2 at  $\xi \rightarrow +\infty$ , and this can happen only along a single unique phase trajectory. To find the only trajectory that enters point 2 at  $\xi \rightarrow +\infty$ , we start in the vicinity of point 2, and integrate Eqs. (21)-(22) backward over  $\xi$ . After locating the intersection of this trajectory on the phase plane  $(U, \Theta_e)$  with the locus of points  $b$ , we can construct the whole solution  $1 \rightarrow a \rightarrow b \rightarrow 2$ , which satisfies the general Hugoniot conditions (13).

The Hugoniot conditions for the viscous sub-shock are different, depending on whether or not the electron viscosity is accounted for. Therefore, for the given outgoing trajectory  $1 \rightarrow a$ , we can plot plane two curves on the phase, each representing a locus of points  $b$ : one for the case when the electron viscosity is accounted for, and the other for the case when it is ignored (dotted and dashed locus curves on Fig. 2, respectively.) From each point  $a_1$  there is a possible viscous shock transition (represented by the dotted horizontal segment) either to  $b_1$  or to  $b_2$ , depending on whether or not the electron viscosity is accounted for. Each of the two locus  $b$  curves intersects with the only trajectory entering 2 at  $\xi \rightarrow +\infty$  at a different location. Note that solutions of Eqs. (20)-(22) in the vicinities of pre- and post-shock states are exactly the same, no matter whether or not the electron viscosity is accounted for. The only difference between them is in the

location and strength of the viscous sub-shock. Not surprisingly, with electron viscosity included, the pre-heat zone is a little longer, and the electrons are pre-heated to a higher temperature, whereas the temperature relaxation zone is accordingly shorter, and the ions in the viscous sub-shock are less over-heated compared to the electrons. For the example of Fig. 2 ( $Z = 22$ ,  $M_1 = 5 > M_{cr}(22) = 1.32$ ) we find: without electron viscosity the peak ion temperature in the viscous sub-shock exceeds the peak (that is, post-shock) electron temperature by the factor 3.8, whereas once electron viscosity is taken into account this ratio is reduced down to 1.7. The shock profiles, for both cases, are plotted in Fig. 3.

Why are the ions still overheated when the viscous energy release per electron is higher than per ion (by a factor of  $\sim 5$ , in this example)? The reason is that thermal energy is drained from the electrons via thermal conduction upstream. The heat released in the viscous sub-shock is instantly spent to heat the electrons upstream. On the contrary, the length scale characteristic of the ion heat conduction (which is ignored here) is of the same order as the thickness of the viscous sub-shock. Thus, although the viscosity generates less heat per particle in the ion component of the plasma, the ions keep this energy, only slowly sharing it with electrons behind the viscous sub-shock, in the temperature relaxation zone. Figure 4 shows how the ion overheating (characterized, as above, by the ratio of the peak ion temperature to the post-shock plasma temperature) for a strong shock wave ( $M_1 = 10$ ) varies as  $Z$  is varied from 13 (aluminum) to 36 (krypton). If the electron viscosity is ignored, then overheating is seen to be a linearly increasing function of  $Z$  for a given Mach number. With electron viscosity taken into account, overheating is virtually constant, about 1.7, in the range of  $Z$  shown. The physical meaning of both scalings is quite clear. If electron viscosity is neglected, then each ion

dissipates, in the viscous sub-shock, its own kinetic energy, which is proportional to the ion mass for a given shock velocity. Hence, the dissipated energy per ion scales as  $A$ , or, equally, as  $Z$ ; whereas, far downstream, this energy is shared with  $Z$  electrons, thus reducing the ion temperature by a factor of  $Z$ . If electron viscosity is included in the energy dissipation, this energy sharing between an ion and its  $Z$  electrons starts already in the viscous sub-shock, making the overheating virtually independent of  $Z$ .

### III. Effect of electron viscosity on radiating Z-pinch plasmas

Let us study in a more realistic and time-dependent hydrodynamic calculation one example of a physical situation involving plasma shock waves where taking the account of the electron viscosity makes a difference. Shock heating is known to be a major mechanism for converting kinetic energy of imploding Z-pinch plasmas into thermal energy, making the kinetic energy available for producing hard x-ray radiation.<sup>13</sup> To obtain K-shell emission in the multi-keV range, the ions have to be stripped down to high- $Z$  helium- or hydrogen-like states, e. g., we need to reach  $Z = 20 - 21$  or  $34 - 35$  in order to produce either titanium or krypton K-shell radiation, respectively. The Z-pinch plasma is shocked at least once, in the case of an empty annular shell imploding onto the axis. In the case of a gas-puff load, whether it be a gaseous "shell" or a uniform fill, there is always some gas near the axis, so a converging shock wave reaches the axis ahead of the current sheath, after which the plasma is re-shocked in a reflected wave. In wire-array implosions, the so-called precursor plasma also reaches the axis prior to the main plasma mass,<sup>14, 15</sup> hence plasma near the axis can be shocked twice, too. Three or more plasma shock fronts could be produced with more advanced loads, like double gas puffs<sup>16</sup> or nested wire arrays.<sup>17</sup>

With ionization starting in the pre-heat zone,<sup>2</sup> even as the first (and particularly the subsequent) viscous sub-shocks compresses and heats a high-Z plasma, electron viscosity becomes important. Its role is illustrated by the results of one-dimensional (1-D) simulations of titanium and krypton Z-pinch implosions given below. We did not undertake a systematic and thorough study of how electron viscosity affects Z-pinch implosions. Rather, our present results represent only a first look at how the electron viscosity influences K-shell emission, and about how this influence in certain implosions is affected by the atomic number of the plasma.

We simulated titanium and krypton load implosions with the 1-D radiative-MHD code described in Ref. 18. The calculations were carried out using from 60 to 100 Lagrangian zones. A collisional-radiative equilibrium (CRE) ionization dynamics was employed in all cases. The standard form of artificial viscosity was used. The heating it produced was either conventionally put entirely into the ions *or* divided between electrons and ions according to the ratio of their physical viscosity coefficients, Eq. (4), and the results of the two procedures were compared.

Our calculations were done for two kinds of imploding loads: 1) uniform fills of krypton and titanium, and 2) nested titanium shell-on-fill plasmas. In the first set of calculations, the initially uniform density fills of krypton and titanium plasmas were at a temperature of 4 eV. The mass of the fill, its initial density, and the energy input were varied so that comparisons of the ion temperature profiles and K-shell yields and powers could be made with and without electron viscosity in the calculations. A nested titanium plasma geometry was set up by moving an outer portion of the above described fill farther out from the inner portion, and creating a small mass of reduced density (by a

factor of 10) between the inner and the outer plasmas. The loads were driven by a linearly rising current pulse that was terminated when a prescribed energy input was achieved. Fill masses were varied between 1.25 and 10 mg/cm. Most of this interval physically corresponds to next generation of multi-MA current drivers capable of producing krypton K-shell emission (energy delivered to the plasma up to  $\sim 12$  MJ/cm, current up to  $\sim 80$  MA). The nested calculations were performed with a plasma mass of 1.25 mg/cm, which corresponds to an amount of plasma mass that can be successfully imploded on the Z accelerator to velocities that are needed to effectively excite the K-shell of titanium (energy delivered to the plasma  $\sim 0.5$  MJ/cm, current  $\sim 18$  MA.)<sup>7</sup>

When electron viscosity is ignored and all of the viscous heating is put into ions, the rate of ion heating exceeds the electron rate, which, in this case, is due to adiabatic compression heating alone. Thus, the ions become significantly hotter than the electrons (cf. Fig. 3, dashed lines), in all the classical shock structure calculations that include ion viscosity only. As the plasma become highly ionized, the addition of electron viscosity should, therefore, reduce ion temperatures (Fig. 3, solid lines) and raise electron temperatures slightly, which suggests the possibility of converting some of this energy into extra K-shell emission. However, this possibility depends on the plasma conditions that are generated during the actual dynamics of a time-evolving implosion, since the viscosity coefficient ratio is substantially reduced when  $T_i$  is allowed to become much larger than  $T_e$  in the early phases of the implosion. Moreover, in a dynamic implosion, radiation cooling becomes a significant drag on the electron temperature that acts on the ions only indirectly through electron-ion collisions. Thus, the ions can get hotter than the electrons when radiation losses are high and the electron-ion coupling is too weak. Under

conditions of too low an ion density, and too small an electron-ion collision rate, the rerouting of ion thermal energy into K-shell emission is inhibited.

Figure 5, 6 show our results for a 10 mg/cm Kr uniform fill with an initial 4 cm radius driven by an energy input  $\sim 12$  MJ/cm. This corresponds to  $\eta^* = 2$ , where  $\eta^*$  stands for the energy delivered per ion divided by the energy required to strip the ion into He-like excited states. Figure 5 demonstrates the electron and ion temperature profiles during the run-in phase, at 80 ns (a) and near the peak of the K-shell emission, at 113.5 ns (b). We see that the inclusion of electron viscosity produces significant reductions in the ion temperature. Reduced ion heating and the corresponding increase in electron heating led to a 20% increase in the K-shell energy output, making the total K-yield approach 4 MJ/cm, see Fig. 6. All of the K-shell emission originated from the core of the compressed plasma. The outer portion of plasma, which contains a sizable fraction of the plasma mass, emitted only in the L-shell. Prior to the K-shell emission [Fig. 5(a)], the electron temperature profile shows only slight changes due to electron viscosity in contrast to the ion temperature profile since there are  $Z$  times as many electrons to share the energy as there are ions.

For a 10 mg/cm uniform-fill of titanium imploded with an initial radius of 2 cm, similar, but smaller reductions in ion temperature were seen, as illustrated by Figs. 7, 8. Figure 7 shows the ion temperature profiles near the peak of compression for  $\eta^* = 1.8$ , which corresponds to the current  $\sim 40$  MA and the energy delivered to the pinch about 3 MJ/cm, almost 30% of which is emitted in the K-shell. The reductions in the ion thermal energy again showed up as increases in K-shell emission, although to a somewhat smaller extent, 8% in Fig. 8. Doubling the energy input twice, to  $\eta^* = 3.6$ , and then to  $\eta^* = 7.2$

(this was achieved by reducing the rise time of the current), we find corresponding increases in the K-shell emissions of the same order, 15% and 10%, respectively.

Figure 9 shows the ion temperature profiles obtained for implosion of a nested titanium wire array. The nesting used in the calculations was done by dividing the 1.25 mg/cm uniform-fill plasma into two parts and by moving the outer part in radius, by roughly a factor of two. Since one cannot have a perfect vacuum between plasmas in a simulation, the calculations were zoned so that the density between the inner and the outer plasmas could be reduced by a factor of 10. Therefore, the calculations reported here are of the shell-on-fill rather than shell-on-shell variety, thereby representing a very rough model of the actual "Z" experiments. Still, even though a perfect vacuum did not exist between the two plasmas in the calculation, the collision time is well defined. In the run illustrated by Fig. 9, the outer-to-inner mass ratio was taken to be 2, the outer plasma radius 4.2 cm, energy input 0.42 MJ/cm (which translates into  $\eta^* = 2$  and current of 16 MA), total number of zones 100. The temperature profiles are shown in Fig. 9 at the onset of the K-shell emission. Here again, the inclusion of electron viscosity, by reducing the ion temperature, allowed an additional 20 kJ of K-shell x rays to be extracted from the plasma, which increased the K-shell yield by about 10%.

#### IV. Conclusions

Two methods were used to evaluate the influence of electron viscosity on the shock heating of highly ionizable moderate atomic number plasmas. Classical, analytic shock structure calculations were first carried out to quantify the amount by which the ion temperature discontinuity across the unresolved sub-shock structure of a plasma shock



wave was reduced by taking electron viscosity into account. The strength of this calculation is that it can make use of real classical viscosities and accurately resolve the shock structure that is determined mainly by the electron thermal conduction. On the other hand, its weaknesses are that it cannot treat convergent shock waves and that it must assume a steady flow and a fully ionized plasma on both sides of the shock front. A second method involved the use of computer calculations to quantify how electron viscosity influences ion heating in strongly driven and shock-heated Z-pinch plasmas. The strengths of these calculations were that they could treat both time-evolving, ionizing and radiating plasmas, and convergent shock wave dynamics. However, their weaknesses were that they could not resolve the shock structure, nor could they properly treat the non-equilibrium ionization dynamics across the sharp temperature and density gradients. Consequently, artificial viscosities were used in these calculations, which do not include any of the  $Z$  or temperature dependences of the real viscosities. These dependences were included though in the way the artificial viscosity heating was divided between electrons and ions.

We have demonstrated that the inclusion of previously neglected electron viscosity can significantly affect the results of hydro simulations of shock-heated high- $Z$  plasmas. The main effect is a considerable reduction of the ion over-heating in the shock waves. Hence we predict that, for instance, direct measurements of ion temperature in high-current Z-pinch (e. g., those based on Doppler broadening) are likely to show the ion temperatures that are much lower than those expected from simulations in which electron viscosity is not taken into account. A more subtle effect is the corresponding rather small increase in the electron temperature. If electron viscosity is neglected, the ion

overheating in the viscous sub-shock scales approximately as  $Z$  (Fig. 4), the same as the number of electrons per ion. By including the electron viscosity, we split most of the ion's extra thermal energy between all  $Z$  electrons. Consequently, when electron viscosity is added, the resulting relative increase of the electron energy (temperature) must be a relatively weak function of  $Z$ . This conclusion is consistent with our simulation results, where, in the range of  $Z$  between 22 and 36, increases of the K-shell output due to the extra energy diverted by the electron viscosity was found to vary only between 10 and 20%. Therefore we can conclude that, whenever a shock compression of high- $Z$  plasmas is modeled, the electron viscosity should be taken into account. This is particularly true if we are interested in more accurately predicting the ion temperature, or if our results are sensitive to the value of the electron temperature.

## References

- <sup>1</sup> Ya. B. Zel'dovich and Yu. P. Raizer, *Physics of Shock Waves and High-Temperature Hydrodynamic Phenomena* (Academic Press, New York, 1966), Vol. 1.
- <sup>2</sup> M. A. Liberman and A. L. Velikovich, *Physics of Shock Waves in Gases and Plasmas* (Springer, Heidelberg, 1986).
- <sup>3</sup> L. D. Landau and E. M. Lifshitz, *Fluid Mechanics*, 2<sup>nd</sup> edition (Addison-Wesley Publishing Co., Reading, MA 1962), pp. 86-95.
- <sup>4</sup> S. I. Braginskii, "Transport processes in a Plasma," *Reviews of Plasma Physics*, ed. by M. A. Leontovich, Vol. 1 (Consultants Bureau, New York, 1965), p. 205.
- <sup>5</sup> K. G. Whitney, *Phys. Plasmas* **6**, 816 (1999).
- <sup>6</sup> H. Sze, J. Banister, P. L. Coleman, B. H. Failor, A. Fisher, J. S. Levine, Y. Song, E. M. Waisman, J. P. Apruzese, R. W. Clark, J. Davis, D. Mosher, J. W. Thornhill, A. L. Velikovich, B. V. Weber, C. A. Coverdale, C. Deeney, T. Gilliland, J. McGurn, R. Spielman, K. Struve, W. Stygar, and D. Bell, submitted to *Phys. Rev. Lett.* (2001).
- <sup>7</sup> C. Deeney, C. A. Coverdale, M. R. Douglas, T. J. Nash, R. B. Spielman, K. W. Struve, K. G. Whitney, J. W. Thornhill, J. P. Apruzese, R. W. Clark, J. Davis, F. N. Beg and J. Ruiz-Camacho, *Phys. Plasmas* **6**, 2081 (1999).
- <sup>8</sup> J. D. Jukes, *J. Fluid Mech.* **3**, 275 (1957).
- <sup>9</sup> V. D. Shafranov, *Sov. Phys. JETP* **5**, 1183 (1957).
- <sup>10</sup> M. Y. Jaffrin and R. F. Probstein, *Phys. Fluids* **7**, 1658 (1964).
- <sup>11</sup> F. Vidal, J. P. Matte, M. Casanova and O. Larroche, *Phys. Fluids B* **5**, 3182 (1993).
- <sup>12</sup> I. R. Smirnovskii, *Plasma Phys. Reports* **26**, 225 (2000).
- <sup>13</sup> N. R. Pereira and J. Davis, *J. Appl. Phys.* **64**, R1 (1988).

- <sup>14</sup> K. G. Whitney, J. W. Thornhill, P. E. Pulsifer, and J. P. Apruzese, T. W. L. Sanford, T. J. Nash, R. C. Mock, and R. B. Spielman, *Phys. Rev. E* **56**, 3540 (1997).
- <sup>15</sup> J. P. Chittended, S. V. Lebedev, A. R. Bell, R. Aliaga-Rosset, S. N. Bland, and M. G. Haines, *Phys. Rev. Lett.* **83**, 100 (1999).
- <sup>16</sup> A. V. Shishlov, R. B. Baksht, A. V. Fedunin, F. I. Fursov, B. M. Kovalchuk, V. A. Kokshenev, N. E. Kurmaev, A. Yu. Labetsky, V. I. Oreshkin, A. G. Russkikh, A. Fisher, B. Moosman, and B. V. Weber, *Phys. Plasmas* **7**, 1252 (2000); Y. Song, P. Coleman, B. H. Failor, A. Fisher, R. Ingermanson, J. S. Levine, H. Sze, E. Waisman, R. J. Commisso, T. Cochran, J. Davis, B. Moosman, A. L. Velikovich, B. V. Weber, D. Bell and R. Schneider, *Rev. Sci. Instrum.* **71**(8), 3080-3084 (2000).
- <sup>17</sup> J. Davis, N. A. Gondarenko, and A. L. Velikovich, *Appl. Phys. Lett.* **70**, 170 (1997); C. Deeney, M. R. Douglas, R. B. Spielman, T. J. Nash, D. L. Peterson, P. L'Eplattenier, G. A. Chandler, J. F. Seamen, and K. W. Struve, *Phys. Rev. Lett.* **81**, 4883 (1998); S. V. Lebedev, R. Aliaga-Rosset, S. N. Bland, J. P. Chittenden, A. E. Dangor, M. G. Haines, and M. Zakauallah, *Phys. Rev. Lett.* **84**, 1708 (2000).
- <sup>18</sup> J. W. Thornhill, K. G. Whitney, and J. Davis, *J. Quant. Spectr. Rad. Transfer* **44**, 251 (1990).

### Figure captions

Fig. 1. Ratio of electron and ion viscosity coefficients at  $T_e = T_i$ . Points are plotted for the exact values of atomic masses  $A(Z)$ , curves correspond to the approximation  $A = 2Z$ .

For  $Z = 1$ , we take  $A = 2$  (deuterium).

Fig. 2. Phase plane  $(U, \Theta_e)$ . Phase trajectories leaving the upstream point 1 and entering the downstream point 2 correspond to the electron pre-heat zone and to the electron-ion temperature relaxation zone, respectively. Horizontal segments are viscous sub-shocks permitted by the Hugoniot conditions, dotted and dashed curves – loci of points  $b$  with and without electron viscosity, respectively.

Fig. 3. Shock profiles for a  $M_1 = 5$  strong shock wave in a fully ionized titanium plasma,  $Z = 22$ . Here, normalized density equals  $1/U$ , see (13).

Fig. 4. Ion overheating in a  $M_1 = 10$  strong shock wave in a fully ionized high- $Z$  plasma, as a function of  $Z$ .

Fig. 5. Ion temperature profiles for a Kr uniform-fill implosion calculated without (A) and with electron viscosity (B). (a) during the run-in phase; (b) near the peak of K-shell emission.

Fig. 6. Time history of Kr K-shell yield for the conditions of Fig. 5

Fig. 7. Ion temperature profiles for a Ti uniform-fill implosion calculated without (A) and with electron viscosity (B). (a) during the run-in phase; (b) near the peak of K-shell emission.

Fig. 8. Time history of Ti K-shell yield for the conditions of Fig. 7.

Fig. 9. Ion temperature profiles for a Ti uniform-fill implosion calculated without (A) and with electron viscosity (B) near the peak of K-shell emission.

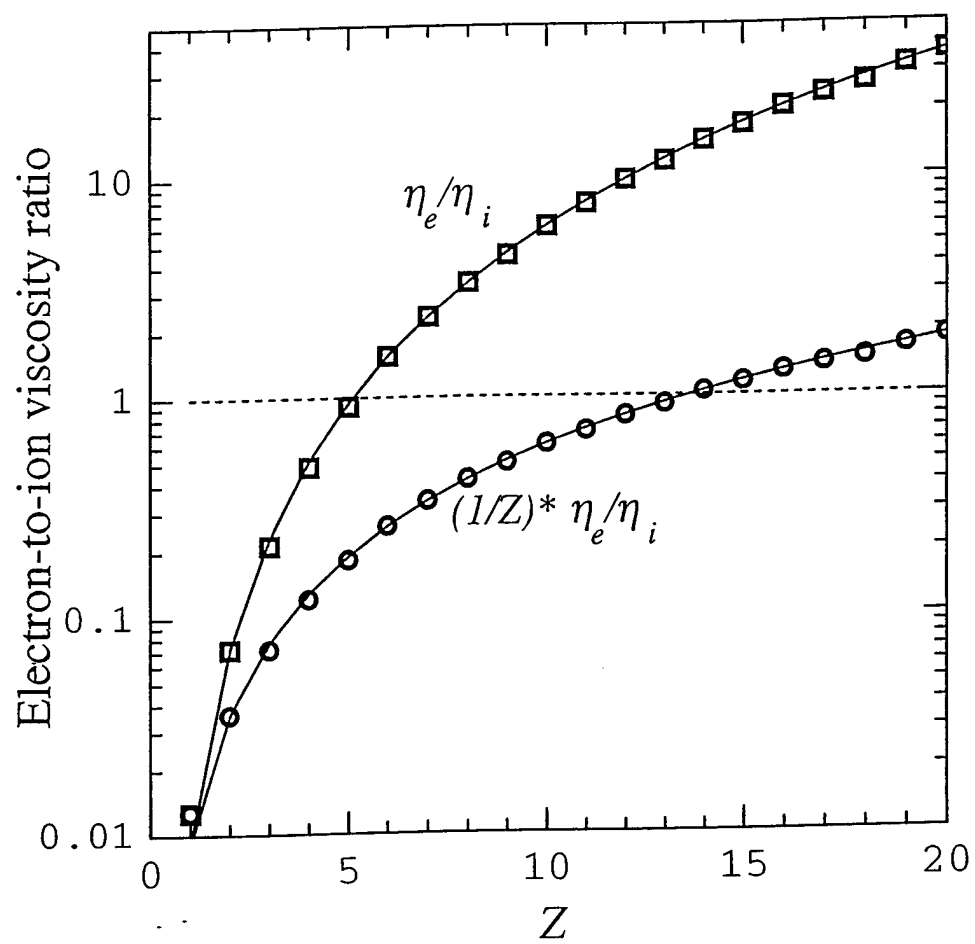


Figure 1

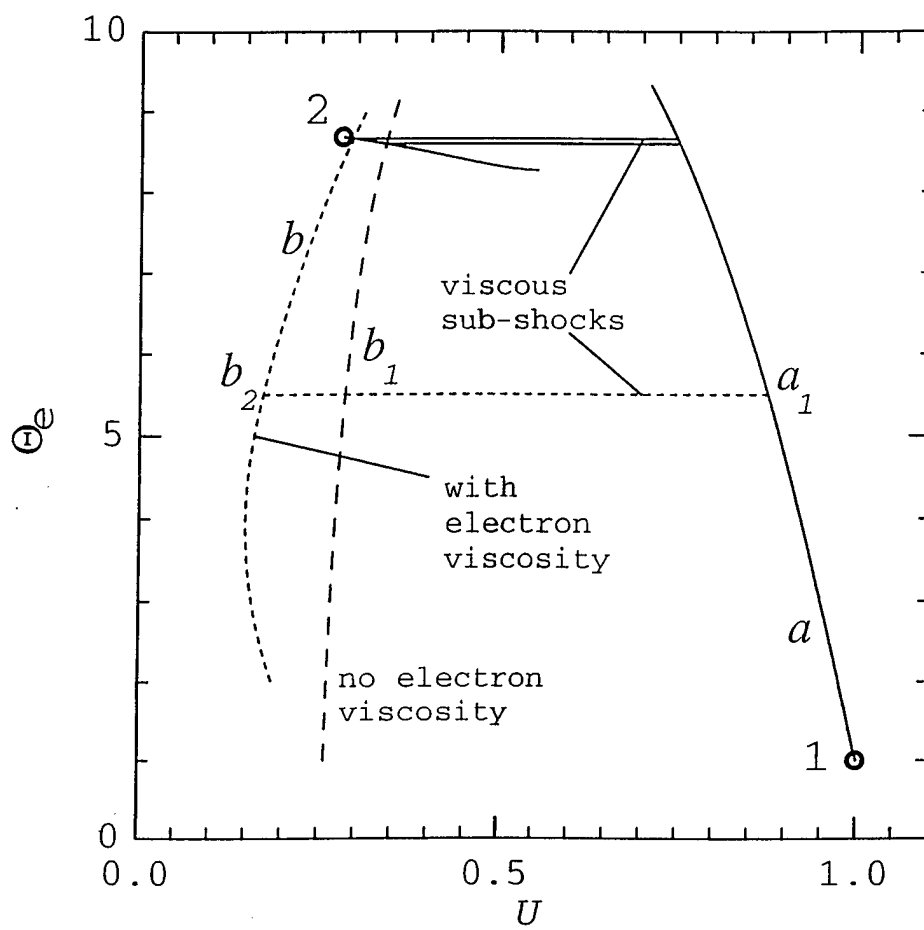


Figure 2

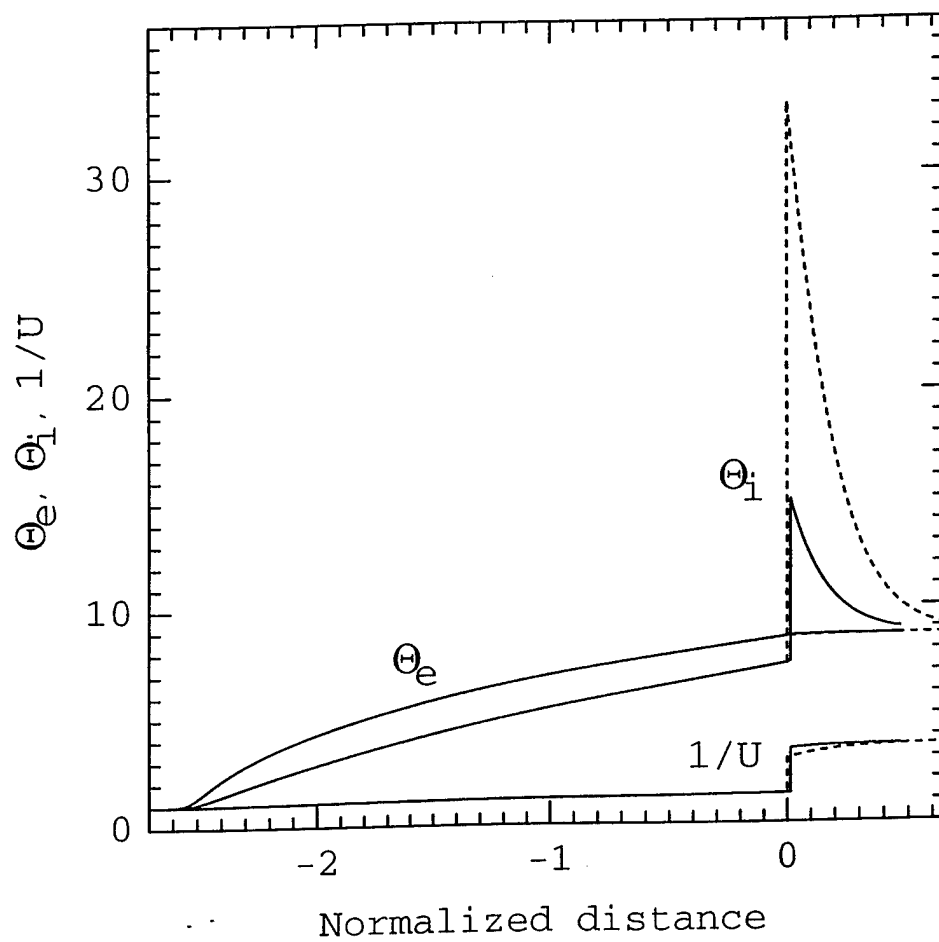


Figure 3



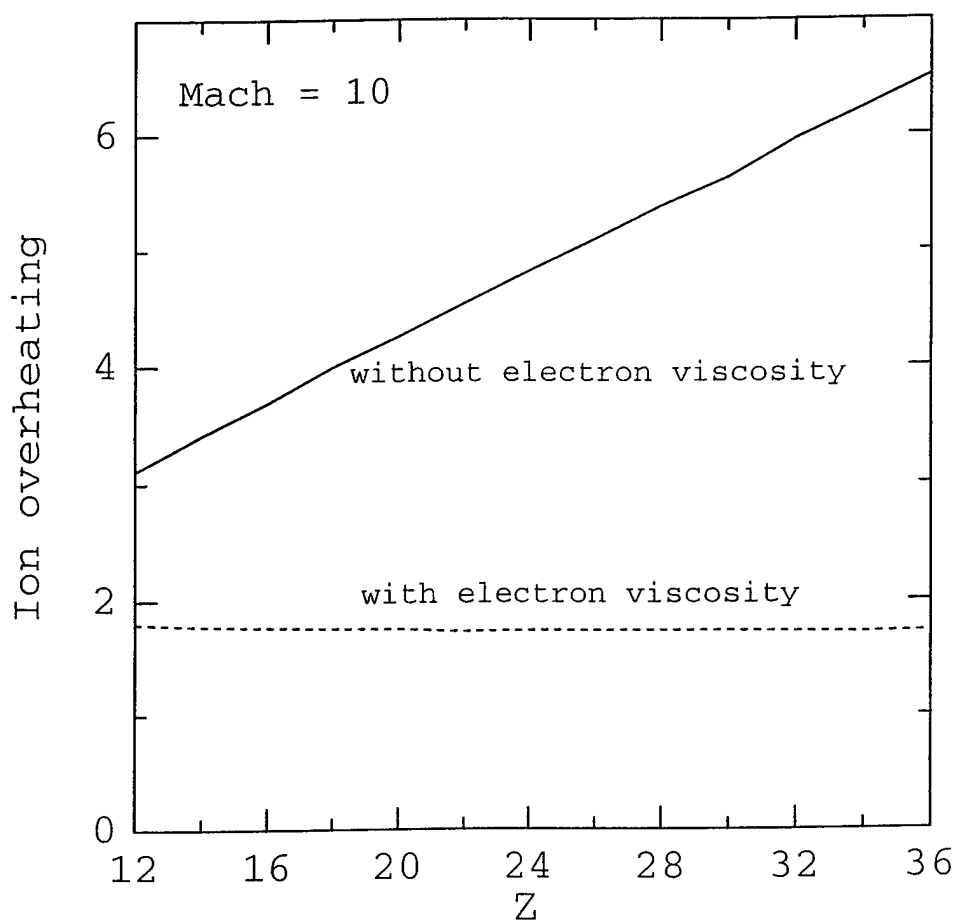


Figure 4

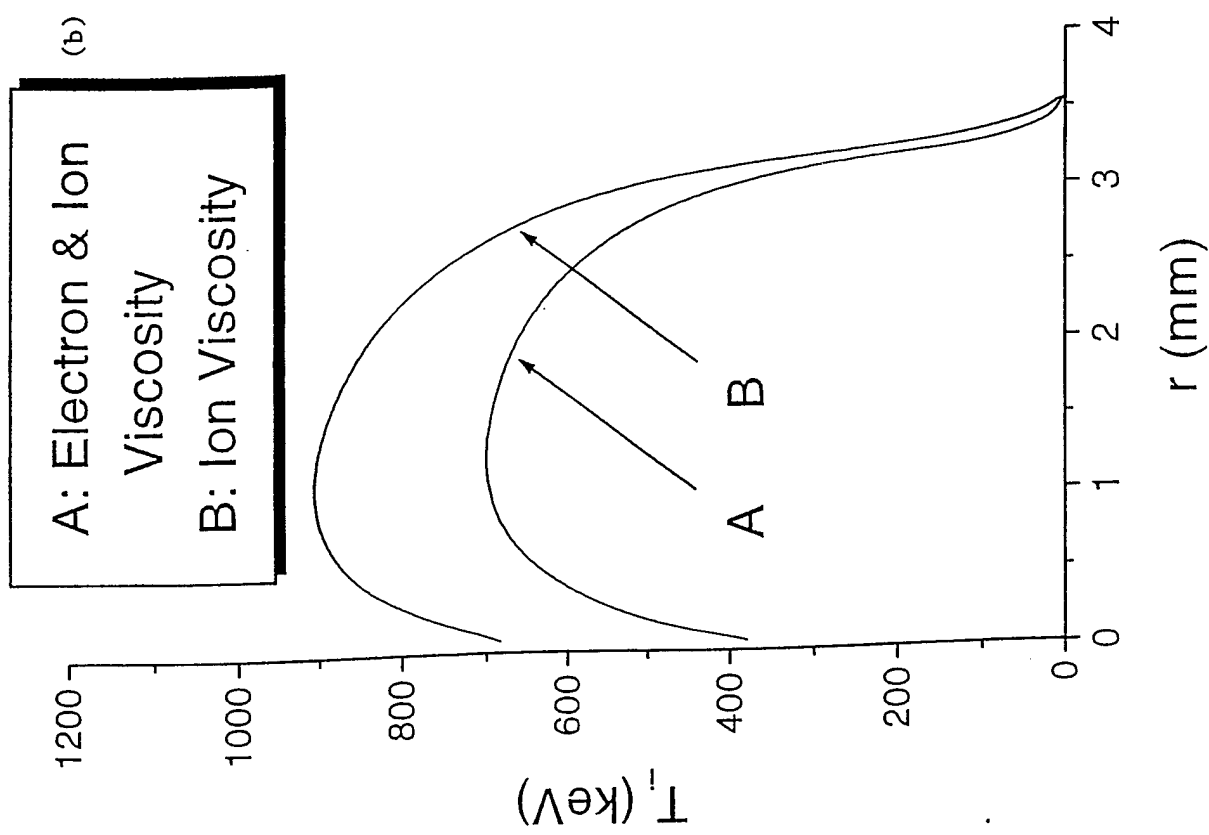
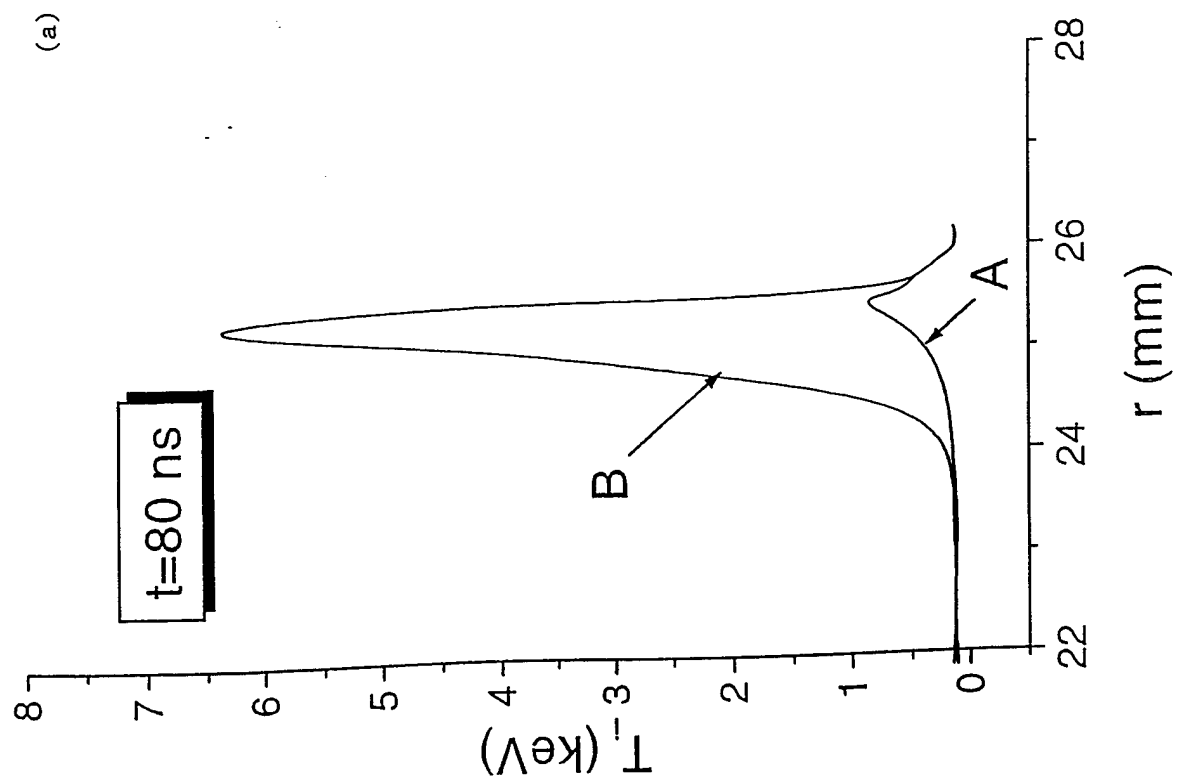


Figure 5

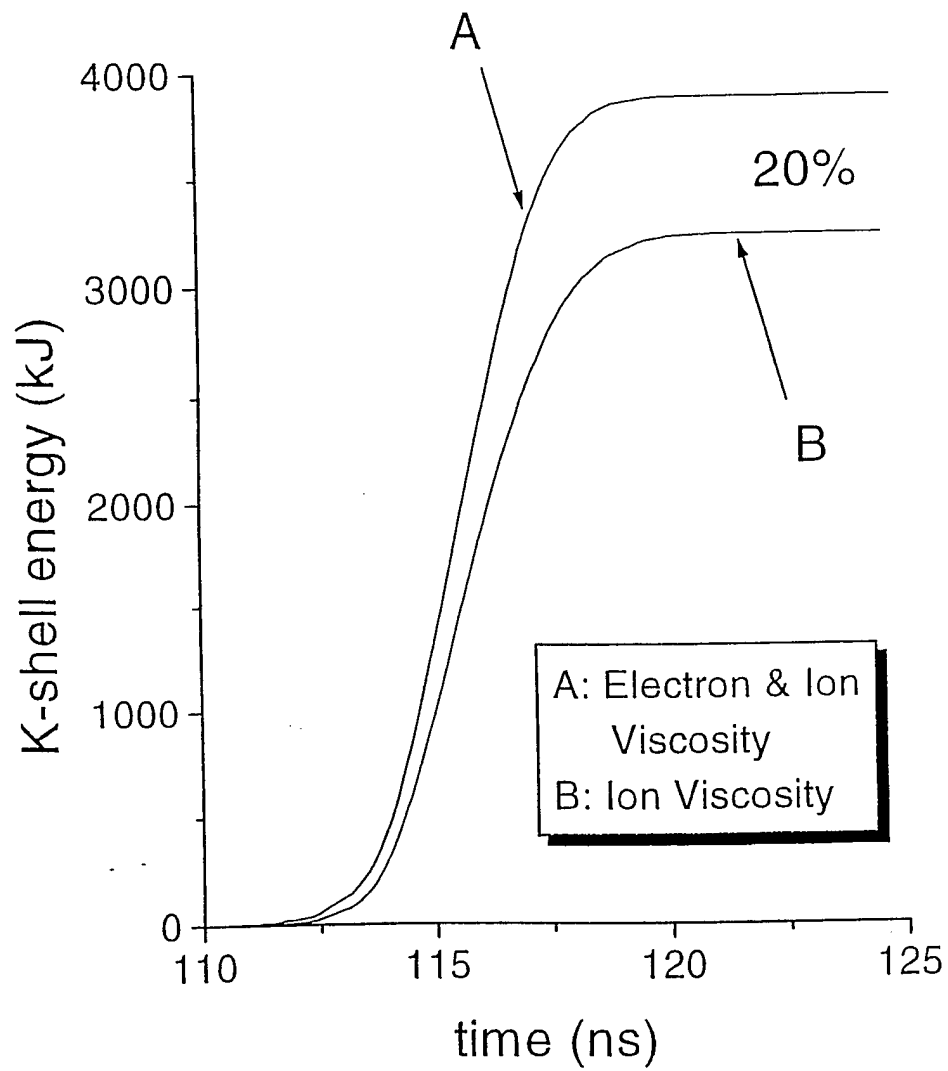


Figure 6

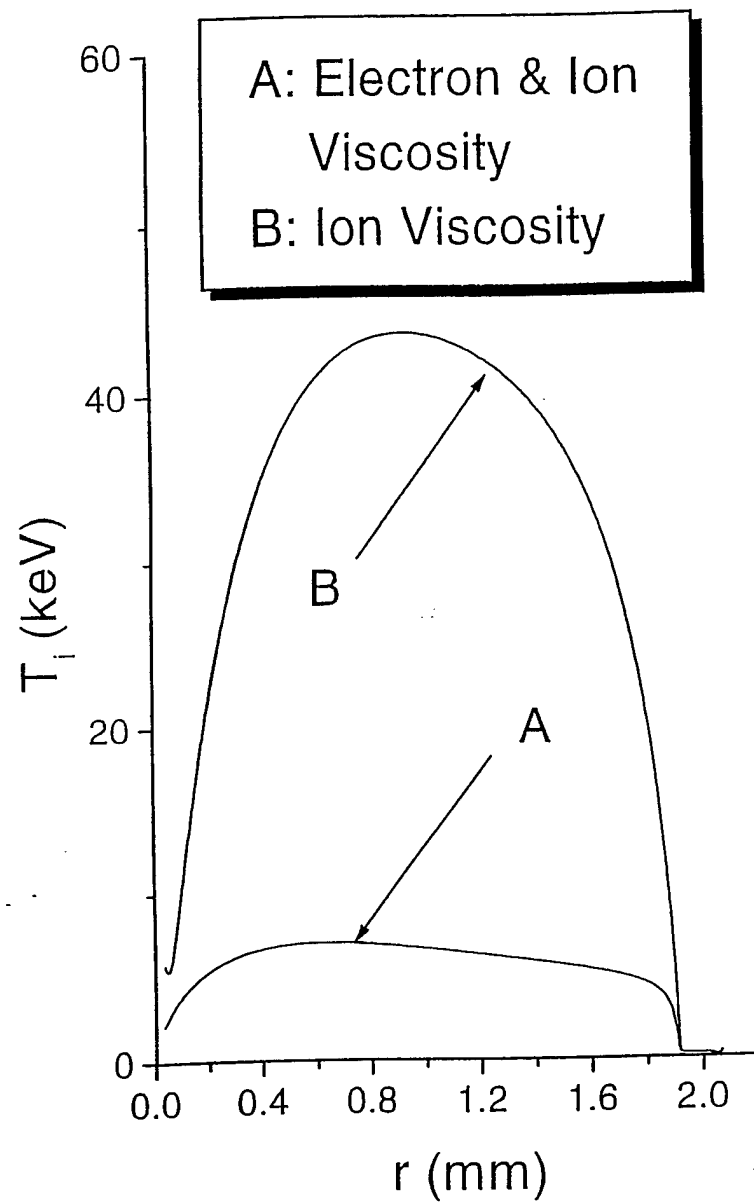


Figure 7

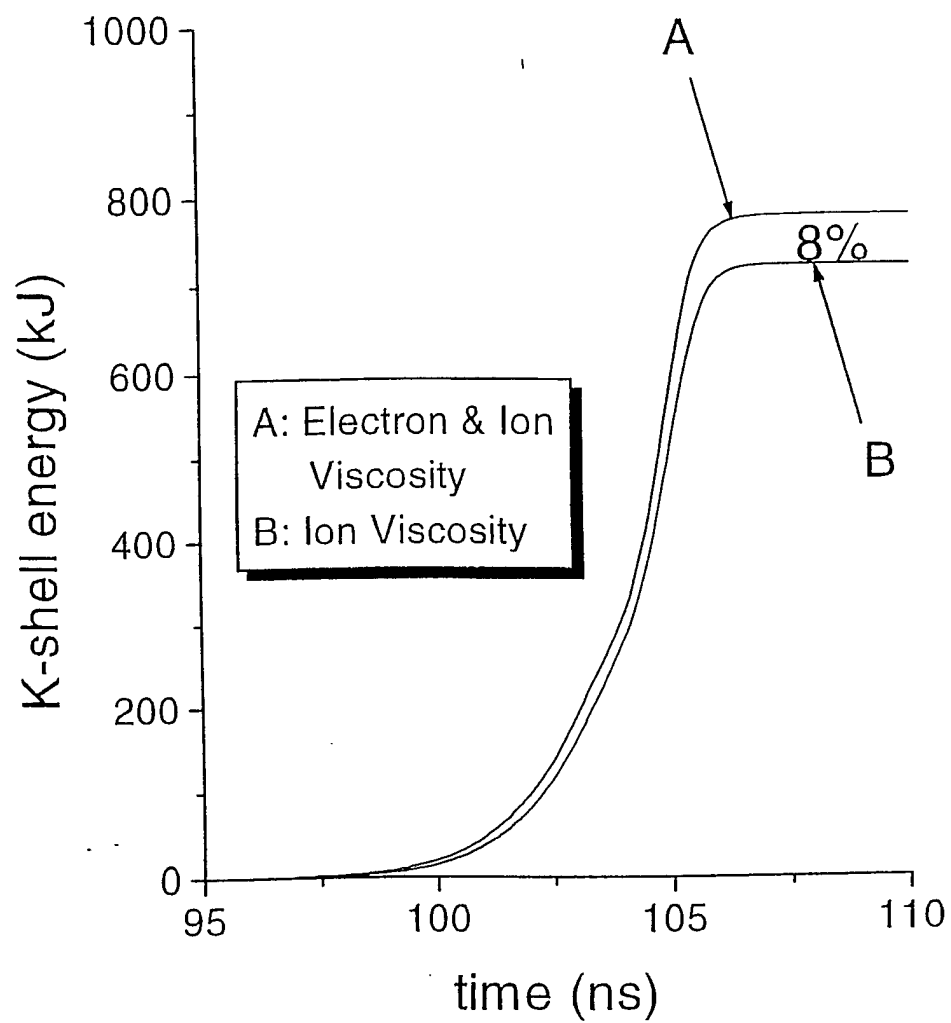


Figure 8

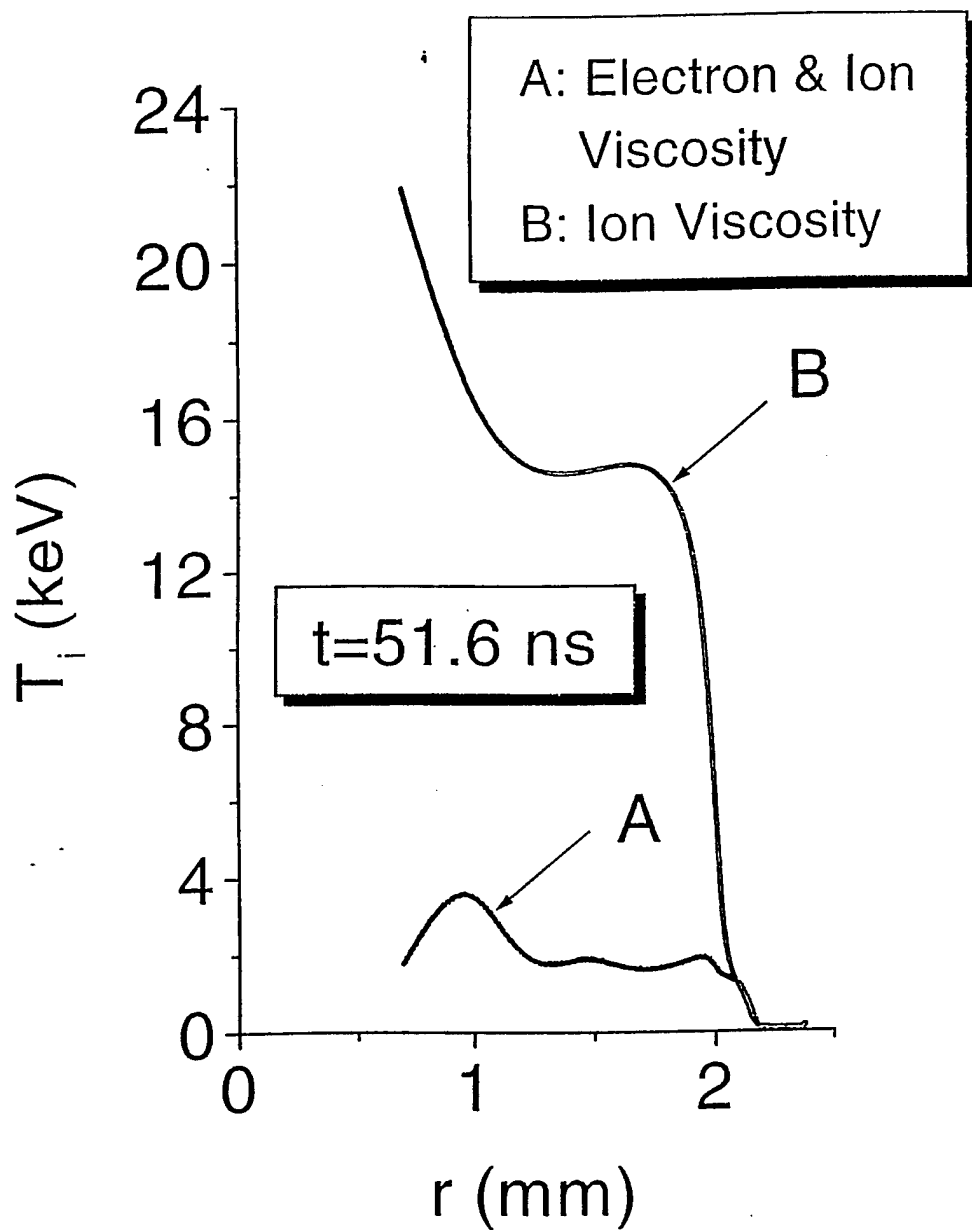


Figure 9

## VII. Improved Bremsstrahlung Radiation Production by Electrode Decontamination

The focus of this work is on the need to demonstrate on Decade the improvements seen in bremsstrahlung radiation production from heating the tantalum anode to white-hot temperatures. Last year a test on the Gamble II machine at NRL, white-hot tantalum anodes showed a noticeable increase in radiation dose rate, and in radiation pulse width. This year the same experiment was repeated with better diagnostics, and with a heating power source that would work with one of the Decade modules, DM2. The actual experiment on DM2 is presently scheduled for mid- to end March.

As is known, DTRA's flagship radiation simulator Decade has suffered from various ills that were supposed to be solved while the machine was being built. However, when the pulsed power community could only demonstrate a partial solution to the various problems, further construction of the machine was suspended until forward projection of progress would give full confidence that Decade would achieve its specifications. This decision allowed enough time to take a new look at all the various components of a bremsstrahlung machine.

During the 1990's pulsed power researchers in various fields had become convinced that observed limits on quantities such as peak power and pulse length in microwave generators and the fraction of lithium atoms in lithium ion beams were substantially affected by surface contamination of the electrodes. The University of Michigan, for example, had a research program to study these issues in the context of microwaves. One of their alumni, Dr. M. E. Cuneo, managed to demonstrate that the excess hydrogen in ion beams also came from electrode contamination. This work, and many discussions with Dr. A. Fisher, inspired an SBIR proposal to DTRA by Dr. Pereira. This proposal's purpose was to see whether electrode contamination should share the blame for Decade's disappointing performance as projected from experiments on the two Decade modules then existing, DM1 and DM2, and more importantly, to come up with a way to suppress contamination.

The SBIR Phase I research successfully demonstrated that heating the anode to red and orange heat, in the range of 1000 to 1200 K, indeed has a marked effect on the pulse length, a twofold increase. However, the experiments were done on a machine, Dr. Gold's Long Pulse Accelerator at NRL. This generator's parameters scaled to DM1 and DM2, but they were far from identical. To make sure that the increase in pulse length would carry over to the Decade program, two other experiments were necessary. One was

a test of DM2's plasma opening switch on DM1, the other a test of a white-hot tantalum anode on Gamble II.

The main experimenter on the tests were, of course, the scientists who best know the pulsed power machines themselves, Dr. J. Goyer at MPI for DM1, and Dr. B. Weber at NRL for Gamble II. Both tests were successful. Heating the plasma opening switch electrodes on DM1 improved the radiation pulse, in various ways that are detailed in a MPI technical report. The Gamble II test developed the parameters needed for heating the tantalum bremsstrahlung anode to 3000 K without doing damage to the remainder of the system, and demonstrated also that the radiation pulse improves. The results are documented in an NRL technical note, and will be written up in conjunction with the experiment that is now ongoing.

1: The present effort intends to test the white-hot tantalum anode on DM2. The initial experiment on Gamble II heated the tantalum white-hot by a pulse from a capacitor bank that happened to be available at NRL. Early on the best way to heat the anode was not clear. Continuous heating as in the earlier experiment did not seem particularly practical, so we settled on a heating technique with an electrical pulse as first suggested by NRL. Contrary to the usual microsecond pulses, the only pulse that worked well was tens of milliseconds long, at the limit of what the available capacitor bank could provide. And the capacitor bank would be too small (and not available) at DM2.

The proper source for such slow pulsed power, as first suggested by NRL, is to use a series-parallel combination of high quality lead-acid batteries. A convenient way to measure the current was improvised that allowed the experiment to proceed without hiccups. For the DM2 experiment the current shunt has been replaced by a standard unit.

2: Hot tantalum suppresses two sources of protons. One is surface contamination, the other hydrogen absorbed in tantalum's bulk. Surface contamination can be handled in other ways also, e. g., discharge or microwave cleaning, and in earlier work both these techniques were tried. Both had positive effects. However, the hydrogen hidden inside the tantalum stays there. In fact, tantalum heated to 1500 K or so is actually a hydrogen getter, absorbing hydrogen from the vacuum until a new, lower, pressure equilibrium is reached. White-hot tantalum, with temperature exceeding 2300 K or so, again loses the hydrogen. The question is, how fast?

In the earlier Gamble II experiment we had stayed with an estimate of the diffusion time, because the tantalum in Gamble II is so thin that the diffusion time turned out to be almost an order of magnitude shorter than the heating time. However, on DM2 the tantalum is twice as thick, 0.1 mm, and diffusion is 4 times slower. Then, the two timescales are more or less on the same order. For this reason a more complete calculation of hydrogen diffusion becomes useful.



Two independent calculations were performed giving essentially the same results. The hydrogen concentration in the tantalum drops by at least two orders of magnitude over the 500 ms long heating pulse, even for the thicker DM2 tantalum.

3: Suppression of the ion current was originally measured by with an electrical method. However, the signals were subject to interpretation. In an attempt to diagnose the ions more directly, a rudimentary ion mass spectrograph that could just fit in the available space was tried. In the discussions about the use of this instrument it appeared that a nuclear activation technique pioneered earlier by NRL would be easier to implement. His nuclear activation measurements demonstrate directly and convincingly that a white-hot tantalum suppresses the proton current coming from the anode, by more than two orders of magnitude (estimated at 400-fold).

4: Tantalum stretching on Gamble II was done in only a single direction. The experimental procedure is to clean the tantalum by a first heating pulse, and then shoot the machine at the end of a second heating pulse. Unidirectional stretching makes the tantalum wavy in a single direction, along the stretch. To avoid this problem on DM2 a way to stretch tantalum in the radial direction was designed and implemented. Whether this approach is successful will be known in the near future.

## Hydrogen diffusion through hot tantalum

N. R. Pereira

Ecopulse, Inc,  
PO Box 528, Springfield, VA, 22150

With sufficient current density, the electrons in a bremsstrahlung diode can heat up the tantalum anode to such a high temperature that the material evaporates completely. Any light atoms liberated from the surface early in the pulse, e.g., loosely bound water or strongly bound oxides or nitrides, may then be swamped by the hydrogen that was stored in the tantalum's bulk. The surface is of course important, and surface properties usually dominates in most common circumstances even though the surface contains little material. On the surface there are light atoms in perhaps a few monolayers, each of which is maybe 0.1 nm thick. All the surface layers together are then at most 1 nm or so. The tantalum itself is 100 000 nm thick, and it takes only a very small fraction of light ions in the bulk tantalum to exceed what is on the surface. Therefore, the maximum density  $N_0$  of hydrogen (or other light atoms) inside the tantalum must be brought down to below something like 10 ppm before light atoms from the bulk can be excluded as contributing to a hydrogen (or other light atom) plasma in the diode gap.

Earlier experiments have demonstrated that heating the tantalum close to its 3200 K melting point before the shot has a strong beneficial effect on diode behavior. Presumably, the reason is that hydrogen or other light atoms have diffused out from the tantalum's bulk, and also disappeared from the surface, so that there remain only high atomic number atoms. These are heavy and slow, and it takes them much longer than the pulse time before they can enter the diode gap. Then, the discharge is over.

The tantalum in a continuation experiment is twice as thick as the tantalum used earlier, so that diffusion is slower and perhaps too slow. This note estimates the diffusion time in a one-dimensional slab of tantalum that is heated by a slow (30 ms) electrical pulse, in preparation for the 100 000 times faster (100 ns) high power pulse that follow after a few 100 ms.

Assuming classical diffusion (and thereby ignoring all kinds of realistic and very interesting and perhaps relevant phenomena such as the difference between the surface and the bulk in capturing hydrogen, the effect of grain boundaries, etc), the one-dimensional linear diffusion equation for the density  $N(x, t) = N_0 n(x, t)$  of hydrogen is

$$\frac{\partial n}{\partial t} = D(T) \frac{\partial^2 n}{\partial x^2}, \quad (1)$$

where  $D(T)$  is the linear diffusion coefficient of hydrogen through tantalum, and  $x$  and  $t$  are the usual space and time. The diffusion coefficient  $D(T)$  depends on the temperature  $T$ , but the temperature is assumed to be the same throughout the tantalum slab. Then  $T = T(t)$ , and also the diffusion coefficient is only a function of time. Any skin effect in the heating of tantalum is thereby ignored.

The normalized hydrogen density  $n(x, t)$  vanishes when there is vacuum on both tantalum edges, at  $d/2$ , so that the simplest spatial dependence that satisfies Eq. (1) is  $\cos(\pi x/d)$ : here  $d$  is the thickness of the tantalum. This simple cosinusoidal profile decays in time according to

$$\frac{\partial n}{\partial t} = -\frac{D(T)\pi^2}{d^2}n(t), \quad (2)$$

where  $n = n(t)$  is the normalized density. Initially, at time  $t = 0$ ,  $n(t = 0) = 1$ .

Since the diffusion is largest at the highest temperature  $T_m$  it is convenient to normalize to unity according to  $D(T) = D_m D'(T/T_m)$ , with the function  $D'(T/T_m) = 1$  at  $T = T_m$ . However, the temperature dependence<sup>2</sup> of the diffusion coefficient follows the usual Arrhenius factor  $D(T) = D_0 \exp(-E_0/kT)$  up to the highest temperature that it has been measured (600 K). Extrapolating this relationship to the much higher temperatures of interest here gives

$$D(T) = D_0 \exp(-T_0/T), \quad (3)$$

where  $D_0/e = 1.5 \times 10^{-8} \text{ m}^2/\text{s}$  is the diffusion coefficient at the characteristic temperature  $T_0 = 1400 \text{ K}$ , so that  $D_0 = 4 \times 10^{-8} \text{ m}^3/\text{s}$ . Then the equation for the normalized cosinusoidal hydrogen density becomes

$$\frac{\partial n}{\partial t} = -\frac{D_0\pi^2}{d^2} \exp[-T_0/T(t)]n(t). \quad (3)$$

Equation (3) is an ordinary differential equation that can perhaps be solved as part of the spreadsheet program that already contains similar differential equations for the temperature  $T(t)$ , the voltage  $V(t)$ , the current  $I(t)$  and the resistance  $R[T(t)]$ .

For estimates to set the heating pulse a normalized form of Eq. (4) is more appropriate, since convenient assumptions about the temperature profile might give analytic insight in how many characteristic diffusion times are enough to reduce tantalum's hydrogen content to an acceptable value. The normalized form is

$$\frac{\partial n}{\partial \tau} = -\exp[-T_0/T(\tau)]n(\tau), \quad (4)$$

where the normalized time  $\tau = t/t_0$  and  $t_0 = d^2 e/D_0 \pi^2$  is the diffusion time at the characteristic temperature  $T_0$ . A more logical definition of a characteristic time would exclude the factor  $e$ : the one chosen here is more convenient, because the combination  $D_0/e$  is the number read from the Arrhenius plots.

At  $T_0 = 1400 \text{ K}$  the diffusion coefficient for hydrogen in tantalum is  $D_0/e = 1.5 \times 10^{-8} \text{ m}^2/\text{s}$ . For a 0.1 mm thick piece of tantalum heated to 3000 K the diffusion time is then  $t_0 = 67 \text{ ms}$ . The electrical heating pulse in the previous experiment is about 30 ms, but for that experiment the tantalum was half as thick and the diffusion time was 17 ms, four times shorter than now. Certainly then, but also now, the diffusion time is short enough for the density to decay appreciably, especially since the temperature decays slowly after heating. The total time that the tantalum is hotter than  $T_0 = 1400 \text{ K}$  may be a few 100 ms, so that it seems safe to ignore the details as expressed by Eq. (4).